



SAPIENZA
UNIVERSITÀ DI ROMA

PhD Thesis

La Sapienza University of Rome, Faculty of Engineering, PhD school of Information and Communications Technologies

Submitted to obtain the title of
Ph.D. in **Electronics Engineering** at La Sapienza

Computational modeling and measurements of electromagnetic fields for diagnostics and therapeutics

Elena LUCANO

<i>Rapporteur:</i>	Prof. N. Kuster	ETH Zurich
	Prof. P. Russo	Universita' Politecnica delle Marche
<i>Supervisor:</i>	Dr. M. Liberti	La Sapienza University of Rome
<i>Second Supervisor:</i>	Dr. E. Piuzzi	La Sapienza University of Rome
<i>Host Supervisor:</i>	Dr. L.M. Angelone	Food and Drug Administration, USA

October 2016

Revised on February 2017 based on Rapporteur comments
at La Sapienza University of Rome, Rome, Italy

Contents

Summary	1
I Computational modeling and measurements of an MRI RF birdcage body coil	3
1 Background and State of the Art	5
1.1 Brief theoretical background of MRI	6
1.2 Radiofrequency coil design and theory	12
1.2.1 RF birdcage coil typologies	12
1.2.2 Other RF coil typologies	13
1.2.3 Field polarization	15
1.2.4 Induced electric field	16
1.3 Methodologies for computational modeling	17
1.3.1 Computational methods	18
1.3.2 VVUQ: Verification, Validation and Uncertainty Quantification	21
1.4 Numerical and physical phantoms in MRI	24
1.4.1 Numerical phantoms	25
1.4.2 Physical phantoms	27
2 Numerical implementation and verification of the RF birdcage coil model	29
2.1 Frequency response and implementation of the resonant circularly polarized mode	30
2.2 Resonance of the FDTD-based coil model convergence study	37
2.3 Sensitivity of electric and magnetic field vs. input parameter	41
2.3.1 Input signal frequency	41
2.3.2 Numerical coil losses	43
2.4 Numerical modeling of the physical phantoms	46
2.5 Effects of Tuning Conditions on Near Field of MRI Transmit Birdcage Coil at 64 MHz	52
3 Assessing the electromagnetic fields generated by a radio-frequency MRI body coil at 64 MHz: defeaturing vs. accuracy	59
3.1 Abstract	59
3.2 Introduction	60
3.3 Materials and Methods	62
3.3.1 Measurements	62

3.3.2	Computational Modeling	64
3.3.3	Accuracy of Numerical Models Versus Measurements	66
3.4	Results	67
3.4.1	Power Requirements	67
3.4.2	Frequency Response	69
3.4.3	EM Fields	69
3.5	Discussion	71
3.5.1	Limitations	75
3.6	Conclusions	76
3.7	Uncertainty quantification	76
4	An inter-laboratory computational and experimental study of a radiofrequency coil model at 64 MHz	79
4.1	Abstract	79
4.2	Introduction	80
4.3	Methods	81
4.3.1	Inter-laboratory project	81
4.3.2	Experimental exposure system and load specifications	81
4.3.3	Computational modeling setup	82
4.3.4	Measurements setup	86
4.3.5	Data analysis	87
4.3.6	Uncertainty analysis	88
4.4	Results	89
4.5	Discussion	92
4.5.1	Limitations	94
4.6	Conclusion	94
	Comprehensive Discussion Part I	95
II	Computational modeling and measurements of human body models and phantoms exposed to MRI RF fields	97
5	Background and State of the Art	99
5.1	Assessing safety for patients in MRI	101
5.1.1	Standards and test methods for safety assessment: overview	106
5.1.2	Transfer function approach	110
5.2	MR Conditional medical devices	112
6	Computation modeling of human body models for SAR evaluation	113
6.1	Homogeneous vs heterogeneous models	113
6.1.1	Power absorption	115
6.1.2	Electromagnetic field and SAR distributions	119
6.2	Impact of the vague partial body SAR definition in the MRI safety standard IEC 60601-2-33 on actual patient exposure	124
6.2.1	Partial body SAR limits estimation through cylinders	124

CONTENTS

6.2.2	Partial body SAR limits estimation through uniform human body models	128
7	A Numerical Investigation on effect of RF coil feed variability on global and local electromagnetic field exposure in human body models at 64 MHz	133
7.1	Abstract	133
7.2	Introduction	134
7.3	Methods	135
7.3.1	Computational models of RF transmit coils	135
7.3.2	Models of the human body	136
7.3.3	Excitation variability	137
7.3.4	Quantities of interest	139
7.3.5	Computational model of partially implanted lead	140
7.4	Results	140
7.4.1	Global exposure	140
7.4.2	Local exposure	141
7.4.3	Case study: human body with partially implanted lead	143
7.5	Discussion	144
7.5.1	Limitations	147
7.6	Conclusion	148
7.7	Supplementary material	148
7.8	Effect of RF coil feed on current density and SAR	154
7.9	Evaluation of RF coil feed variability in the superellipsoidal phantom	161
8	AIMD in MRI: evaluation of RF-coupling with leads	169
8.1	Physical phantom for testing of RF-induced heating in leads	169
8.1.1	Test field diversification method for the safety assessment of RF-induced heating of medical implants during MRI at 64 MHz	169
8.1.2	Applicability of the test field diversification method to AIMD	174
8.2	High dielectric material in MRI: numerical assessment of the reduction of the induced local power on implanted cardiac leads	175
8.2.1	Evaluation of a third landmark position: Pelvis	179
	Comprehensive Discussion Part II	181
III	Computational modeling of human head models exposed to low frequency electromagnetic fields	183
9	Background and State of the Art	185
9.1	Medical devices using EM fields for brain stimulation	186
9.1.1	Invasive devices	187
9.1.2	Non invasive devices	188
9.2	Numerical modeling of the quasistatic approximation	191
9.2.1	Theoretical background	191
9.2.2	Numerical Methods and Numerical Software	194
9.3	Admittance method	196

9.3.1	Applicability of the admittance method in time domain	198
9.3.2	Applicability of the admittance method to an EQS problem . .	199
9.3.3	Applicability of the admittance method for anisotropic tissues	201
10	Time resolved dosimetry of human brain exposed to low frequency pulsed magnetic fields	205
10.1	Abstract	205
10.2	Introduction	206
10.3	Methods	209
10.3.1	Brain model	209
10.3.2	Stimulation signal	209
10.3.3	E field calculation	209
10.4	Results	212
10.4.1	Signal features	212
10.4.2	E and J fields calculation	212
10.5	Discussions	215
10.6	Conclusion	217
	Conclusions	221
	Appendices	225
	A List of Acronyms	227
	B High resolution Figures	229
	Bibliography	247
	Curriculum Vitae	281

Summary

Electromagnetic fields are commonly used in health care for diagnostic and therapeutic applications. The evaluation of patient safety and effectiveness of the device is a fundamental step toward the use of EM fields in medical applications. Dosimetry has been traditionally evaluated using experimental methods and over the past decade, computational modeling has been increasingly used to complement the experimental results. Computational modeling allows performing a systematic analysis of many variables affecting the interaction between the human body and the electromagnetic field, which cannot be accounted for experimentally. Numerical analysis also has reduced costs and increased reproducibility compared to experimental measurements. The validation of the numerical models is necessary to determine if the model is an accurate representation of the physical phenomenon within a specific context of use. In this thesis the use of electromagnetic fields in both diagnostics (first two sections) and therapeutics (third section) was investigated in their numerical and physical implementation.

Among all the medical applications of electromagnetic fields used for diagnostics, magnetic resonance imaging (MRI) is one of the most diffused imaging techniques in the clinical practice, with over 33 million examinations a year in the US. The success of MRI is due to its clinical versatility, the use of non-ionizing radiation, and the high soft-tissue contrast. MRI systems take advantage of the capability of the nuclei of the atoms, composing the human tissues, to be magnetically polarized by external fields. In particular MRI scanners use the combination of three magnetic fields of different nature (i.e., static, time-varying, and spatially-varying) to generate the final image. Applications involving MRI are extensively described in the first two parts of this thesis, with particular focus on the study of the radiofrequency (RF) time-varying component of the magnetic field. Due to the specific nature of the atoms that are magnetized (i.e., typically hydrogen), the frequency range of the time-varying field used in MRI is in the RF.

The first part of the thesis (i.e., Part I) reports the numerical implementation of RF coils, typically used for MRI scanners. The implementation covers the main fundamental steps needed to generate and validate the numerical model against measure-

ments with a physical coil. Comparisons of the computed distribution of the electromagnetic fields against measurement in a coil unloaded and loaded with a phantom are also included in Part I. Phantoms were used to validate the numerical models, and as a first step of exposure assessment for a dosimetric study.

In the second section of this thesis (i.e., Part II) the analysis was focused on patient exposure to a given coil. The study included numerical human body models, and identifying specific problems related to the inclusion within the MRI environment of medical devices intended for treatment. With respect to the patient exposure, investigations were analyzed for different implementation of the RF coil and human body model characterizations. Additional analysis of exposure was conducted with respect to the interaction between the generated RF field and the possible presence of medical devices in the patient. Results presented were compared against guidelines of international standards regulating the patient exposure in MRI.

Electromagnetic fields are also used by medical devices for treatment of specific health and behavioral pathologist. The relevance of the use of electromagnetic field has been recently underlined by the new term *electroceutical* coined in 2013 by the bioelectronics research group at GSK (London) headed by Kristoffer Famm. The new terms identifies the power of using electromagnetic fields as an option over drug treatments. The last part of this thesis presents some of these medical devices, stressing the interest on the physical prospective of the interaction between the fields and the human body. The specific goal of the section will be to show that accurate numerical models can be a support for the understanding of the mechanisms and biological interactions in an electroceutical perspective.

Chapters 3 and 10 have been published in peer-reviewed journals. Chapter 3 was additionally presented to standards building bodies, and the Joint Working Group, working on the MRI product standard related to implantable medical devices, is including the paper as reference of the third edition of the TS ISO 1097. Chapters 4 and 7 have been submitted to peer-reviewed journals and are currently under the first and second step of revisions. The results reported in Chapter 7 raises the issue of a missing standardized methodology for compatibility testing of partially implanted devices.

Each Part begins with a general introduction and with background of the state of the art on the specific topic. Then the work performed and the new results achieved in this context are presented including future developments of the work. Finally Part I and Part II end with a Comprehensive Discussion on the specific topic contextualizing the main outcomes.

Part I

Computational modeling and measurements of an MRI RF birdcage body coil

Chapter 1

Background and State of the Art

Magnetic resonance imaging (MRI) is one of the most used radiological diagnostic tools [1]. It is based on the physical phenomenon of nuclear magnetic resonance (NMR). In 1937 the Columbia University Professor Isidor I. Rabi working in the Pupin Physics Laboratory in New York City, observed for the first time the ability of atomic nuclei to show their presence by absorbing or emitting radio waves when exposed to a sufficiently strong magnetic field. In his paper published in 1936 [2], he reported:

"The results of the theory may be summarized in the statement that if the angular velocity of rotation of the field is small compared with the Larmor frequency $\omega = 2\pi g\mu_0 H/h$ the atom will remain space quantized with respect to the field direction with the same component m of its total angular momentum F (adiabatic transformability); if the angular velocity is of the same order of magnitude as the Larmor frequency there will be non adiabatic transitions to states $m' \neq m$."

This phenomenon was firstly named "nuclear magnetic resonance". However Professor Rabi performed his experiments only in vacuum for individual nuclei isolated from each another [3]. It would not be until 1945 when the two teams led by Felix Bloch and Edward Mills Purcell independently demonstrate NMR in condensed matter. The results of both teams were published within one month, on December 1945 the work of Purcell demonstrated the NMR in paraffine [4], and on January 1946 the one of Bloch demonstrated the process in water at room temperature [5].

The second turning point in the history of the NMR was made by Herman Yaggi Carr as a graduate student of Professor Purcell. In 1950 Hahn [6] introduced for the first time the "spin echoes" to observe the phenomenon of the nuclear magnetic resonance, where he defined:

"echos refer to spontaneous nuclear induction signals witch are observed to appear due to the constructive interference of processing macroscopic moment vectors after more than on r-f pulse has been applied."

As Carr was trying to improve the signal to noise ratio of the "spin echoes" technique introduced by Hahn, in his 1953 paper [7] he described for the first time the use of gradient fields in NMR:

"A gradient G may be obtained at the sample by placing symmetrically on either side of the sample two long current carrying wires or two circular turns of wire. The current directions should be such that the fields oppose."

The idea of using gradient fields was later developed by Paul Lauterbur. In 1973 he published a paper in Nature [8] using for the first time the gradient fields to generate a 2D image. He reported that:

"One of the methods of constructing a two-dimensional projected image of the object, as represented by its H_2O content, is to combine several projections, obtained by rotating the object about an axis perpendicular to the gradient direction (or rotating the gradient about the object), using one of the available methods for reconstruction of objects from their projections."



Figure 4 Proton n.m.r. magnetogram of a cherry-stone clam (small Venus mercenaria) viewed edge-on. The animal was alive and enclosed within its shell. The bright regions in the photographically processed image represent regions of high projected water content. The computer output has been photographically filtered and enhanced.

Figure 1.1: First NMR image of a living animal obtained by Lauterbur in 1974.)

The main contribution of the method was that the magnetic gradient field varies in space, and therefore the Larmor frequency of the proton spins varies in space. Hence if the magnetic resonance signal is measured and separated into different frequencies (Fourier analysis), each frequency component corresponds to the signal from a different location. In the following year (1974) Lauterbur published [9] the first 2D NMR image of a living animal, a clam (Figure 1.1).

From then it was clear that the three prime movers under the formation of an NMR image were the main static field used to align the nuclei, the radio frequency field to cause the nuclear magnetic resonance phenomenon, and lastly the gradient fields for spatial information. Clinical MRI scanners used daily in the medical field as spectroscopy technique, ground their operating principle on the NMR phenomenon.

1.1 Brief theoretical background of MRI

Since the discovery of the NMR phenomenon and its applicability as imaging technique, MRI scanners have been developed and continuously upgraded to improve the

1.1 Brief theoretical background of MRI

final image quality. However, even with all considerable progress made over the years, all the MRI scanners routinely used in clinical and research setting are still based on the same original theoretical founding. Hence current MRI scanners generate the final diagnostic image based on the use of static field, RF field, and gradient fields. Herein a brief description of the three fields used will be introduced following the classical physical interpretation [10].

Static field — Static fields are needed to force the randomly directed spins of the atoms to align in one direction. Once a static field B_0 is applied the spins of the protons inside the nucleus align in two quantum energy states (Zeeman effect) that are separated by an energy gap (ΔE) [10]. Thus each atom with an odd atomic number would show a total elementary magnetization moment ($\vec{\mu}_s$) dependent by the spin angular momentum (\vec{S}), and defined by:

$$\vec{\mu}_s = \gamma \vec{S} = \gamma \frac{\hbar}{2} \quad (1.1)$$

Where γ is the gyromagnetic ratio proper of each atomic element, and $\hbar = h/2$ is the reduced Planck constant. The elementary magnetization moment shows a precessional motion around the main axis defined by the static field (typically identified by the z-axis), and characterized by an angular frequency (ω) known as the Larmor frequency. This frequency is dependent on the energy gap ΔE between the two quantum energy states, as

$$\omega = 2\pi \frac{\Delta E}{h} \quad (1.2)$$

Because the energy gap is directly proportional to the elementary magnetization moment, as defined by:

$$\Delta E = 2\vec{\mu}B_0 = 2\gamma \frac{\hbar}{2} B_0 \quad (1.3)$$

the Larmor frequency can be defined with respect to the applied static field B , as:

$$\omega = \gamma \cdot B_0 \quad (1.4)$$

Within the medium, because the number of protons at the low energy state exceeds the one at the high level of state, a total net magnetization moment \vec{M} equal to the sum of all the elementary atom magnetization moments $\vec{\mu}$ can be defined.

The stable and homogeneous static magnetic field is produced by a large magnet that is the main hardware of an MRI system. Typically, the strenght of static field used in clinical scenario is in the range of 0.1 T to 3 T [10]. Thus up to six million times

higher than earth's magnetic field (i.e., $\sim 0.5\mu T$) are used. For medical research, a few "ultra-high field" systems operating from 7 T to 10 T, and systems up to 11.75 T are in development [11–13].

The MRI static fields can be generated by means of permanent magnets, electromagnets or superconductive magnets. Both permanent magnets and electromagnets are made of ferromagnetic materials that have the capability of being magnetized. Ferromagnetic materials can be categorized as "hard" and "soft". The hard one has the capability of being permanently magnetized during manufacture by aligning their internal microcrystalline structure. Permanent magnets typically operate at field strengths ranging from 0.2 T to 0.7 T. Conversely the soft ferromagnetic materials can be temporarily magnetized through electric current, but they lose the magnetization as the current stops. An electromagnet is made from a coil of wire wrapped around a core of soft ferromagnetic material. These coils can be superconductive or resistive and range from 0.5 T to 1.2 T. MRI scanners using permanent magnets or electromagnets are typically the ones characterized by an open bore hardware design. A third category of magnets used to produce the MRI static field are the superconductive magnets. These are electromagnets made from coils of superconducting wire. Superconductive wires can conduct much larger electric currents than ordinary wires, thus with such magnets intense and stable magnetic fields can be generated. To allow the wire to act as superconductor, the temperature of the structure needs to be as cool as required by the material used, typically around tens of degrees Kelvin. Usually liquid helium is used to keep the temperature low at the defined temperature. These type of magnets characterize systems with a close bore and can work stable at "ultra-high field" strength.

Radiofrequency field — Once the magnetization vector \vec{M} is created by the static magnetic field (B_0), a rotating magnetic field (\vec{B}_1) is used to excite \vec{M} and generate the physical phenomenon of the nuclear magnetic resonance. In order to excite \vec{M} the frequency of \vec{B}_1 has to be equal to the Larmor frequency of the atomic species that needs to be excited. The most common MRI systems work exciting the hydrogen atoms (^1H) as the body is made for 70 % of water. The gyromagnetic ratio of ^1H is $42.577 (MHz/T)/(2\pi)$, thus for a static field of 1.5 T the rotating field used to excite the atoms is in the range of the radiofrequency (RF) fields. In particular for the ^1H eq 1.4 defines a Larmor frequency equal to 63.86 MHz. Recently MRI systems based on Sodium (^{23}Na) have been suggested to generate high resolutions images with information on metabolic processes [14]. Because gyromagnetic ratio of the ^{23}Na is 3.8 times lower with respect to the ^1H (i.e., $11.262 (MHz/T)/(2\pi)$), frequencies involved are 3.8 times higher.

1.1 Brief theoretical background of MRI

When the rotating \vec{B}_1 field is applied on the magnetized atoms, these are forced out from their equilibrium position along the z-axis. The resulting magnetization vector \vec{M} experience the torque of the static field and is rotated to lay in a different plane with respect to the original one. The angle by which the \vec{M} is rotated is named "flip-angle". The flip-angle (α) experienced by \vec{M} is dependent on the atom species used, the magnitude of the rotating field \vec{B}_1 , and on the duration of the excitation (t):

$$\alpha = \omega_1 \cdot t = \gamma \cdot B_1 \cdot t \quad (1.5)$$

where ω_1 is the rotational or precessional frequency of the magnetization vector. Typically more the one RF excitation is produced within the imaging sequence. The first one generally excite \vec{M} by a 90° angle, such that it lies on the transverse plane of the static field (i.e., the applied \vec{B}_1 is perpendicular to B_0). Because it is typically defined that the B_0 field is applied on the z-axis direction, then with a 90° pulse the \vec{M} would lie on the xy-plane. After the 90° primary excitation, other RF excitations may follow with different flip-angles depending on the specific imaging sequence followed. Common second excitation angles used for imaging are 90° and 180° (spin-echo sequence [7]). For atoms of ^1H , with a typical $\|B_1\|$ field of $1 \mu\text{T}$, a theoretical required duration of the RF excitation would be about 5.9 ms and 11.7 ms , for 90° and 180° respectively. However in real MRI scanner flip-angles are affected by the shape of the RF excitation signal used (e.g., Gaussian, sinc, truncated-sinc), presence of gradient field, and B_0 field inhomogeneities. These effects become particularly problematic as field strengths increase to 3.0 T and above [15].

Once the RF signal used for excite the nuclei is turned off, the excited magnetization vector \vec{M} continue to process about the z-axis at the precessional frequency proportional to the magnitude of the applied \vec{B}_1 field (eq. 1.5). This phenomenon is known as "relaxation". Two different kinds of relaxation can be defined: the "Spin-Lattice", and the "Spin-Spin". The two relaxations are related to different components of the magnetization vector. Once \vec{M} start to process about the z-axis, it can be decomposed on two components one parallel to the z-axis (i.e., \vec{M}_z), and the other lying on the xy-plane (i.e., \vec{M}_{xy}). The "Spin-Lattice" refers to the relaxation of the \vec{M}_z component, and it identifies the transfer of energy between the nucleus and the lattice (i.e., what surrounds the atom). The "Spin-Lattice" relaxation is quantified by the T_1 time quantity. Whereas, the "Spin-Spin" refers to the relaxation of the \vec{M}_{xy} component, and it identifies the interactions between spins. The "Spin-Spin" relaxation is quantified by the T_2 time quantity. The T_1 and T_2 relaxation times are tissue-dependent, and they are part of the information included in the final MRI image.

Out of all the hardware components needed to assemble an MRI scanner in the early

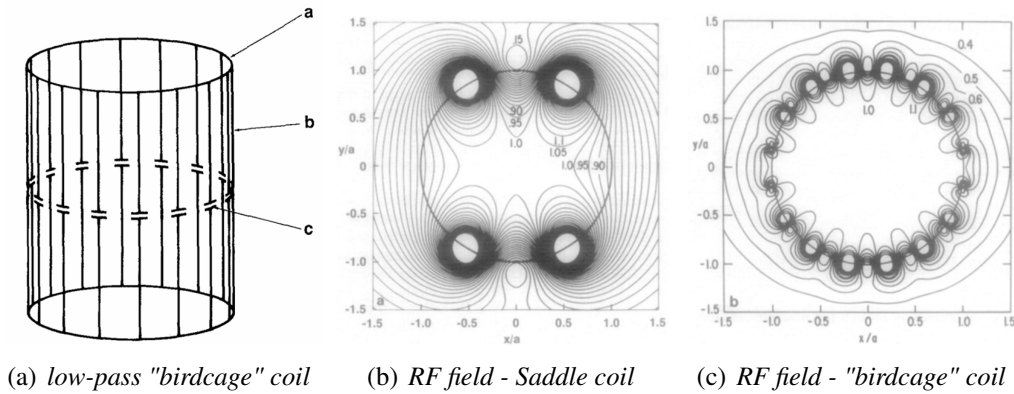


Figure 1.2: The coil typology presented by Hayes et al. in 1985 [18]. (a) structure of the low-pass "birdcage" coil, (b) contour plot of RF field strength produced in the transverse mid-plane of a 270 mm diameter saddle coil, (c) contour plot of RF field strength produced in the transverse midplane of a 285 mm diameter 16-wire birdcage resonator.

1980s, the RF coil was one of the least well understood [16]. At the early stages of the MRI systems, RF signals for atoms excitation were produced using saddle coils. This type of coils are able to produce very homogeneous and stable \vec{B}_1 field that is essential for a high quality of the images. However these type of coils were not suitable for imaging large samples because they would lose their homogeneity. In 1981 Hoult presented his work about techniques to built RF coils for MRI at the International Symposium on Nuclear Magnetic Resonance Imaging held at the Bowman Gray School of Medicine, Wake-Forest University (Winston-Salem, N.C.) [17]. In his work he made the assumption that saddle coils could not be used for total length of conductors more than about $1/20^{th}$ of a wavelength long. Thus, considering a length of the trunk of 70 cm, the maximum frequency for a saddle coil would be 21.4 MHz and a corresponding static field of 0.5 T. Nevertheless, efforts were already put in increasing the strength of the static fields to allow for high resolutions images, as the signal-to-noise ratio (SNR) is directly proportional to the strength of B_0 [10]:

$$SNR \propto \frac{B_0^2}{\sqrt{B_0^2}} = B_0 \quad (1.6)$$

To overcome this issue and allow for imaging of large samples, such as patient thorax, with a good SNR, Hayes and colleagues in 1985 [18] introduced their invention: the so called low-pass "birdcage" coil (Figure 1.2a). The new coil typology was able to generate a magnetic field with a greater homogeneity with respect to a saddle coil for a frequency of 64 MHz (Figure 1.2 b and c).

From its invention in 1985, the birdcage resonator is still used in clinical body scan MRI systems, whereas saddle coils are still used for imaging of the knee [19, 20]. Reporting the development of the RF birdcage coil resonators over the years, Hayes in

1.1 Brief theoretical background of MRI

2009 wrote [16]:

"For 25 years, the birdcage resonator and its variants have been the volume coil of choice for MRI. As the title of the original publication stated, it has been an efficient, highly homogeneous RF coil for whole-body NMR imaging at 1.5 T as well as at a wide range of other frequencies."

RF coils are additionally used as receiver coils to detect the relaxation of the magnetization vector \vec{M} . In fact, the precessing magnetization is able to generate a small electromotive force that generates a variation of flux in the coil that is now used as a receiver. The resulting time signal in the coil is commonly named "free induction decay" and represent the MR signal that is recorded and then converted into the final image. The same coil used as transmit coil for the excitation signal can also be used as receiver. However, typically separate transmit and receive system are used in the design of MRI systems.

Gradient field — The precessional frequency of \vec{M} is dependent on the magnitude of the applied \vec{B}_1 field, that in turn is dependent on the applied static field B_0 . Then, because is not possible to excite a single region, if the entire body of the patient is exposed to the same static field, then all the spins and resulting magnetization vectors would possess the same resonance frequency ω_1 . To allow for spatial encoding of the signal, linear gradient magnetic field are applied in addition to static B_0 . As a result, the resonant frequencies of the hydrogen nuclei are spatially dependent within the gradient. With the gradient fields applied, the direction of the combined static field (B_c) is still along the z-axis, but the strength varies within the volume location. Three gradients fields G are typically used along the three orthogonal axes, such that:

$$B_c = B_0 + G_x x + G_y y + G_z z, \text{ with } \begin{cases} G_x = \frac{dB_z}{dx} \\ G_y = \frac{dB_z}{dy} \\ G_z = \frac{dB_z}{dz} \end{cases} \quad (1.7)$$

Thus, the frequency of the spins become a function of spatial location:

$$\omega(x) = \gamma B_0 + \gamma G_x x \quad \omega(y) = \gamma B_0 + \gamma G_y y \quad \omega(z) = \gamma B_0 + \gamma G_z z \quad (1.8)$$

With the application of the gradient fields, the time signal detected by the RF receiver coil (i.e., free induction decay) contains the contribution of oscillators emitting signals over a range of frequencies. For example if a gradient field in the x direction of 10 mT/m is activated, the resulting for the ^1H varies of 425.8 kHz/m. Typical range of field strength used by gradient coils is 10-400 mT/m. The spatial information are then reconstruct by using the emitted resonant RF-frequency and phase information.

Historically gradients coil were implemented following Helmholtz or saddle coil designs. Nowadays however, more complex designs are manufactured. Typically MRI scanners use distributed windings in a "fingerprint" pattern. Fingerprint coils consist of multiple metallic of complex patterns on a cylindrical layout. The are preferred because they have a high switching efficiency and can be easily shielded to avoid flowing of eddy-currents due to the the RF field [21].

1.2 Radiofrequency coil design and theory

The work described in this thesis is focused on the study of the electromagnetic (EM) fields generated by the transmit RF birdcage coils. A more detailed description of the electrical implementation and theory of RF coil used in MRI will follow.

1.2.1 RF birdcage coil typologies

The birdcage body coils are implemented using two circular rings named end-rings connected by a certain number N of straight longitudinal connectors named rungs or legs [22]. The RF magnetic field produced by the birdcage coil is the result of the currents flowing in the rungs, that can be defined for each rung n , as:

$$I_n = I_0 e^{i2\pi n/N} \quad (1.9)$$

where N is the number of rungs, and I_0 the maximum current. The currents flowing in the coil system is the result of the resonance of each network component of the coil structure.

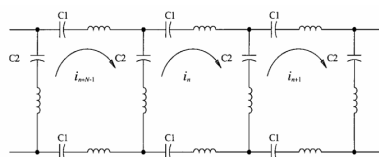


FIG. 1. A section of the birdcage transmission line showing mesh currents I_n . The line is periodic, that is, the left- and right-most ends are connected together.

Figure 1.3: Leifer simplification of the birdcage coil network [22].

In his 1997 work, Leifer [22], accurately describes the theory behind the birdcage resonator. Leifer solves the birdcage coil using Kirchoff's mesh equations on the coil network reported in figure 1.3. Leifer described the network as a generalized "band-pass" birdcage containing capacitors in both the end-rings and rungs. From the same structure "low pass" and "high pass" coils as special cases when $1/C1$ or $1/C2$ is respectively set to zero. The three coil typologies are characterized by a different resonant "mode".

In fact, because of its geometry, the birdcage resonator shows a periodic or cycling nature. The periodic waves produced are named "mode" of resonance and their number is dependent on the number of coil rungs, such that the mode of resonance are that who show an integral number of wavelengths around the coil structure each with a different

1.2 Radiofrequency coil design and theory

field pattern and frequency of operation. Theory shows that the number of resonant modes in a birdcage coil is strictly related to the number of rungs N , and equal to $N/2 - 1$. In addition to those, Leifer [22] showed that a mode of resonant can exist in which the currents flow in the same direction in each end ring. Because of co-rotating currents in the end rings, this mode was named Helmholtz or co-rotational (CR) mode, and it can not be constructed from any combination of currents in the network of figure 1.3. This mode however doesn't produce any propagating wave around the coil, hence it does not generate a magnetic field in the sample region. With the addition of this last Helmholtz mode, a total of $N/2 + 2$ resonant mode exist in a birdcage coil of N rungs. Between the $N/2 + 2$:

- The mode of resonance with periodicity or order equal to 0 has equal and opposite ring currents and zero rung currents. It is called the anti-rotational (AR) ring mode.
- The 0 mode is followed by the CR mode that is not identified by a periodicity or order number.
- The mode of resonance with periodicity or order equal to 1 is the only one able to generate an homogeneous magnetic field. Thus this is the typical mode used for imaging.
- All the other modes generate a magnetic field with a null at the center of the birdcage coil.

Low pass and high pass models present the same number of resonance modes, but they differ by showing a low or a high resonance spectrum, respectively. In particular for a low pass birdcage type, the AR and CR mode degenerate at zero frequency, with higher-order modes increasing in frequency. Conversely, in high pass birdcage type, the AR and CR mode form a doublet in high frequency, with higher-order modes decreasing in frequency.

1.2.2 Other RF coil typologies

Over the years, the RF birdcage coils have been proffered as the main implementation of RF coil for \vec{B}_1 propagation in the patient [16]. However, even when using a RF birdcage coil, in presence of a patient the B_1 homogeneity is lost. As a result there may be areas within the body of the patient in which the transmit field is significantly weaker than in other regions. Additionally, the loss of homogeneity increase with the static magnetic field strength and with the coil dimensions.

Over the years other technologies have been implemented to overcome the loss of field homogeneity. The more relevant ones are the Transverse Electromagnetic (TEM) resonator coils, and the parallel multi-transmit RF coils [3].

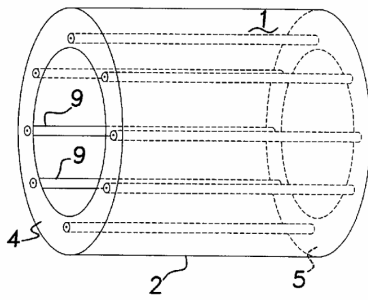


Figure 1.4: Structure of the TEM resonator

TEM — The TEM resonator was invented by JT Vaughan in 1999 [23]. Figure 1.4 report the original patented TEM design. The structure of the TEM resonator differ from the one of the birdcage coil in two ways: i) firstly longitudinal connectors of the birdcage coil are replaced in the TEM coil with microstrips are affixed to the inner surface of a nonconducting cylinder; and ii) secondly in the birdcage coil the rungs current use the end-rings as a return path, whereas in the TEM resonator the microstrips are all connected to the outer thin metallic shield. Thus inductance and self resonance of the TEM coil are independent of coil diameter, because the TEM coil return path follows the shield rather than the end rings.

The main characteristic of the TEM resonator is that at high frequencies it becomes a cavity resonator or longitudinal transmission line in which oscillating standing waves develop.

Parallel multi-transmit coils — The increase of the SNR has always been the main target of improvement for RF birdcage body coils. Starting form the 80's studies, such as the one by Sotgiu and Hyde [24], proposed the use of multi elements excitation as a measure to improve the RF homogeneity in the excited volume. The simple birdcage coil was seen as a multielement transmit coil array, that could allow for an independent adjustment of amplitude and phase of the signal feeding each element of the coil. Starting from 2000s this concept was evolved and were made to take advantage of this method to reduce the RF inhomogeneities in the patients, particularly for high static fields [25]. This new RF modality is also known as parallel multi-transmit or RF shimming.

The degree of freedom given for each element of the coil to be fed with a specific waveform, allowed to more carefully control and increase the homogeneity of the B field generated by the RF excitation. Thus, the main concept of multi-transmit coil is that the power is distributed to the feeding sources of the RF transmit coil (typically a TEM resonator) using two or more independent channels.

A second advantage of the transmit coils is that they can be also used in parallel receiving mode with a consequent reduction of the acquisition time [25].

1.2 Radiofrequency coil design and theory

1.2.3 Field polarization

The structure of the birdcage coils allows for multiple feeding conditions within the coil rings [16,22]. Depending on the source number, and feeding phase and amplitude, different polarization of the produced magnetic field can occur. Historically in the '80s, the birdcage coils were fed using a single port coil, such to achieve a linearly polarized field. However with such polarization "quadrupole" artifacts were present in the resulting MR image [26]. These artifacts manifested as "holes" of decreased image intensity that could not be attributed to any anatomical feature of the patient scanned. Running simulations with cylinders of different size and material, they observed that the "holes" were caused by the asymmetric nature of eddy currents induced that derive from the finite conductivity of the medium. Similar results will be later discussed in section 6.2. To overcome the artifacts problems the authors suggested to implement a circularly polarized birdcage coil implemented with two feeding ports. The two ports were fed with the same amplitude and differential phase of 90° in order to generate a purely rotating wave. With the new polarization a 1.4 and 1.6 higher SNR was observed with respect to a left/linear and right/linear polarization, respectively.

The linear polarization is then considered less efficient for MR imaging because half of the transmitted power is not used for imaging. In fact, the rotating \vec{B}_1 field generated by a linear polarization can be decomposed into two counter-rotating subfields each of half of $\|B_1\|$ and rotating in the two opposite direction, namely right and left polarizations or B_1^+ and B_1^- . For a \vec{B}_1 linearly polarized along \vec{x} , the \vec{B}_1 can be express as:

$$\vec{B}_1(t) = \frac{\|B_1\|}{2}(\vec{x}_0 \cos(\omega t) + \vec{y} \sin(\omega t)) + \frac{\|B_1\|}{2}(\vec{x}_0 \cos(\omega t) - \vec{y} \sin(\omega t)) \quad (1.10)$$

However, out of the two counter-rotating subfields, only one is effective at inducing NMR (i.e., B_1^+) because is the one that rotates in the same direction as the precessional magnetization vector generated by the B_0 static field. Thus only one of the two subfields is required for MRI, while the second one does not provide any effect besides depositing extra thermal energy into tissue.

The circular polarized field is obtained by adding to the original linearly polarized field, a second field generated by sinusoidal current phase shifted by 90° [26]. This is typically obtained by a quadrature transmission of signals in the RF birdcage coil. This can be achieved by two or more feeding sources around the coil ring. When such circularly polarized field is generated the two counter-rotating components of the two generated fields (i.e., B_1^-) cancel each other, whereas the subfields effective at inducing NMR (i.e., B_1^+) add together. Hence all the power is used for imaging, and an

overall higher efficiency is achieved. Today RF coil for clinical MRI scanner use the higher efficient quadrature excitation. Conversely linearly polarized transmit RF-coils are restricted for use in very small animal imaging [3].

1.2.4 Induced electric field

Magnetically induced — The main purpose of the RF birdcage body coil is to produce a time-varying magnetic field (\vec{B}_1) for the excitation of the magnetization vector. However if a conductive media is present inside or in close vicinity with the coil, then by Faraday's law (eq. 1.11) an altering voltage or electromotive (EMF) force is induced about this conductor by the variation of the magnetic flux Φ_B [27].

$$\begin{aligned}\Phi_B &= \iint_{\Sigma} \vec{B}_1(\vec{r}, t) dA \\ EMV &= -\frac{d\Phi_B}{dt}\end{aligned}\tag{1.11}$$

where dA is an element of surface area of the surface Σ . The Faraday's law is often generalized on its more common definition of the Maxwell-Faraday equation (eq. 1.12), where it is defined that a time-varying magnetic field it is always be coupled with a spatially-varying, non conservative electric field (\vec{E}):

$$\nabla \times \vec{E} = -\frac{\partial \vec{B}_1}{\partial t}\tag{1.12}$$

This is strictly related to the altering voltage defined by eq. 1.11. In fact the \vec{E} is stronger as greater the time rate of change of \vec{B}_1 . In MRI, this electric field is typically named "magnetically induced" or "inductive" [28].

Because the conductor surrounded by the varying magnetic flux is a resistive medium, the induced voltage generated altering currents (or eddy currents) within the medium [27, 29]. This altering currents can be described simply by Ohm's law if the EMF of eq. 1.11 is considered. Additionally, the created eddy-currents can also be described by the coupled \vec{E} of eq. 1.12, as:

$$\vec{J} = \sigma \vec{E}\tag{1.13}$$

where \vec{J} is the current density vector, and σ is the tissue conductivity.

The created eddy-currents (I) consequently generate a secondary magnetic field defined by Ampere's law (eq. 1.14) and a corresponding additional voltage by the Faraday's law (eq. 1.11). This additional voltage is named secondary voltage.

$$\oint_C \vec{B} dl = \mu_0 \iint_{\Sigma} \vec{J} dA\tag{1.14}$$

1.3 Methodologies for computational modeling

Overall the induced internal fields are strongly dependent on both the incident field, and the size, shape, and dielectric properties of the exposed medium. The voltage induced by \vec{B}_1 is much larger than the secondary one. However, within the human body it can be considerably high to perturb the primary field. This is due to the complexity of the body anatomy, and to the inhomogeneity of the dielectric properties of the tissues [30].

Capacitive — Additionally, electric field within the body can also be generated by the distribution of electrical potential specific of the resonant structure. In MRI such electric field is typically named "conservative" or "capacitive" [28], as described by the Gauss's Law:

$$\nabla \cdot \vec{E} = \frac{\rho}{\epsilon_0} \quad (1.15)$$

One possible situation in which the capacitive effect should be taken into account is when the medium is in close vicinity to the RF resonator.

1.3 Methodologies for computational modeling

A "computational model" is a mathematical model which requires computational resources to be able to solve a physical system with a high level of complexity [31]. The solution is obtained by means of numerical simulations. With respect to the MRI simulations are meant to solve computational EMs models, because the physical system that has to be solved is ruled by Maxwell's equations.

Numerical modeling of birdcage body coils is extensively used in the evaluation of RF field interaction with the human body during magnetic resonance imaging [32,33]. Over the past years, the use of computational modeling to evaluate the RF field distribution in the human body during an MRI has increased dramatically. Such increase was supported by the possibility of performing systematic analyses of the several variables affecting RF heating with decreased costs and increased reproducibility [34–40]. In fact, with the use of computational models it is possible to study several variables affecting the EM field propagation with reduced costs and increased reproducibility compared to experimental measurements. Thus, the results of model simulations allow to make predictions about what will happen in the real system that is being studied in response to changing conditions.

1.3.1 Computational methods

Several numerical methods exist, each of them solving the Maxwell's equations following a specific algorithm. However every numerical method has the implicit limitation of not solving solutions in the linear continuum. Every physical system has to be discretized in finite domain such that the numerical solution is computed based on partial differential equations. The geometry of the physical systems involved in the problem is partitioned into elements of space or cells, in which the differential equations can be computed. The entire net of elements discretized into the numerical system is typically named "mesh" [41].

Several meshes can be implemented based on the specific grid of elements defined. In general, mesh can be classified based on:

- *domain dimension*: 1D, 2D or 3D.
- *element type*: triangular, tetrahedral, quadrilateral, hexahedral, or a mix of more than one type.
- *element aspect ratio*: isotropic or anisotropic.
- *mesh density*: uniform or graded mesh.
- *topology*: structured or unstructured mesh. A structured mesh presents a regular topology with a well known pattern; conversely, an unstructured mesh have an irregular topology where the connectivity of the grid is part of the data structure.

Once the mesh is defined then the relations of the physical system within each element of the numerical space has to be found. What needs to be defined then is the algorithm that is able to solve the physical problem in the discretized space for the specific characteristics chosen. Several numerical methods exist to solve a physical system, however each one is defined with respect to its numerical implementation. Hence every method cannot be independently defined by the algorithm.

The methods used to solve Maxwell's equations in physical system are based on differential or integral equation solvers, such that they discretize the differential or integral form of Maxwell's equations. Both methods can be solved in the time or frequency domain. In time domain, the frequency range of interest is specified, and a Gaussian signal with the frequency information is defined; then the signal is transformed into time domain by using an inverse Fourier transformation, resulting in a time signal with a Gaussian envelope. The system is then excited with this time pattern. Conversely, in the frequency domain, the behavior of a physical system is usually relevant in a specified frequency range. Thus no information can be concluded for a single frequency. Hence, several simulations in the frequency band of interest have to be performed, the number of which are defined by the software algorithms to achieve a predefined accuracy of results by interpolation of points.

1.3 Methodologies for computational modeling

The numerical work described in this thesis was mainly performed using the Finite Difference Time Domain (FDTD) method, which is based on differential equation approach with a voxel-based mesh, described more in detail in the following section.

FDTD The FDTD method is a related space-grid time-domain technique that involves the resolution of Maxwell's equations on their differential form. Since its introduction by Yee in 1966 [42], the FDTD method has been widely used for broad range of EMs applications including geophysical, bioelectromagnetic, and biophotonics [43]. The employment of the FDTD method saw an exponential growth starting from its first proposal [44]. One of the major reasons of such growth is the increase of computational performances for a given cost of technological resources. Because the FDTD algorithm is based on the solution of Maxwell's equations on their differential form, it is required to define in the boundaries condition of the problem. In particular for wave-propagation problems in unbounded media, artificial boundary conditions have to be used to eliminate the reflections from the edge of the finite computational domain [45]. A big turning point of the method for the study of wave-propagation problems was the introduction of the perfectly matched layers (PML) by Berenger in 1992 [46].

One of the characteristics of the FDTD method is that as the resolution of the sampled object is refined, the time required by the simulation to reach the Courant Friedrich Levy condition grows. This is a direct consequence of the intrinsic definition of the time-step as directly proportional to the square root of space resolution [43]. Thus smaller the resolution smaller the time-step and higher the number of time-step intervals required to perform a time-defined simulation. Nowadays computers are able to simulate increasing simulation space with higher resolution steps within a reasonable amount of time for each simulation.

As described in the reference work of Taflove and Hagness [43], there are several reasons to the popularity of this method, including its robustness and systematicity. On the other hand, one of the major disadvantages consists on the inability of modeling smooth curved and tilted profiles. Without the implementation of a specific algorithm, a curved or tilted profile implemented in FDTD will be affected by staircasing. Although the simplest and most frequently used approach is the staircasing approximation [44], Cangellaris and Wright in 1991 [47] and Holland in 1993 [48] reported solution inaccuracy related with staircasing effect. Moreover Railton and Schneider in [44] and Cangellaris and Wright in [47] also quantified that a 2% error can be committed in the evaluation of the resonance frequency of a resonant object respect to the tilted angle of the object with Cartesian axes of the grid. Railton and Schneider [44]

also report how the error committed for the different angles is highly related to the spatial resolution of the Yee cell. Beside the staircasing approximation, in the past years several methods have been proposed to generate a conformal mesh for tilted and curved profiles [49, 50]. Among all, four categories can be highlighted: the contour path (CPFDTD) algorithm [51–56], the non-orthogonal FDTD [57–59], the hybrid methods using FDTD and the Finite Element Method (FEM) [60–62] or FDTD and the Method of Moments (MoM) [63–65], and the sugridding method [66–70]. Even though these methods have been extensively discussed and compared [44, 71, 72] it is still common to find new literature publications using the original FDTD Cartesian grid for the simulation of a RF birdcage coil for MRI, such as [34, 38, 73–78].

Section 2 of this thesis reports the results of the effect of different staircasing steps on the frequency response and on the EM fields of a RF birdcage body coil at 64 MHz. The frequency response and EM field were evaluated in terms of: i) simulation convergence, ii) variable cell size on the three-dimension space, iii) coil orientation respect to the Cartesian grid, and iv) application of multigrid. The results were analyzed in terms of memory request and they have been compared to EM measurements of a physical 64 MHz birdcage body coil.

Other computational methods Other computational methods are typically used in the context of the RF field in MRI to solve Maxwell equations [79]. Some of them are:

- *FEM*: this method is a near-neighbor, volume method for solving Maxwell’s differential equations in the frequency domain; the physical space is divided into a non structural grid, composed of meshes of small volumes or cells of tetrahedral elements, and this fact makes this method very suitable in modelling inhomogeneities and complex geometries. Once the volume has been subdivided, the unknown field within each element is approximated using linear extrapolation, starting from a sparse system equations matrix; the solution is given by the inversion of this matrix. The FEM can couple the EM solution with other physics, like, for example, mechanical and thermal problems. However, it could be inefficient in the treatment of highly conductive radiators due to the requirement to have some mesh between the radiator and the absorber, and the mesh could be very complex, far as to have meshing time longer than solution time [79].
- *Method of Moments (MoM)*: this method is a full wave solution of Maxwell’s integral equations in the frequency domain. The radiating/scattering structure is replaced by equivalent currents (normally surface currents) that are discretized into wire segments; then, a matrix equation is derived, able to describe the interaction of every source segment on every other segments, computed with the

1.3 Methodologies for computational modeling

Green's function. The strong points of this method are that: i) it is not necessary discretize the "air space" around the antenna, but only the antenna and the region of interest; ii) only the surface is meshed; iii) efficient treatment of highly conducting surfaces. However, the MoM doesn't handle electromagnetically penetrable materials, especially if the material is inhomogeneous, and requires the surfaces to be closed, that is often impractical [79].

1.3.2 VVUQ: Verification, Validation and Uncertainty Quantification

Although performing a numerical test has numerous benefits, experimental validation of the numerical model remains a complementary and fundamental step to determine the degree to which a model is an accurate representation of the real world from the prospective of the intended uses of the model. Verification, Validation, and Uncertainty Quantification (VVUQ) is a complex set of procedures for the assessment of the overall quality of the physical system results obtained with numerical simulations. The process of determining the accuracy with which a computational model can produce results deliverable by the physical system on which it is based, is a development process that follows several steps. The flowchart reported in figure 1.5, from the ASME guide on V&V for Solid Mechanics [80], is a good outline of all the steps required in the VVUQ process.

The VVUQ can be essentially divided in three fundamental steps: the verification of the numerical code implemented, the validation of the numerical results with experimental measurements, and lastly the quantification of the uncertainty of both numerical and experimental results. In accordance with the FDA guidance [31] these can be defined as:

- *Verification*: The process of determining that a computational model accurately represents the underlying mathematical model and its solution from the perspective of the intended uses of modeling and simulation.
- *Validation*: The process of determining the degree to which a model or a simulation is an accurate representation of the real world from the perspective of the intended uses of the model or the simulation.
- *Uncertainty Quantification*: the estimated amount or percentage by which an observed or calculated value may differ from the true value.

Ultimately, the numerical outcomes can be considered a good representation of the reality if the data are within the combined uncertainty of the numerical and experimental results. However it is important to specify that a numerical code can never be fully verified for any conditions, but every code is verified against a set of numerical tests

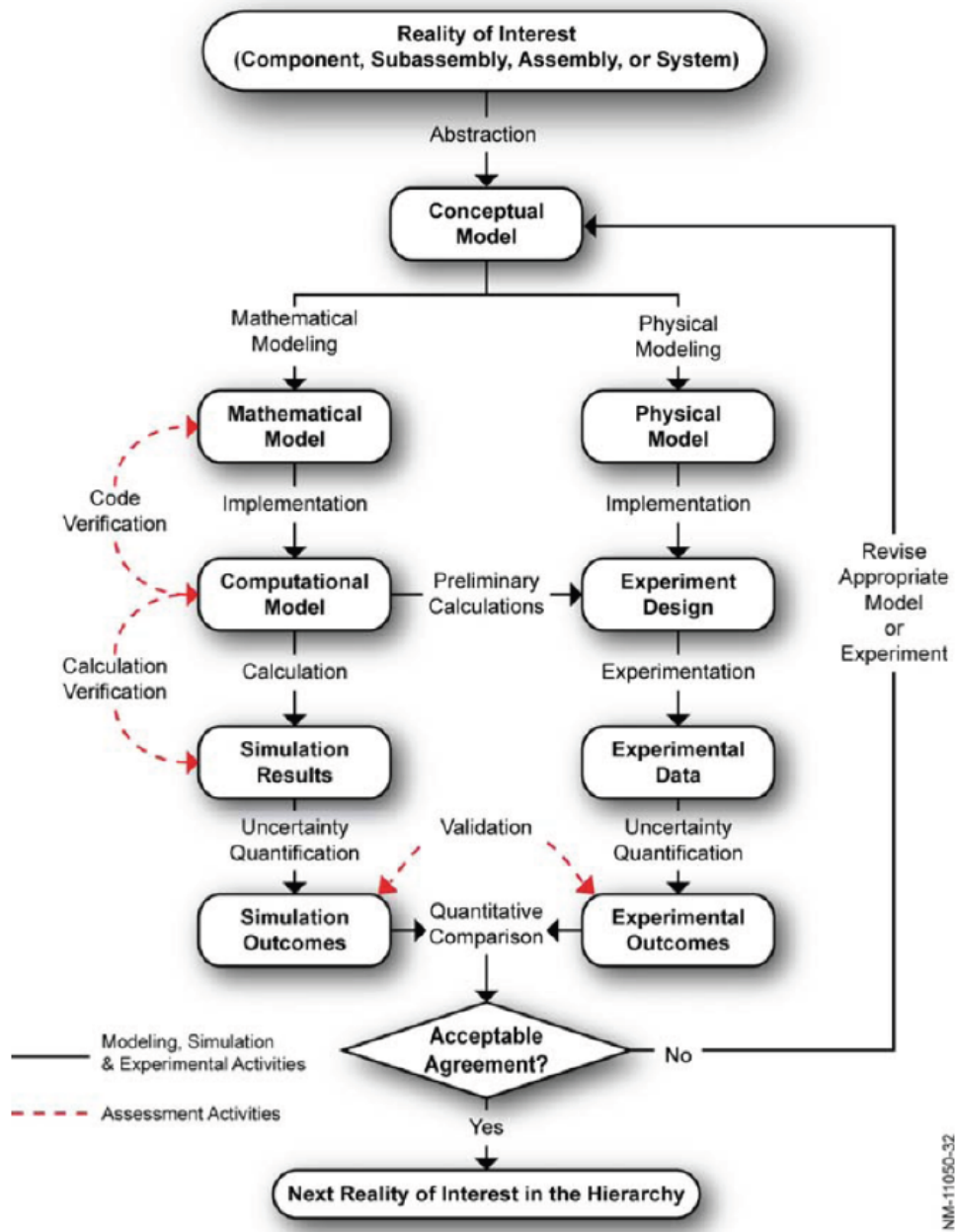


Figure 1.5: Flowchart describing the VVUQ (from ASME guide on V&V for Solid Mechanics [80])

1.3 Methodologies for computational modeling

for the specific physical system of interest.

Over the years the FDTD methods was thoroughly verified with respect to experimental results. Verification of the code is typically performed for simplified geometries and has to be done for any algorithm implementing the numerical method. In the context of the RF field in an MRI system, the first procedure was followed by Ji Chen in 1998 [81]. The main goal of the study was to analyze the specific absorption rate (SAR) and EM fields in a realistic human head model excited by shielded RF coils. The SAR will be more extensively explain later in section 5.1 of this thesis. The authors proposed a numerical method based on the combination of the FDTD with the MoM. To verify the numerical code the authors compared the numerical solutions of the magnetic field generated in a square waveguide excited by a current sheet with respect to the analytical calculation of the same distribution. Similar approaches were also followed by Bowtell and Bowley for the magnetic field generated by a gradient coil [82], and Collins et al. [83] for the evaluation of temperature rise and SAR in a human head exposed to a EM field at 64 and 300 MHz, respectively.

Once the implemented algorithm has been verified, the specific physical scenario modeled has to be validated with respect to the experimental measurements. In the context of the RF field in MRI, this step is not trivial given that it is not possible to measure EM field distribution in a real life situation inside patient. However over the years several suggestions were made to validate the numerical results. Seifert et al. [84] validated the numerical results with respect to the absolute value of the complex amplitude of the positively rotating component of the RF magnetic field $\|\vec{B}_1^+\|$, and the phase of the MR signal. Those quantities are indeed part of the information included within the MRI image of the patient. The validation of results based on the \vec{B}_1 maps was also followed by Homann et al. [85] for different patient location within the RF coil, by Voigt in [86], and by Van den Berg et al. in [87]. A good alternative for numerical results validation with experimental data is the use of phantoms. Because of their reproducibility in terms of geometrical and physical characteristics (e.g., electrical properties, thermal properties), phantoms can be easily implemented in the numerical environment with a high physical accuracy. Section 1.4 will report more details about the phantoms typically used for RF field testing in MRI. Moreover, a second advantage of the use of phantoms is the possibility of measuring field values and distribution inside the medium. As for the imaging of human body, results in phantom can be validated as well with respect to \vec{B}_1 maps. Ibrahim et al. [88] validated FDTD results of three implementation of a RF coil at 340 MHz, loading the numerical and physical coil with a plastic cylindrical phantom (15.0 cm in diameter and 21.2 cm in length) filled with mineral oil. Cabot et al. [37] extended the validation process mea-

asuring the EM field within a 64 MHz RF coil, and Mattei et al. [40] in terms of return loss of the resonant coil and currents along the rungs. Lastly the uncertainty quantification comes from both experimental and numerical data. This can be due to several factors such as instrumental, environmental, due to operator or to the followed measurement process. Typically experimental uncertainty is assessed by performing the measurement process more than one time, and then estimated using statistical analyses of the set of measurements. Several studies showed a high variability of results with respect to mesh used, simulation setup (such as boundary conditions), or computation convergence such as in [?,87,89]. Oberkampf et al. [90] categorized the numerical uncertainty as:

- *Aleatory uncertainty* to describe the inherent variation associated with the physical system or the environment under consideration. Sources of aleatory uncertainty can commonly be singled out from other contributors to total modeling and simulation uncertainty by their representation as distributed quantities that can take on values in an established or known range, but for which the exact value will vary by chance from unit to unit or from time to time.
- *Epistemic uncertainty* as a potential inaccuracy in any phase or activity of the modeling process that is due to lack of knowledge.

The aleatory uncertainty is usually an irreducible uncertainty that is typically quantified by a probability distribution [90]. Whereas the epistemic uncertainty is considered a reducible uncertainty. An important and thorough study including experimental and numerical uncertainty was performed by Neufeld et al. [91]. The goal of the study was to compare experimental setup and simulations of RF-induced heating at the tip of two generic implants for standardized testing. For each quantity of interest studied (e.g., electric field, SAR, temperature) the uncertainty was calculated assuming a linear dependence of the measured values with respect to a varying parameter. Example of parameters considered are: phantom position and electrical properties, measurements probe position, lead geometry, and numerical resolution. Section 3.7 reports the numerical uncertainty study performed with respect to some variables of the RF birdcage coil used for the work described in this thesis.

1.4 Numerical and physical phantoms in MRI

As already introduced at the beginning of this chapter, the success of computational modeling is due to the possibility of performing systematic analyses of the several variables affecting RF with reduced costs and increased reproducibility compared to experimental measurements [34–40]. While numerical models present several advan-

1.4 Numerical and physical phantoms in MRI

tages, a proper experimental validation of these models remain a fundamental step, as it allows determining the degree to which the model is an accurate representation of the real physical phenomenon within a specific context of use [31]. For these reasons phantoms are often used to assess exposure, and in the context of the RF field they can be categorized in numerical and physical phantoms.

1.4.1 Numerical phantoms

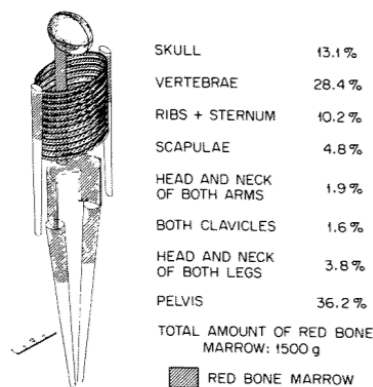


Figure 1.6: The refined MIRD model introduced by Snyder in 1987 [92].

Stylized phantoms — These phantoms are the first generation of computational phantoms and are also called the *mathematical phantoms* [93]. They were implemented and used mainly between the 1960s and 2000s. Stylized phantoms were introduced to assess the dose exposure in body organs and tissues that were described by mathematical expressions representing planes or cylindrical, conical, elliptical or spherical surfaces. All the model developed over the years were representative of the "average or standard individual" as defined by ICRP's data on reference man (ICRP 1975) [92].

The most used stylized phantom model was the MIRD model. The phantom was named after the initials of the Medical Internal Radiation Dose Committee of the US society of Nuclear Medicine. The MIRD phantom was firstly introduced by Snyder and fisher in 1967 and then refined by Snyder in 1987 [92]. The refined model in figure 1.6 was representative of an adult human model. In the following years several other models part of the MIRD-type phantoms were released representing infants and children of various age [94], separate male and female adult models named Adam and Eva [95], and three phantoms representing the adult female three stages of pregnancy [96].

Voxel phantoms — These phantoms are the second generation of computational phantoms. The voxel models were firstly presented as "tomographic-type" were introduced in 1984 by Gibbs et al. and in 1986 by Williams et al. [94]. These numerical models were generated from medical imaging data collected through MR or computed tomography (CT). The voxel models were able to provide 3D representations of the human body by volume elements of the same size (i.e., voxel) but representing the anatomical structures of the human body (e.g., white matter, muscle, bone).



Figure 1.7: Virtual Population voxel models [97]

Since their introduction in 1980s the voxel models are still in use, and a very high number of them are free to download or commercially available [98]. In the context of the MRI RF exposure assessment, one of the first studies for exposure assessment was performed by Dimbylow in 1996 [99]. The exposure was computed on the NORMAN (i.e. NORmalized MAN) human voxel model of 73 kg for 1.76 m of height. The model was implemented based on MRI data from a series of continuous partial body scans of a single subject. Because the concept of the ICRP reference man was still strong, the final dimensions of the model were scaled so that the height and the mass would agree with the new values of reference man [99]. Over the years additionally the Visible Human Man (VHM) and Visible Human Woman (VHW) were completed in November 1994 and 1995, respectively. The VHM and VHW were the result of the visible human project led by the U.S. National Library of Medicine that started in 1956. In literature is it possible to find the VHM implemented under the name of the "Hugo" model (later used in paragraph 6.2 of this thesis). With the growth of computation power and imaging resolution several other models were introduced. Among all the models, one of the more used for RF exposure assessment are the phantoms part of the Virtual Family first [100], then expanded to the Virtual Population [97] (figure 1.7). The populations include models of males and females going from the baby to the aged human [101]. Models of pregnant women and obese humans are also present. The spacial resolution available for the models is $500 \mu\text{m}$. Because of their high accuracy it is nowadays common to refer to these voxel models as human body models. Section 6.2,7, 8.2 reports the numerical results using the voxel models of the Virtual Population, specifically of the adult male "Duke", the adult female "Ella", the young male "Thelonious", the old male "Glenn", and the obese male "Fats".

Beside models of the entire body, it is also possible to find voxel phantom of specific parts of the body. In particular, the interest has been focused on the implementation of detailed voxel phantoms of the head as one of the most complex body part. One of

1.4 Numerical and physical phantoms in MRI

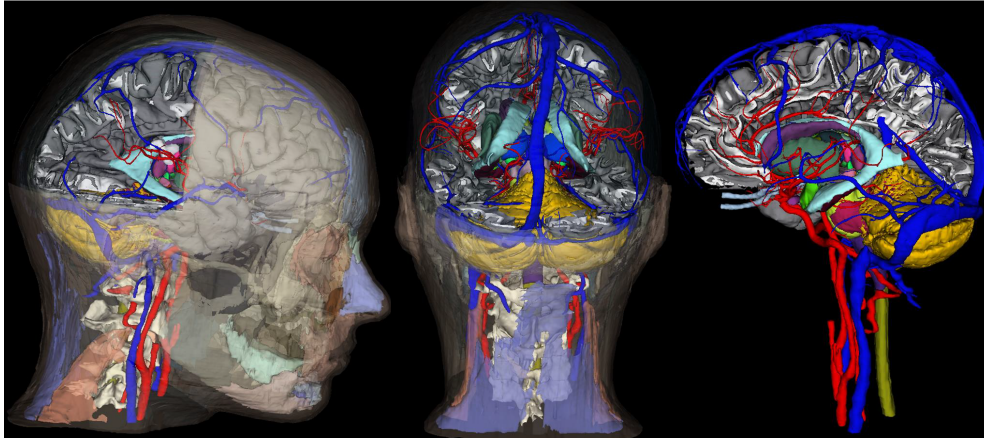


Figure 1.8: MIDA phantom [102]. The model is a detail representation of the human head. It includes 153 anatomical structures with a resolution of $500 \mu\text{m}$

the commonly used voxel head phantom in the MRI RF studies is the "BoMA" head model proposed by Makris et al. in 2008 [103]. The phantom is the model of the head of an adult male, it is composed of 22 anatomical structures with a spatial resolution of 2 mm. A novel and very detailed phantom has also been recently presented by Iacono et al. [102] and shown in figure 1.8. The phantom is a model of the head of an adult female, it is composed of 153 anatomical structures with a spatial resolution of $500 \mu\text{m}$.

BREP phantoms — These phantoms are the third generation of computational phantoms [93]. Boundary representation (BREP) phantoms are computational human models that contain exterior and interior anatomical features of a human body using boundary representation method. With respect to the voxel models the BREP phantoms are deformable phantoms whose geometry can be conveniently transformed to fit particular physical organ shapes, volumes, or body postures. The operations that is possible to perform on BERP phantoms are: extrusion, chamfering, blending, drafting, shelling, and tweaking [93]. These features allow BREP models to include very complex anatomical features, and surface deformation.

1.4.2 Physical phantoms

Physical phantoms are made of solid materials which are radiologically equivalent to human tissues. Physical phantoms can be based on simplified designs or they can be anthropomorphic phantoms. Simplified phantoms have the advantage to be easily standardized. In literature it is possible to find simplified phantoms made of different geometries such as: "oblong saline bath to simulate an endovascular intervention" [104], square frustum [34], cylindrical phantom [105–108], or spherical [109]. Because of

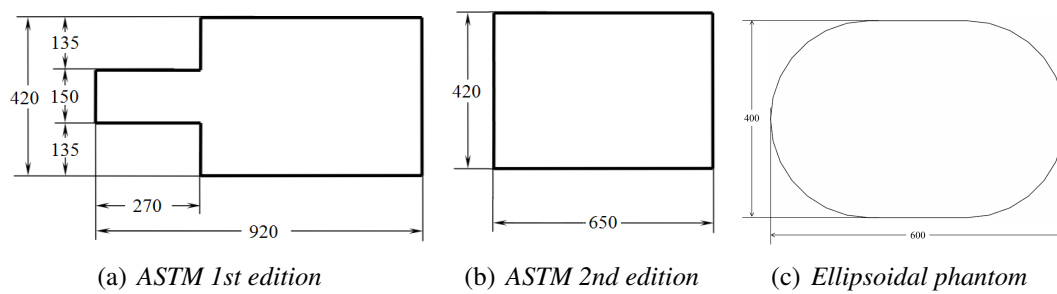


Figure 1.9: ASTM phantoms (a) 1st edition and (2) 2nd edition suggested by the ASTM F2182 standard [110]; (c) Ellipsoidal phantom suggested in the TS ISO 10974 [111]

their simplicity simplified physical phantoms were also standardized.

In the context of MRI RF exposure the standardized phantom is the ASTM phantom developed by the American Society for Testing and Materials (ASTM) [110]. In the first editions of the standard the phantom had a shape based on a simplified human torso (Figure 1.9a). In the 2011 edition of the standard [110] the phantom to be used for testing was updated suggesting the box shape (Figure 1.9b) used in section 2.4 and in the interlab study of section 4. The ASTM phantom of the standard is a container filled with a gel phantom material with electrical and thermal properties in the same range of the ones of the human body at frequencies of interest (i.e., 64-128 MHz). An additional phantom suggested for controlled exposure conditions is the ellipsoidal phantom (Figure 1.9b) suggested in the Annex M-3 of the technical specification (TS) ISO 10974 [111]. Throughout the work performed for this thesis an additional phantom was implanted based on the ellipsoidal phantom, the superellipsoidal phantom (see paragraphs 3, and 7).

Additionally to simplified phantoms, anthropomorphic phantoms have been also implemented for a more realistic representation of the human body heterogeneity. This phantom typically consist of several tissue-equivalent materials that are molded into shapes of organs or bones to represent part or all of the body [93]. Among all, the bottle manikin absorption (BOMAB) phantom represents the ICRP reference man and it consists of 10 high-density polyethylene containers [112]. Other of these phantoms are representative of body sections, such as: head phantoms [113–116], human torso [117, 118].

Chapter 2

Numerical implementation and verification of the RF birdcage coil model

All the studies described in part I and part II were performed using a numerical model of a transmit RF birdcage coil implemented based on the dimensions of the physical high pass Medical Implant Test System (MITS1.5) for RF Safety Evaluation (Zurich Med Tech, Zurich, Switzerland) at 64 MHz (figure 2.1a). The studies presented were performed using the two simulation platforms based on the FDTD algorithm XFDTD (Remcom Inc., State College, PA, USA), and Sim4Life (ZurichMedTech, Zurich, Switzerland).

The CAD model (figure 2.1b) of the birdcage coil was composed of 16 rungs made of rectangular slabs with a dimension of $650 \times 25 \times 4 \text{ mm}^3$, and disposed with a cylindrical symmetry of 740 mm in diameter (figure 2.1c). The rungs were connected at each end by two hexadecagonal rings with a rectangular section of $30 \times 4 \text{ mm}^2$. The coil was shielded by a 32-sided irregular polygon enclosure consisting of 16 panels and two end-rings (figure 2.1c). Each of the panels included five holes of 25 mm diameter symmetrically centered and spaced 5 mm apart. The enclosure was 847 mm long, 14 mm thick and with a diameter of 824 mm. In this chapter, the excitation of the coil model was always performed in quadrature as in the physical system (i.e. I and Q in figure 2.1a). In the next chapter 3 the same CAD model of the coil will be used but diverse excitation will be investigated.

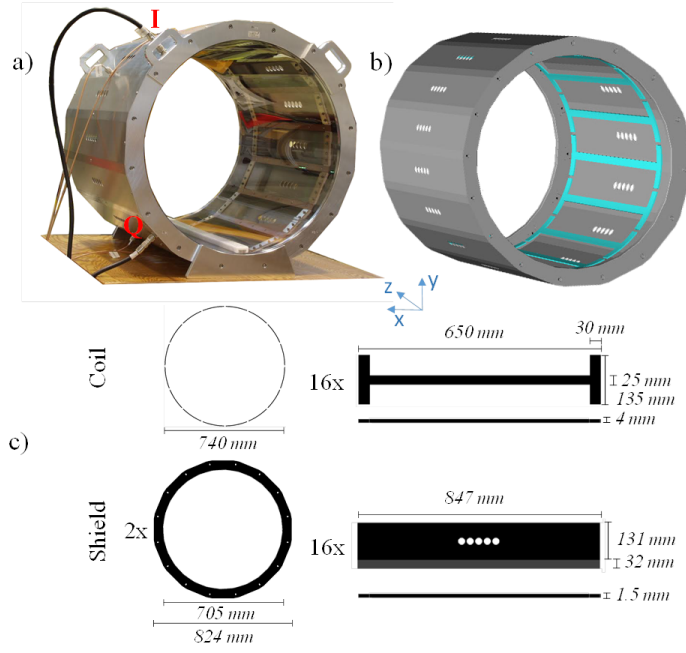


Figure 2.1: (a) MITS1.5 physical coil (b) 3D view of the computational model as implemented in the software. (c) Geometrical characteristics and measures of the coil and the shield. The computational RF body coil system was modeled to match the physical coil geometry.

2.1 Frequency response and implementation of the resonant circularly polarized mode

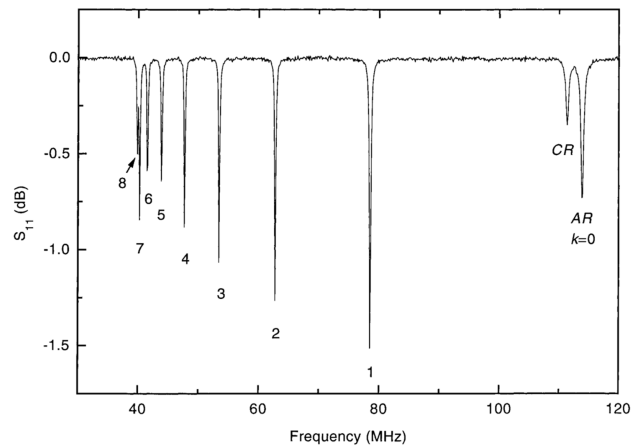
A first analytical validation of the numerical model of the RF coil was performed against the solution expected by theory. The coil was tuned to work at the frequency of resonance of 64 MHz. To generate a high pass resonant birdcage coil, the theoretical scheme reported in figure 1.3 was followed. Thus a capacitor C1 was placed within the rings of the coil between each of the 16 rungs for a total of 32 capacitors. The inductance of the simplified circuit reported in figure 1.3 is given in each rung by the birdcage coil itself. The initial value of the tuning capacitor was set based on the theoretical value selected among the nine resonant modes existing for the 16 rungs coil.

Neglecting the mutual inductance between the coil rungs, the resonant frequency corresponding to the mode equal to 1 is [22]:

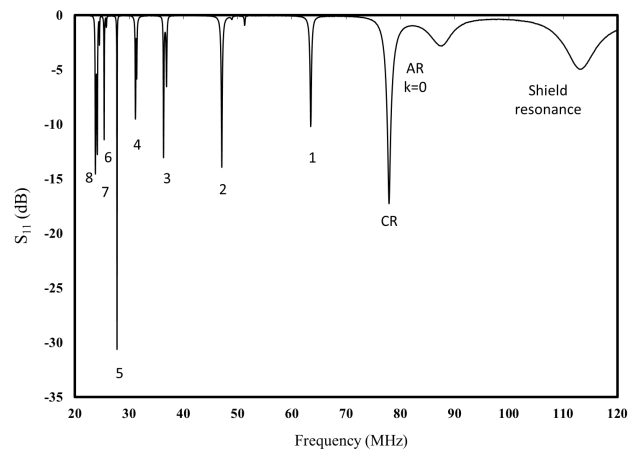
$$\omega = \sqrt{\frac{1}{C[L_{rung} \cdot 2\sin^2(\frac{\pi}{16}) + 2L_{ring}]}} \quad (2.1)$$

where L_{rung} and L_{ring} are the inductance of the rungs and the two end-rings respectively.

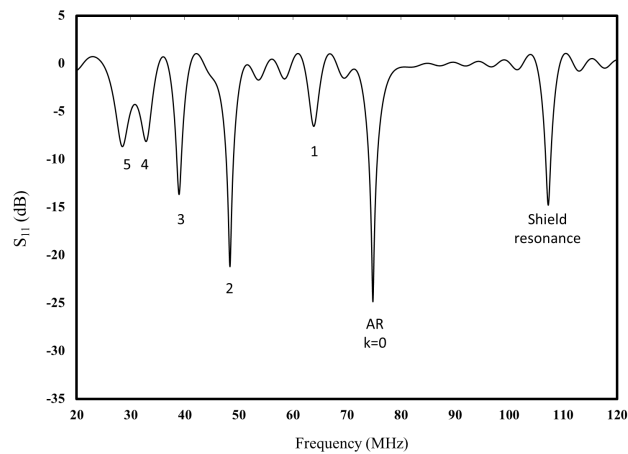
2.1 Frequency response and implementation of the resonant circularly polarized mode



(a) S_{11} - Leifer [22]



(b) S_{11} - MITS1.5 system



(c) S_{11} - Numerical model

Figure 2.2: Comparison of scattering parameter at one of the two feeding sources, for (a) theoretical profile of a highpass birdcage coil, as described by Leifer [22], (b) measured profile of the MITS1.5 system, (c) simulated profile of the numerical model based on the MITS1.5 system.

Numerical implementation and verification of the RF birdcage coil model

The values of L_{rung} and L_{ring} can be theoretically calculated as the inductance of a strip of with w and length l (with $l \gg w$) for the rungs considering the thickness negligible, and the inductance of a circular wire of radius a and length l (with $l \gg a$) for the ring, as defined by:

$$\begin{aligned} L_{rung} &= \frac{\mu_0 l}{2\pi} \left(\log\left(\frac{2l}{w}\right) + \frac{1}{2} \right) \\ L_{ring} &= \frac{\mu_0 l}{2\pi} \left(\log\left(\frac{2l}{a}\right) + 1 \right) \end{aligned} \quad (2.2)$$

where μ_0 is the permeability of vacuum and it equal to $4\pi 10^{-7}$. From eq. 2.1 and 2.2 it is possible to obtain the theoretical value of the capacitance. For the geometry considered, the theoretical C1 value is equal to 46 pF. However the numerical implementation of the resonant structure and specifically the mesh resolution, affects the corresponding capacitance for the resonance. In particular the mesh resolution imposed to the the numerical model to obtain the numerical solution, highly affect the corresponding capacitance value needed for the resonance. To verify the resonance of the implemented structure an isotropic uniform grid of $3 \times 3 \times 3 \text{ mm}^3$ was defined. In the next chapter (2.2) a deep investigation of the resonance frequency with respect to the numerical grid defined will be investigated. The final capacitance value required for the specific mesh implemented to obtain a resonant structure at 64 MHz was 68 pF.

As discussed in 1.2.3 the optimal RF field for imaging is a circularly polarized field, which can be obtained by feeding the birdcage coil in quadrature (see section 1.2.3). In this work the numerical implementation of the quadrature excitation for the RF coil was obtained by means of two feeding sources set in two gaps of one of the two end-rings of the coil 90° apart (I and Q in figure 2.1a).

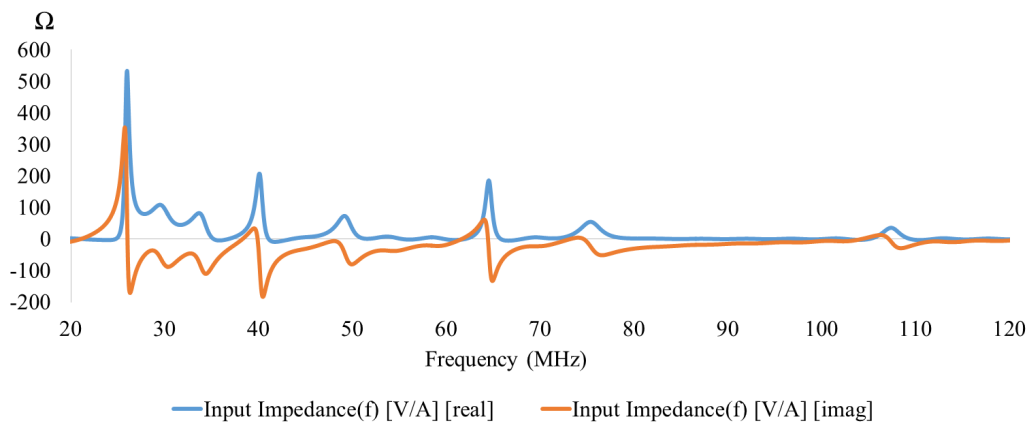


Figure 2.3: Frequency response of the real and imaginary part of the impedance at one of the two feeding sources.

2.1 Frequency response and implementation of the resonant circularly polarized mode

The frequency response of the RF coil model was studied by feeding independently each of the two sources with a broadband signal. The frequency profile of the S-parameter for one of the two sources (S11) was then compared with a theoretical profile and the one measured in the MITS1.5 system. As reported in figure 2.2, the MITS1.5 system showed a S11 with a similar profile as the one expected by theory for a 16 rungs highpass coil, and reported by Leifer in [22]. In addition to the eight typical modes of a 16-rung birdcage coil, the MITS1.5 system showed the additional mode at around 100 MHz. This can be identified as the resonance mode of the shield surrounding the coil. The numerical model was able to reproduce a similar resonance profile, however, the S11 did not show all the 8+1 resonance mode expected by a 16 rungs coil. The ripples in the profiles are due to the absence of lossy elements (e.g., resistors) in the coil. The variation of the S11 with respect to the use of resistance in the model will be discussed in section 2.3.2.

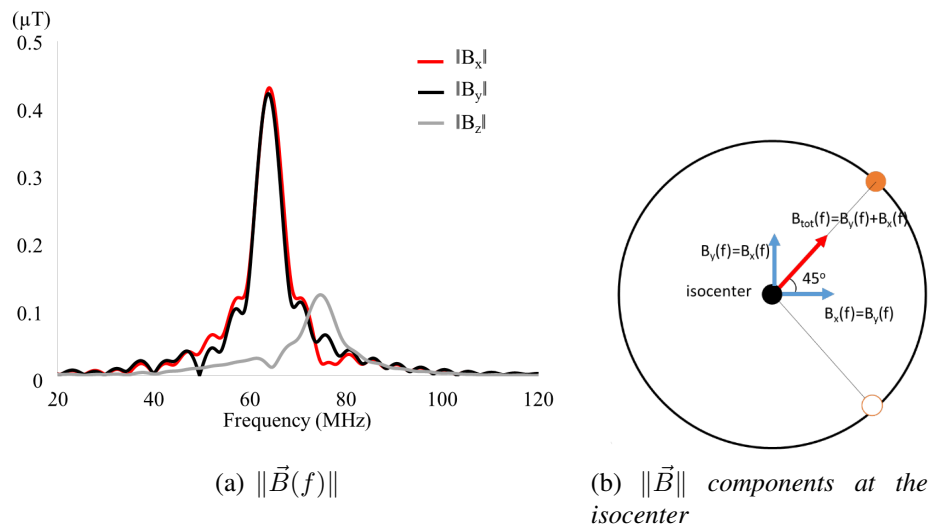


Figure 2.4: (a) frequency profile of the magnetic field simulated at the isocenter of the coil with respect to the three components of the field; (b) definition of the components profile with respect to feeding sources position, for the defined model (figure 2.1) the sources are oriented at 45° so the total B field has both Y and X component equal.

For a coil with only capacitance included, it is usually better to look at the profile of the real and imaginary part of the impedance at the source (figure 2.3). Resonance mode are identified where the impedance is purely real, and the imaginary part is zero between an inductive and capacitive behavior.

Without all the resonance modes present in the frequency spectrum, the identification of the $k=1$ mode was not trivial. However to identify the correct resonance mode it is also possible to evaluate the magnetic field magnitude at the isocenter of the coil with respect to frequency; the correct resonant mode is the only one able to generate

a homogeneous magnetic field within the coil without a null at the isocenter. As reported in figure 2.4a the frequency profile of the magnetic field at the isocenter of the coil showed a flat profile with a peak only at one of the resonant modes of 2.2c. In particular the profile of the three components of the field is dependent on the specific orientation of the sources with respect to the isocenter of the coil for the defined FDTD grid. For the position defined in coil model (figure 2.1), the sources were 45° oriented with respect to the Cartesian axes. Hence the X and Y components of the magnetic field at the isocenter had the same magnitude. Conversely the Z component was almost zero at the resonance. This is expected as the \vec{B}_1 is oriented on the XY plane. The combination of the sets of results (i.e., S11, impedance at the source, and H field in frequency) confirmed that the numerical coil model implemented was resonant at the desired 64 MHz frequency.

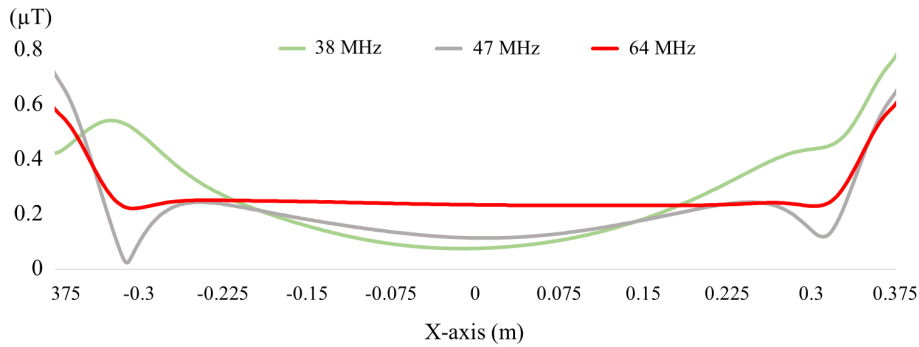


Figure 2.5: Magnetic field profile along the x-axis for three of the resonance mode observed in figure 2.2c

The next step was to combine the results for the two feeding sources in order to obtain a circular polarized field. As already reported in section 1.2.3, a circularly polarized field can be obtained by a proper combination of linearly polarized field. For this study the two sources were placed 90° apart, thus the phase difference of 90° had to be imposed to the two linearly polarized field of the same amplitude produced by the two sources. The homogeneity of the magnetic field in was checked again to confirm the proper resonance (Figure 2.5). Figure 2.6 shows how the two linearly polarized field combine to generate a circularly polarized field. AS expected the two linearly polarized field produced by the two sources are both perpendicular (direction of the arrows in figure 2.6), and complementary with one high when the other is low (color strength in figure 2.6). This is true at any phase of the input signal. Thus when the two linearly polarized field are combined to generate the circular polarization the magnitude of the resulting field was constant, and the direction in compliance with the input signal.

Finally to confirm that a circular polarized field has the highest efficiency in terms

2.1 Frequency response and implementation of the resonant circularly polarized mode

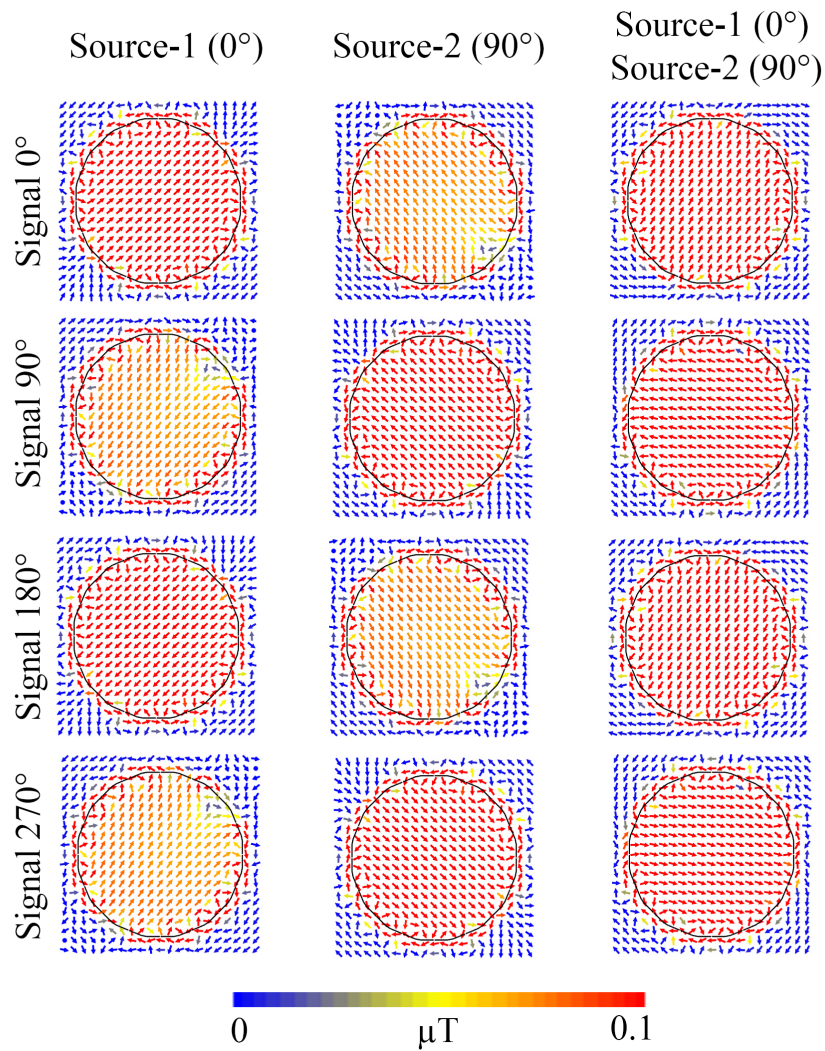


Figure 2.6: Magnetic field with each one of the sources active, and for the combined field to obtain the circular polarization. Data are represented for different phases of the input signal. The field is represented by arrows with the arrow tip showing the field direction, and the color the field strength.

of power delivered the B_1^+ and B_1^- components were studied for the two linearly polarized field produced by each source, as well as for the combined circularly polarized field. As shown by figure 2.7 the counter-rotating components generated by the linearly polarized field are of the same magnitude. However because the components of the two linearly polarized field show opposite phase, when combined to generate a circular polarized field they cancel each other out inside the coil.

2.2 Resonance of the FDTD-based coil model convergence study

When using FDTD algorithm it is often assumed that the error in a simulation result always decreases with decreasing mesh size. However, errors can arise from several sources. For example:

- A - Simulation convergence
- B - Variable cell size on the three-dimension space
- C - Coil orientation respect to the Cartesian grid
- D - Application of multigrid

The variability of the birdcage coil resonance with respect to such parameters was evaluated.

For all the simulation setups, a 20-cell free space padding (i.e., Yee cubic cell of 30 mm, $\sigma = 0S/m$, $\epsilon_r = 1$) was added to ensure free propagation of the field outside the coil volume without reflection [43]. The number of cells was calculated to have a length of free space padding equal to at least 10% of the wavelength. In addition to the free padding, twelve PML layers were placed as the boundary conditions of the volume. As already described in section 1.3.1, PML are used in the FDTD environment to reduce the reflections of the fields at the boundaries of the numerical environment to mimic an open or unbounded space condition.

A - Simulation convergence — A high resolution uniform grid with Yee cubic cell of 2 mm [119] was used to construct the electrical mesh of the volume containing coil and shield. Simulations were performed imposing an increasing maximum simulation time dependent on the period of the sinusoidal signal T at 64 MHz (i.e., $T_{64MHz} = 15.6ns$). Figure 2.8 shows the convergence of the H_{iso} field at the isocenter, and the resonance frequency of the coil simulated with the increasing of the simulation time. The simulation time is indicated as a function of T , as typically done for resonating coils. After 30 periods both H_{iso} and the resonance frequency showed differences lower than 0.023 % with respect to the results at the previous time step. Differences went lower than 0.00003 % after 50 periods. Based on these results, a 30 periods was selected as a suitable convergence threshold.

B - Variable cell size on the three-dimension space — The effect of the Yee-cell 3D spacial resolution on the frequency response of the resonance system was studied. Each dimension of the cell was progressively increased until geometrical characterization of the system was no more guaranteed by the mesh step. The z-dimension of the Yee-cell was established as the one parallel to the longitudinal axis of the system

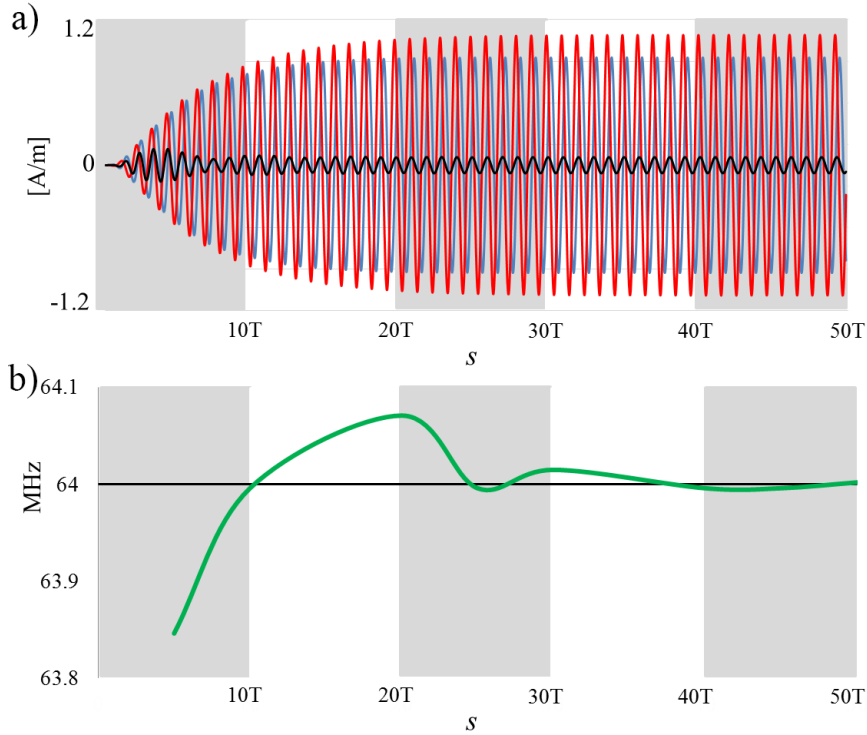


Figure 2.8: Simulation convergence results from 0 to 50 periods at 64 MHz. a) H field magnitude at the isocenter of the coil, b) the resonance frequency convergence.

coil/shield. For the first simulation setup, the Yee-cell z-dimension was varied imposing a uniform grid with Yee cubic cell of 2 mm for the x- and y- dimensions of the cell, and increasing the z-dimension from a minimum of 1 mm to a maximum of 8 mm with 1 mm step. For the second simulation setup, the x- and y- dimensions were progressively and independently imposed equal to 0.5 mm, 1 mm, 2 mm, 3 mm, and 4 mm. A resolution step higher than 4 mm did not allowed a correct discretization of the gaps within the rings (i.e., 5 mm). The previously found convergence limits of 30 periods were imposed to the simulations.

Results showed that within the variability range studied the frequency response varied less than 2 %. On the z-direction it was possible to apply a Yee-cell dimension up to 8 mm without a significant variation in frequency. This can be explained by the specific geometry of the coil in witch the rungs along the z-direction have a total length of 650 mm. Thus the numerical geometry related to the mesh is less sensitive to the millimetric increase of the grid. Conversely, in the x- and y-direction the coil has a circular geometry that can not be discretized with large Yee-cell without committing a staircasing error.

— In order to quantify the difference in terms of resonance frequency [44,47], results of the coil tilted with different angles respect to the Cartesian grid were compared.

2.2 Resonance of the FDTD-based coil model convergence study

Each rung of the coil was characterized by a rectangular section with a specific relative position with respect to the grid of the mesh (figure 2.9). Because the coil was composed of 16 rungs, the space angle of each rung with its adjacent sides equal to 22.5° (i.e., $360/16$).

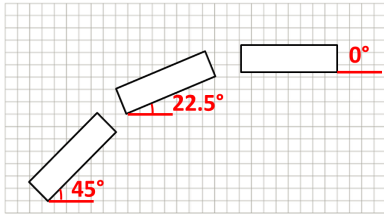


Figure 2.9: Relative position of three of the 16 rungs of the coil with respect to the FDTD grid.

C - Coil orientation respect to the Cartesian grid Simulations were implemented turning the coil/shield system around the longitudinal axis of 4.5° , 9° , 11.25° , 13.5° and 18° . The study was performed for two different Yee-cell configurations, namely by imposing or not the conformal mesh feature to a mesh space definition of x- and y-dimension equal to 3mm, and z-dimension equal to 8 mm.

Variation of resonance frequency less than 3 % using the classical Cartesian grid. Conversely, when a conformal mesh was imposed to the coil the variability of results decreased to 1 %.

D - Application of multigrid — When evaluating the RF exposure in phantoms it is common to use multigrid mesh, such as in [120]. This is done especially if voxel models are used, in order to correctly discretize the heterogeneities of the body. A finer Yee-cell resolution is typically used around geometries of smaller dimension. Herein, two step of multigridding were performed. A resolution of x- and y-dimension equal to 3 mm, and z-dimension equal to 8 mm was imposed to the system coil/shield (figure 2.10a). For the first multigridding step a uniform resolution of 2 mm was imposed to a cuboid region of $420 \times 90 \times 650 \text{ mm}^3$ (w x d x h) isocentrically with the coil miming an ASTM phantom (figure 2.10b). For the second multigridding step an additional uniform resolution of 0.5 mm was imposed to a cuboid region of $2 \times 2 \times 400 \text{ mm}^3$ (w x d x h) isocentrically with the coil (figure 2.10c). This last multigrid step is typically used when medical implant are simulated within the phantom. More details about safety of implants in MRI will be discussed in Part II of this thesis. Results showed a frequency variation less than 1 %.

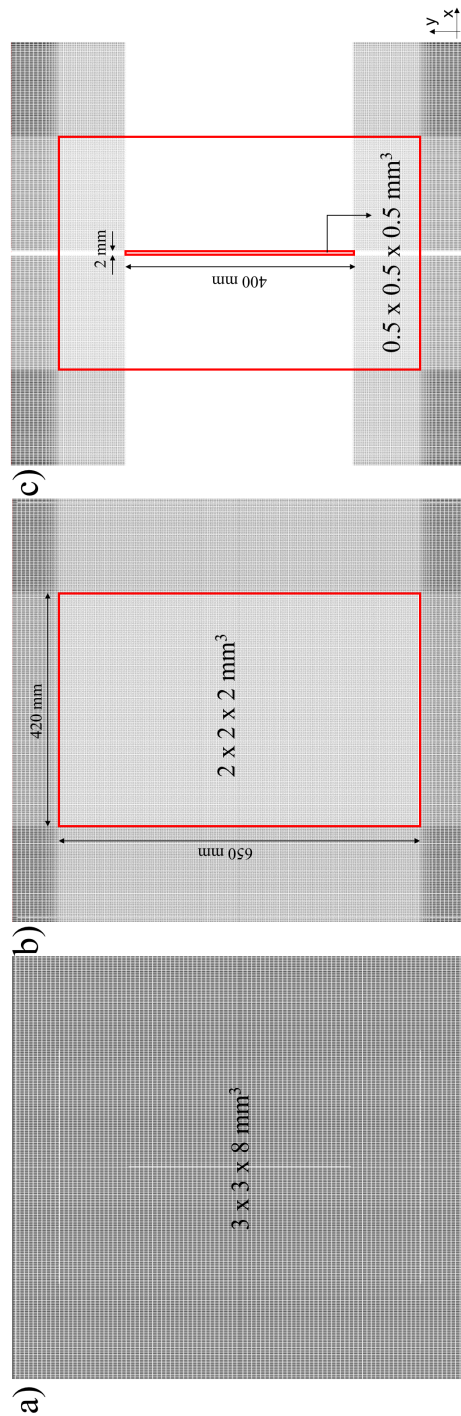


Figure 2.10: Implementation of the multigrad evaluation based on two steps. The FDTD grid reported are on the xy plane. a) original FDTD grid of $3 \times 3 \times 8 \text{ mm}^3$ (x, y, z); b) implementation of the first multigrad step imposing a finer grid of $2 \times 2 \times 2 \text{ mm}^3$ (x, y, z) in a space typically occupied by the ASTM phantom; c) implementation of the second multigrad step imposing a finer grid of $0.5 \times 0.5 \times 0.5 \text{ mm}^3$ (x, y, z) isocentrically with the coil.

2.3 Sensitivity of electric and magnetic field vs. input parameter

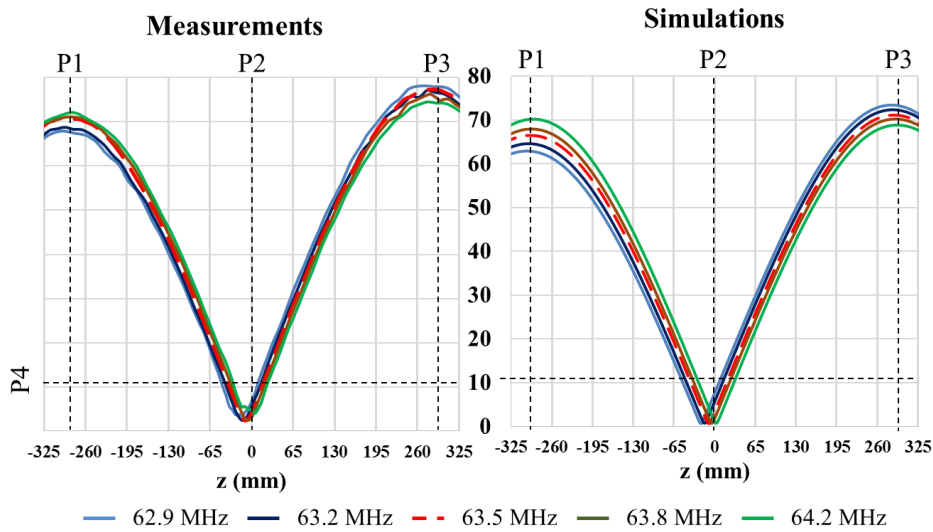


Figure 2.11: Amplitude of the measured and simulated E field along the longitudinal central line of the coil when fed off-resonance. The coil feeding sources are placed on the negative side of the z-axis as shown in figure 2.1.

2.3 Sensitivity of electric and magnetic field vs. input parameter

2.3.1 Input signal frequency

For the FDTD convergence cases studied, results showed an overall frequency variation less than 3 %. Here in the variability of the $\|E\|$ and $\|B\|$ with respect to the frequency of the input signal was studied. Firstly a convergence study similar to the one already performed was done looking at the profile of the $\|E\|$ and $\|B\|$ fields along the z-axis. Less than 4 % difference was observed for simulation time higher than 30 periods, and less than 0.1 % for simulation time higher than 50 periods. Thus accordingly to what previously found, the convergence limits of 30 periods were imposed to the simulations.

Because the nominal resonance frequency of the physical coil was of 63.52 MHz, the numerical model was adjusted to resonate at the same frequency. The capacitance was adjusted to $C = 72.8$ pF. To study the coil sensitivity with respect to the input waveform frequency, a set of simulations and measurements were performed driving the coil at 0.5% and 1% above and below the 63.52 MHz resonant frequency.

The $\|B\|$ was invariant with respect to frequency for both the physical and numerical coils. Conversely, when the coil was forced to work out of resonance, the symmetry of the $\|E\|$ changed for both the physical coil and the numerical model (figure 2.11). To quantify the sensitivity, four fixed point were chosen in the profile of the electric

Numerical implementation and verification of the RF birdcage coil model

Input frequency			$f_r - 1\%$ 62.9MHz	$f_r - 0.5\%$ 63.2MHz	f_r 63.5MHz	$f_r + 0.5\%$ 63.8MHz	$f_r + 1\%$ 64.2MHz
Meas.	P1 285mm	V/m	64.67	68.55	70.55	71.16	72.04
	P2 0mm	V/m	6.73	5.48	3.92	3.12	4.93
	P3 285mm	V/m	77.92	76.78	77.23	75.87	74.35
	P4 10V/m	mm mm	-45 10	-40 15	-35 15	-30 20	-25 25
Sim.	P1 -285mm	V/m	62.66	64.41	66.38	67.87	70.15
	P2 0mm	V/m	7.6	5.64	3.37	1.78	1.17
	P3 285mm	V/m	73.78	-72.31	71.08	70.18	68.77
	P4 10V/m	mm mm	-51 6	-45 12	-39 18	-33 24	-27 30

Table 2.1: $\|E\|$ field value in P1, P2, P3 and P4 for the five analyzed frequencies.

field:

- three points with the fixed coordinates on the longitudinal axis (i.e., z-axis): at the isocenter (P2) and at 285 mm from the isocenter (P1 and P3);
- a fourth point was where the value of $\|E\|$ was fixed at 10 V/m (P4)

Table 2.1 reports the $\|E\|$ values for the measured and simulated coil in the four selected points.

At the resonant frequency, both the physical and numerical coil showed an asymmetric profile of the $\|E\|$ along the z-axis. The profile showed a minimum 7 mm out from the isocenter, and two unequal maxima. In particular the maximum at the end-ring with the feeding sources (P1) was 10 % lower than the one on the opposite side (P2). When the sources were fed at different frequencies, the asymmetry of the field was affected. In particular with frequencies lower than the resonance, the local minimum at the isocenter of the coil (z-axis = 0 mm) moved closer to the feeding sources (negative values of the z-axis). Conversely, with the increase of the frequency the local minimum moved farther. Additionally, the two maxima of $\|E\|$ were unbalanced, with the maximum in P1 increasing as the frequency increased and the one in P2 decreasing as the frequency increased.

Table 2.2 reports the sensitivity analysis with respect to the frequency. As expected by the fields profiles, while the sensitivity of H was always less than 0.011%/%, the sensitivity of E was significantly higher in both the physical and numerical coil, with values up to 120%/%, which highlights the need of a proper numerical implementation. Where %/% indicates the percentage variation of the observed quantity (e.g., H field) with respect to the percentage variation of the parameter (i.e., frequency).

2.3 Sensitivity of electric and magnetic field vs. input parameter

MEASUREMENTS							
Frequency source	z (mm)	$\ \vec{E}(f_r, z)\ $ (V/m)	$\ \vec{E}(f_r + 1\%, z)\ $ (V/m)	Sens. %/%	$\ \vec{E}(f_r - 1\%, z)\ $ (V/m)	Sens. %/%	
	-325	95.37	98.34	3.12	92.34	3.18	
	0	4.12	6.73	63.25	9.19	122.85	
	325	104.85	101.50	3.20	106.37	1.45	
	z (mm)	$\ \vec{H}(f_r, z)\ $ (A/m)	$\ \vec{H}(f_r + 1\%, z)\ $ (A/m)	Sens. %/%	$\ \vec{H}(f_r - 1\%, z)\ $ (A/m)	Sens. %/%	
	-325	0.48	0.48	0.00	0.48	0.00	
	0	1.00	1.00	0.00	1.00	0.00	
	325	0.48	0.48	0.00	0.46	2.86	
	SIMULATIONS						
	Frequency source	z (mm)	$\ \vec{E}(f_r, z)\ $ (V/m)	$\ \vec{E}(f_r + 1\%, z)\ $ (V/m)	Sens. %/%	$\ \vec{E}(f_r - 1\%, z)\ $ (V/m)	Sens. %/%
-325		90.62	93.88	3.60	100.16	10.53	
0		4.60	1.60	65.28	10.37	125.52	
325		97.03	95.76	1.31	85.54	11.85	
z (mm)		$\ \vec{H}(f_r, z)\ $ (A/m)	$\ \vec{H}(f_r + 1\%, z)\ $ (A/m)	Sens. %/%	$\ \vec{H}(f_r - 1\%, z)\ $ (A/m)	Sens. %/%	
-325		0.52	0.52	0.00	0.52	0.00	
0		1.00	1.00	0.00	1.00	0.00	
325		0.51	0.51	0.00	0.51	0.00	

Table 2.2: Sensitivity of E and H magnitude for the physical and numerical coil with respect to the frequency. The values of E and H were calculated in the three points P1, P2, and P3 identified in figure 2.11 along the longitudinal axis of the coil.

2.3.2 Numerical coil losses

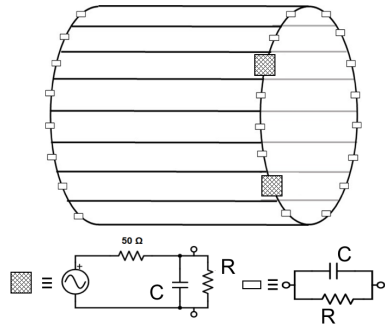


Figure 2.12: Position of the two sources and of the lossy components within the numerical RF coil model. On the bottom of the figure the electrical schematic used for the sources and the lossy components is also reported.

As discussed in section 2.1, capacitances are used within coil to generate a resonance system. However, physical capacitors and inductors as used in electric circuits are not ideal components, but they are made of materials with a proper finite electrical resistance. Hence each physical component has some resistance in addition to its property (i.e., capacitance or inductance). For RF applications these components are typically treated as ideal capacitors (C) and inductors in series with a resistance (R) defined as the equivalent series resistance (ESR). It is also common to find components as R in parallel to C, that as in [121]:

$$R_{parallel} = \frac{\omega^2 ESR^2 C^2 + 1}{\omega^2 ESCR^2} \quad (2.3)$$

Numerical implementation and verification of the RF birdcage coil model

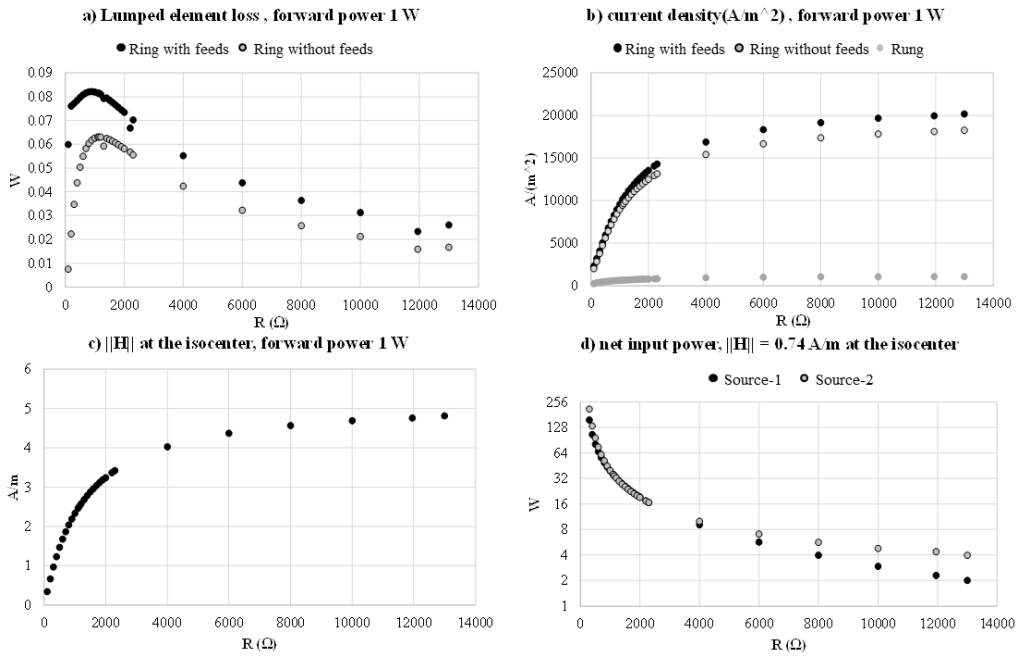


Figure 2.13: Effect of the resistance variability on (a) losses of the impedance composed by the parallel of R and C , b) current density on the rungs/rings, c) H field at the isocenter, and d) net input power required by the coil to obtain $0.73 A/m$ at the isocenter.

Throughout these sections R was modeled as a parallel resistor (figure 2.12, because the simulations were found more stable for a high value of resistance rather than a small one.

The effect of the resistance defined for the simulations was studied with respect to several parameters: losses of the RC elements, current density on the rungs/rings, H amplitude at the isocenter, and net input power required by the coil to generate a given magnetic field (e.g., $0.74 A/m$) at the isocenter of the coil. The simulations were performed varying R between 100Ω and $13 k\Omega$. The values were normalized to the same available power (i.e., $1 W$) at the two feeding sources.

The component losses and the current density were higher on the ring where the feeding sources were placed as a result of the asymmetric implementation of the coil models, where the signal is fed only in one side of the resonator. As a consequence the electric field magnitude was also asymmetric along the z -axis, as shown in figure 2.11.

Overall results show that (figure 2.13) as the resistance increased, the losses of the RC element decreased, the current density in the rungs/ring increased, and the H field generated at the isocenter of the coil increased. Thus, with increased R the net input power required to obtain a given H field magnitude at the isocenter of the coil decreased.

To quantify the sensitivity of the E and H field with respect to both R and C , sim-

2.3 Sensitivity of electric and magnetic field vs. input parameter

R	z (mm)	$\ \vec{E}(R_p, z)\ $ (V/m)	$\ \vec{E}(R_p + 1\%, z)\ $ (V/m)	Sens. %/%	$\ \vec{E}(f_r - 1\%, z)\ $ (V/m)	Sens. %/%
	-325	90.62	90.56	0.01	90.58	0.01
	0	4.60	4.70	0.26	4.75	0.41
	325	97.03	97.09	0.01	97.10	0.01
	z (mm)	$\ \vec{H}(R_p, z)\ $ (A/m)	$\ \vec{H}(R_p + 1\%, z)\ $ (A/m)	%/%	$\ \vec{H}(R_p - 1\%, z)\ $ (A/m)	%/%
-325	0.52	0.51	0.33	0.51	0.33	
0	1.00	1.00	0.00	1.00	0.00	
325	0.51	0.52	0.34	0.52	0.34	
C	z (mm)	$\ \vec{E}(R_p, z)\ $ (V/m)	$\ \vec{E}(R_p + 1\%, z)\ $ (V/m)	Sens. %/%	$\ \vec{E}(R_p - 1\%, z)\ $ (V/m)	Sens. %/%
	-325	90.62	99.68	2.00	81.70	1.23
	0	4.60	12.07	32.46	19.77	41.21
	325	97.03	88.34	1.79	106.10	1.17
	z (mm)	$\ \vec{H}(R_p, z)\ $ (A/m)	$\ \vec{H}(R_p + 1\%, z)\ $ (A/m)	%/%	$\ \vec{H}(R_p - 1\%, z)\ $ (A/m)	%/%
-325	0.52	0.53	0.33	0.55	0.66	
0	1.00	1.00	0.00	1.00	0.00	
325	0.51	0.52	0.34	0.51	0.00	

Table 2.3: Sensitivity of $\|\vec{E}\|$ and $\|\vec{H}\|$ for the numerical coil model with respect to the lossy component composed of a resistance R and capacitance C in parallel. The values of E and H were calculated in the three points P1, P2, and P3 identified in figure 2.11 along the longitudinal axis of the coil.

ulations were additionally performed varying the nominal values of $\pm 1\%$. Results are reported in table 2.3.

As shown in the table 2.3, the overall profile of E and H was not affected by the resistance, with a maximum sensitivity of 0.34 %/% and 0.41 %/% respectively. The sensitivity of E and H with respect to the capacitance was 2 %/% and 0.66 %/% for the E and H respectively, with the exception of the isocenter where the sensitivity was up to 41.21 %/%. This was in line with the relation between the two quantities, as suggested by equation 2.1. The sensitivity with respect to the capacitance followed a similar trend of the sensitivity with respect to the tuning frequency reported in table 2.2.

2.4 Numerical modeling of the physical phantoms

Experimental measurements with phantoms can be useful not only for validation of numerical results, but also for exposure assessment in different conditions. EM field distribution within phantoms can be easily controlled because of their geometry simplicity. As theoretically explained in section 1.2.4, if a non conductive object is present within the coil, then the varying \vec{E} "curls" around the \vec{B}_1 with a distribution that is dependent on the geometry of the object [122].

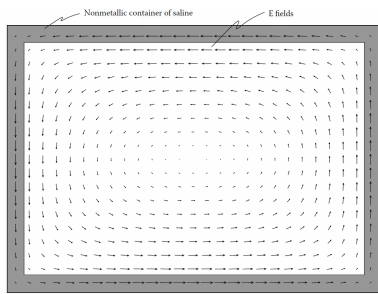


Figure 2.14: Calculated E fields at one instant of time consisting of a 1 kHz B field (directed out of the paper) applied to a saline phantom [122].

Figure 2.14 reports the theoretical distribution of the calculated \vec{E} inside a phantom made of saline solution [122]. The direction of the \vec{E} is shown by the arrows, whereas the strength of the field is defined by the arrow dimension. As a verification step, the E field produced by the varying $\|\vec{B}\|$ was herein studied for the numerical RF birdcage coil previously described. The \vec{E} field was computed for the coil unloaded (i.e., empty condition), and loaded with phantoms of simplified geometries (i.e., a cylinder and a sphere), and phantom of different shapes typically used for RF

exposure assessment (figure 2.15). Additionally, the ellipsoidal phantom (figure 2.15b) was herein studied for two different positions within the coil: with the major axis perpendicular (Pos1) and parallel (Pos2) to the z-axis. This was done because position Pos1 is suggested by the TS ISO 10974 [111], but Pos2 allowed for a comparison of results with the other two phantoms (ASTM and superellipsoidal).

As in the theoretical case, the \vec{E} field is represented by arrows, showing the field direction, but the strength is represented by the colorbar intensity. All the results were normalized to obtain a B_1^+ RMS equal to $3 \mu T$ in the central axial slice of the coil. This normalization was chosen according to the value suggested by the IEC [123].

Because the \vec{E} field is time-varying the results were here reported for the phase 0 of the input signal. It is important to notice that the direction of the \vec{E} field generated by the time-varying \vec{B}_1 is orthogonal to the z-axis. This is expected because the \vec{B}_1 generated to excite the magnetization vector of the spins has to be perpendicular to the direction of the main static field B_0 that is directed along the z-axis. A deep analysis of the E field distribution within the physical coil and for different numerical implementation will be studied in section 3. Results will show how the \vec{E} distribution is affected not only by the phantom shape, but also by the numerical implementation of the coil.

Results reported in figure 2.16 shows the dependency of the \vec{E} field distribution

2.4 Numerical modeling of the physical phantoms

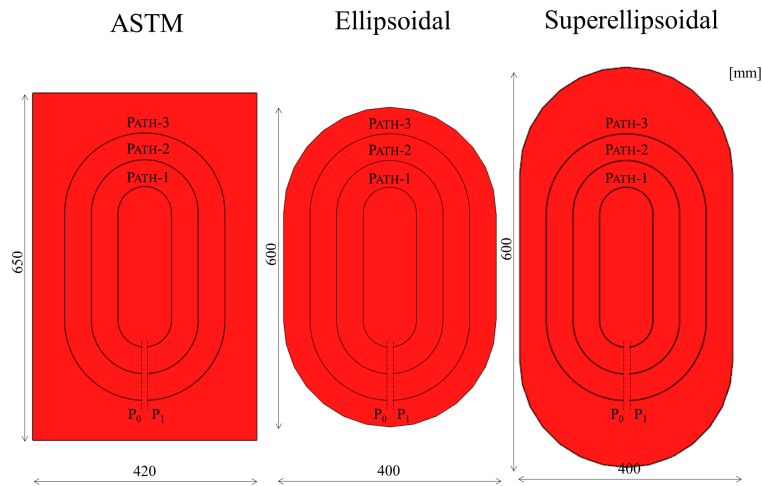


Figure 2.15: Numerical phantoms: ASTM, ellipsoidal and superellipsoidal. In each phantom the three extraction lines were defined for the evaluation of the E filed distribution. The phantom were filled with saline solution, with values of electrical properties as indicated by the standard [110]: $\varepsilon = 78$ and $\sigma = 0.47S/m$. the three phantoms were 90 mm thick.

with the shape of the object loading the phantom. The sphere and the cylinder show the same behavior of the curling \vec{E} in the XY plane where the two object are represented by the same sections. Similarities are also visible in the other two planes (XZ and YZ), however as expected by theory the \vec{E} in the cylinder curls along the object boundaries causing a different profile with respect to the one of the spheres.

For the same reasons with different phantoms loading the coil, it is possible to observe different behaviors of the curling \vec{E} 2.17. Because the three phantoms presented in figure 2.15 were characterized by the same thickness (i.e., 90 mm) the distribution of the curling \vec{E} within the YZ and XY planes was similar. This was expected by the results with the sphere and the cylinder. Differences were observed in the XZ plane where the geometries of the three phantoms affected the behavior of the \vec{E} field. The \vec{E} file in the ASTM phantom was similar to the theoretical one (figure 2.14), with profile of the curling \vec{E} affected by the presence of the phantom corners where the strength of the \vec{E} dropped. The corner effect was avoided with the ellipsoidal and superellipsoidal phantoms, where the distribution of the \vec{E} was more homogeneous. The profile showed a uniform gradient drop of the filed strength to the center of the phantom everywhere in the perimeter. Superellipsoidal and ellipsoidal-Pos2 showed the same profiles of \vec{E} , with the superellipsoidal characterized by a longer section with curled \vec{E} field parallel to the z-axis because of its longer longitudinal dimension (i.e., 600 mm for the ellipsoidal and 750 mm for the superellipsoidal).

Uniformity of \vec{E} field distribution within the phantom can be defined studying the profile of the \vec{E} field tangential to a defined path (figure 2.15). Three different paths

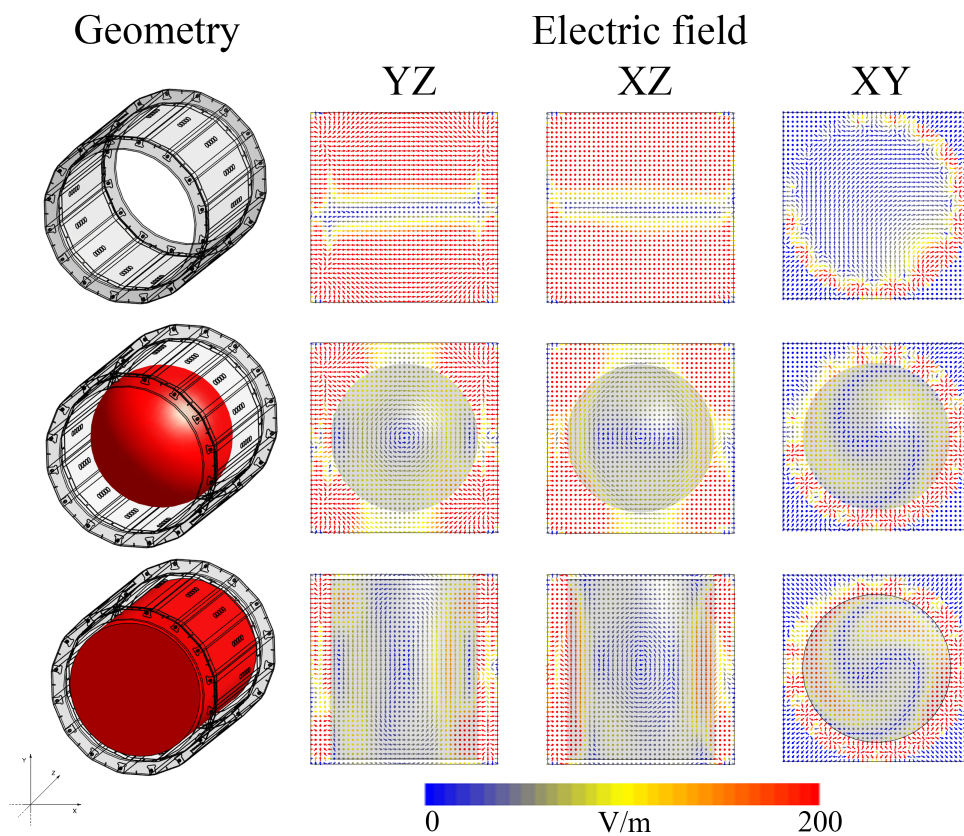


Figure 2.16: Curled E field generated by the time varying B field for the coil empty and loaded with a cylinder and a sphere of the same radius as the cylinder. \vec{E} field is represented at phase 0 of the input signal, in the three central planes YZ, XZ, and XY. *N.B. An higher resolution representation of this figure is included in Appendix B.*

2.4 Numerical modeling of the physical phantoms

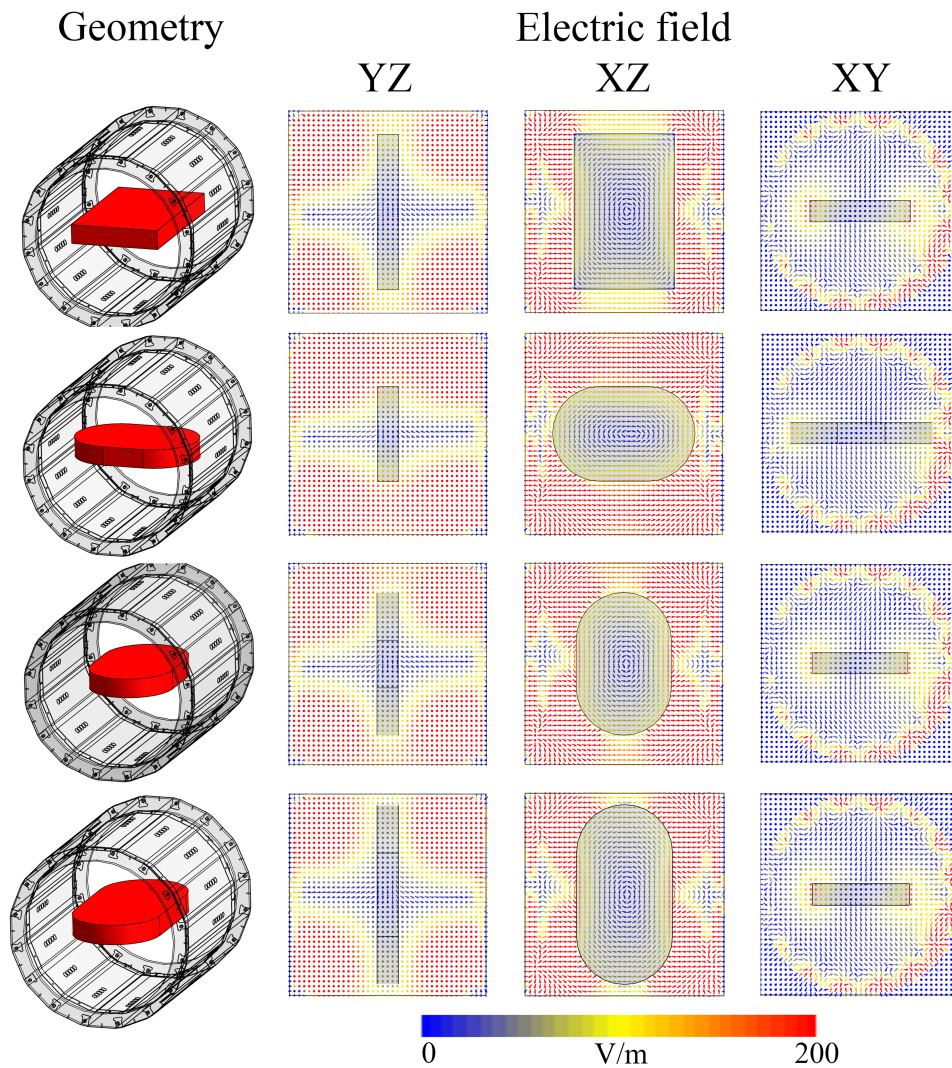


Figure 2.17: Curled \vec{E} field generated by the time varying \vec{B}_1 field for the coil loaded with the ASTM phantom, the 600 mm phantom in two positions, and the superellipsoidal phantom. E field is represented at phase 0 of the feeding, in the three central planes YZ, XZ, and XY. *N.B. An higher resolution representation of this figure is included in Appendix B.*

Numerical implementation and verification of the RF birdcage coil model

[%]	ASTM	Ellipsoidal-Pos1	Ellipsoidal-Pos2	Superellipsoidal
Path-1	34	37	40	20
Path-2	31	16	16	42
Path-3	46	27	34	52

Table 2.4: Percentage variation of the $\|E_{tan}\|$ profile for the three phantoms along the three paths defined in figure 2.17.

were chosen to study and compare the variability of distribution in different position inside the phantoms.

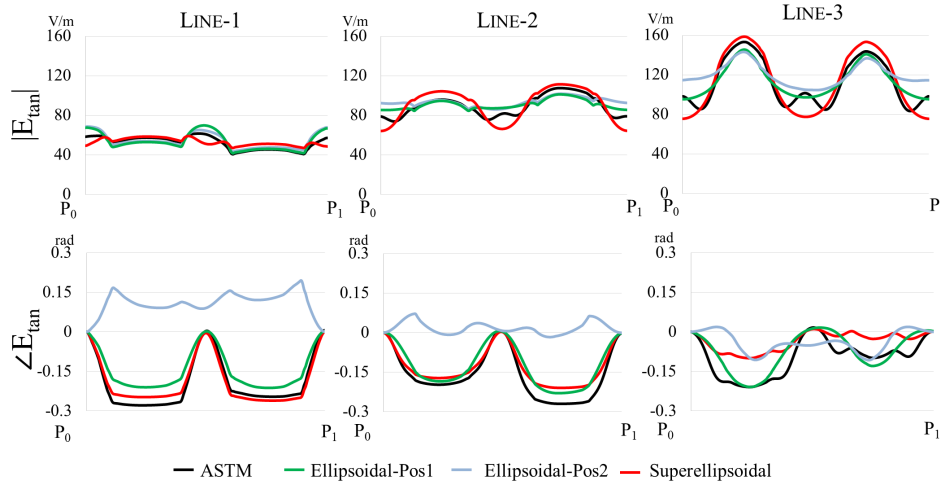


Figure 2.18: Magnitude and phase of the tangential component of the electric field along the three paths defined in figure 2.15, for the three analyzed phantoms. The ellipsoidal phantom was tested in the two positions with the longitudinal line parallel (Pos1) and perpendicular (Pos2) to the z axis. *N.B.* An higher resolution representation of this figure is included in Appendix B.

Profiles of the \vec{E} along the three paths show an increasing of E field strength as the field gets closer to the phantom edge (Path-3). This was already expected from the results shown in figure 2.17. The $\|E_{tan}\|$ within the three phantoms showed different uniformity of the profile. In particular, as reported in table 2.4, the superellipsoidal phantom showed a increasing homogeneity as the path got closer to the center, representing the one with the minor variability of 20 % for Path-1. Conversely, the ASTM and ellipsoidal phantom showed the minimum variability for Path-2, namely 31 % and 16 % respectively.

The Ellipsoidal-Pos1 was the one characterized by the most homogeneous phase distribution with variation always less than 0.2 rad. Conversely, the ASTM, Ellipsoidal-Pos2 and Superellipsoidal where showed a less homogeneous phase profile with variation up to 0.3 rad for all the three analyzed paths.

2.4 Numerical modeling of the physical phantoms

The higher homogeneity in Ellipsoidal-Pos1 was expected because the phantom was placed with its longer dimension laying on the plane where the curly \vec{E} field is directed by theory (i.e., perpendicular to the z-axis). Thus the \vec{E} field distribution is not broken by the phantom geometry, allowing for a more uniform field distribution within the phantom, with respect to the same phantom in Pos2. However in chapter 3 the 750 mm superellipsoidal was used for testing of partially implanted lead along the z-axis, because it was the one offering the longer uniform distribution of $\|\vec{E}\|$ along this axis (figure 2.18). The lead insertion path defined for the phantom was chosen based on the minimum variability of 20 % shown for Path-2.

2.5 Effects of Tuning Conditions on Near Field of MRI Transmit Birdcage Coil at 64 MHz

This study ¹ investigates how the tuning conditions of a 64 MHz / 1.5 T RF birdcage coil modeled with an RF circuit and 3D EM co-simulation affect the electric and magnetic near-field distribution.

The near-field generated by the RF transmitter depends on the geometry of the coil (i.e., coil length and diameter), as well as on the feed sub-circuit and radiative element decoupling [125]. In sections 2.3.1, and 2.3.2 the sensitivity of the EM fields with respect to the signal frequency and coil losses was studied. This section investigates how the tuning conditions for different feed sub-circuits affect the electric and magnetic near-field distribution.

Birdcage coils installed in clinical MRI systems have fixed tuning conditions – optimized for coil loaded with a patient – that are based on proprietary techniques implemented to improve field polarization and homogeneity. The main goals of this study were:

1. to perform EM simulations of a 64 MHz RF birdcage body coil with variable tuning conditions;
2. to evaluate difference between numerical results and measurement done at commercially available RF birdcage body coil.

Theoretical background — The RF feed sub-circuits provide impedance matching functionality to ensure maximum power transfer to the coil from the amplifier. The RF feed sub-circuits can be represented by a single variable reactance element, for example trim capacitor, or a more sophisticated multielement sub-circuit. The birdcage coil tuning - as optimization of any other multi-channel RF transmitter - is guided by the minimization of an error function (EF), which is a measure of the difference between the actual and desired array conditions (“optimization criteria”). Commonly used criteria for multichannel RF transmitters, at the desired frequency, are:

1. the element reflection coefficient (S_{xx}) must be set and equal to a required value (i.e., S_{xx_t}) for each array element;
2. the element coupling S_{xy} must be equal to a required value (i.e., S_{xy_t}) for each decoupled element pair.

Hence:

$$EF = \sum_{Elem} W_x \|S_{xx} - S_{xx_t}\|^2 + \sum_{all_dec} W_{xy} \|S_{xy} - S_{xy_t}\|^2 \quad (2.4)$$

¹Majour content of this paragraph was published as conference paper for the 2016 IEEE Engineering in Medicine and Biology Society [124]

2.5 Effects of Tuning Conditions on Near Field of MRI Transmit Birdcage Coil at 64 MHz

where: $Elem$ is number of elements (inputs) of the transmitter, all_{dec} is number of decoupled element pairs, W_x and W_{xy} are weighting factors. The weighting factors may have different values from one criterion to another, and they are used to emphasize one vs. the other optimization criteria. For the case herein evaluated, namely a birdcage coil excited by two RF sources, $Elem = 2$ and $all_{dec} = 1$. Because a birdcage coil has several resonance modes resulting in similar scattering parameter values at the different resonance frequencies, the circuit level optimization based on EF defined in 2.4 can result in improper rung currents that should be for generation of circularly polarized magnetic field [126]:

$$I_n = I_0 \cdot e^{i2\pi n/16} \quad (2.5)$$

Therefore our EF included criteria for both S parameter values and I_n , i.e. included the third term:

$$\sum_{all_rung} W_r \|I_n - I_0 \cdot e^{i2\pi n/16}\|^2 \quad (2.6)$$

When a coil is loaded by a phantom more than one local minimum of EF occur, and their location (i.e. values of variable components) substantially depends on ratios between waiting factors W_x , W_{xy} and W_r .

A 16 rung birdcage coil becomes a 16 element array if the coil is connected to 16 power sources with independently defined RF amplitudes and phases. As known from MRI transmit array theory, an increased number of RF sources allow generating a current distribution with smaller variations from required pattern. It was also shown in [127] that single optimization minimum is obtained for $EF = \|\vec{P}_{refl}\|^2$, where \vec{P}_{refl} is the total power reflected by the entire multi-channel RF transmitter array. The birdcage tuning procedure using the \vec{P}_{refl} for a given load could be proposed as a good approach to model a commercial birdcage coil, for which the field optimization techniques are typically confidential information.

Numerical simulations — The numerical simulations were performed using RF circuit and 3D EM co-simulation [128]. The RF circuit simulations were performed with ADS 2015 (Agilent, Santa Clara, CA, USA), and the 3D EM simulations with HFSS 2014 (ANSYS, Canonsburg, PA, USA). In the numerical part of this study, the coil was loaded with ASTM phantom [110] and then tuned. The Q factor of all capacitors was defined at the beginning of the optimization process. Two options were investigated: a) $Q = 365$ (similar to the losses of capacitors used in MITS1.5), and b) $Q = 10000$ (corresponding to a practically loss free condition). Overall, four different tuning cases were studied. In case #1 the RF feed sub-circuit was a single trim capacitor and capacitor Q factor was equal to 365.

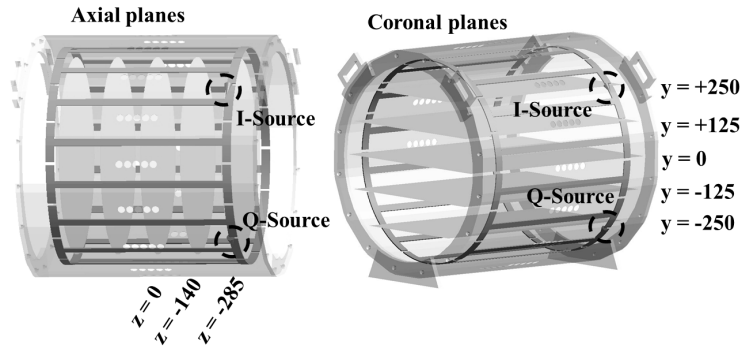


Figure 2.20: Coordinates of the measured planes in the unloaded condition. $\|\vec{E}\|$ and $\|\vec{H}\|$ were measured in 2 axial and 5 coronal planes.

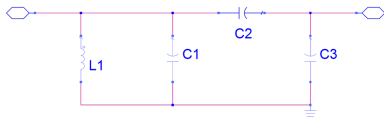


Figure 2.19: RF feed subcircuit used for case #2 and case #3 with capacitor Q factor value of 365 and 10000 respectively

In case #2 the RF feed sub-circuit was the multi-element subcircuit shown in figure 2.19 and the capacitor Q factor was equal to 365. In case

#3 the RF feed sub-circuit was the same as in case #2 but with a capacitor Q factor equal to 10000.

In case #4 the capacitor Q factor was equal to 365 and the EF was as defined in 2.6. For the birdcage investigated, the following components were op-

timized: a) complex impedance of each element of RF feed sub-circuit, b) complex impedance of capacitors placed in each ring gap. S_{xx_t} was equal to -20 dB and S_{xy_t} was equal to -16 dB. The amplitude and phase of the RF sources used to excite the coil were fixed, namely same amplitudes with the phase shift between RF sources 90° , as in quadrature excitation.

Experimental measurements — EM field measurements were collected in the labs of the FDA using the DASY5NEO robotic measurement system (SPEAG, Zurich, Switzerland) with the ER3DV6 electric field probes (SPEAG) and the H3DV7 magnetic field probe (SPEAG).

Measurements were performed in unloaded condition for two axial and 5 coronal planes (figure 2.20). For each measurement point the probes returned three RMS values – one for each field component x, y, and z; the total magnitude was then computed based on the quadratic norm. The comparison between measured and simulated field was performed for each measured plane, with all results normalized to the norm of the magnetic field vector at the center of the RF-coil ($\|H_{iso}\|$).

2.5 Effects of Tuning Conditions on Near Field of MRI Transmit Birdcage Coil at 64 MHz

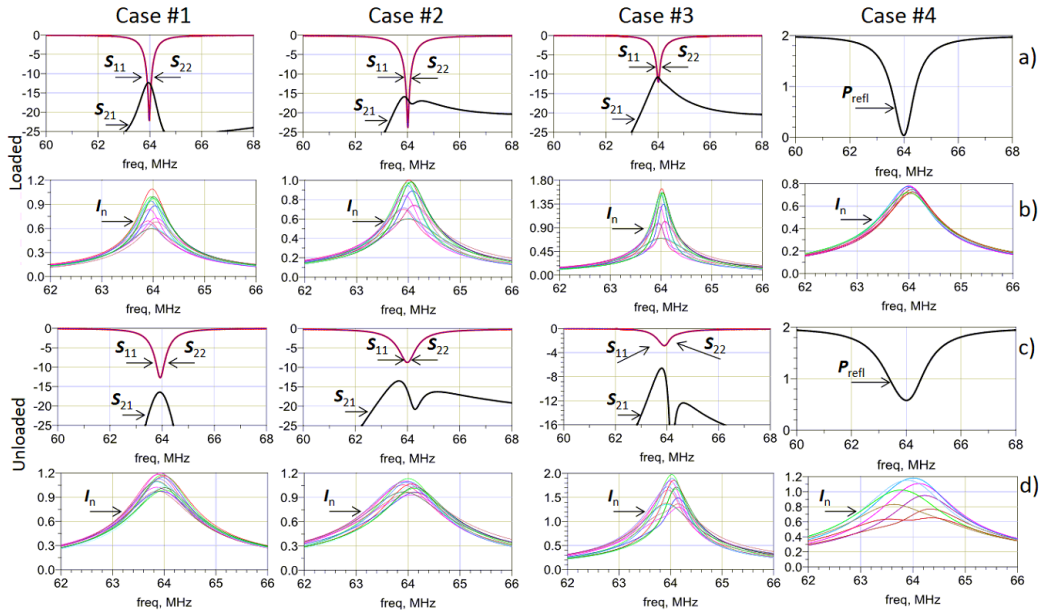


Figure 2.21: (a) and (b) ASTM phantom as a load. (a) Cases #1, #2, and #3: S parameters; Case #4: Power reflected. (b) Rung currents (values in A) for all cases. The transmit power of each RF source was 1W. (c) and (d) Unloaded coil with tuning condition obtained for ASTM phantom. (c) Cases #1, #2, and #3: S parameters; Case #4: Power reflected. (d) Rung currents (Values in A) for all cases. The transmit power of each RF source was 1W.

Implementation comparisons — In case #1, as it shown in figure 2.21, the ADS optimization was not able to find a solution that fulfilled S parameter criteria (figure 2.21a). The range of current amplitudes was from 0.6 to 1.1 A at the resonant frequency for transmit power of each RF source equal to 1W (figure 2.21b). For the case of coil unloaded, S11 increased, S21 decreased (figure 2.21c), and the range of current amplitudes was also smaller (i.e., from 0.9 to 1.2 A) (figure 2.21d). In case #2 the ADS optimization was able to find a solution that fulfilled the S parameter criteria (i.e., $S_{xx_t} = -20dB$). The multi-element sub-circuit substantially improved S21 of the birdcage coil (figure 2.21a) whereas the rung currents (figure 2.21b) did not meet the criteria defined by 2.4 and 2.6. In the case of unloaded coil, when comparing to case #1 the S11 was smaller, S21 was comparable (figure 2.21c), and the range of current amplitudes was decreased (figure 2.21d).

In case #3, when compared to case #2, the capacitor losses decreased, resulting in an increase of current amplitudes (i.e., up to 1.8 A), but also in degraded S parameters (figure 2.21a) and in a significantly broad range of currents in rungs (i.e., 0.6 to 1.5 A) (figure 2.21b). For unloaded coil, S11 was = - 4 dB (value characteristic of a non-tuned coil) and P_{refl} was 27% of transmit power, while the current amplitudes were still larger compared to the cases #1 and #2. In case #4, the optimization P_{refl} resulted in a value of P_{refl} equal to zero (figure 2.21a) and rung currents (figure 2.21b) close

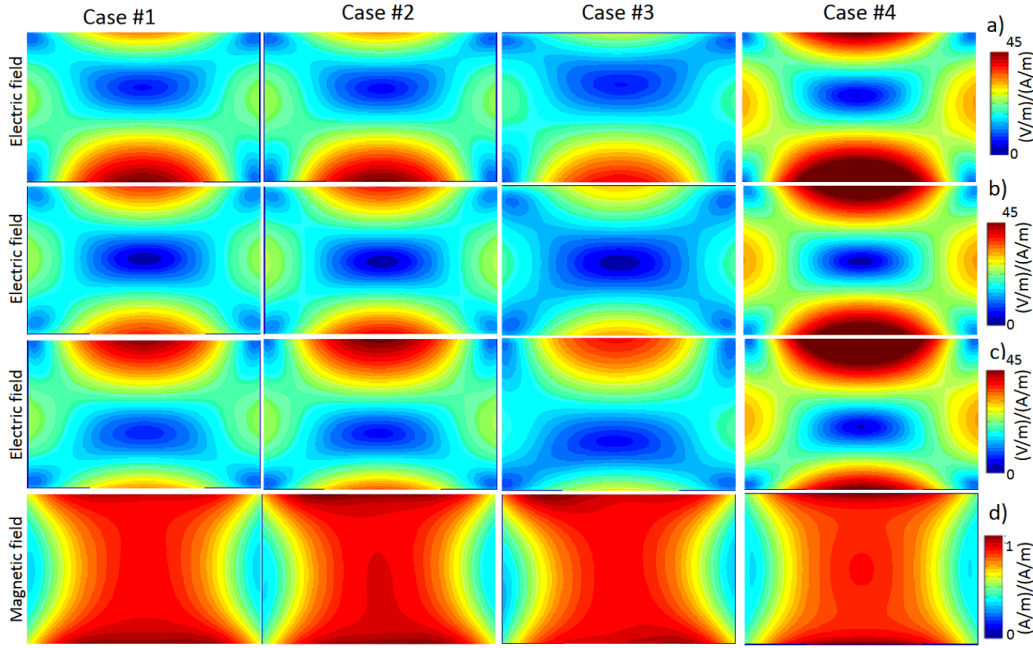


Figure 2.22: Result of the simulated $\|\vec{E}\|$ and $\|\vec{H}\|$ inside the ASTM phantom for the 4 cases. Magnitude of electric (a, b, c) and magnetic (d) field for all cases. All results were normalized to the magnitude of the magnetic field at the isocenter of the RF-coil (i.e., $\|H_{iso}\|$). (a) and (d) results for the central coronal plane ($xz = 0$); (b) Results for the coronal plane $xz = -30$ mm from the isocenter. (c) results for the coronal plane $xz = +30$ mm from isocenter.

to the values defined by 2.5. Conversely, in the case of coil unloaded the variation of current amplitudes was the largest (i.e., from 0.6 to 1.2 A at the resonant frequency) when compared to the other cases (i.e., 0.6 to 1.2 A).

The different tuning conditions affect the incident electric field. Moreover, as shown in figure 2.22, the distribution of $\|\vec{E}\|$ inside the ASTM phantom substantially depends on the plane selected within the phantom and its distance from the iso-center. Specifically, the distribution of $\|\vec{E}\|$ in planes at 3 cm from the isocenter was visibly different than the $\|\vec{E}\|$ at the isocenter.

All the cases resulted in a rather uniform distribution of magnetic field as expected. Additionally, when conducting the validation process it is also important to take into consideration the reverse engineering steps that include: a) coil component tolerances, b) variation of trimming elements with unknown precise values, and c) dependence of RF sources amplitudes and phases on the near field optimization procedure. The focus of this study was on the effect of tuning conditions on the EM field induced in a phantom at 64 MHz. While the effect of coil geometry at 64 MHz has been extensively studied in literature, the reflected power caused by mismatch or detuning occurring for cases when the actual coil load differs from the one for which the coil was designed to be perfectly matched/tuned. Additional work may be of interest to evaluate how

2.5 Effects of Tuning Conditions on Near Field of MRI Transmit Birdcage Coil at 64 MHz

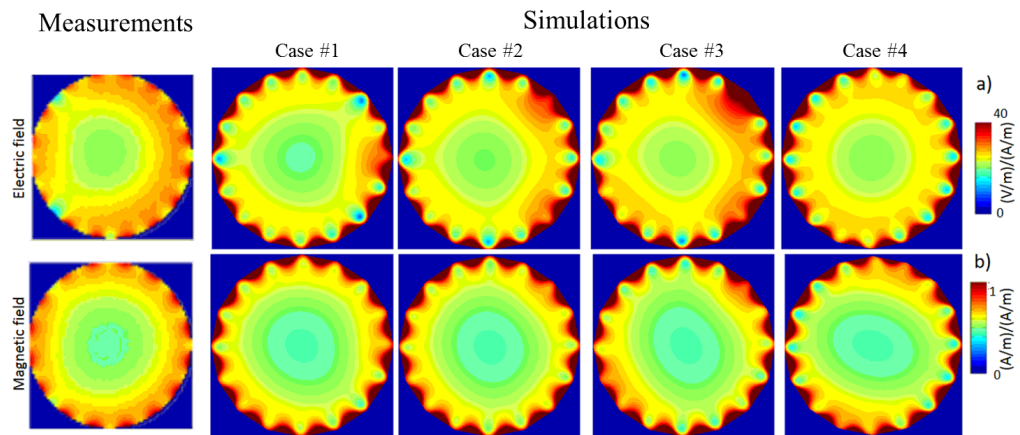


Figure 2.23: Magnitude of electric (a) and magnetic (b) field in the physical coil and all numerical cases studied. Images are for the axial plane $xy = 140$ mm from the isocenter. All results were normalized to the magnitude of the magnetic field at the isocenter of the RF-coil ($\|H_{iso}\|$).

changing loading conditions (i.e., asymmetric loads) may affect such mismatch, both at 64 MHz and also at higher frequencies (i.e., 128 MHz).

Chapter 3

Assessing the electromagnetic fields generated by a radio-frequency MRI body coil at 64 MHz: defeaturing vs. accuracy

The text from paragraph 3.1 to paragraph 3.6 was published as it is in IEEE Transactions on Biomedical Engineering [129]. For this reason concepts and definitions maybe already previously discussed in this thesis. The work was performed in collaboration with the DBP/CDRH/OSEL of the FDA (MD-USA) as part of Cooperative Research and Development Agreement with Imricor Medical Systems (MN-USA).

Paragraph 3.7 has been included in this thesis in addition to the original paper. The section discusses the numerical uncertainty quantification of the S2 coil model presented in the paper.

3.1 Abstract

Goal : This study aims at a systematic assessment of five computational models of a birdcage coil for magnetic resonance imaging (MRI) with respect to accuracy and computational cost.

Methods : The models were implemented using the same geometrical model and numerical algorithm, but different driving methods (i.e., coil “defeating”). The defeatured models were labeled as: specific (S2), generic (G32, G16), and hybrid (H16, $H16_{fr-forced}$). The accuracy of the models was evaluated using the "symmetric mean absolute percentage error" ("SMAPE"), by comparison with measurements in terms of frequency response, as well as electric ($\|\vec{E}\|$) and magnetic ($\|\vec{B}\|$) field magnitude.

Assessing the electromagnetic fields generated by a radio-frequency MRI body coil at 64 MHz: defeating vs. accuracy

Results : All the models computed the $\|\vec{B}\|$ within 35% of the measurements, only the S2, G32, and H16 were able to accurately model the $\|\vec{E}\|$ inside the phantom with a maximum SMAPE of 16%. Outside the phantom, only the S2 showed a SMAPE lower than 11%.

Conclusions : Results showed that assessing the accuracy of $\|\vec{B}\|$ based only on comparison along the central longitudinal line of the coil can be misleading. Generic or hybrid coils when properly modeling the currents along the rings/rungs were sufficient to accurately reproduce the fields inside a phantom while a specific model was needed to accurately model $\|\vec{E}\|$ in the space between coil and phantom.

Significance : Computational modeling of birdcage body coils is extensively used in the evaluation of radiofrequency-induced heating during MRI. Experimental validation of numerical models is needed to determine if a model is an accurate representation of a physical coil.

Index Terms —Field probes, finite-difference time domain (FDTD), safety, symmetric mean absolute percentage error (SMAPE), validation.

3.2 Introduction

Magnetic Resonance Imaging (MRI) is a radiological imaging technique widely used in clinical practice, with Over 33 million examinations a year in the U.S. [1]. The success of MRI is due to its clinical versatility, the use of non ionizing radiation, and the high soft-tissue contrast [130]. Birdcage body coils are the most common type of radiofrequency (RF) coil used in MRI in the clinical environment and have been shown to provide a highly homogeneous \vec{B}_1 field [16, 131, 132]. Birdcage body coils are typically driven by a two or four-port excitation with the power sources placed in one of the two end rings of the birdcage [18].

An accurate characterization of the electromagnetic (EM) field generated by the RF coil is needed to assess RF-induced heating of tissue during MRI [133, 134]. Hence, an accurate assessment of the overall or local SAR is important for the safety of the patient [34–36, 135–139] or in patients with conductive medical devices that are totally [37–40, 91, 134, 140, 141], or partially implanted, or in contact with the skin [133, 142]. In this context, computational modeling allows systematic and faster analysis of many variables affecting RF-induced heating, which cannot be accounted for experimentally [32, 33]. Over the past 20 years, computational modeling has been increasingly used to address the RF safety issue [34–40]. Several models of RF birdcage coil have been

3.2 Introduction

implemented following different levels of complexity, that here we categorized as: specific, generic, and hybrid. Specific models [36, 76, 107, 135, 136, 141, 143, 144] replicate the number and position of the input excitation in the real physical coil by the presence of lumped elements (i.e., resistors and capacitors) representing the input impedance of the ports. This allows reproducing the physical forward and reflected power. The importance of using a specific model was emphasized, for example, by Ibrahim et al. [36, 107] in order to correctly replicate the EM coupling between the coil and its load. A generic model [34, 35, 137, 145–149] makes use of a multiport excitation and forces currents inside the coil to a specific amplitude and phase, without the implementation of lumped elements. Liu et al. [35] supported the use of a generic model because of its low computational cost (i.e., no tuning required). Generic models were shown to well replicate the homogeneity of the magnetic field, electric field, and SAR distribution inside the ASTM phantom [76], the cylindrical phantom [150], and the human body models [35]. Finally, a hybrid model [77, 138, 150, 151] includes both the multiport excitation and the presence of lumped elements, the convenience of such an approach, over a specific model, is the independence of the frequency response from the loading conditions [91].

There are several studies that compared the different approaches [35, 76, 150] as well as studies that compared the models against measurements [37, 107, 145, 151]. However, the comparison between simulated and measured electric and magnetic field magnitude ($\|\vec{E}\|$ and $\|\vec{B}\|$, respectively) has been mostly performed along 1-D lines through the isocenter of the coil. In this study, we aimed to evaluate the effect of "defeaturing" the numerical model with respect to the computational cost of the simulations as well as accuracy against measurements. The term "defeaturing" was used to indicate that the birdcage model systems were implemented using different driving methods, while maintaining the same geometrical model and the same numerical algorithm. Five numerical models were implemented: one specific (i.e., S2, [36, 40, 136, 143]), two generic (i.e., G32 [34, 35, 147] and G16 [145, 146, 148]), and two hybrid (i.e., H16 [138, 150] and $H16_{fr-forced}$ [77]). The assessment of accuracy versus defeaturing was performed by comparing each numerical model with a physical coil in terms of frequency response, as well as $\|\vec{E}\|$ and $\|\vec{B}\|$. In line with the literature, as a first step $\|\vec{E}\|$ and $\|\vec{B}\|$ were compared along the longitudinal central line. Furthermore, the state-of-the-art approach was extended by including the evaluation of the fields performed for different planes both inside the phantom and in the space between phantom and coil. The field inside the phantom is of interest for SAR assessment with or without implanted conductive devices, while the space between phantom and coil must be characterized in the presence of conductive devices partially implanted or in con-

Assessing the electromagnetic fields generated by a radio-frequency MRI body coil at 64 MHz: defeaturing vs. accuracy

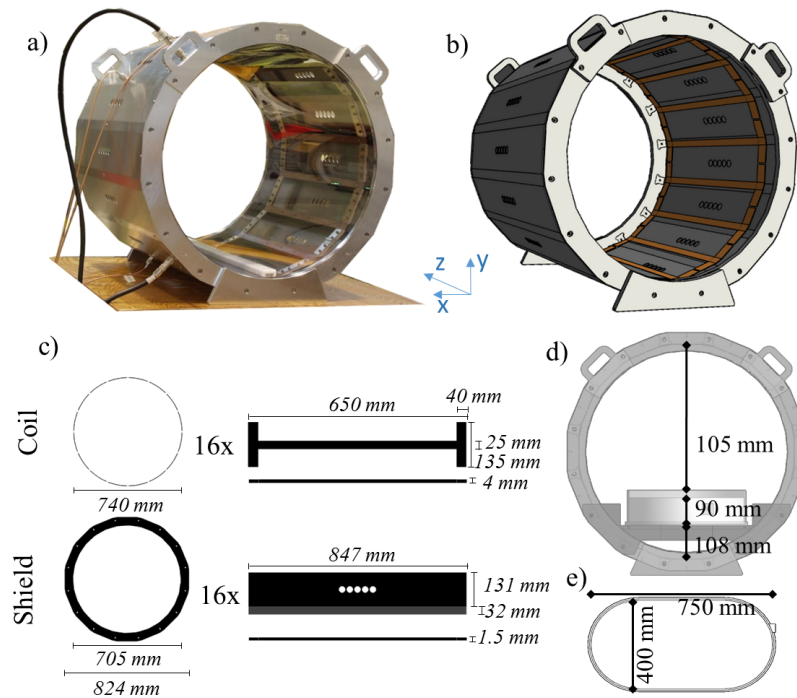


Figure 3.1: Geometry characterization of the system (a) MITS1.5 physical coil (b) 3-D view of the computational model as implemented in the software. The computational RF body coil system was modeled to match the physical coil geometry (c) During measurements a superellipse-shaped phantom (d) was placed in the bottom of the coil (e). The physical phantom was filled to a depth of 90 mm with a 2.5-g/L saline solution with a conductivity of 0.47 S/m.

tact with the skin. Therefore, the region of interest, where the model accuracy must be evaluated is dependent on the specific target of the study.

3.3 Materials and Methods

3.3.1 Measurements

Birdcage Coil Specifications — A commercially available high-pass birdcage body coil (MITS1.5, Zurich Med Tech, Zurich, Switzerland) was used for the measurements (see Figure 3.1a). The coil is composed of 16 rectangular strips (rungs) 570-mm long, which are laid out with cylindrical symmetry (diameter = 740 mm). The rungs are connected at each end by 16 distributed capacitors composed of a 40-mm wide strip. The coil is shielded by a 16-sided regular polygonal enclosure (see Figure 3.1c). The coil was driven at two ports (I and Q, located 90° apart) in quadrature mode (i.e., equal amplitude with a 90°

phase shift between each port excitation) by two AN8102–08 RF power amplifiers (Analogic Co., Peabody, MA, USA). Two baluns were present at the entrance of the

3.3 Materials and Methods

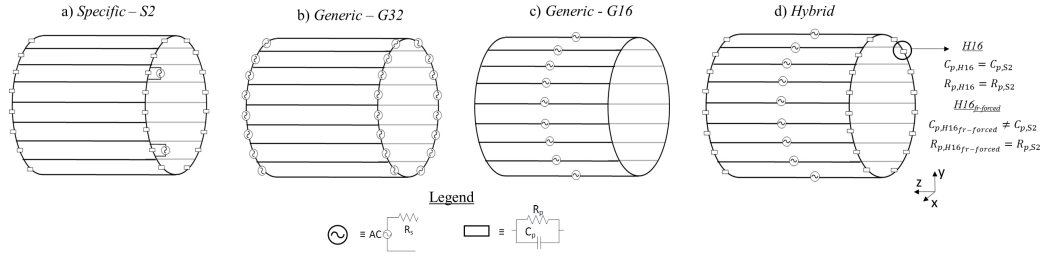


Figure 3.2: measured and computed both in air and in saline. In line with the literature, a first analysis was performed along the central longitudinal line of the coil (a). As complete domain analysis, measurements inside the phantom were performed in three coronal planes at three different saline depths of 35, 40, and 45 mm (corresponding to the absolute coordinates of $y = -175\text{mm}, -185\text{mm}, -195\text{mm}$) (b). Measurements in the space between phantom and coil were performed in air (c) in five axial planes (i.e., $z = -279, -144, 0, 144, 279\text{mm}$), and three coronal planes (i.e., $y = 0, 126, 252\text{mm}$). For each plane, the ξ index was calculated.

sources to assure a low reflected power to the amplifiers. The nominal resonant frequency of the physical coil was $f_{r,ph} = 63.5\text{MHz} \pm 0.5\text{MHz}$. The net input power was set to obtain of

$$\|\vec{B}_{(x_c, y_c, z_c)}\| = 3\mu T \quad (3.1)$$

where $\|\vec{B}_{(x_c, y_c, z_c)}\|$ is the root mean square (RMS) value of $\|\vec{B}\|$ at the isocenter of the coil $(x_c, y_c, z_c) = (0, 0, 0)$. Custom made software included with the system was used to control and modify the settings of the input signal.

Measurements setup — Data of $\|\vec{E}\|$ and $\|\vec{H}\|$ were collected using a robotic measurement system (DASY 5NEO, SPEAG, Zurich, Switzerland) [91, 152, 153] with two $\|\vec{E}\|$ probes (ER3DV6 and EX3DV4 for measurements in air and saline, respectively) and one $\|\vec{H}\|$ probe (H3DV7) (SPEAG, Zurich, Switzerland). For each measurement point the probes returned three RMS values — one for each field component x, y, and z. The total magnitude was then computed based on the quadratic norm (i.e., $\|\cdot\|$). The values of $\|\vec{H}\|$ were then converted to $\|\vec{B}\|$ based on the following relation:

$$\|\vec{B}\| = \mu_0 \|\vec{H}\| \quad (3.2)$$

where μ_0 is the permeability of vacuum. A superellipse-shaped phantom was used for the measurements (see Figure. 3.1d). The phantom consisted of a plexiglass container (6-mm thick, 750-mm long, and 400-mm wide) supported by a plexiglass table (see Figure. 3.1e). The physical phantom was filled to a depth of 90 mm with a 2.5-g/L saline solution with a conductivity $\sigma = 0.47\text{S/m}$ at room temperature [110, 154]. The conductivity

was measured with the YSI model 30 conductivity meter (YSI Incorporated, Yellow Springs, OH, USA). Measurements were carried out with the coil loaded with the

Assessing the electromagnetic fields generated by a radio-frequency MRI body coil at 64 MHz: defeaturing vs. accuracy

phantom as shown in Figure. 3.1e. Spatial calibration between the robot-guided field probes and the birdcage coil was achieved by importing a 3-D CAD model of the coil into the DASY-5NEO software, defining three points on the coil model, and manually aligning the field probes with corresponding points on the physical coil. Experimental data of $\|\vec{E}\|$ and $\|\vec{H}\|$ were collected with a spatial resolution of 1 cm

- along the longitudinal central line in (x_c, y_c) (see Figure. 3.2) ;
- inside the phantom (see Figure. 3.2b) , at three saline depths of 35, 40, and 45 mm within an elliptical area of 2025, 1995, and 1935 cm^2 , respectively;
- outside the phantom, in the space between phantom and coil (see Figure 3.2c) :
a) in five axial planes at $z = -279, -141, 0, 141, \text{ and } 279$ mm within an area of 2270 cm^2 ; and b) in three coronal planes at $y = 0, 126, \text{ and } 252$ mm within an area of 5184 cm^2 , 4492 cm^2 , and 2322 cm^2 , respectively.

The dimensions of the measurement planes were such to avoid possible collision of the probe with the coil and/or the phantom.

3.3.2 Computational Modeling

EM Numerical Implementation — EM simulations were implemented with the commercially available software XFDTD (Remcom Inc., State College, PA, USA), which has been extensively used in the literature for MRI RF-safety evaluation [38, 139, 155, 156].

The computational model of the birdcage coil was based on a reverse engineering approach, because the specific electronic characteristics of the physical coil were unknown. The model matched the geometry of the physical coil (see Figure 3.1b). Twenty cells of free space padding (20 mm×20 mm×20 mm) were added to ensure free propagation of the field outside the coil volume without reflection [107]. Additionally, eight absorbing layers were set as boundary conditions [46, 144]. The mesh grid was optimized based on the PrOGrid tool included in XFDTD ensuring a finer grid resolution near the boundaries of good conductors. A finer isotropic resolution (2.5 mm×2.5 mm×2.5 mm) was imposed for the phantom to accurately resolve the measurement grid. The model included over 52 million cells and the simulation time step used to ensure the finite-difference time domain (FDTD) Courant–Friedrich–Levy stability [157], proportional to the smallest cell size, was 4 ps. Simulations run on a PC Intel(R) Core(TM) i7-4930K CPU at 3.40 GHz, with 64 GB of RAM and NVIDIA Tesla K40c graphic processing units.

Computational Models of the Birdcage Coil and the Phantom — Simulations were performed with the coil loaded with a superellipse-shaped phantom with same

3.3 Materials and Methods

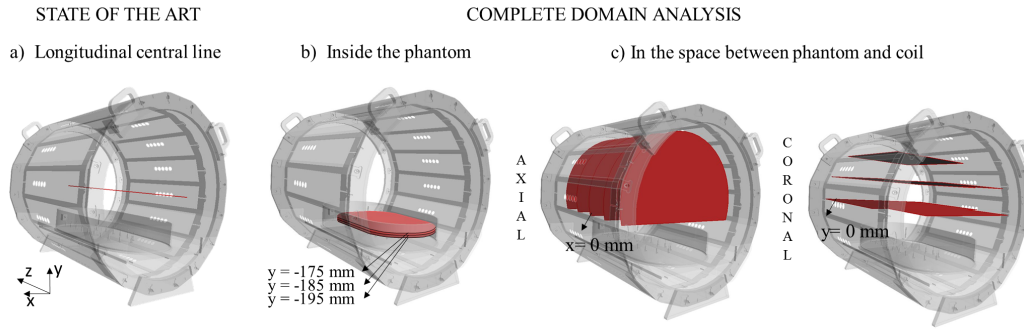


Figure 3.3: Five electrical models implemented: (a) specific 2 port (S2), (b) generic 32 port (G32), (c) generic 16 port (G16), (d) hybrid 16 port (H16) and hybrid 16 port frequency forced ($H16_{fr-forced}$).

dimensions of the physical phantom. Both the coil and the shield were modeled as copper ($\sigma = 58.13 \times 10^6 S/m$). The table supporting the phantom and the phantom case were modeled as plexiglass ($\sigma = 0 S/m$, and $\epsilon_r = 3.2$). Finally, the load of the phantom was modeled as saline solution ($\sigma = 0.47 S/m$, $\epsilon_r = 3.2$, and $\rho = 1500 kg/m^3$). As described later, five different approaches of simulating a birdcage coil were implemented. The distributed capacitors present in the physical coil were modeled as two conductive rectangular slabs connected by numerically defined lumped elements, as in [91]. The two baluns present at the physical sources were not modeled in the numerical coils.

$S2 \stackrel{def}{=} \text{Specific 2 port}$ (see Figure 3.3a): The rings were interrupted by a 5-mm gap centered between two adjacent rungs. A lumped element composed of a resistor R_p in parallel with a capacitor C_p was placed in each gap. Additionally, two ports were set in two gaps of one of the two rings, 90° spatially apart, as in the physical coil. The ports were placed on one of the two rings on one side of the phantom, and with respect to the isocenter in the negative part of the z-axis.

$G32 \stackrel{def}{=} \text{Generic 32 port}$ (see Figure 3.3b): The rings were interrupted by a 5-mm gap centered between two adjacent rungs; each gap included a port; no lumped elements were used.

$G16 \stackrel{def}{=} \text{Generic 16 port}$ (see Figure 3.3c): The rungs were interrupted in the middle by a 5-mm gap; each gap included a port; no lumped elements were used.

$H16 \stackrel{def}{=} \text{Hybrid 16 port}$ (see Figure 3.3d): The rings were interrupted by 5-mm gaps centered between each two adjacent rungs with a lumped element composed of a resistor R_p in parallel with a capacitor C_p placed in each gap; each of the 16 rungs was interrupted in the middle by a 5-mm gap containing the driving port; the lumped elements used were the same as in the S2 model. $H16_{fr-forced} \stackrel{def}{=} \text{Hybrid 16 port frequency forced}$ (see Figure 3.3d): The location of the ports was the same as for the

Assessing the electromagnetic fields generated by a radio-frequency MRI body coil at 64 MHz: defeaturing vs. accuracy

H16. For each lumped element, the resistor was the same as for the S2, whereas the capacitor was changed to force one of the S11 minima to 63.5 MHz.

In all models, the ports were modeled as a voltage source with a resistor $R_s = 50\Omega$ in series (see Figure 3.3). For the S2 model, the voltage input at the two sources was

$$V_{2port}^0 = \sqrt{R_s \cdot P_{in,ph}^Q} V_{2port}^{90} = \sqrt{R_s \cdot P_{in,ph}^I} \quad (3.3)$$

where $P_{in,ph}^Q$ and $P_{in,ph}^I$ are the total net input power at Q (i.e., 0° shifted), and I (i.e., 90° shifted) port of the physical coil, respectively.

For the other four models, the voltage input at the sources was 1 V. The results for all five models were normalized as in (3.1). The phase of the signal feeding the source was equal to its azimuthal position (i.e., 0° and 90° for the S2, 22.5° for each source in the 16 port, G16 and G32). Additionally for the G32, the ports at the same azimuthal position in the two rings were 180° out of phase.

Simulation Setup

- In the first set, the frequency response of the models was studied by feeding a single port with a broadband waveform, while the other/s port/s was/were connected to a $50 - \Omega$ load. Additionally, the S2 broadband simulations were used to calculate the final values of C_p and C_p to replicate both the tuning and matching conditions of the physical coil. A similar approach was followed for the $H16_{fr-forced}$, albeit only applied to C_p (i.e., $R_{p,H16_{fr-forced}} = R_{p,H16}$). The final values were: $R_{p,S2} = 1940\Omega$, $C_{p,S2} = 72.8fF$, and $C_{p,H16_{fr-forced}} = 16pF$. With the 4-ps time step, the virtual computing time needed to reach convergence of the frequency response was $0.8 \mu s$ (i.e., 2×10^5 steps.) Different tests were performed changing the resistor value of the lumped element to verify whether or not the coil matching would affect the EM field results.
- In the second set, all the ports were fed simultaneously with a sinusoidal waveform at 63.5 MHz with a phase shift equal to the azimuthal position of the port inside the coil. A total computing time of 30 periods was enforced to ensure a convergence of the field higher than 30 dB within two computation cycles. Convergence level was chosen to assure that a steady-state condition was reached for both frequency response and field distribution.

3.3.3 Accuracy of Numerical Models Versus Measurements

Experimental validation of the computational coils was performed by comparing the frequency response of the models, as well as $\|\vec{E}\|$ and $\|\vec{B}\|$ generated by the physical coil. For each simulation, the field values were computed inside a 3-D sensor

3.4 Results

including the coil and the phantom. Numerical results were returned as three complex values — one for each field component x , y , and z — at each point of the predefined sensor. In order to compare the numerical data with the measurements, the total RMS magnitude of the field was then computed based on the quadratic norm accordingly to:

$$\begin{aligned}\|\vec{E}\| &= \frac{1}{\sqrt{2}}\sqrt{\vec{E}_x + \vec{E}_x^* + \vec{E}_y + \vec{E}_y^* + \vec{E}_z + \vec{E}_z^*} \\ \|\vec{B}\| &= \frac{1}{\sqrt{2}}\sqrt{\vec{B}_x + \vec{B}_x^* + \vec{B}_y + \vec{B}_y^* + \vec{B}_z + \vec{B}_z^*}\end{aligned}\quad (3.4)$$

where the symbol $*$ represent the complex conjugate of the complex field — \vec{E} or \vec{B} — and the subscripts x , y , and z the spatial component of the field. As done in [36,76,145], a comparison was first performed on the profile of $\|\vec{B}\|$ along the central longitudinal axes of the coil ($x_c = 0$ mm, $x_c = 0$ mm). This analysis was then herein extended to the $\|\vec{E}\|$ [37]. An additional comparison was performed computing the "symmetric mean absolute percentage error" ("SMAPE") [158] (ξ) between simulated and measured values

$$\xi_k = \frac{|X_k - Y_k|}{\frac{X_k + Y_k}{2}} \quad (3.5)$$

where X_k and Y_k are the values of $\|\vec{E}_{(x,y,z)}\|$ or $\|\vec{B}_{(x,y,z)}\|$ in the k^{th} voxel of the area considered for the measured (X_k) and simulated (Y_k) data, respectively. ξ was calculated along the longitudinal central line and in the planes described in Section 3.3.1 and displayed in Figure 3.2b-d. In addition, as a term of comparison between the models, the mean SMAPE $\bar{\xi}$ was evaluated for each plane.

$$\bar{\xi} = \sum_{k=1}^N \xi_k \quad (3.6)$$

where N number of voxels inside the plane.

3.4 Results

3.4.1 Power Requirements

Comparing the loaded coil with the unloaded condition, the field polarization at the isocenter was highly affected by the presence of the phantom. In the loaded condition, the physical coil required a total net input power of 219 W to obtain a $\|\vec{B}\| = 3\mu T$ at the isocenter, with $P_I^{in,ph} = 44W$ and $P_Q^{in,ph} = 175W$. The available power (i.e., the power injected into each port) was the same for both I and Q ports, however, the Q port had less reflected power. This was caused by the phantom being closer to the Q

Assessing the electromagnetic fields generated by a radio-frequency MRI body coil at 64 MHz: defeaturing vs. accuracy

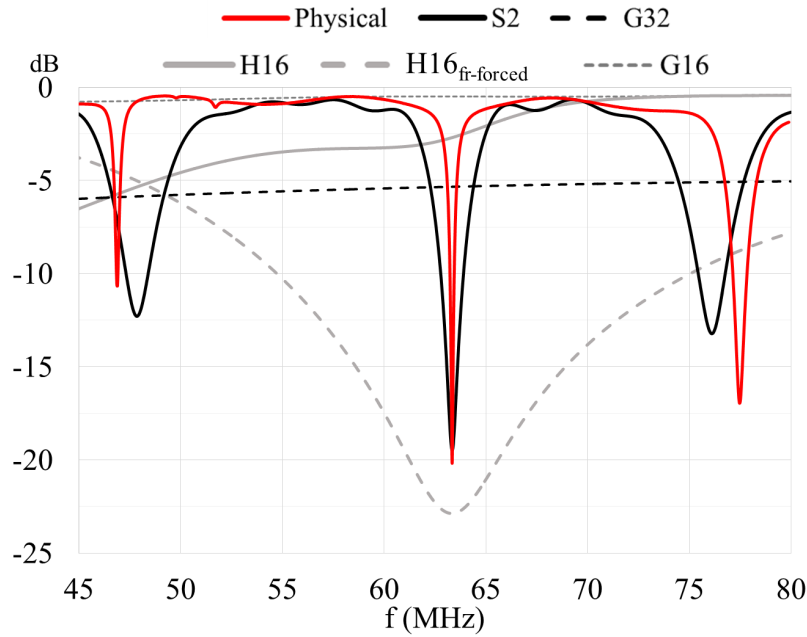


Figure 3.4: Scattering parameters (i.e., S_{11}) of the physical coil and five computational models. The resonance frequency of the physical coil was captured only by the S2 and $H16_{fr\text{-}forced}$ models. The G32, H16, and G16 showed a flat frequency response around 63.5 MHz.

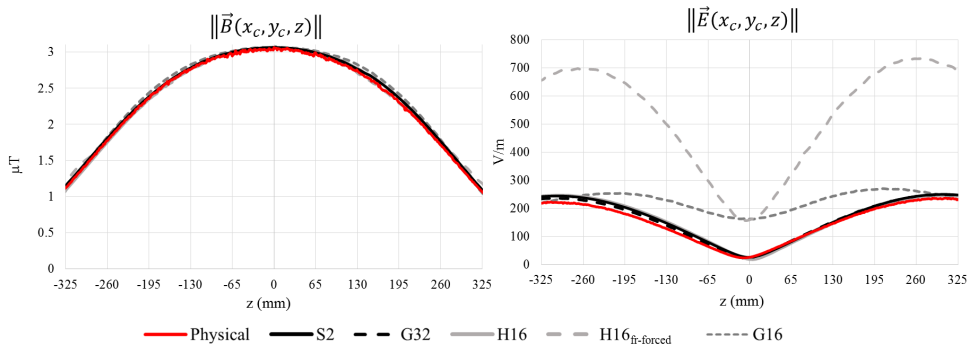


Figure 3.5: $\|\vec{E}\|$ and $\|\vec{B}\|$ along the longitudinal axis z in the center of the coil (i.e., $x_c = y_c = 0$ mm). The figure shows the values measured in the physical coil as well as simulated. The five computational models were able to model the measured profile of $\|\vec{B}\|$. Conversely, $\|\vec{E}\|$ was accurately modeled only by the S2, G32, and H16. $\|\vec{E}\|$ was about threefold higher along the entire axis for the $H16_{fr\text{-}forced}$, while it was up to seven fold higher at the measured minimum (i.e., $z = -10$ mm) for both the $H16_{fr\text{-}forced}$ and G16. Values were normalized accordingly to eq. 3.1

3.4 Results

port, and thus, loading the coil asymmetrically. The polarization was clockwise with respect to the sources and elliptical with a ratio of the field components equal to 0.63. Conversely, in the unloaded case, the polarization was clockwise with respect to the sources and circular with a ratio of the field components equal to 0.9. The simulations performed with different resistor values confirmed that the matching affected only the overall power requirements, generating fields linearly proportional in magnitude to the net input power.

3.4.2 Frequency Response

For the physical coil, the S_{11} at $f_{r,ph} = 63.5\text{MHz}$ was -18.9dB (see Figure 3.4, red trace) with a Q-factor of 800. As reported in Figure 3.4, the five computational models gave different results in terms of scattering parameters. The S2 and $H16_{fr-forced}$ showed a resonance peak at $f_r = 63.5\text{MHz}$ of -19.1dB and -22.9dB , respectively. The Q - factor for the S2 and the $H16_{fr-forced}$ were 160 and 14, respectively. The H16 presented an almost flat frequency response of -3.2 ± 2.4 dB in the frequency range selected (i.e., from 40 to 80 MHz). Around $f_{r,ph}$, the G32 and the G16 presented also a flat response of -6.3 and -0.8dB , respectively.

3.4.3 EM Fields

Longitudinal Central Line — As shown in Figure 3.5, all the models were able to replicate the measured values of $\|\vec{B}\|$ along the central longitudinal line of the coil. For the five models, the maximum ξ for the magnetic field $\|\vec{B}_{(x_c,y_c,z)}\|$ compared to the measured values was less than 5%. Conversely two of the models showed significantly different profiles of measured $\|\vec{E}\|$ when compared to the physical coil, with values of $\bar{\xi}$ up to 147% for both the $H16_{fr-forced}$ and G16. Finally, in the physical coil, the value of $\|\vec{E}\|$ along the longitudinal line was the smallest at 10 mm from the isocenter with a magnitude of 24 V/m. Conversely, the H16, the S2, and the G32 showed a minimum at the isocenter with a magnitude of 17 V/m, 26 V/m, and 23 V/m, respectively, whereas $H16_{fr-forced}$ and G16 showed a minimum of 160 V/m.

Inside the Phantom — As shown in figure 3.6, the values of $\|\vec{E}\|$ and $\|\vec{B}\|$ simulated by the five models were significantly different when compared to each other and to the measured data inside the phantom. In particular, only the S2, G32, and H16 were able to accurately replicate $\|\vec{E}\|$ and $\|\vec{B}\|$ inside the phantom.

- For $\|\vec{B}\|$, the $\bar{\xi}$ was always better than 14% for the S2, G32, and H16, while for $H16_{fr-forced}$ and G16 was worse than 18%.

Assessing the electromagnetic fields generated by a radio-frequency MRI body coil at 64 MHz: defeaturing vs. accuracy

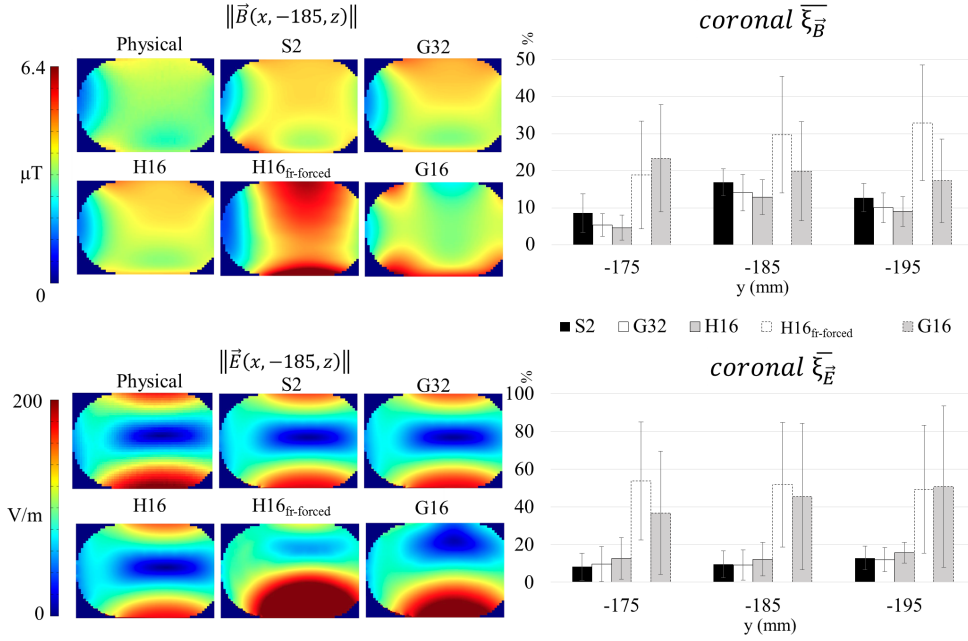


Figure 3.6: $\|\vec{E}\|$ and $\|\vec{B}\|$ on coronal planes inside the phantom. For each plane, the mean SMAPE $\bar{\xi}$ value (see eq. 3.6) is reported in the histogram. In all three planes, $\|\vec{E}\|$ and $\|\vec{B}\|$ of the physical coil were well replicated only by the S2, G32, and H16 models, with a ξ less than 17% for both. Conversely, models $H16_{fr\text{-}forced}$ and G16 reported an ξ between 17% and 32% for $\|\vec{B}\|$ and between 37% and 54% for $\|\vec{E}\|$. This result exemplifies how the analysis of the central longitudinal line (see figure 3.5) is not sufficient to assess how well a model replicates the magnetic field of a physical coil.

- For $\|\vec{E}\|$, the $\bar{\xi}$ was always better than 16% for the S2, G32, and H16, while for $H16_{fr\text{-}forced}$ and G16 was worse than 37%.

In the Space Between Phantom and Coil — The field data outside the phantom are reported only for the S2, G32, and H16 because these models were the only ones able to accurately replicate $\|\vec{E}\|$ and $\|\vec{B}\|$ (see Section IV-C). Outside the phantom similar values of $\bar{\xi}$ (i.e., between 3.9% and 11.1% for the axial planes, and between 6.8% and 17.3% for the coronal planes) were obtained in all the planes, except for the central axial plane. The $\|\vec{E}\|$ throughout the central axial plane was only accurately modeled by the S2, with a $\bar{\xi}$ equal to 11% and maximum ξ of 58% on the left of the map (see figure 3.7). Conversely, the G32 did not show any field peak while the H16 was affected by the presence of the multipoint excitation. The G32 showed values of ξ up to 158% (i.e., $\|\vec{E}\|$ up to 80 V/m lower compared to the measurements in proximity of the source) and an overall $\bar{\xi}$ of 31%. The H16 showed a local ξ up to 134% (i.e., $\|\vec{E}\|$ up to 80 V/m higher compared to the measurements on the left of the map in figure 3.7), and an overall $\bar{\xi}$ of 45% (see figure 3.7). On the other axial planes, $\bar{\xi}$ was always under 9.15% when evaluating both the planes farther (i.e., 279 mm) and closer (i.e.,

3.5 Discussion

-279 mm) to the physical sources. Additionally, $\bar{\xi}$ for $\|\vec{B}\|$ was always lower than 11% for the three models in both axial and coronal planes.

The distribution of $\|\vec{E}\|$ was asymmetric with respect to the isocenter, with values 12% higher in the planes far from the sources. This result is in line with the measured field along the central longitudinal line (see Figure 3.5b), where the field showed a 7% asymmetry between the two maxima. The same asymmetry in the axial planes was well replicated by the S2 (i.e., 10%), while it was less pronounced for the G32 (i.e., 6%), and for the H16 (i.e., 4%).

3.5 Discussion

The main contribution of this study is the characterization, against measurements from a physical coil, of five different computational coil models representative of the three main modeling approaches available in the scientific literature: generic, specific, and hybrid coils. All of the coil models represented different implementations of the same physical birdcage body coil. Three quantities were taken into account for the comparison: frequency response, $\|\vec{E}\|$, and $\|\vec{B}\|$.

The fields were analyzed both inside the phantom and in the space between the phantom and the coil. Different applications may require different levels of field accuracy in specific locations. An accurate assessment of the EM field inside the phantom is important when evaluating SAR levels as overall safety of the patient [34–36, 135–139] or the RF-induced heating in patients with conductive medical devices that are fully implanted in the body [91] like deep brain stimulators [37, 38, 134], or pacemakers [40, 140, 141]. In addition an accurate representation of $\|\vec{E}\|$ in the space between the coil and the load is important when evaluating safety in patients with conductive medical devices that are partially implanted or in contact with the skin [133, 142]. High temperature changes in gel were reported in the presence of external devices that are in contact with the skin, such as electroencephalography leads [159–161], electrocardiography leads [162–164], catheters in interventional MRI [104, 165], and orthopedics external fixators [77, 166].

Data presented in this paper were normalized based on the $\|\vec{B}\|$ magnitude at the isocenter of the coil. This choice is in accordance to the state of the art to compare $\|\vec{B}\|$ along the longitudinal central line (see Figure 3.5), and because the maximum $\|\vec{B}\|$ occurs at the isocenter of the coil. Different normalization procedures could be considered. As an additional test, results were also compared with a normalization based on the mean of the $\|\vec{B}\|$ in the central plane of the phantom (i.e., $y = -185$ mm). Comparison between models showed the same overall behavior of the results

(data not shown).

The choice of performing the comparison of the numerical models with the simulations based on the SMAPE relied on its definition. The SMAPE is self-limited by definition to an error rate of 200%, reducing the influence of the low items such as low value of the field. Conversely, when calculating error normalized to a single value, low values can be problematic because they could have infinitely high errors that skew the overall error rate (e.g., data in central axial plane).

In this study, three of the five models (i.e., G32, H16, and G16) were characterized by definition by a flat frequency response, whereas the two additional models (i.e., $H16_{fr-forced}$ and S2) were implemented to be tuned at the resonance frequency of the physical coil. Out of these latter models, the $H16_{fr-forced}$ was adjusted to replicate the tuning characteristics of the physical coil, while the S2 replicated both the tuning [167] and the matching characteristics, by adjusting the losses via the resistor of the lumped elements. The Q-factor of the S2 was lower compared to the physical coil possibly due to the presence of components generating loss of energy (e.g., in the resistor of the numerical model). Nevertheless, this did not affect the overall field at the single excitation frequency used to generate $\|\vec{B}\|$ and $\|\vec{E}\|$ (second settings in Section 3.3.2), given that the results were normalized with respect to $\|\vec{B}\|$, as previously done in the literature [107, 145].

Measuring $\|\vec{B}\|$ and $\|\vec{E}\|$ inside the phantom was considered essential for the numerical models validation. The position chosen for the study was due to physical constraints set by the DASY measurement system (e.g., minimum distance needed between the physical probe and the coil) and it allowed field measurements inside the phantom.

When simulating using an FDTD approach, the biggest advantage of using either a generic or a hybrid model was related to the computational cost of the simulation. The latter could be reduced in terms of: 1) time required for each simulation, or 2) number of simulations required to obtain the final solution. When using a multiport excitation, the simulation time was reduced by approximately one third, because forcing the currents inside the model allowed reaching the steady-state convergence with a smaller number of periods. Therefore, with the system used, simulating a multiport excitation would reduce the simulation time of approximately 1 h and 20 min. Furthermore, the number of simulations was reduced since tuning and matching of the model were not required. Indeed, while one simulation (i.e., the excitation only) was needed for the generic model, at least two — one for tuning and one for the excitation (see Section 3.3.1) — were needed for the specific model. Both computing time and number of simulations can be reduced for a generic model, whereas only the computing time was

3.5 Discussion

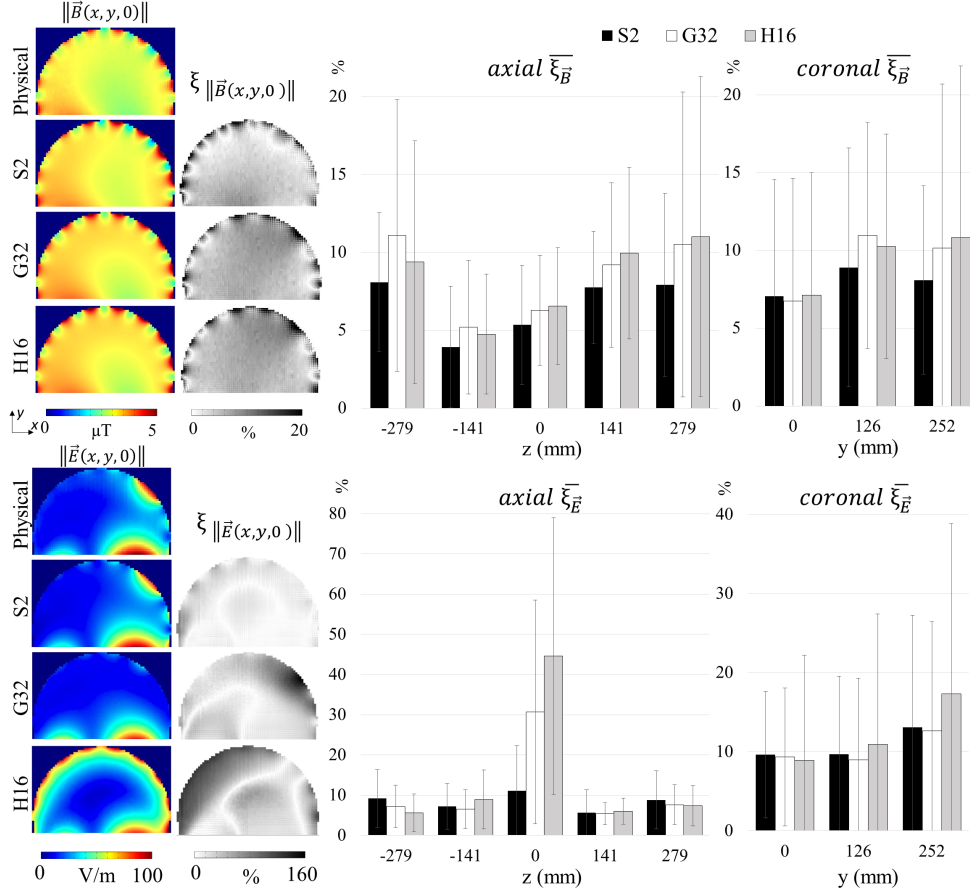


Figure 3.7: $\|\vec{B}\|$ (top) and $\|\vec{E}\|$ (bottom) maps on the central axial planes (i.e., $z = 0$ mm) in air for the physical coil and the three numerical model S2, G32, and H16. The ξ (SMAPE) maps (see eq. 3.5) are reported on the right side of the field maps. On the right, the calculated $\bar{\xi}$ (see eq. 3.6) and the relative standard deviation are reported for the five axial and three coronal planes measured. In all the planes, $\|\vec{B}\|$ of the physical coil was well replicated by the three computational models with $\bar{\xi}$ always less than 11%. In the central axial plane, only the S2 model was able to replicate the $\|\vec{E}\|$ peak due to the ports position, whereas the G32 showed a uniform $\|\vec{E}\|$ and the H16 model was highly affected by the multiport excitation increasing the $\bar{\xi}$ of the plane up to 45%.

Assessing the electromagnetic fields generated by a radio-frequency MRI body coil at 64 MHz: defeaturing vs. accuracy

reduced for a hybrid model, which is thus more computationally intensive. In fact, a hybrid model relies on the specific model to assess the lumped element values to be used.

The analysis of $\|\vec{E}\|$ and $\|\vec{B}\|$ performed in this study suggest that: 1) an accurate representation of the frequency response does not guarantee an accurate estimation of $\|\vec{E}\|$ and $\|\vec{B}\|$; 2) assessing the accurate modeling of $\|\vec{B}\|$ based only on the results along the central longitudinal line of the coil can be misleading; 3) when defeaturing a hybrid type of coil, the proper selection of lumped element values is crucial to assure a good representation of $\|\vec{E}\|$ and $\|\vec{B}\|$ inside the phantom; and 4) simplified models via proper defeaturing still allow accurate modeling of $\|\vec{E}\|$ and $\|\vec{B}\|$ inside the phantom.

An accurate representation of the frequency response does not guarantee an accurate estimation of $\|\vec{E}\|$ and $\|\vec{B}\|$. This is proven by comparing the results of the S2 and $H16_{fr-forced}$. Both models showed a resonance profile similar to the physical coil, however, only the S2 was able to accurately model $\|\vec{E}\|$ and $\|\vec{B}\|$ inside and outside the phantom with $\bar{\xi}$ less than 17. The G32 and the H16 were able to accurately model $\|\vec{E}\|$ and $\|\vec{B}\|$ even though they did not show a resonance profile. Thus, the accurate representation of the frequency response is neither a necessary nor sufficient condition for an accurate estimation of $\|\vec{E}\|$ and $\|\vec{B}\|$.

Assessing the accurate modeling of $\|\vec{B}\|$ based only on the results along the central longitudinal line of the coil can be misleading. In previous studies [36,76,145], models were compared by analyzing the profile of $\|\vec{B}\|$ along the central longitudinal line. The results of this study show how this analysis may not ensure the accuracy of the models. This is directly deductible from the comparison of magnetic field graphs versus plane maps (see figure 3.5 versus figure 3.6). While all of the models simulated the same $\|\vec{B}\|$ along the longitudinal line (see figure 3.5), neither $H16_{fr-forced}$ nor G16 were able to accurately model the $\|\vec{B}\|$ of the physical coil (see figure 3.6), with a mean SMAPE higher than 20%. The G16 showed an $\|\vec{E}\|$ outside (see figure 3.5) and inside (see figure 3.6) the phantom up to seven fold different compared to the physical coil, even if the $\|\vec{B}\|$ along the central line was similar. Hence, a comparison based only on $\|\vec{B}\|$ may not be sufficient to validate a computational model. As a consequence, the G16 showed an $\|\vec{E}\|$ outside (see figure 3.5) and inside (see figure 3.6) the phantom up to seven fold different compared to the high-pass physical coil.

When defeaturing a hybrid type of coil, the proper selection of lumped element values is crucial to assure a good representation of $\|\vec{E}\|$ and $\|\vec{B}\|$ inside the phantom. When comparing a generic to a hybrid model (i.e., H16 and $H16_{fr-forced}$, figure 3.3), the values of $\|\vec{E}\|$ were significantly different, depending on the specific value of capacitance used for the lumped element. Specifically, the H16 showed a SMAPE

3.5 Discussion

within a few percentage compared to the S2 (see Figures 3.5-3.7). The $H16_{fr-forced}$ generated results similar to the G16 (see Figures 3.5-3.6). Hybrid models are designed to reproduce $\|\vec{E}\|$ and $\|\vec{B}\|$ of a specific model by forcing the currents along the coil. However, the frequency response of a hybrid model cannot be directly compared to the one of a specific model, because of the different feeding conditions. Thus, an S_{11} minimum of a hybrid model cannot be considered equivalent to a resonance mode of a specific model. The implementation of a model such as the $H16_{fr-forced}$ is equivalent to changing the frequency response of the original specific model, causing a different current distribution inside the coil. As a consequence, the $H16_{fr-forced}$ and the S2 will in fact represent two different coils, thus generating different $\|\vec{E}\|$ and $\|\vec{B}\|$.

Simplified models via proper defeaturing still allow for accurate modeling of $\|\vec{E}\|$ and $\|\vec{B}\|$ inside the phantom. The S2, G32, and H16 all showed similar results inside the phantom with $\bar{\xi}$ lower than 17% for both $\|\vec{E}\|$ and $\|\vec{B}\|$. This was already shown by different studies comparing specific and hybrid [37, 150] or generic models [35, 76, 145]. However, when comparing the field outside the phantom in the space between the coil and the load which was not done in previous studies differences among these three models were more evident. On the central axial plane, the S2 was the only one able to replicate the $\|\vec{E}\|$ peak of the source (see figure 3.7), with a mean SMAPE of less than 11%. The $\|\vec{E}\|$ peak in the central axial plane is due to the current distribution along the rung, which is higher at the center. The G32 showed a uniform $\|\vec{E}\|$ around the coil underestimating the measured field of up to 80 V/m, while the H16 exhibited high values of $\|\vec{E}\|$ all around the coil generated by the multipoint excitation in the middle of the rungs, causing an overestimation of the field of up to 80 V/m. This effect was reduced in points farther from the sources. As such, this study suggests the need of additional work to assess whether or not a fully featured S2 may be necessary to accurately evaluate the safety of the conductive medical devices that are partially implanted or in contact with the skin.

3.5.1 Limitations

The analysis conducted in this study focused only on $\|\vec{E}\|$ and $\|\vec{B}\|$, because the available measurement system was not capable of measuring the phase of the fields. A complete analysis of the phase of $\|\vec{E}\|$ and $\|\vec{B}\|$ fields may be important to assess the safety of an implant, because the coupling of the implant with the field is both dependent on the magnitude and phase of the radiated field. Additionally, a full uncertainty analysis, both numerical and experimental, will be performed as a second step of the validation work [91, 168, 169].

3.6 Conclusions

We evaluated five computational models of a birdcage body coil, including one specific (S2), two generic (G32, G16), and two hybrid (H16, $H16_{fr-forced}$). The computed results were compared against a physical coil at 63.5 MHz. The comparison was based on the frequency response, and on $\|\vec{E}\|$ and $\|\vec{B}\|$ in the coil loaded with a phantom. Depending on the specific application, different level of accuracy may be needed inside or outside the phantom. Thus, in this study, the fields were evaluated both inside the phantom and in the space between phantom and coil. All the coil models computed $\|\vec{B}\|$ within 35% relative to the measured results. However, only the S2, G32, and H16 were able to accurately model $\|\vec{E}\|$ and $\|\vec{B}\|$ of the physical coil inside the phantom, with a maximum mean SMAPE $\bar{\xi}$ of 16%. Additionally, outside the coil only the S2 was able to accurately simulate the $\|\vec{E}\|$ in proximity of the feeding port in the central axial plane, with $\bar{\xi}$ equal to 11%. Conversely the G32 and the H16 showed $\bar{\xi}$ equal to 31% and 45%, respectively. In conclusion: 1) all the models were able to accurately model $\|\vec{B}\|$ along the longitudinal line; 2) the generic G16 and the hybrid $H16_{fr-forced}$ were not able to model either $\|\vec{E}\|$ nor $\|\vec{B}\|$ inside the phantom; 3) the generic G32 and the hybrid H16 were able to accurately model $\|\vec{E}\|$ inside the phantom; and 4) only the S2 was able to accurately model $\|\vec{E}\|$ both inside and outside the phantom. Because computational modeling of birdcage body coils is extensively used in the evaluation of RF-induced heating during MRI, experimental validation of numerical models is recommended to determine if a model is an accurate representation of a physical coil.

3.7 Uncertainty quantification

As a full VVUQ procedure the validation of a numerical model should include the comparison of the measurements and simulations, as well as the uncertainty quantification. Neufeld and colleagues [91], which used a similar measurements setup to the one used in this thesis, indicated as possible sources of measurement uncertainty the field drift (6.1%), electric field probe position (10.8%), and magnetic field probe position (1.39%). Under the assumption that these parameters are independent from each other, the suggested total uncertainty of the measurements would be about 13%.

A sensitivity analysis related to the signal frequency and value of resistor and capacitor was already performed for the same birdcage coil model in section 2. Here the analysis was extended to the sensitivity of results with respect to: properties of the saline solution of the phantom (i.e., conductivity, permittivity and density), the phantom position (i.e., along the x-,y-, and z-direction), and with the grid resolution.

3.7 Uncertainty quantification

The uncertainty was calculated with respect to the E field, H field, and SAR following the same rationale presented in [91]:

- The quantity of interest (i.e. $\|\vec{E}\|$, $\|\vec{H}\|$, SAR) was computed for a reference condition, then additional simulations were performed varying the parameter of interest (e.g., saline conductivity) \pm a defined percentage Δ .
- The average (Δ_{avg}) and the peak (Δ_{peak}) of the quantity of interest was calculated for all the simulations.
- The *variance* of the quantity of interest with respect to the specific parameter was calculated as percentage variation from the reference.
- The *sensitivity* of the quantity of interest with respect to the parameter was computed as the ratio of the *variance* with the percentage of variation Δ .
- The percentage standard deviation (std %) of the value was calculated as the standard deviation (std) of the parameter uncertainty multiplied by the reference of the parameter. Values for the standard deviation of the parameter uncertainty were taken from literature [91].
- The *uncertainty* (U) of the quantity of interest related to the specific parameter was computed multiplying the *sensitivity* with the std %.

The combined uncertainty due to all the parameter studied was then computed based on:

$$\sqrt{\sum_i U_i^2} \quad (3.7)$$

with i the nine *parameters* considered for the analysis. Table in figure 3.8 reports the data of the uncertainty quantification. The highest uncertainty of the parameter was found with respect to the the grid resolution with respect the the average SAR when going higher than 3 mm (i.e., 18.95 %), and for the H field when going lower than 2 mm (i.e., 16.33 %). Conversely the uncertainty calculated for the other parameter was always less than 6.6 %. Overall, for all the parameter considered the peak SAR was the one showing the lowest combined uncertainty of 4.7 %.

Chapter 4

An inter-laboratory computational and experimental study of a radiofrequency coil model at 64 MHz

This chapter was submitted as it is to the journal for Magnetic Resonance in Medicine [170]. For this reason concepts and definitions maybe already previously discussed in this thesis. The work was performed as part of an inter-laboratory collaboration between the DBP/CDRH/OSEL of the FDA (MD-USA), with the IT'IS foundation (Zurich-CH), MR:COMP GmbH (Gelsenkirchen-DE), and ANSYS HFSS (PA-US).

4.1 Abstract

Purpose : This study aims to perform a comparison of different numerical implementations obtained by users modeling a non-fully disclosed RF exposure system with experimental measurements of a 1.5 T RF coil system.

Methods : Four teams participated in the computational arm of the study using their software platform of choice. Each team independently computed the electric and magnetic field inside a birdcage body coil based on a common protocol. Additionally, one of the teams performed experimental measurements on an RF exposure system. The numerical electric and magnetic results were compared to data collected in the physical coil.

Results : The numerical model of the coil differed among the teams primarily in terms of electrical components and feed implementations. The results showed that the implementation of each group generated different coil losses, coil polarization, and ultimately different electric field and magnetic field maps.

Conclusions : Our results suggest that providing limited information on the coil (i.e., diameter, length, feed position, and fixed resonant frequency) can generate visibly different results across users, especially for off-center planes inside the saline or planes in air between the phantom and coil.

4.2 Introduction

Magnetic resonance imaging (MRI) is a widely used diagnostic imaging technique which employs a radio-frequency (RF) field generated by an RF resonator to produce images. The absorption of RF energy by a human subject during the MRI exam can lead to a temperature rise in tissue, the magnitude being a function of the electromagnetic (EM) and thermal properties of each tissue and the exposure time. An accurate assessment of the RF exposure of a patient, which includes the evaluation of the EM field generated by the coil, is the first step toward a comprehensive assessment of patient safety.

A variety of birdcage coil designs are used in commercial MRI systems. For example, each manufacturer varies the exact coil geometry (e.g., coil diameter, coil length, widths of rings and rungs), the properties of electrical components (e.g., capacitor values, capacitor losses), the exact conditions of the RF coil excitation (e.g., feed position, feed phase orientation), as well as the specific frequency behavior of the coil, to achieve the desired field behavior. These design details are rarely shared publicly as they are considered proprietary information by scanner manufacturers.

Due to the complexity of RF exposure assessment, computational models are often used to simulate the MRI RF field. This is because they allow for systematic analysis of the variables that affect RF-induced heating, which are cumbersome to evaluate experimentally [32, 33]. Computational EM modeling has been used by researchers to calculate the EM field generated by an MRI RF coil [171–175]. Given the limited information available on birdcage coil designs, the assumptions and simplifications on which computational models are based include, but are not limited to, approximated coil and shield dimensions (e.g., diameter and length), coil feed characteristics (e.g., quadrature excitation), locations of electrical components, electrical properties of components, and frequency response. Such simplifications and assumptions introduce an important factor of variability in the computational assessment of RF exposure, which has not been systematically evaluated in literature.

We present herein the results of an inter-laboratory study that compares the numerical data obtained by four modeling teams, who used various commercially available software platforms to model a simplified, and partially disclosed, representation of a

4.3 Methods

commercially available RF exposure system. The computational data were also compared to experimental measurements.

4.3 Methods

4.3.1 Inter-laboratory project

Four teams (referred to as Team1, Team2, Team3, and Team4) participated in the computational arm of the study using their software platform of choice. Each team independently computed the electric and magnetic field inside a birdcage body coil (figure 4.1) based on a common protocol, which included a shielded coil model loaded with a phantom distributed in CAD format. Additionally, one of the teams (Team2) performed experimental measurements on an RF exposure system. The numerical electric and magnetic results were compared to data collected in the physical coil. Figure 4.2 summarizes the software package used (figure 4.2a) and coil model implementation of each team (figures 4.2b and c).

4.3.2 Experimental exposure system and load specifications

Experimental measurements were performed by Team2 and Team1 at the Team2 laboratories using the Medical Implant Test System (MITS1.5) for 64 MHz / 1.5 Tesla RF safety evaluation (Zurich Med Tech, Zurich, Switzerland) (figure 4.1a), which was comprised of a shielded 16 rung high-pass RF body coil, power amplifiers, and a control system. Two baluns were present at the entrance of the coil feeds. The coil was driven by two AN8102-08 RF power amplifiers (Analogic Co., Peabody, MA) at two feeds geometrically located 90° apart along one of the coil rings. A 40% duty cycle square sequence (i.e., UID 10084 ZMT) was used to excite the coil for a total average power transmitted by each amplifier equal to 16 W. Two opposite polarizations, denoted as clockwise (CW) and counterclockwise (CCW), were obtained by switching the phases of the two RF sources.

An ASTM phantom was positioned isocentrically inside the coil during data collection (figure 4.1b) [176, 177]. The phantom consisted of a rectangular box (650 mm x 420 mm x 90 mm), constructed of 12 mm thick Plexiglas walls. The phantom was filled with a 2.5 g/L NaCl solution with distilled water, with a conductivity $\sigma = 0.47 S/m$ and permittivity $\epsilon = 78 \pm 5\%$. Electrical properties of the test solution were measured at the beginning and at the end of each experiment using a DAK System (SPEAG, Zurich, Switzerland).

An inter-laboratory computational and experimental study of a radiofrequency coil model at 64 MHz

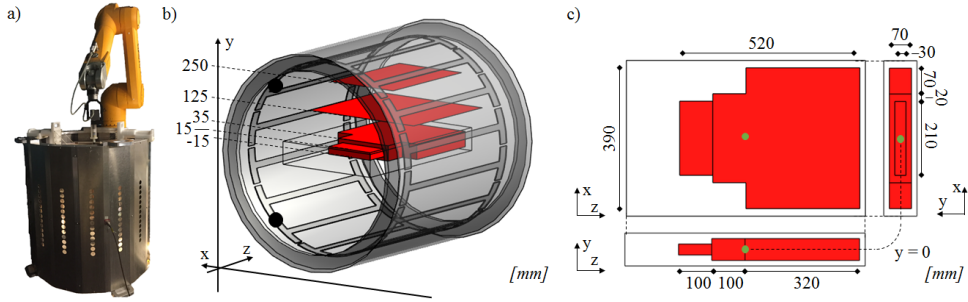


Figure 4.1: Experimental system. a) MITS1.5 coil (in vertical configuration) with DASY robotic arm (yellow). The DASY system was used with probes measuring electric and magnetic field RMS magnitude ($\langle \|\vec{E}^M\| \rangle$ and $\langle \|\vec{H}^M\| \rangle$). b) Graphical representation of the coil and measurement planes. The coil shield (transparent) is the outermost shell, then the coil rings and rungs, then the phantom box. The position of the two sources is indicated by the black dots. The coronal planes measured in inside the saline solution of the phantom and in air between the phantom and the coil are shown in red. c) Dimensions of the phantom volume where field measurements were taken. The measurements were not taken over the entire volume because of physical constraints of the probes.

4.3.3 Computational modeling setup

The dimensions of the model were based on the MITS1.5 system. In order to limit the computational cost, the numerical model was simplified with respect to the physical system as follows: 1) the coil rings and rungs, as well as the shield shape, were implemented using simplified geometries not including certain details of the physical system; 2) features such as balun shielding boxes, plastics covers, and the patient table were not incorporated; 3) the distributed capacitors present in the physical coil were modeled as gaps containing lumped elements (figure 4.2c, Q1-Q4: Team1-Team4), and 4) the resonance frequency was defined to be exactly 64 MHz.

The coil model (figure 4.1b) was a 64 MHz 16-rung high-pass birdcage body coil with an inner diameter of 740 mm and 16 rectangular rungs (570 mm long, 25 mm wide and 4 mm thick). The two coil rings were modeled as strips (40 mm wide and 4 mm thick). Along the rings, a capacitor with high-pass birdcage functionality was centered in the 5-mm gap between each pair of adjacent rungs. Additionally, the coil was shielded by a solid conductive enclosure (figure 4.1b).

The numerical coil was also loaded with a model of the ASTM phantom positioned isocentrically within the coil. The material properties of the medium representing the 2.5 g/L NaCl solution (saline solution) were as follows: $\sigma = 0.47 S/m$, $\epsilon_r = 80$, and $\rho = 1000 kg/m^3$ [178]. The amplitude of the RF feeds used to excite the coil was the same for both feeds, whereas the phase shift between RF sources was 90° , as in quadrature excitation. Simulations were performed imposing two opposite polarizations, CW and CCW, by changing the sign of the relative phases of the two RF

4.3 Methods

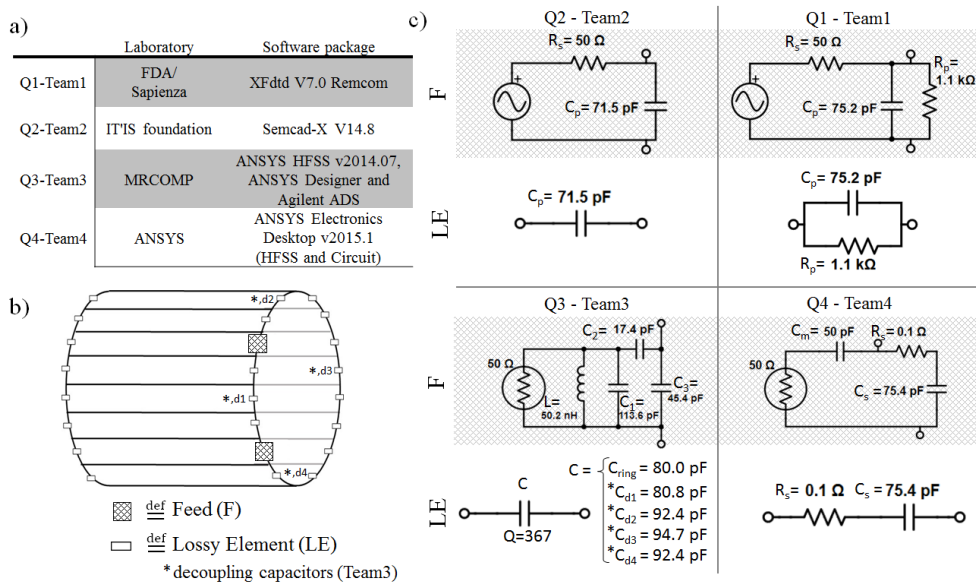


Figure 4.2: Electrical model of the coil. A CAD model of the coil, including a fixed location of feeds and lossy elements, was distributed to all teams. a) EM solver used by each Team (table on top left); b) Schematic representation of coil, indicating relative locations of feeds and lossy elements; c) Preferred circuit for the feeds and the lossy elements implemented by each team, each quadrant reports implementation from one team (i.e., Q1-Q4 for Team1-Team4, respectively).

sources.

The inter-laboratory study protocol imposed four constraints on the teams: 1) use the CAD files of the shielded coil and phantom as provided; 2) report numerical results on a grid that is less than the measurement grid (1 cm); 3) excite the coil by two feeds (with defined amplitudes and phases), placed at the same location as the physical coil (figure 4.1b and figure 4.2a); and 4) define the values of electrical components (e.g., capacitors, resistors, inductors) so that the numerical model of the coil loaded with the ASTM phantom was resonant at 64 MHz. Given the protocol constraints, each team was then free to apply their preferred numerical strategy to calculate the electric field RMS magnitude (i.e., $\langle \|\vec{E}^{team}\| \rangle$) and magnetic field RMS magnitude (i.e., $\langle \|\vec{H}^{team}\| \rangle$) on the planes defined below. These values were calculated inside the saline in the isocenter axial plane of the coil ($z = 0$), in the isocenter coronal plane of the phantom ($y = 0$) and along six off-center coronal planes ($y = -30, -20, -10, 10, 20, 30$ mm), and in air between the phantom and coil on two coronal planes (see figure 4.1b). The numerical results were compared to electric and magnetic field data collected on the corresponding planes in the physical coil.

Team1 numerical implementation — EM simulations were implemented with the commercially available software platform XFtd v7.0 (Remcom Inc., State College,

An inter-laboratory computational and experimental study of a radiofrequency coil model at 64 MHz

PA), which is based on the finite difference time domain (FDTD) method. The shield, the coil rings and rungs were modeled with electrical properties equal to those of copper. An isotropic mesh resolution of $2.5 \times 2.5 \times 2.5 \text{ mm}^3$ was imposed inside the coil. Twenty cells of free-space padding ($20 \times 20 \times 20 \text{ mm}^3$) were added to ensure free propagation of the fields outside the coil volume without reflection. Additionally, eight absorbing layers were utilized as boundary conditions. The model included over 50 million cells and the simulation time-step was 4.8 ps. The two feeding ports were modeled as a voltage source with a resistor ($R_s = 50 \Omega$) in series. The EM field inside the loaded coil was obtained by feeding the coil with a sinusoidal excitation at 64 MHz. A total computing time of $0.468 \mu\text{s}$ (i.e., 30 sinusoidal periods, for a total of approximately 105 time steps) was enforced. To obtain a numerical model with resonance at 64 MHz, electrical components consisting of a lumped resistor R_p in parallel with a lumped capacitor C_p were connected to the coil in the positions of the lossy elements, as shown in figure 4.2. To obtain the values for R_p and C_p , a series of single port simulations with broadband excitation — cutoff frequency set to 1 GHz — were performed using the loaded coil. The S-parameter of the model was analyzed, and the values of the R_p and C_p were adjusted until obtaining resonance at 64 MHz. The resulting values for the electrical components were $R_p = 1100 \Omega$ and $C_p = 75.2 \text{ pF}$ (figure 4.2c).

Team2 numerical implementation — EM simulations were implemented with the commercially available software SEMCAD-X 14.8 (ZurichMedTech, Zurich, Switzerland), which is based on the FDTD method. The shield, the coil rings and rungs were modeled with electrical properties equal to a perfect electric conductor (PEC). A non-uniform grid resolution (max. grid dimension = 6 mm, with the dominant grid dimension = $4.6 \times 5.6 \times 5 \text{ mm}^3$ within the volume modeling the saline solution) was imposed within the computational domain. Free-space padding of approximately 1/10th of the free-space wavelength was added and 15 layers of a uniaxial perfectly matched layer absorbing boundary condition were used to truncate the computational domain. The model included approximately 30 million cells and the simulation time-step was 7 ps. The two feed ports were modeled as a resistive voltage source [179] with source resistance ($R_s = 50 \Omega$). The EM field inside the coil was obtained by feeding the coil with a sinusoidal excitation at 64 MHz. A total time of $0.936 \mu\text{s}$ (i.e., 60 sinusoidal periods, for a total of approximately 1.3×10^5 time steps) was enforced. Purely capacitive lumped elements, C_p , were used as the electrical component to obtain a coil resonant at 64 MHz. Electrical components were placed in the position of the lossy elements, as shown in figure 4.2. To determine the values for C_p at each port, a se-

4.3 Methods

ries of simulations with broadband excitation (full-width half-max bandwidth of 0.25 GHz) were performed using the loaded coil. The value of C_p when the imaginary part of the complex input impedance at each feed-port vanished was selected and averaged for both ports. The resulting value was $C_p = 71.5$ pF (figure 4.2c).

Team3 numerical implementation — The Team3 numerical simulations were performed using RF-circuit and 3D EM co-simulation [180]. The coil was centered in an air box with dimension $5 \times 5 \times 5$ m³, surrounded by perfectly matched layer boundaries on all sides. The Plexiglas box of the ASTM phantom was included in the simulations. The shield, the coil rings and rungs were modeled with electrical properties equal to those of copper. The co-simulation approach included the following steps: 1) substitute all electrical components by lumped ports to perform 3D-EM simulation of the coil and the ASTM phantom; 2) connect variable (lumped) components, feed network, and other networks at the circuit level; 3) obtain the specific values of the variable component using circuit-level optimization; and 4) computation of the EM fields in the 3D EM domain (please see [124] and section 2.5 for additional details). The RF-circuit simulations were performed with ADS 2015 (Agilent, Santa Clara, CA, USA), and the 3D EM simulations with ANSYS HFSS 2014.07 (ANSYS, Inc., Canonsburg, PA, USA), which is based on the finite element method (FEM). HFSS generated a variable 3D mesh that was automatically refined as part of the "adaptive meshing pass" procedure during the solution process. Each adaptive meshing pass automatically refined the 3D mesh in areas of high field gradients. The convergence criterion for mesh refinement required that the change (delta value) in the scattering matrix for each element between two consecutive adaptive passes (ΔS) should be less than a given value. The analysis ends when ΔS is less than the convergence criterion from one adaptive pass to the next. 3D EM results were obtained using an S-parameter convergence criterion of $\Delta S < 0.002$. The final number of second-order mesh elements was approximately 8.6×10^6 . The RF feed sub-circuit was the multi-element sub-circuit shown in figure 4.2 and the capacitor Q factor was equal to 365. The following electrical components of the coil were optimized: a) inductance or capacitance of each element of the RF feed sub-circuit, b) four decoupling capacitors ($C_{d1} \dots C_{d4}$) at locations defined in figures 4.2b, and c) capacitance (C_{ring}) of remaining capacitors placed in the ring gaps. Capacitor values were: $C_{ring} = 80$ pF, $C_{d1} = 80.84$ pF, $C_{d2} = 92.42$ pF, $C_{d3} = 94.71$ pF, $C_{d4} = 92.42$ pF. These elements were included in the coil as shown in figure 4.2c.

Team4 numerical implementation — EM simulations were implemented with the commercially available software ANSYS Electronic Desktop 2015.1 (ANSYS, Canons-

An inter-laboratory computational and experimental study of a radiofrequency coil model at 64 MHz

burg, PA, USA), which is based on FEM. Because EM field radiation outside the coil was expected to be at a low level, a simple absorbing boundary condition was defined at approximately 1.1 m from the coil shield. HFSS generated a variable 3D mesh that was automatically refined as part of the "adaptive meshing pass" procedure during the solve process. A convergence criterion of $\Delta S < 0.02$ was used, as described in the Team3 procedure. Additionally, 2D sheets with a length-based mesh operation (max tetrahedral size not to exceed 10 mm) were defined for all planes over which measurements were taken. The total number of second-order mesh elements was over 10 million. The shield, the coil rings and rungs were modeled with electrical properties equal to those of copper. To obtain a numerical model of a resonant coil at 64 MHz, electrical components consisting of a lumped resistor R_s in series with a lumped capacitor C_s , with the same value all around the coil, were connected to a series of ports (lossy elements), as shown in figure 4.2. The two feeding ports were each modeled as 50Ω ports with a matching lumped capacitor C_m in series (figure 4.2c). To calculate the values for R_s , C_s , and C_m resulting in a resonant coil at 64 MHz, 34 ports were defined in the 3D model – 16 between each rung around each of the two rings, and two additional ports for the feed circuits. The 34-port model was dynamically linked to HFSS circuit tools and variable resistors and capacitors were connected in the configuration previously described. The values were adjusted until 64 MHz resonance was obtained. The final values for each parameter were: $R_p = 0.1 \Omega$, $C_p = 75.4 \text{ pF}$, and $C_m = 50 \text{ pF}$ (figure 4.2c).

4.3.4 Measurements setup

All principle measurement equipment was manufactured by SPEAG (Zurich, Switzerland). Measurements were performed in an anechoic chamber using a robotic measurement system DASY 52NEO with: a) free-space electric field probe (i.e., ER3DV6), calibrated for measurements in air; b) isotropic dosimetric probe (i.e., EX3DV4), calibrated for measurements in saline; c) magnetic field probe (i.e. H3DV7), calibrated for measurements in both air and saline; and d) data acquisition electronics (i.e., DAE4). The field data was collected at 1 cm³ spacing, with the isocenter of the coil established as a reference point. EM field data were collected in the air and the saline (figures 4.1b and c). The ER3DV6 and H3DV7 probes returned three RMS magnitude values for each measurement, one for each field component x, y, and z (i.e., $\langle \|\vec{E}_x^M\| \rangle$, $\langle \|\vec{E}_y^M\| \rangle$, $\langle \|\vec{E}_z^M\| \rangle$ in V/m; and $\langle \|\vec{H}_x^M\| \rangle$, $\langle \|\vec{H}_y^M\| \rangle$, $\langle \|\vec{H}_z^M\| \rangle$ in A/m). The total RMS magnitude was then computed based on the quadratic norm. Conversely, the EX3DV4 probe returned only the total RMS magnitude ($\langle \|\vec{E}^M\| \rangle$) of the measured field. The fields were measured: 1) in air on two coronal planes (figure

4.3 Methods

4.1b), and figure 4.2) in the saline solution in the volume described by the red region in figure 4.1c. The measurement volume was selected to avoid possible collisions between any measurement equipment (i.e., robotic arm and probes) and the coil and/or phantom walls. The system was not driven with fixed a-priori quadrature conditions; rather the two exposure conditions were defined by enforcing a circular polarization of the magnetic field at the isocenter in two orientations (CW and CCW) of the unloaded coil; the amplitude and phase of the input signal to the system were adjusted until the difference of the x and y components of the magnetic fields (i.e., $\langle \|\vec{H}_x^M\| \rangle_{iso}$ and $\langle \|\vec{H}_y^M\| \rangle_{iso}$) returned by the H3DV7 probe (positioned at the isocenter of the unloaded coil) was less than 0.25 dB at every 10° increment rotation about the z-axis. The CW and CCW measurements were collected to investigate the effect of different exposure scenarios.

4.3.5 Data analysis

Data analysis was performed using Matlab (Mathworks Inc., Natick, MA). The spatial average Specific Absorption Rate (avgSAR) inside the saline measurement volume was calculated from the measured electric field RMS magnitude $\langle \|\vec{E}^M\| \rangle$ for each polarization as follows:

$$avgSAR^M_P = \frac{1}{N} \sum_{n=1}^N \frac{\sigma(\langle \|\vec{E}_P^M\| \rangle_n)^2}{\rho} \quad (4.1)$$

where N is total number of measurement points in saline measured over the measurement volume V (i.e., 0.0111 m³) reported in figure 4.1c; σ and ρ are the properties of the saline, and P is the polarization (i.e., CW or CCW). The normalization of the numerical results was obtained using the following steps: 1) the numerical data of each team was resampled on to a uniform grid of 1 cm² (corresponding to the measurement grid spacing); 2) the area of the planes representing the numerical data was reduced to match the measurements planes; 3) for each team, the values of electric field RMS magnitude $\langle \|\vec{E}^{team}\| \rangle$ inside the saline volume were used to calculate the following quantity:

$$avgSAR^{team}_P = \frac{1}{N} \sum_{n=1}^N \frac{\sigma(\langle \|\vec{E}_P^{team}\| \rangle_n)^2}{\rho} \quad (4.2)$$

and 4) for each polarization P, the values of $\langle \|\vec{E}^{team}\| \rangle$ and $\langle \|\vec{H}^{team}\| \rangle$ were rescaled to the polarization based quantity $\sqrt{avgSAR^{team}_P / avgSAR^M_P}$ to obtain the normalized RMS magnitude of electric and magnetic field, namely $\langle \|\vec{E}\| \rangle$ and $\langle \|\vec{H}\| \rangle$.

An inter-laboratory computational and experimental study of a radiofrequency coil model at 64 MHz

	Uncertainty Description	Unc. +/- %
	Probe, DAE	
1	calibration	8.5
2	linearity	2.7
3	isotropy (axial)	0.0
4	isotropy (spherical)	2.3
5	integration volume	5.8
6	field distortion	0.0
7	SNR	0.8
8	integration time	1.0
9	readout electronics	0.3
10	modulation response	2.7
	<u>combined</u>	<u>11.3</u>
	MITS, phantom	
11	epsilon	1.2
12	sigma	5.0
13	phantom (x)	0.9
14	phantom (y)	0.9
15	phantom (z)	0.8
	<u>combined</u>	<u>5.4</u>
	point measurement	
16	<u>probe, DAE</u>	<u>11.3</u>
17	<u>MITS, phantom</u>	<u>5.4</u>
18	E drift	6.1
19	sensor positioning	6.8
	combined	15.5
	expanded	30.9

Table 4.1: Probe uncertainty table of the principle equipment used in measurements.

4.3.6 Uncertainty analysis

The probe uncertainty analysis is summarized in Table ???. Data in rows 1, 2, 3, 4, and 10 are specified by the probe calibration certificates from the manufacturer, line 5 describes the worst-case deviation for sensor offset from center axis assessed with field distribution of S-AIMD1 tip (spatial gradient of 4.6 dB/mm); line 6 is specified by the manufacturer for measurements performed at 2 mm away from any interface; because the measurements conducted for the study were at more than 1 cm from the phantom wall, to avoid collision, this term is set to 0; line 7 presents results assuming a field of typically 15 V/m and a probe noise level of 1.5 V/m; line 8 presents results for 0.5 s integration time of the applied signal not synchronized with the integration; line 9 is specified by the data acquisition electronics calibration certificate; line 12-16 and 19 are based on [91]; lines 16 and 17 are the combined uncertainty of the probe and the phantom, listed above, respectively. Line 18 assumes a 27 %/mm of sensor positioning uncertainty and the positioning is assumed ± 0.25 mm per DASY52 budget of the robot positioning.

4.4 Results

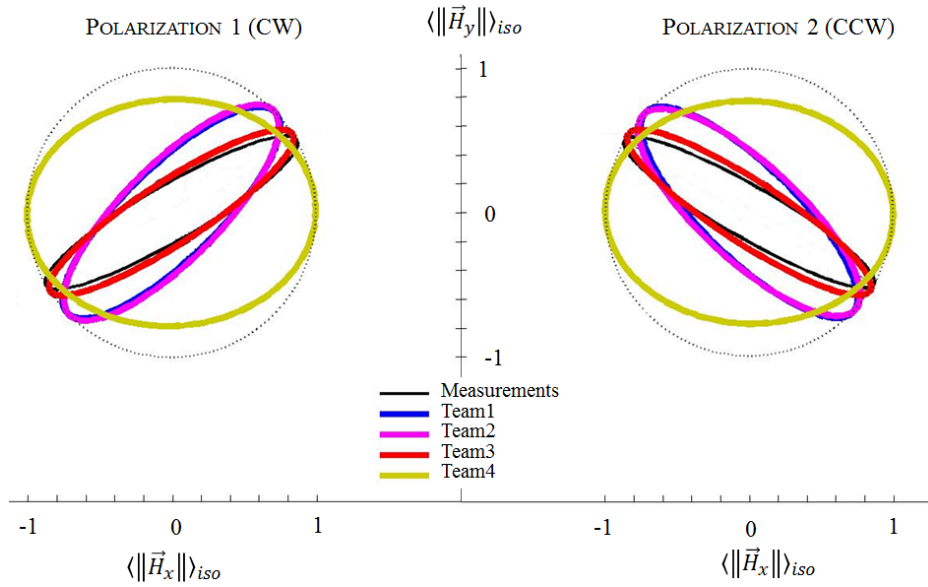


Figure 4.3: Graphical representation of measured and simulated polarizations at the isocenter of the loaded coil (inside the saline). The measured data were not distributed to the teams before the simulations. The polarization of Team4 was visibly different compared to all other values. The polarization of Team2 and Team3 were comparable (i.e., lines superimposing in the graph). The simulated data of Team3 had similar polarization to the measured values. The initial phase of the plots is arbitrary. The grey dashed circle is included as reference to indicate a fully circular polarization.

4.4 Results

The numerical model of the coil differed among the teams primarily in terms of electrical components and feed implementations (figure 4.2). Figure 4.3 compares the polarizations of the H-fields at the isocenter of the ASTM phantom, obtained numerically from the four teams, to the experimental result (black line). Notably, the exposure conditions were defined by enforcing a circular polarization for unloaded coil, while the measurements presented in figure 4.3 refer to a loaded coil. Team1 and Team2 yield similar results due to the similarity in the numerical implementations. The polarizations of Team3 (indicated in red) best resembled the measured exposure conditions, while the polarizations of Team4 (indicated in yellow) were visibly different compared to the other teams and compared to the measurements.

Figure 4.4 and figure 4.5 illustrate the results inside the saline within the isocenter axial and coronal planes ($y = 0$ mm and $z = 0$ mm) of the phantom for CW and CCW polarizations, respectively. The correlation between measurement and numerical values obtained by the four teams are further demonstrated in 2D histograms of figure 4.6.

The measured and numerical values are represented on the vertical and horizontal

An inter-laboratory computational and experimental study of a radiofrequency coil model at 64 MHz

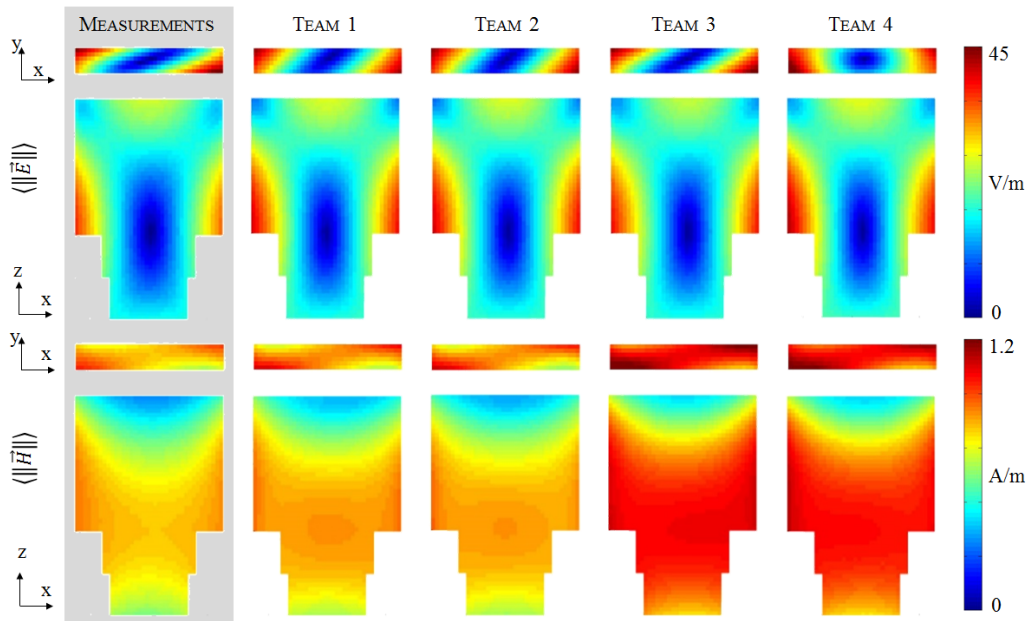


Figure 4.4: Normalized EM field maps inside phantom with CW polarization. Axial and coronal view of $\langle \|\vec{E}\| \rangle$ (top) and $\langle \|\vec{H}\| \rangle$ (bottom) for the central plane inside the ASTM phantom. Values of $\langle \|\vec{H}\| \rangle_{iso}$ 0.81 A/m, 0.87 A/m, 0.86 A/m, 1.1 A/m, 0.99 A/m for Measurements, Team1, Team2, Team3, and Team4, respectively.

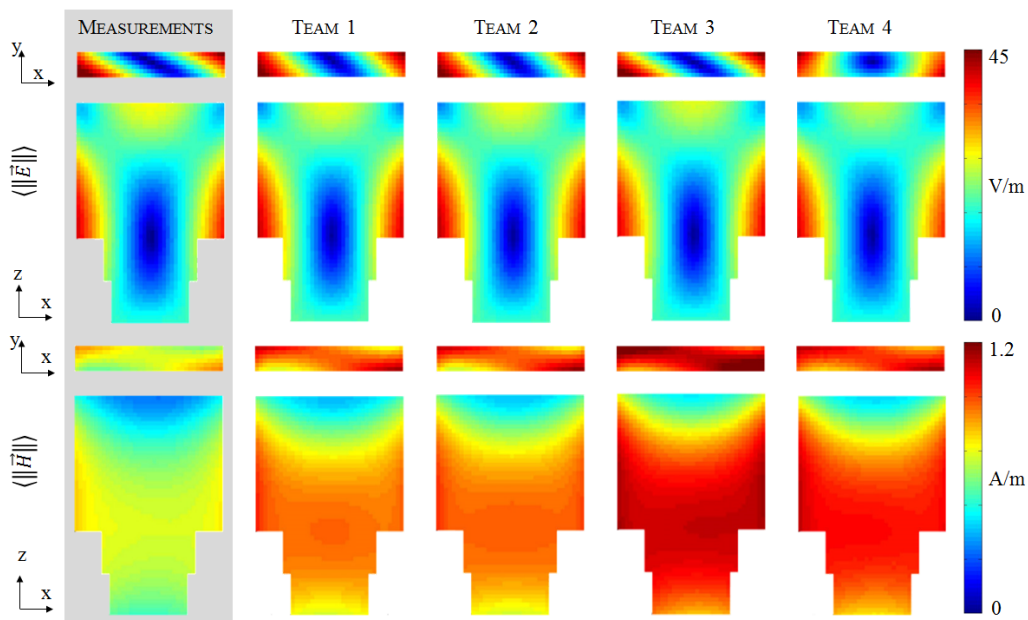


Figure 4.5: Normalized EM field maps inside phantom with CCW polarization. Axial and coronal view of $\langle \|\vec{E}\| \rangle$ (top) and $\langle \|\vec{H}\| \rangle$ (bottom) for the central plane inside the ASTM phantom. Values of $\langle \|\vec{H}\| \rangle_{iso}$ were: 0.70 A/m, 0.92 A/m, 0.93 A/m, 1.1 A/m, 1.0 A/m for Measurements, Team1, Team2, Team3, and Team4, respectively.

4.4 Results

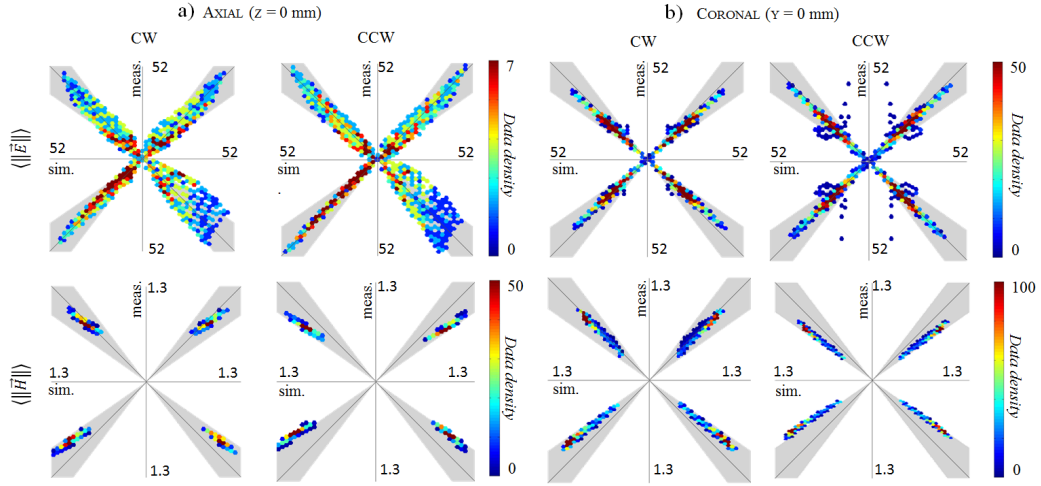


Figure 4.6: Measured values were plotted against numeric values as data-point distributions on the Cartesian plane. Data is shown here for the isocenter axial plane ($z = 0$ mm, left panel) and the isocenter coronal plane ($y = 0$ mm, right panel). Each quadrant reports data from one team (i.e., Q1-Q4 for Team1-Team4, respectively). The grey region indicates the 95% uncertainty region. Maximum values for each axis (i.e., 52 V/m and 1.3 A/m) are chosen for visualization purposes. The colorbar indicates the data density for each point. The dimension of the points for each graph represents the data resolution, equal to 2 V/m for $\langle \|\vec{E}\| \rangle$ and 0.05 A/m for $\langle \|\vec{H}\| \rangle$. *N.B. An higher resolution representation of this figure is included in Appendix B.*

axes, respectively. Each quadrant corresponds to the results obtained from each team (Q1-Q4: Team1-Team4). For ease of comparison, uncertainty data, as described above, were included as a cone plot. On the isocenter coronal plane, the $\langle \|\vec{E}\| \rangle$ distribution was similar across all numerical results for all teams as well as the measurements (figure 4.6). In the isocenter axial plane, the pattern of the $\langle \|\vec{E}\| \rangle$ obtained by Team4 for both polarizations was visibly different from others teams and from Measurements, which can be also seen from the spread of the corresponding histograms in Q4 of figure 4.6. In the isocenter coronal plane, the pattern of the $\langle \|\vec{E}\| \rangle$ for all teams and Measurements were comparable, as also shown in figure 4.6. Finally, the $\langle \|\vec{H}\| \rangle$ of Team3 and Team4 was always higher than the values obtained by Team1 and Team2.

The numerical results showed mostly mirrored data and similar SAR_{team} when comparing CW vs. CCW polarization (numerical data in figure 4.4 and figure 4.5). The measurements data for CCW polarization did not mirror exactly the data with CW polarization, however. Visible discrepancies in $\langle \|\vec{H}\| \rangle$ on the isocenter axial and coronal planes were observed, as shown by different patterns of correlation in figure 4.6. The CW polarization clearly shows better correlation between measured and numerical $\langle \|\vec{H}\| \rangle$ values in both axial and coronal planes; which is signified by the clustering of data points near the diagonal lines. Additionally, there was

An inter-laboratory computational and experimental study of a radiofrequency coil model at 64 MHz

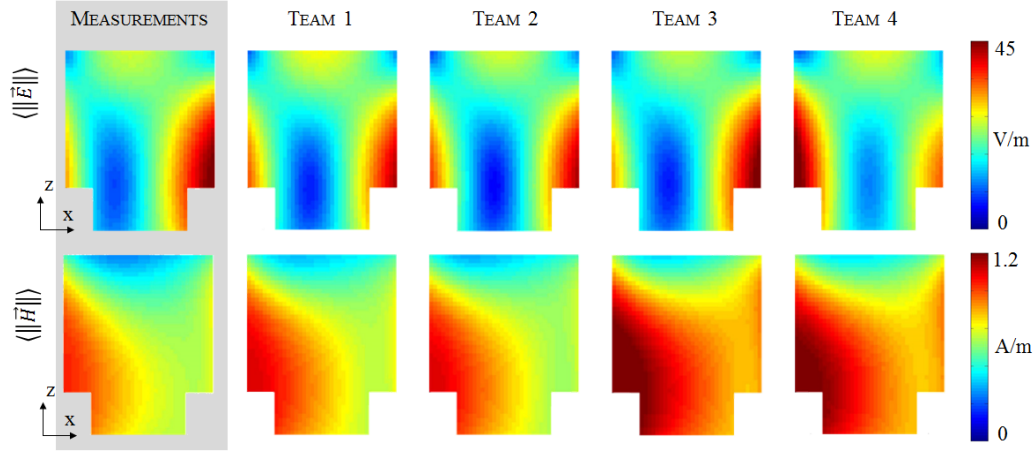


Figure 4.7: Normalized EM field maps inside phantom with CW polarization. Off-center coronal view of $\langle \|\vec{E}\| \rangle$ (top) and $\langle \|\vec{H}\| \rangle$ (bottom) for the plane $y = 30$ mm inside the saline.

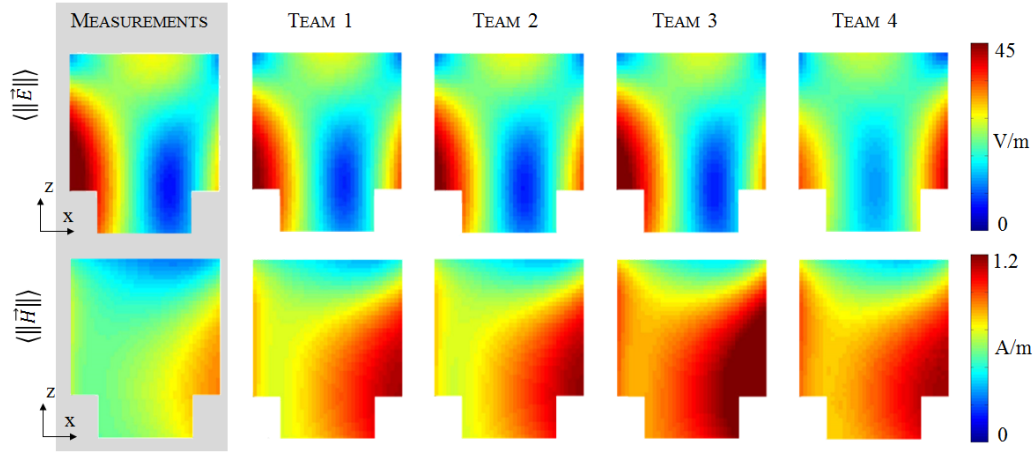


Figure 4.8: Normalized EM field maps inside phantom with CCW polarization. Off-center coronal view of $\langle \|\vec{E}\| \rangle$ (top) and $\langle \|\vec{H}\| \rangle$ (bottom) for the plane $y = 30$ mm inside the saline.

a 10% discrepancy of avgSAR in the measurements (i.e., $avgSAR^M_{CW}=0.21$ W/kg; $avgSAR^M_{CCW}=0.23$ W/kg). These discrepancies resulted in more points outside the uncertainty cone for CCW polarization in the coronal plane, suggesting that the uncertainty in the near-field generated by the experimental system could not be considered as zero.

4.5 Discussion

The different implementation of each group generated different coil losses, coil polarization, and ultimately different electric field and magnetic field maps. These differences, already visible in Figs. 4 and 5, were even more evident in the off-center

4.5 Discussion

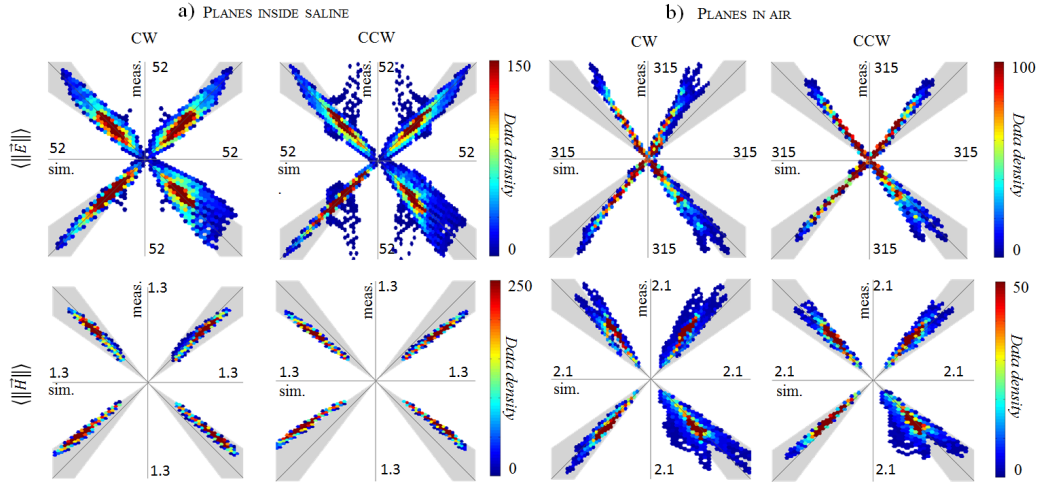


Figure 4.9: Measured values were plotted against numerical values as data-point distributions on the Cartesian plane. Data for the entire volume measured, inside the saline (left panel), and in air (right panel). The grey region indicates region with the 95% uncertainty of probes. The colorbar indicates the data density for each point. The dimension of the points for each graph represents the data resolution, equal to 2 V/m for $\langle \|\vec{E}\| \rangle$ and 0.05 A/m for $\langle \|\vec{H}\| \rangle$ (inside the saline) and equal to 12 V/m for $\langle \|\vec{E}\| \rangle$ and 0.08 A/m for $\langle \|\vec{H}\| \rangle$ (in air). *N.B. A higher resolution representation of this figure is included in Appendix B.*

coronal planes. In these planes values of $\langle \|\vec{E}\| \rangle$ calculated by Team4 showed a visibly different symmetry compared to the results of Team1, Team2, and Team3 as well as compared to the measurements (figure 4.7 and figure 4.8). The maximum values of $\langle \|\vec{E}\| \rangle$ in these planes increased with increasing distance from the isocenter.

When comparing data inside the saline vs. in air (figure 4.9), the average deviation of data-points from the 1:1 line was smaller for $\langle \|\vec{E}\| \rangle$ compared to $\langle \|\vec{H}\| \rangle$ inside the saline. Conversely, the deviation of data-points from the 1:1 line was visibly higher for the data in air compared to the data inside the saline (figure 4.9). The specific results were affected by the normalization selected. For example, normalizing the data based on the ratio $\sqrt{\text{avgSAR}^{\text{team}}_P / \text{avgSAR}^M_P}$ (see Eqs. 4.1 and 4.2) resulted in relatively small average differences across the teams for $\langle \|\vec{E}\| \rangle$ inside the saline. The results were also checked by imposing another normalization (not shown) based on $\langle \|\vec{H}\| \rangle$ at the isocenter ($\langle \|\vec{H}\| \rangle_{iso}$), for which the average deviation of data-points from the 1:1 line of $\langle \|\vec{H}\| \rangle$ approximately half than the same quantity of $\langle \|\vec{E}\| \rangle$. These results were in line with the observation that the measurements and the different coil model implementations ultimately resulted in a different ratio $\langle \|\vec{H}\| \rangle_{iso} / \sqrt{\text{avgSAR}_P}$. Specifically, the values for CW exposure were: 1.74, 1.88, 1.87, 2.28, 2.14 A/m/W/kg for measurements, Team1, Team2, Team3, and Team4, respectively; and the values for CCW exposure were: 1.45, 1.90, 1.93, 2.29, 2.13 A/m/W/kg, respectively.

4.5.1 Limitations

The study was based on a limited set of planes within the coil volume, which may not fully represent the variation of the electric field throughout the coil. The interpolation used during post-processing may add additional source of uncertainty that may deserve further exploration. The numerical and measurement results were herein compared by imposing a normalization of the data based on avgSAR, which was obtained by interpolating the electric field values on to a 1 cm^2 grid. However, such interpolation may introduce some uncertainty of the results, as the electric field may not vary linearly within the 1 cm^2 . Notably, this issue would not be present when comparing simulations results against each other, but it is only present when comparing the simulation results against the measurements. The results of the study are limited to the RF exposure system and experimental setup described herein and cannot be generalized to the wider range of birdcage coils available commercially.

4.6 Conclusion

The goal of this study was to perform a comparison of different numerical implementations obtained by users modeling a non-fully disclosed RF exposure system. The results showed that the implementation of each group generated different coil losses, coil polarization, and ultimately different electric field and magnetic field maps. Our results confirm that a data comparison based solely on magnetic field data may not be sufficient to properly characterize an RF exposure system, especially on non-isocenter planes. While the results of this study cannot be directly applied to clinical MR systems, they suggest that providing limited information on the coil (i.e., diameter, length, feed position, and fixed resonant frequency) can generate visibly different results across users, especially for off-center planes inside the phantom saline or planes in air between the phantom and coil. Future steps will include the distribution of additional information on the RF exposure system, such as frequency response and EM field measured data, to investigate how this information could help to further refine the computational prediction of the behavior of these systems.

Comprehensive Discussion Part I

Part I presented and analyzed the results of several implementations of a RF coil model for MRI. Results showed that each implementation is characterized by a peculiar EM field distributions strictly related to the electrical implementation of the model. Specifically the coil model implementation presented were categorized in specific and simplified. The specific coil model presented was characterized by a finite number of feeding sources directly related to the one typically used in physical system, whereas simplified models use a multport feeding condition.

The analysis presented in Part I showed that specific coil models, such as the S2, are able to accurately reproduce the resonance profile and the EM field distribution of a physical system. Thus the use of such specific model allows to drive quantitative conclusions of the results. However to be interpretable in a physical manner, the results have to be always combined with a reliable VVUQ procedure (see chapter 1.3.2). In fact, an accurate VVUQ procedure is able to determine if the numerical coil model implemented is an accurate representation. This procedure is particularly important for the S2 model due to its high sensitivity to parameters variability. In fact, this model typology showed to be very sensitive to variation of parameters such as input frequency, coil losses used to implement the resonance structure, and FDTD grid (see paragraphs 2.2, 2.3.1, 2.5).

On the other side, simplified implementations of the coil model showed to be a very useful alternative to specific models to easily reproduce with a good accuracy the EM field distribution within the coil and a phantom, such as for the G32 and H16 models. However results also proved that simplification of the coil implementation may also generate an EM field distribution far from the one of the physical coil used, as for the case of G16 and H16_{fr-forced}. Thus also for simplified implementation the VVUQ procedure is essential to determine where the model is a good representation or not of the reality. Once proven to be correctly implemented these models are a very useful tools to obtain a fast and reliable overview of the exposure within the coil and phantom. These models can be implemented by first time users that are interested to understand the physical aspects of the RF MRI exposure of phantoms and voxel models, such as the one introduced in chapter 1.4. Additionally they can be very

An inter-laboratory computational and experimental study of a radiofrequency coil model at 64 MHz

useful to expert users that need to assess the dependency of the EM exposure related to affecting variables independent by the exposure system. For example different position of a voxel phantom within the coil, or variability of the EM field distribution with the numerical environment and electrical properties of the material used.

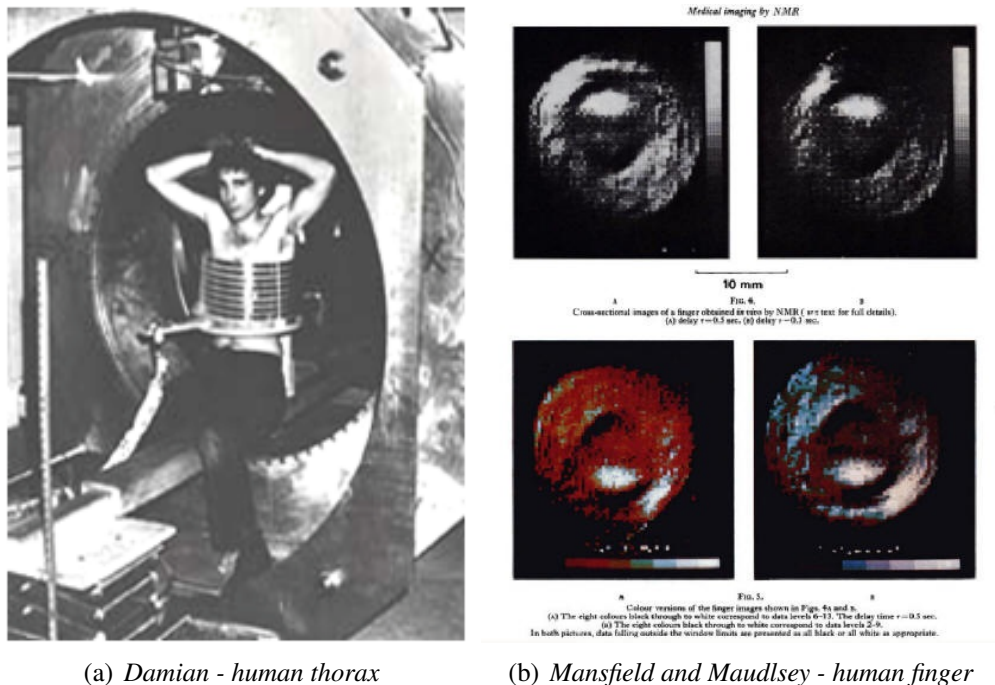
The last chapter of Part I reported the analysis of results with respect to the variability of the simulating user and software platform. Outcomes showed that different users may generate variable results even following the same protocol and using the same geometrical coil model. This was particularly evident comparing the results of Team3 and Team4 that were additionally using the same software platform (i.e., ANSYS HFSS). Reasons for such differences were due to the already observed high sensitivity of the coil model that could be categorized as specific. Comparing the results between the four teams involved showed that under the same simulation protocol, each team freely implemented a different electrical representation of the coil model that generated differences in the EM field distributions within the coil and the phantom. This result confirmed that with respect to the same geometric model more than one electrical implementation could be developed. Thus any numerical outcome needs a VVUQ analysis to drive specific conclusions. Further developments of this study should include the analysis of the results generated by the teams with the increasing of the constrains given by the protocol. It is expected that the more the constrains to be followed the less the variation of results between the teams. Such analysis would also allow for a direct evaluation of the variability related to the use of diverse numerical method such as FDTD or FEM (see chapter 1.3.1 for more details).

Part II

Computational modeling and measurements of human body models and phantoms exposed to MRI RF fields

Chapter 5

Background and State of the Art



(a) *Damian - human thorax*

(b) *Mansfield and Maudlsey - human finger*

Figure 5.1: First MR images performed in 1977 by (a) Damian of the human thorax [181], and (b) Mansfield and Maudlsey of the human finger [182].

In 1971 Raymond Damadian had the intuition to use the phenomena of nuclear magnetic resonance for biomedical applications. In his work published in Nature [183], he described the use of the physical phenomena for tumor imaging. Thank to his contribution, the research on the application of nuclear magnetic resonance for human imaging made big progress in short time. The first in-vivo human MR images were produced by Damadian in 1977 [181] for a human thorax (figure 5.1a) and by Mansfield and Maudlsey [182] for a human finger 5.1b). In 1978, Damadian founded the FONAR Corporation, which manufactured the first commercial whole-body MR scanner in 1980 and received the first US FDA approval on 1984. Additionally, in

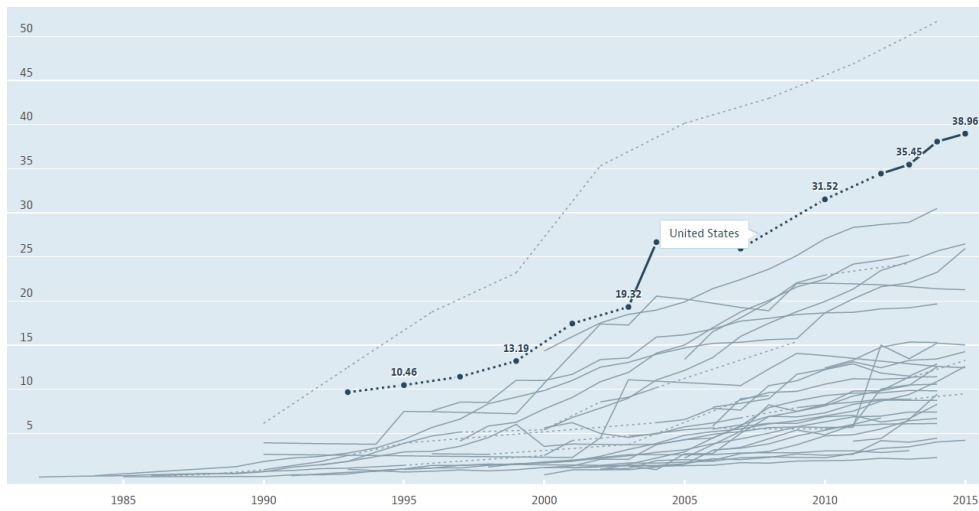


Figure 5.2: Growth of MRI scanners for 81 countries worldwide from 1982 to 2015. The USA showed a growth of more than 300 %. Data were found in the OECD website. data also reported in [185].

1983 Toshiba entered the market with the first approved MRI scanner by the Ministry of Health and Welfare in Japan. General Electric and Siemens entered the market shortly after.

Since that time, MRI technology has evolved significantly, becoming an essential clinical diagnostic tool [184]. Figure 5.2 reports the indication of the numbers of equipment per million of habitats for 81 countries of the word from 1982 to 2015. The growth of the USA was highlighted as the county with the highest rate of growth after Japan with more than 300 % from 1993 to 2005. The chart was found in the website of the Organisation for Economic Co-operation and Development (OECD), data were also published by the OECD in [185].

Other important applications of the MRI scanner goes beyond diagnostic. This was possible thank to the improvement or technology, computers speed increase, and empowerment or real-time acquisition with high resolution images. One example of employments of MRI systems beyond diagnostic is interventional MRI (iMRI).

iMRI is a radiological procedure that takes advantage of the high resolution MR images to guide real-time interventional procedures. This interventional procedures gained increasing importance in medical areas such as primarily radiological, cardiovascular, neurological, interventional tumor therapy or pediatric radiology and cardiology. The iMRI allows for several benefits to the patient. The biggest advantage is that it allows to perform interventional endovascular procedures avoiding the conventional X-ray fluoroscopy. Hence both the patient and the interventionists avoid the exposure to dangerous ionizing radiations. This is particularly relevant for the pediatric population.

5.1 Assessing safety for patients in MRI

The compatibility problem with the iMRI is that possible procedures may require the use of conductive devices used for guiding or tracking the interventional procedure. Examples of those are guiding thermal ablation of tissues or diagnostic catheterization such as biopsies of lesions. The problem with these devices is that portion of the guiding catheter is outside of the body, where the EM fields are high in magnitude and strongly affected by the coil design.

5.1 Assessing safety for patients in MRI

The attention to patient safety started as soon as the first MR images of humans were produced, the interest on the safety aspect raised. In 1978 Bottomley and Andrew [186] published the first study evaluating power deposition in biological tissue samples during an MR imaging experiment. The power deposition was computed within samples assumed semi-infinite planar and infinitely long cylindrical models of homogeneous biological tissue. Results showed that at frequencies higher than 5 MHz the local power density safety limit of that time (i.e., $1 \text{ mW} \cdot \text{cm}^{-3}$), UK Ministry of Technology 1968) was exceeded.

Since then, in the following decade, several authors studied, both numerically and experimentally, the RF power deposition within patients and animal models [33, 187]. Potential bioeffects of the MRI fields (i.e., static, gradient, and RF; see section 1) were firstly summarized by Budinger in 1979 [188] and in 1981 [189]. Budinger suggested that the exposure to the RF field and to the time varying magnetic field of the gradient coils may induce an amount of current in the tissue sufficient to generate observable heating. Afterwards, since 1985 [33] several studies showed data concerning thermal or other physiological response of human subjects exposed to RF radiation during an MR scan [190–194].

Generally the study of the tissue exposure to an external EM field is referred with "Dosimetry". As described by Cynthia and colleagues in [122] a dosimetric study mainly consist of two parts: i) first, calculate the external fields, which are produced by a given source, ii) second determine the internal fields within the exposed medium. In the context of this thesis, the incident field is considered the one generated by the RF coil of the scanner, as previously described in I. Conversely, the internal fields are the EM fields generated inside the body. The correlation between dosimetry of patient and the patient safety in MRI with respect to the RF field, are mainly due to the thermogenic qualities of the internal RF field. It is true in general for any RF source, that temperature rises in biological tissues exposed to RF field are due to power losses in the form of Joule heating within the tissues. The internal field is identified by the electric

field induced in the exposed medium (i.e., human body) by the alternating magnetic field (i.e., the RF field of the coil). In the specific case of the RF field used in MRI scanners, relation between the magnetic field and the electric field have been already theoretically explained in section 1.2.4.

The dosimetric term used to identify the absorption of RF radiation is the SAR. During patient exposure typically the whole body SAR (wbSAR) and the local peak SAR are monitored to assure patient safety. The WbSAR is defined as the amount of energy absorbed over the whole body of the patient over any 6 minutes, divided by the patient mass [28]. Conversely, the local peak SAR is the amount of energy absorbed within a small volume of tissue, typically 0.1 g, 1 g or 10 g. The SAR calculated over a volume can be defined as:

$$SAR = \int_{\Gamma} \frac{\sigma |\vec{E}|^2}{2\rho} dV \quad (5.1)$$

where Γ is the total volume of the sample, and σ and ρ are the conductivity and density of the tissue.

Evaluation of RF dosimetry within the human body can be extremely complicated because of the complexity of human body structures. The different organs present inside the body affect the SAR distribution through two factors. The first complexity step is directly related to the different electrical properties of the organs. As reported in [195] even if the inductive electric field, due to the time-varying magnetic, is not strongly affected by the complexity of human body structure, the resulting SAR patterns are strongly tissue-dependent. As suggested by 5.1 the SAR calculation is related to the specific conductivity of the tissue. The dielectric properties of a biological tissue result from the interaction of EM radiation with its constituents at the cellular and molecular level [196]. For biological tissues the cell membrane has a capacitance of about $0.01 \text{ F}/\text{m}^2$ which introduces a frequency dependence of σ [197]. At 65 MHz, the conductivity values in the body range from the one of the fat (i.e., $\sigma = 6.62e - 2$) to the one of the cerebrospinal fluid (i.e., $\sigma = 2.07$) [198]. The second complexity step is related to distribution of eddy currents within the human body [78]. The evaluation of SAR distribution within the body is additionally complicated because the inhomogeneities of body may generate concentration of eddy currents in certain points of the body with a resulting concentration of RF energy. Consequentially, high levels of temperature may be present, typically at the interface between tissues with high dielectric contrast such as at muscle-fat or muscle-bone interfaces. This phenomenon is explained by the secondary voltage produced by the eddy-currents explained in section 1.2.4. Especially for specific situations in which only part of the body may be exposed, it is important to consider a considerable section of the body to avoid miscalculation of

5.1 Assessing safety for patients in MRI

the peaks. In particular several studies showed how the inclusion or not of the shoulders for simulation of head exposure may affect the result accuracy [36, 103, 135, 147, 199].

RF dosimetry in MRI has been performed over the years by mean of numerical models. As already reported in section 1.4, models of sections or of the entire of human body of different size and ages were developed, such as the one reported in [100, 102, 200–202]. Murbach et al. in [138] investigated the impact of nine different human anatomy and ten different position within the RF coil on local SAR. Enhancements, nine different anatomical models were used for numerical evaluations in ten different Z-axis positions. Additionally the study showed potential increases of local SAR due to the presence of loops formed within the body (e.g., arms, legs) that increase body coupling with the RF field. Differences of local SAR with respect to human body model and its landmark position inside the coil were also reported by Yeo et al. [203]. In another study by Findlay and Dimbylow [204] the dependence of SAR with the posture of the body is reported.

While SAR is the dosimetric parameter used in literature to evaluate RF energy, the analysis of the patient safety requires additionally and most importantly the evaluation of temperature (and related thermal damage). In fact for any type of exposure, it is the temperature and not the SAR that is directly related to tissue damage [33, 205, 206]. The relation between SAR and temperature is not straightforward, as it is influenced by the thermal properties of the tissue (thermal capacity, thermal conductivity) as well as the presence of perfusion. For example, in areas of high perfusion, such as the brain, moderate to high SAR levels can result in a minimal temperature increase, while in areas of lower perfusion, such as muscle at rest and the eye, temperature may increase even with relatively low SAR levels [207]. Thermal conduction and heat loss to the environment also bring dissimilarity between SAR and temperature distributions. To overcome the gap between SAR and temperature, several studies performed numerical solution of the Pennes bioheat equation 5.2 [208–216].

$$\rho C_p \frac{\partial T}{\partial t} = \nabla \cdot (k \nabla T) - b(T - T_b) + Q \quad (5.2)$$

where T is the temperature in a point at time t , ρ is the medium density ($kg \cdot m^{-3}$), C_p is the heat capacity ($J \cdot kg^{-1} \cdot ^\circ C^{-1}$), k is the thermal conductivity ($W \cdot m^{-1} \cdot ^\circ C^{-1}$) is the blood perfusion constant, T_b is the blood temperature, and Q is the heat source ($W \cdot m^{-3}$) at the point. For RF exposure in MRI, Q is defined with respect to the SAR, with $Q = \rho SAR$ in the tissue. Several studies, such as [214, 217], showed how the Pennes equation 5.2 is able to accurately simulate temperature changes only due to exposures shorter than 10 minutes. This because the equation lack of modeling of the spatial and temporal variation of the blood temperature assuming the blood as an infinite heat sink. Thus for long exposures Pennes equation underestimate the temperature increase.

With the years several studies overcame the issue formulating new Bioheat equations that would model the temperature rise more precisely [217–220].

Once the temperature within the body is estimated, it is fundamental to evaluate the related thermal damage, in order to properly assess patient safety. For a healthy patient a rise of 1°C is generally acceptable. However special care must be taken for patients with certain medical disorders or under medication. Patients with compromised thermoregulatory function may be particularly susceptible to RF heating [221]. Several studies also suggested that female pregnant patients and children of age less than one year, should be included in the category of patients that need special care [74, 138, 139, 222–225].

The extent of thermal damage to tissue depends on tissue sensitivity, temperature and exposure time [206]. The thermal characteristics differ among human organs. For example the eyes have very little blood flow, and the lens of the eye have none; therefore more time is required by the eyes to disperse thermal energy. A second examples of a very sensitive organ is the testes. These are organs separated from the main volume of the body and are regarded as heat sensitive [221]. Sherlock reports in his review [33] these two organs (i.e., eyes and testis) as "primary sites of potential harmful effects if exposure to RF radiation during MR procedure is excessive".

An interesting approach for the evaluation of tissue damage is the "thermal dose model" proposed by Sapareto and Dewey in 1984 [226]. The approach is based on the Arrhenius-damage formula 5.3 [227], and it quantifies the damage using temperature and exposure time of cumulative equivalent minutes at 43 °C.

$$CEM43^{\circ}C = \sum_{i=1}^n t_i \cdot R^{43-T_i} \quad (5.3)$$

where $CEM43^{\circ}C$ is the cumulative number of equivalent minutes at $43^{\circ}C$, t_i is the i -th time interval, R is related to the temperature dependence of the rate of cell death (i.e., $R(T < 43^{\circ}C) = 1/4$, $R(T > 43^{\circ}C) = 1/2$) and T is the average temperature during time interval t_i . The $CEM43^{\circ}C$ method has been recently suggested a potential guide to assess MRI RF exposure levels [206, 228, 229].

Implantable medical devices in the MRI environment

The number of patients with medical devices has been increasing steadily over the past years. Hence, important considerations have to be done about safety of the MRI procedure for patients with medical devices. As such, given the diagnostic benefits of MRI, the need to allow MRI for patient with medical implants has also increased. This devices are used to treat a wide variety of clinical indications throughout the entire

5.1 Assessing safety for patients in MRI

body, and they can be fully implanted within the patient body or partially implanted showing external parts.

As already discussed in section 5.1, the risks associated with medical devices in MRI can be broadly categorized by the interaction between the device and the main field used by the MRI system. The greatest risk from this strong magnetic field is the attraction of ferromagnetic objects into the scanner causing movement, torque, or dislodgment of the device that can result in patient injury or even damage to the MRI system in the case of “projectile effect”. With respect to the field produced by the gradients coil, the rapidly changing magnetic fields can induce electrical currents in device leads, causing oversensing or undersensing of the device [230]. Lastly when a conductive elongated structures as the lead of a medical device is immersed in an RF field, it couples with the field and scatters the incident field at its tip becoming a transmitting antenna. Then, because of the impedance mismatch between the lead and the tissue, an accumulation of charges occurs generating a current and thus a scattered electric field. The energy of the electric field generated is then convert into heat because of homic losses in the tissues. An additional safety concern that needs to be accounted for is linked to the image artifact that a device can produce during imaging. Even if these artifact are not a direct risk for the patient during the scanning procedure, their occurrence can pose risk reducing the quality of the examinations.

Medical devices can be categorized in two main group namely "active" and "passive". Active devices are those which have a source of electrical energy or any source of power other than that directly generated by the human body. Examples of active devices are pacemakers, defibrillators, neurostimulators, cochlear implants and drug pumps. Whereas passive devices do not require any power source for their function. Examples are hip/knee joint replacements, heart valves, aneurysm clips, coronary stents and breast implants. Several accidents happened in the past. Delfino and Woods [184] report examples of people killed or badly injured during MRI scan. Ferreira et al. [230] also reported that over the years at least 17 supposed MRI-associated deaths among patients with pacemakers. They also suggested that the number of cases is probably an underestimation of the real number of fatalities, because several cases of patients with a cardiac pacemaker who died after exposure to MRI have never been reported in the medical literature.

One of the first studies concerning possible hazards for conductive medical devices exposed to RF field, was performed by Davis et al. in 1981 [231]. The work represents one of the first attempts to quantify the heating in small surgical clips exposed to a RF field. Over the years many groups performed numerical and experimental tests to evaluate safety of medical devices in MRI. Examples of studies reported different

increasing of temperature at the tip of the lead of medical devices. In Achenbach et al. [232] has been measured a 63.1 °C increase of temperature at the tip of a cardio stimulator during a MRI session of 90s. Rezai et al. [233] reported a 25 °C increased of temperature near a DBS implant in the phantom. The risk for high energy deposition was also reported in patients cables for Electroencephalography (EEG), such in [148, 234].

5.1.1 Standards and test methods for safety assessment: overview

Both standards and test methods are available to assess safety of patients undergoing an MRI scan. The standards report limits and test methods define the procedures to be follow to assure and assess safety conditions. Special reference can be found for patient not in normal conditions, such as infants, pregnant women, and people with impaired thermoregulatory ability as a result of age, disease or the use of medications. Whereas, separate standards and test methods are dedicated to the condition of patient with implanted medical devices. However no standard or test method is actually available for patient with partially implanted medical devices (such as the on used for iMRI) or for patient with metallic plate in contact with the skin.

MRI standards for patient safety

MRI systems are considered both medical devices and radiation-emitting electronic products [235]. As such, both the International Commission on Non-Ionising Radiation Protection (ICNIRP) and the International Electrotechnical Commission (IEC) have set limits for patient exposure in MRI. With respect to MRI clinical exposure to patients, ICNIRP published a statement in 2004 [236] with a second update in in 2009. Conversely, the IEC developed the IEC 60601-2-33 standard [237], which focuses on the safety requirements of MRI equipment used for medical diagnosis.

The ICNIRP and IEC standards define the exposure safety limits with respect to the SAR. They both define three levels of operation with specific limits identified by the region of the body. Definition of levels and limits by the two standards follows.

ICNIRP:

- Normal operating mode for routine scanning of patients
- Controlled operating mode for specific examinations above normal operating mode output level, carried out under medical supervision
- Experimental operating mode carried out at levels above the controlled operating mode and for which a research ethics committee approval has been obtained.

IEC:

- Normal operating mode of operation of the MRI equipment in which none of the

5.1 Assessing safety for patients in MRI

outputs have a value that may cause physiological stress to patients

- First level controlled operating mode of operation of the MRI equipment in which one or more outputs reach a value that may cause physiological stress to patients which needs to be controlled by medical supervision
- Second level controlled operating mode of operation of the MRI equipment in which one or more outputs reach a value that may produce significant risk for patients, for which explicit ethics committee approval is required (i.e., a human studies protocol approved to local requirements).

(a) ICNIRP

Level [W/kg]	Whole Body	Partial body		Local		
		Head	Not Head	Head	Trunk	Extremities
Normal	2	3	2-10	10	10	20
Controlled	4	3	4-10	10	10	20
Experimental	>4	>3	>(4-10)	10	>10	>20

(b) IEC

Level [W/kg]	Whole Body	Partial body		Local		
		Head	Not Head	Head	Trunk	Extremities
Normal	2	3.2	2-10	10	10	20
First	4	3.2	4-10	20	20	40
Second	>4	>3.2	>(4-10)	>20	>20	>40

Table 5.1: SAR limits identified by the region of the body for the (a) ICNIRP standard, and (b) IEC standard

In both ICNIRP and IEC limits (tables 5.1), the "local" SAR is the SAR averaged over the mass of 10 g of tissue. Additionally, the "head" SAR is the SAR averaged over the head of the patient, where the "head" is defined as the body as the body section between the top of the head and the beginning of the C4 vertebra. Lastly, the section named "partial" refers to the SAR dynamically scaled with the ratio between the patient mass exposed and the total patient mass, as described by:

$$Partial_{SAR} = 10 \frac{W}{kg} - \left(SAR_{limit} \frac{W}{kg} \cdot \frac{Mass_{exposed}}{Mass_{total}} \right) \quad (5.4)$$

where the SAR_{limit} is the SAR limit value with respect to the specific level used (e.g., IEC/Normal $SAR_{limit} = 2W/kg$, the $Mass_{total}$ is the entire patient mass, and the $Mass_{exposed}$ is defined in the IEC standard [237] as: " It is given by the Patient mass within the effective volume of the RF transmit coil. The Effective Volume of The RF Transmit Coil shall be that volume n which no more than 95% of the total absorbed RF power is deposited inside a homogeneous material which fills the volume normally accessible by the Patient". Section 6.2 present a computational analysis evaluating the sensitivity of the results with respect to the vague definition of partial SAR.

The two standards set the same limits with respect to temperature rise, namely:

- Normal Operating Mode: Exposure of extended volumes of the body should be such as to avoid a rise of more than 0.5°C in the body temperature of patients and volunteers, including those compromised with respect to their thermoregulatory ability.
- Controlled First Level Operating Mode: a relaxation of the basic restrictions on the rise in body temperature to 1°C can be envisaged if defined monitoring protocols are followed.
- Experimental Second Level Operating Mode: any scanning in this mode, which may result in a whole body temperature rise above 1°C, requires ethics committee approval.

In particular the 2004 ICNIRP report conclusions [236] regarding RF field exposure are: "*For whole-body exposures, no adverse health effects are expected if the increase in body core temperature does not exceed 1°C. In the case of infants and persons with cardiocirculatory impairment, the temperature increase should not exceed 0.5°C. With regard to localized heating, it seems reasonable to assume that adverse effects will be avoided with a reasonable certainty if temperatures in localized regions of the head are less than 38°C, of the trunk less than 39°C, and in the limbs less than 40°C.*"

NEMA standard test method

In addition to the standards with the standards defining the safety limits, there are documents standardizing the test methods to assess compliance with limits. The U.S. National Electrical Manufacturers Association (NEMA) in 1993 defined a test method standard for SAR calculation in MRI. A second edition followed in 2008 [238]. The NEMA standard described two measurement procedures for whole body SAR measurements, namely the calorimetric method and the pulse-energy method. The methods were only defined for volume RF transmit coils producing relatively homogeneous RF fields. Additionally, the standard text specify that the test methods don't apply to local SAR nor to final definition of temperature rise of the patient.

Standards for patients with medical devices undergoing MRI

At the beginning of the '90s no standard or test methods was available to limit and test the exposure of patient with medical devices undergoing an MRI scan. In 1993 the Center for Devices and Radiological Health (CDRH) of the FDA recognized the need for standards to address the safety of implants and other medical devices in the MR environment [239]. Hence, starting from 1998 the ASTM decided to develop test methods for evaluating magnetically-induced displacement force and torque, RF heat-

5.1 Assessing safety for patients in MRI



Figure 5.3: The standardized icons MR Safe, MR Conditional, and MR Unsafe as defined in ASTM F2503 [240]

ing, and image artifact. Over the years the ASTM society published several standards covering test methods for both passive and active devices. Delfino and Woods [184] report a complete review of all ASTM. The ASTM standard F2503 reports that after conducting all the testing appropriate for a given device, it is critical that the device labeling clearly communicates the conditions for safe use in the MR environment. The terminology to be used for the labeling is reported in the ASTM F2503 [240], and the same terminology has also been published by IEC as standard IEC 62570:2014 for marking medical devices and other items for safety in the MR environment. The standards report as labeling categories the following (figure 5.3):

- **MR Safe:** "an item that poses no known hazards resulting from exposure to any MR environment. MR Safe items are composed of materials that are electrically non-conductive, non-metallic, and non-magnetic".
- **MR Conditional:** "an item with demonstrated safety in the MR environment within defined conditions. At a minimum, address the conditions of the static magnetic field, the switched gradient magnetic field and the RF fields. Additional conditions, including specific configurations of the item, may be required".
- **MR Unsafe:** "an item which poses unacceptable risks to the patient, medical staff or other persons within the MR environment".

Most implants are MR Conditional; while, examples of MR safe devices are silicone catheters and polymer sutures, and of MR unsafe include ferromagnetic oxygen tanks and scissors [184]. Over the years test methods were published by the ASTM society both for active and passive devices. With respect to the RF field and passive devices the ASTM F2182 was first published in 2002 and finalized in the 2009 [110]. Within the standard, a phantom it is suggested for exposure assessment. The phantom has been already introduced in sections 1.4 2.4, and it is not intended to be representative of clinical exposure conditions, as the electric field distribution inside the phantom is not the same as the electrical field distribution inside the human body. The aim of the phantom is to provide a location with known exposure conditions. Even if standardize for passive implants the ASTM phantom is widely used also for safety assessment of

active implants.

To address the safety issues of active implants, a joint working group (JWG) between the International Organization for Standardization (ISO) and the IEC has developed TSs for active implantable medical device (AIMD) in MRI. The first edition of the TS was published on 2012 [111]. Additionally, implant-specific standards are being revised or newly drafted to include acceptance criteria and device-specific requirements for MRI safety testing and labeling [184]. The TS ISO 10974 describes a methodology for numerical assessment of in vivo exposure of the AIMD, based on a four-tier approach. The level of complexity for the evaluation of the RF-induced heating increases with each tier. The last tier involves numerical simulation of the RF coil plus body plus AIMD. In the Annex M-3 of the TS ISO 10974 an additional phantom to the ASTM [110] was presented to test active implants. The phantom proposed is the ellipsoidal phantom already presented in sections 1.4 2.4. The rationale is to generate an electric field distribution within the phantom with a uniform magnitude and a constant phase. The phantom used in 2.4 and in 3 was a implemented based on the one of the standard. Additionally, the field distribution within a cylindrical phantom as a proposal for a new phantom will be discussed in 8.1.

5.1.2 Transfer function approach

The local RF-induced heating is one of the most dangerous hazards for patients with AIMDs undergoing an MRI scan. Elongated conductive structures may pick up the RF-energy during MR exposure, and locally deposit it in the tissue near the implant electrodes; typically the lead tip.

For the numerical evaluation of a system including an object of dimensions in the μm range (i.e., AIMD) inside an object of dimensions in the meter range (i.e., coil), the computational cost of the simulations can be high when a simulation platform based on the FDTD method is used. An interesting solution to this problem is the use of the transfer function approach described by Park et al. in [241], and included in the Tier 3 approach of the TS ISO 10974 [111]. According to tier 3, three distinct tasks are identified:

1. assessment of the fields incident to the patients in an MRI environment without the AIMD in place ;
2. development a validated EM model of the AIMD;
3. assessment of the power deposition of the AIMD from electric field coupling.

The approach described aims to decouple the problem of the sensitivity of the lead to the electric field from the effective exposure level. At the base of the transfer function approach, there is the concept that the only component of the E field responsible for

5.1 Assessing safety for patients in MRI

the coupling with a conductive wire is the tangential component of the same (E_{tan}) along the wire itself. Because of that, the power dissipated at the tip of an AIMD can be computed by multiplying the sensitivity function – or transfer function – of the specific lead with the electric field tangential to it. Thus the scattered electric field $vecE_s$ in a point \vec{P} close to the tip of the AIMD lead can be described by the integral along the entire lead length as:

$$\vec{E}_s(\vec{P}) = \vec{E}_1(\vec{P}) \int_0^L \vec{h}_1(\tau) E_{tan}(\tau) d\tau \quad (5.5)$$

where $\vec{E}_1(\vec{P})$ is the scattered electric field due to a unit E_{tan} along the length of the lead L , and h_1 is a normalized transfer function of the lead. Because the spacial dependence of the shape of the electric field surrounding the electrode is independent of the form of the E_{tan} , the total power dissipated around the lead tip W_T can be determined by the spacial integration of the SAR, as:

$$W_T = \int_V \rho(\vec{P}) SAR(\vec{P}) dV = \int_V \rho(\vec{P}) \left[\frac{\sigma(\vec{P})}{2\rho(\vec{P})} \vec{E}_s(\vec{P}) \cdot \vec{E}_s^*(\vec{P}) \right] dV \quad (5.6)$$

where σ and ρ are the conductivity and density of the tissue in \vec{P} , respectively. Putting together 5.5 and 5.6, we can conclude:

$$\begin{aligned} W_T &= \int_V \frac{\sigma(\vec{P})}{2} \left[\vec{E}_1(\vec{P}) \cdot \vec{E}_1^*(\vec{P}) \right] \cdot \left[\int_0^L \vec{h}_1(\tau) E_{tan}(\tau) d\tau \right] \cdot \left[\int_0^L \vec{h}_1(\tau) E_{tan}(\tau) d\tau \right]^* dV \\ &= W_1 \cdot \|\alpha\|^2 \end{aligned} \quad (5.7)$$

with

$$W_1 = \int_V \frac{\sigma(\vec{P})}{2} \left[\vec{E}_1(\vec{P}) \cdot \vec{E}_1^*(\vec{P}) \right] \quad (5.8)$$

identifying the power dissipation due to the unit E_{tan} along the lead, and

$$\|\alpha\|^2 = \left[\int_0^L \vec{h}_1(\tau) E_{tan}(\tau) d\tau \right]^* \quad (5.9)$$

Typically the $\|\alpha\|^2$ term is computed by simulating the E_{tan} inside the human body model as for a realistic exposure, whereas the h_1 the of the AIMD lead can be computed or measured. In section 8.1 the study performed follows the described steps using a measure transfer function h_1 of three generic leads, and the simulated E_{tan} inside a cylindrical phantom.

Using this methodology, the complexity of the features compounding the AIMD lead affects the sensitivity function but doesn't need to be underestimated for the calculation of the temperature increase. An open question related to the use of the transfer function approach is the validity of the method in a heterogeneous environment. In clinical configurations, the leads of AIMDs (e.g., spinal cord stimulators, deep brain stimulators), are typically implanted in a patient through tissues with different electrical properties.

5.2 MR Conditional medical devices

To implement an MR Conditional devices issues related to all the three fields needs to be overcome. With respect to the static field efforts have been made to reduce the amount of ferromagnetic material present in the implant, such that the attraction effects are reduced. With respect to gradient field, dedicated devices programming or device circuitry can overcome problems related to oversensing or undersensing of the physiological signals. Lastly with respect to the RF the goal is to minimize the amount of heat and electrical currents that are induced on the leads. To achieve this, the resonant frequency should be avoided to prevent the lead from acting as a receiver of EM impulses. Within the years several on the lead design side several solutions were proposed considering the inclusion within the lead of RF-traps, shielding, coiling, billabongs, level of insulation etc. [178, 242, 243].

With the years, efforts were also put on RF coil design to overcome the RF induced heating issue. Murbach et al. [244] recently showed that diverse feeding coil conditions leading to diverse polarization of the field (named also "MR-shimming"), may lead to a high variability of whole body and local SAR in the patient. The study was performed considering the B_1^+ uniformity as important for imaging. Based on the study, it is considered possible to keep or even increase the B field homogeneity with a decrease of the amount of power absorbed by the patient. About this, over the year particular attention was posed to the use of multi-transmit coil array to reduce implant coupling. Multi-transmit coil array, presented in section 1.2.2, were designed to reduce field inhomogeneities, shorten the time for image acquisition, selection of the spatial excitation and improved management of the RF power absorbed by the patient's body [245]. The advantage of paying with the configurations of multi-transmit array to obtain E-field-free zones in the body were reported by Eryaman et al. and McElcheran et al. [246, 247]. Additionally a procedure considering the possibility for a more complex lead pattern was studied by Golestanirad et al. [248].

Chapter 6

Computation modeling of human body models for SAR evaluation

6.1 Homogeneous vs heterogeneous models

Section¹ 1.4 reported the all the numerical phantoms typically used in the contest of computational studies in MRI. When comparing homogeneous with heterogeneous models the main difference is that in heterogeneously composed specimens, reflections and refraction at tissue interfaces can occur. Thus RF inhomogeneity are present within the heterogeneous model that cannot be found in the the homogeneous model. These field inhomogeneity has the potential to create regions of high absorption inside the model that may be underestimated with homogeneous models.

Van der Berg et al. [250] compared EM field and SAR distribution between two elliptical phantoms made of homogeneous material, and five heterogeneous models of patient trunk. The study concluded that a "homogeneous elliptical phantom and a human pelvis are qualitatively very similar". However some limitations present in the study may had allowed for underestimations of dissimilarities. The heterogeneous models were characterized only by four anatomical structures (i.e., bone, fat, inner air, and muscle), the numerical resolution used ($5 \times 5 \times 5 \text{ mm}^3$) was not able to correctly resolve the fine body heterogeneity, and lastly the use of a truncated model did not allow to modeling the continuity of the induced fields within the body. This paragraph presents the results of a study where EM exposure of heterogeneous and homogeneous models was analyzed. In the first part, the profile of the power absorption was studied for the human body model Thelonious landmarked in two positions within the coil, and for the human body model Duke landmarked in four positions within the coil. In the second part a deeper analysis was carried out comparing the distribution of EM field

¹Major content of this paragraph was used for a manuscript ready to be submitted to the journal for International Journal for Numerical Methods in Biomedical Engineering. [249]

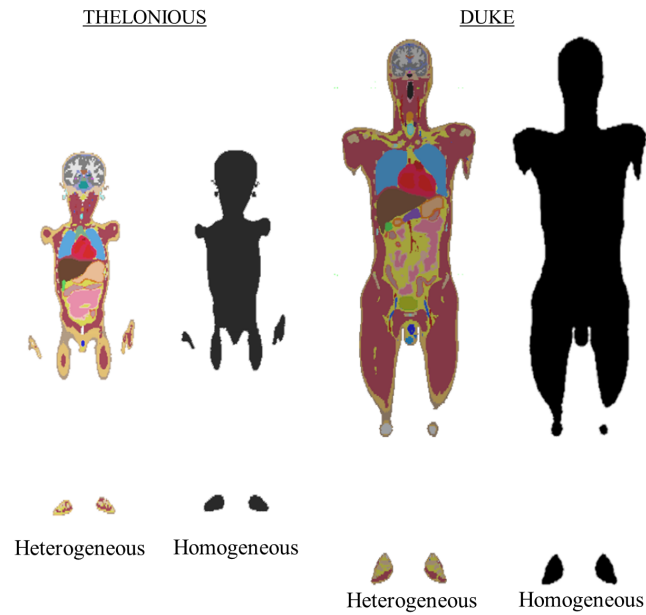


Figure 6.1: Heterogeneous and homogeneous model of the human phantom Thelonious and Duke. Models are in scale. In the heterogeneous models the different colors identify different anatomical structures present in the model (e.g., brown = liver, light blue = lungs, yellow = fat, dark purple = muscle).

and SAR in Duke.

EM field simulations were implemented using the software Sim4Life V2.2 (ZurichMedTech, Zurich, Switzerland). The RF field was computed by the model of the transmit RF high-pass birdcage body coil already introduced and used in section 3. The coil was driven in quadrature mode and was operating at 64 MHz. The human models (see paragraph 1.4) were representative of a child - Thelonious - and of a male adult - Duke - both used in their heterogeneous and homogeneous form (Figure 6.1). The heterogeneous models were part of the Virtual Population (ViP) 3.0 [97, 100], and their were composed of 299 and 305 different anatomical structures for Thelonious and Duke, respectively. The physical properties assigned to the anatomical structures (i.e., electrical conductivity and permittivity, and mass density) were based on literature [251]. Conversely, the two homogeneous model were based on the Virtual Population 1.0, and were composed of only one tissue material. The physical properties of the homogeneous structure were based on the ASTM standard for frequency of 64 MHz (ASTM: $\sigma = 0.47S/m$ and $\varepsilon = 80$ [110]).

To reduce numerical errors due to FDTD staircasing, the same simulations grid was used for the models. The imposed grid was uniform with a space volume of $3 \times 3 \times 3 \text{ mm}^3$. The entire simulation space was composed of 44.940 MCells. Staircasing effects due to the FDTD mesh were avoided not including in the analysis localized values of high field.

6.1 Homogeneous vs heterogeneous models

6.1.1 Power absorption

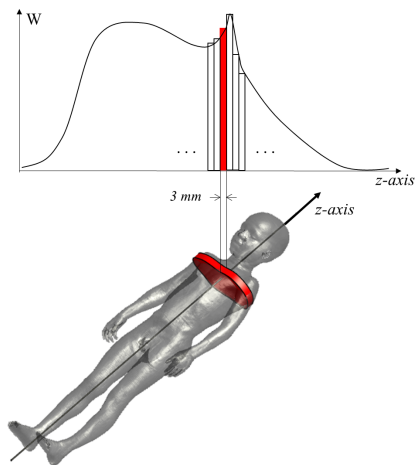


Figure 6.2: Calculation of the power absorbed in Thelonious along the longitudinal axis (z-axis).

The analysis was performed for the human body models Thelonious and Duke landmarked at the Pelvis and at the Heart. The head and knee landmarks were additionally studied for the homogeneous human body model Duke .

The RF power deposited in the models was computed along the longitudinal axis (z-axis) for each slice of the model defined by its numerical resolution (i.e., 3 mm, see figure 6.2). All the results were normalized: i) by imposing B_1^+ RMS equal to 3 μ T in the central axial slice of the model, and ii) by imposing the whole body averaged SAR equal to 2 W/kg. Both the heterogeneous and homogeneous human models were exposed to the same RF field generated by the RF coil described in section 2 and fed in quadrature.

(a) *Pelvis*

	Thelonious		Duke	
	Homog.	Heterog.	Homog.	Heterog.
Total profile power (W)	10.1	8.6	60.3	57.1
Weight (kg)	18.3	18.3	68.6	70.2
WbSAR (W/kg)	0.6	0.5	0.88	0.81

(b) *Heart*

	Thelonious		Duke	
	Homog.	Heterog.	Homog.	Heterog.
Total profile power (W)	9.1	7.7	70.9	65.9
Weight (kg)	18.3	18.3	68.6	70.2
WbSAR (W/kg)	0.5	0.6	1.0	0.9

Table 6.1: Data normalized with respect to the B_1^+ RMS. Integral of the RF absorbed power profile of figure 6.3, weight of the model considered, and corresponding WbSAR calculated for the model in the specific landmark.

The profiles of the RF absorbed power of the homogeneous model were similar but with higher values compared to the ones of the heterogeneous models, for both human models in the two landmarks (figure 6.3). However the profile calculated with the heterogeneous models were more jagged due to the presents of the organs of different

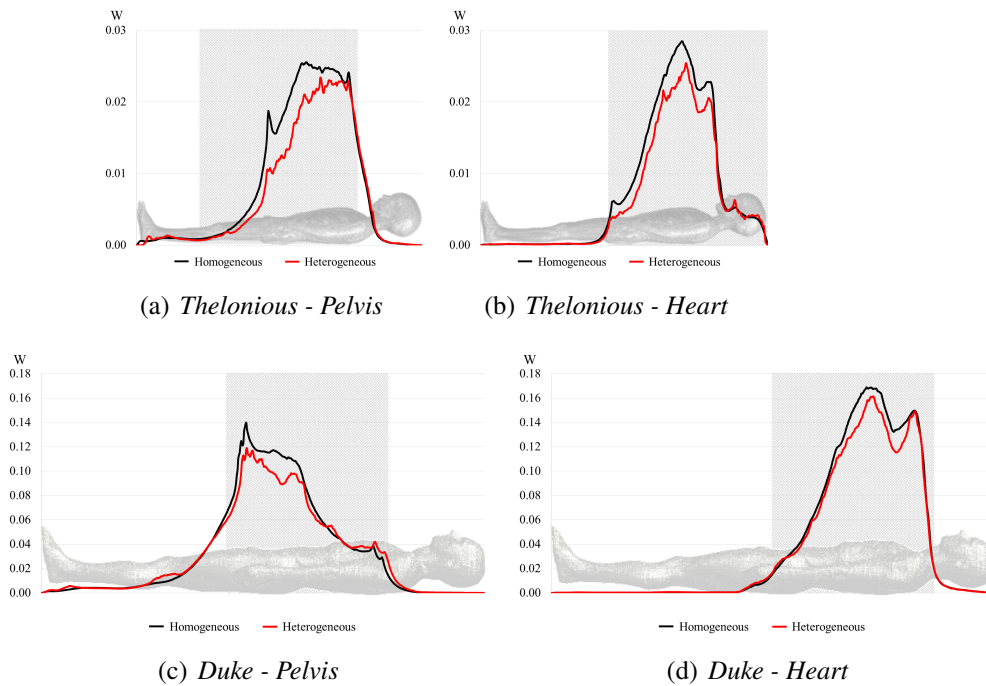


Figure 6.3: Data normalized with respect to the B_1^+ RMS equal to $3\mu T$. Profile of the RF absorbed power calculated along the z-axis (as in figure 6.2), for the human body model Thelonious and Duke landmarked at the Pelvis and Heart. The gray region identifies the area occupied by the coil.

tissue materials. For example, there was an observable difference near the knee region in Duke landmarked at the pelvis. The heterogeneous profile showed a peak at the level of the patella that was not present in the homogeneous model. This specific case can be explained because the eddy-currents produced by the varying B_1 field can concentrate at muscle/bone interfaces where peaks of power absorption occur (more details about differences due to body morphology will be given in the next section). The same was observed in Thelonious and Duke, where the peaks were observed close to the pubic bone and iliac crest. However, in Duke - landmarked at pelvis - peaks of power absorption were also due to different reason. Because the same peak was observed both for the homogeneous and heterogeneous Duke models, peaks of power abortion were also due to the concentration of the currents given by the specific shape. The same was observed for both models in the region near the neck for the heart landmark. It is of interest to notice that the profile in the heterogeneous Duke landmarked at the Pelvis showed a minimum at the center of the profile.

The RF absorbed power in Thelonious was 85 % lower than Duke, while the wb-SAR was 50 % lower. This because Thelonious weights 73 % less than Duke. Differences between the heterogeneous and homogeneous weights of table 6.1 is due to the presence in the heterogeneous model of the organs with different density, compared

6.1 Homogeneous vs heterogeneous models

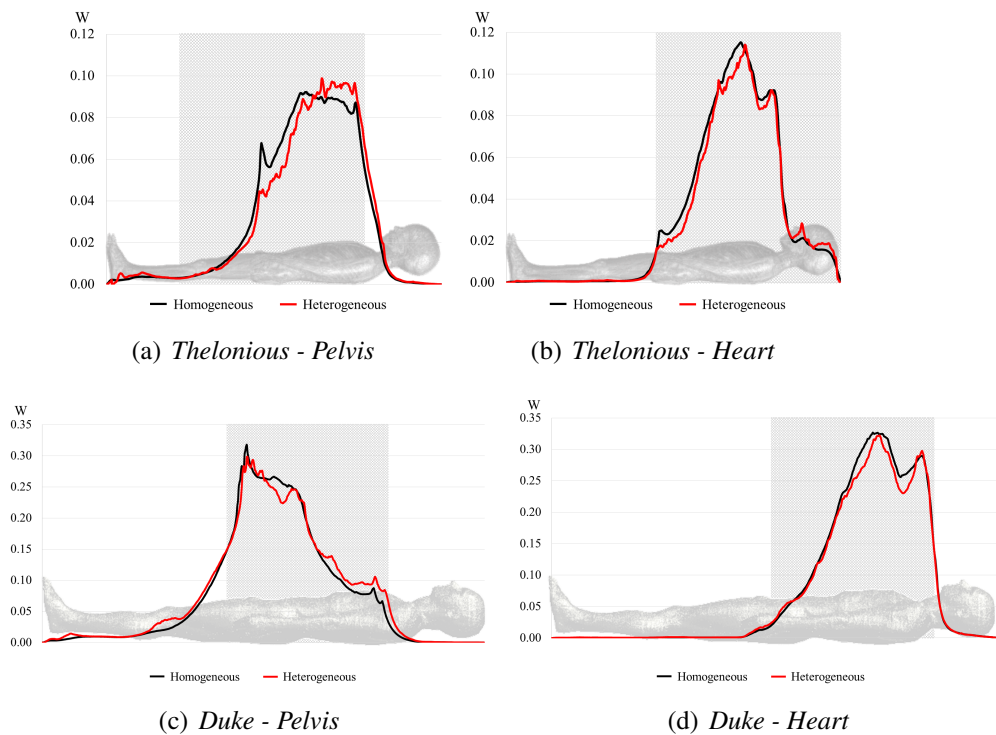


Figure 6.4: Data normalized with respect to the WbSAR. Profile of the RF absorbed power calculated along the z-axis (as in figure 6.2), for the human body model Thelonious and Duke landmarked at the pelvis and Heart. The gray region identifies the area occupied by the coil.

with the same density of the homogeneous model (i.e., $\rho = 1010$). Examples are the lumens of the organs (i.e., $\rho \sim 1.2$) or the lungs (i.e., $\rho = 394$).

As expected when the results were normalized with respect to the same wbSAR, the profiles of the homogeneous and heterogeneous models equalized (figure 6.4).

To better explain the dependency of the jagged profile with the body morphology, the eddy current profiles, and the power absorption was additionally studied for the homogeneous human body model Duke for the head and knee landmark. As reported in figure 6.5 the eddy-current induced by the B-field inside the model were highly affected by the model shape. For the central landmarks (i.e., Heart and Pelvis), the arms and legs highly affected the current distribution, as they are extremities not in contact with the body and between them. Thus the profile of the flowing eddy current was broken by the discontinuities of the body morphology.

As the homogeneous model was moved in the other two landmark positions (i.e., head and knee), the currents were more concentrated in the area of the body included in the coil region. An exception was found for the armpit region in Duke, with the knee landmark, where a higher concentration of currents was found (figure 6.6). Such results were also in line with the local peak of power absorption in the same region. As a comparison with the Pelvis landmark, the same peak in the pubic area was found

6.1 Homogeneous vs heterogeneous models

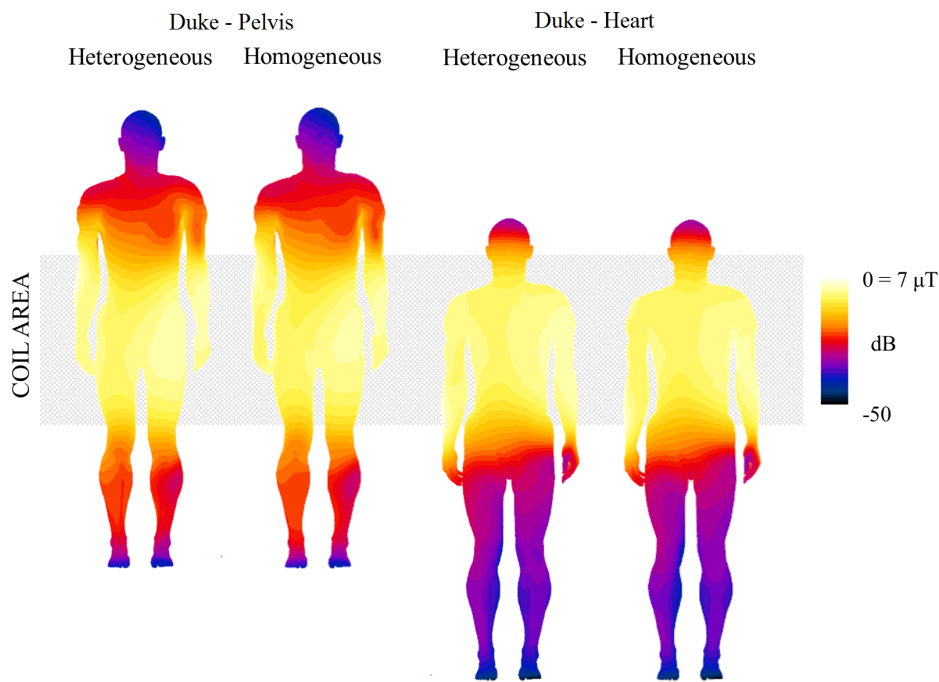


Figure 6.7: Magnetic field distribution on the external side of the heterogeneous and homogeneous Duke model for the two defined landmarks: pelvis and heart. The grey area defines the coil dimension. Data were normalized to B_1^+ RMS equal to $3\mu T$.

6.1.2 Electromagnetic field and SAR distributions

The analysis was performed for the human body model Duke landmarked at the Pelvis and at the Heart. Comparisons between the homogeneous and heterogeneous models was assessed analyzing the E field and SAR distribution, and computing the SMAPE of the E field and SAR distribution based on eq. 3.5.

All the results were normalized with respect to the B_1^+ RMS equal to $3\mu T$.

Both the heterogeneous and homogeneous human models were exposed to the same RF field as in the previous paragraph. Exposure was performed using the RF coil described in section 2 and fed in quadrature. Thus because the external shape of the models was the same, the magnetic field distribution was the same as shown in Figure 6.7. Differences between the two \vec{B} field distributions were less than 3 %.

As described by Faraday's equation (eq. 1.12), the induced electric field within the body depends on the radiated \vec{B} field. However different internal structure of the body would result in different eddy-currents pattern within the tissues, thus different E-field distribution would be observed. The overall distribution of the E field was similar with higher values on the side of the body in both landmark for the homogeneous model, and on the groin and low neck/shoulders for the pelvis and heart landmark for the heterogeneous model, respectively (figure 6.8a). The main differences characterized

the local behavior of the field that was affected by the tissue discontinuities in the heterogeneous model.

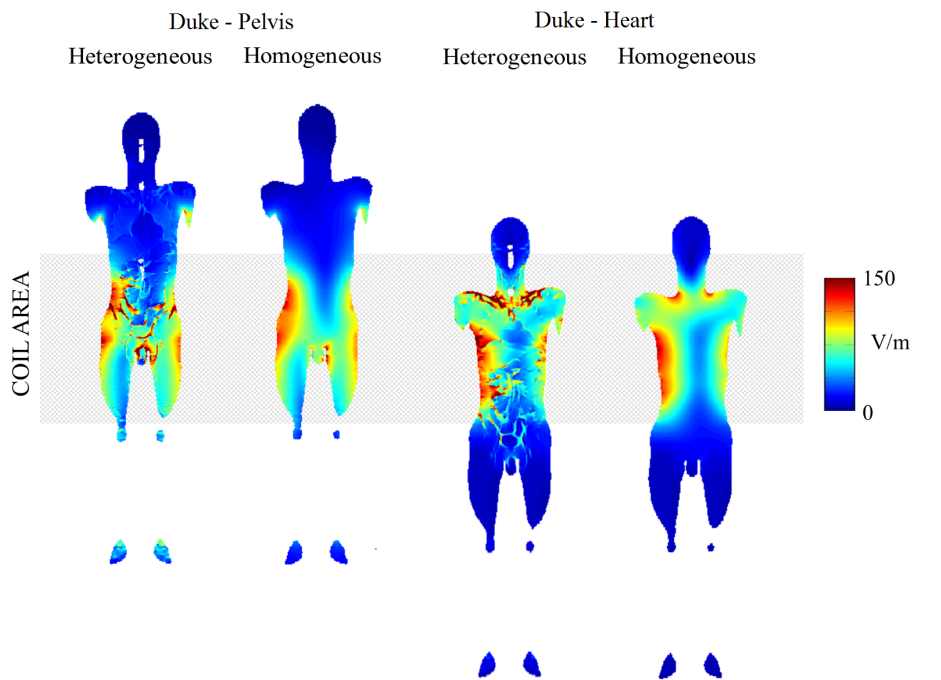
In the heterogeneous model the E field pattern is influenced by the tissue having different conductivity (σ) and permittivity (ϵ) values. The different conductivity would create charges at the interface of the two anatomical structures generating an higher E field inside the tissue with lower conductivity. Additionally because the permittivity is directly related to the electrical susceptibility, the tissues with a lower permittivity (such fat and bones) would show a higher E field. The two combined phenomena caused high level of E-field in the fat. The occurrence of this first phenomenon can be identified looking at the interaction between the liver and lung, where high E field would occur at the interface on the side of the lung that has the lower conductivity. Whereas the second phenomenon can be observed as the fat having an overall higher E field everywhere in the body, because it is the tissue with one of the lowest permittivity values. Results of SAR distribution (figure 6.8b) fantasize the differences between the two models. The SAR calculation directly depends on the conductivity value and tissue density (see eq. 5.1). In particular the conductivity plays a role in the fat were even high values of E field resulted in low values of SAR due to the low conductivity of the tissue ($\sigma = 0.06S/m$). A dependency on tissue density can be found comparing the anatomical structures liver and lung. In fact even if the liver conductivity ($\sigma = 0.45S/m$) is higher than the one of the lungs ($\sigma = 0.29S/m$), the density of the lungs are almost one third of the one of the liver ($\rho_{lung} = 394kg/m^3$, and $\rho_{liver} = 1078kg/m^3$). Hence the SAR in the lungs was approximately one third of the one in the liver, because the SAR is inversionally proportional to the density.

The SMAPE distribution of the E field and SAR summarized the overall differences between the homogeneous and heterogeneous model (figure 6.9). The distributions clearly identifies the internal organ of the heterogeneous model, as the homogeneous one was not able to reproduce the effect of interference due to the different tissues present. For the E field up to 60 % SMAPE was found in the small intestine in both models. Additionally with the pelvis landmark high values of SMAPE were found in the lungs and shoulders. Whereas in the Heart landmark peaks were found in the groin. As for the E field, the SMAPE of the SAR up to 150% was found in the small intestine and in the lungs. The high values of SMAPE of E field in the feet were due to the presence of small bones in the heterogeneous model.

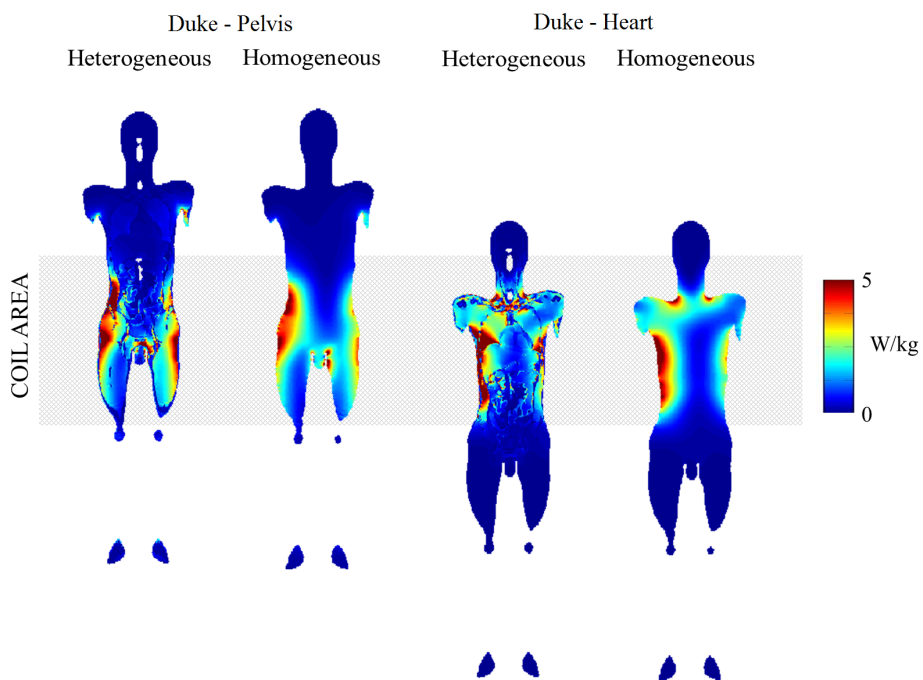
Differences between the results in the heterogeneous and homogeneous models can also be found comparing the maximum values of E field and SAR between the two models.

As reported in Table 6.2, in both landmark position the ratio between maximum

6.1 Homogeneous vs heterogeneous models



(a) *E-field*



(b) *SAR*

Figure 6.8: (a) Induced E field, and (b) SAR inside the heterogeneous and homogeneous Duke model in the central coronal plane ($x = 0$ mm), for the two defined landmarks: pelvis and heart. The grey area defines the coil dimension. Data were normalized to B_1^+ RMS equal to $3\mu T$.

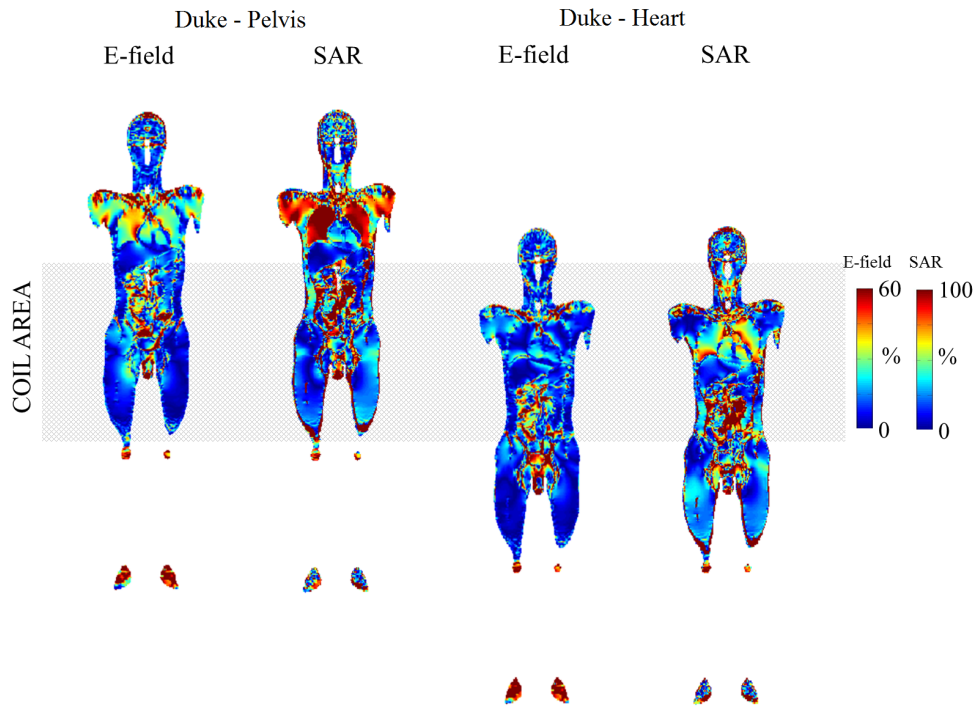


Figure 6.9: SMAPE distribution between the homogeneous and heterogeneous Duke models computed for the E field and SAR for the two defined landmarks: pelvis and heart. The grey area defines the coil dimension. Data were normalized to B_1^+ RMS equal to $3\mu T$.

		E field				SAR			
		Max	90 th	85 th	80 th	Max	90 th	85 th	80 th
		(V/m)	%	%	%	(W/kg)	%	%	%
Pelvis	Hetero	238	0.73	0.94	1.21	0.17	0.44	0.56	0.72
	Homo	154	2.11	3.58	5.8	5.53	1.23	1.66	2.24
Heart	Hetero	213	0.37	0.51	0.73	7.33	0.45	0.6	0.82
	Homo	144	2.42	3.9	5.94	5.17	1.03	1.39	1.89

Table 6.2: Maximum values and percentiles of E field and SAR for the heterogeneous and homogeneous model in the two landmark positions studied: pelvis and heart. The percentiles (90th, 85th, 80th) define the percentage volume of the body experiencing the value equal to the relative percentage of the maximum.

6.1 Homogeneous vs heterogeneous models

values of E field and SAR between the two models was always around 1.5 with highest values observed with the heterogeneous models. Highest peak values were observed in the heterogeneous models with respect to the homogeneous even if the power absorption profile observed in the previous paragraph was higher for the homogeneous one (see figure 6.3). This results reinforce the evidence that complex anatomical structures may generate high level of localized power absorption that cannot be account in homogeneous models. The effect of heterogeneity it is also shown by the results of percentile volumes extension (table 6.2). In the homogeneous model the percentiles were higher because there were no discontinuity in the propagation path of the fields. Thus the extension of the volumes are primary due to the profile of the induced E field and external body morphology.

The results of the study showed local differences of E-field, in particular near the interface between two structures of the heterogeneous model. The heterogeneity particularly affects the E field and SAR peak values, with the heterogeneous model showing an average of 55 % higher values. These results highlight the need of using realistic heterogeneous human body models to correctly characterize the peaks of E field and SAR. Electrically homogeneous models may underestimate the local absorption peaks generated by the presence of structures with different electrical parameters.

6.2 Impact of the vague partial body SAR definition in the MRI safety standard IEC 60601-2-33 on actual patient exposure

As² already discussed in section 5.1.1, specific standards define the limits to be followed during MRI procedures to guarantee a "safe" exposure to the patient undergoing an MRI scan. The standard reports that the RF power is controlled by either the whole body averaged SAR (WbSAR), the head averaged SAR (hSAR), or the partial body averaged SAR (PbSAR)(table 5.1).

Depending on the actual exposure – defined by the coil geometry, source placement, source driving conditions, the anatomy of the patient, and his/her imaging landmark position– the maximum allowed RF power is controlled by either the WbSAR, hSAR, or the PbSAR. While the hSAR is the limiting factor for landmarks closer to the head, the PbSAR usually plays a role for lower extremities of the body (from pelvis to feet).

As already described, the calculation of the PbSAR is related to the definition of the "*Patient mass within the effective volume of the RF transmit coil*" ($M_{ass_{exposed}}$ in eq. 5.4). Where the effective volume is determined by the 95% of power absorbed by the body. A suitable model to determine the effective volume of the coil, as suggested by the standard, is to simulate the patient's body by a variety of homogeneous phantoms loading the coil. However, the standard does not give any indication about the dimensions and material to be used. Herein the the variability of the PbSAR limit was quantified when using different geometries filled with three homogenous materials. In particular, in the first section two cylinders with extreme dimensions were used, whereas in the second section the first cylinders were compared with three uniform human body and their equivalent cylinders.

6.2.1 Partial body SAR limits estimation through cylinders

The study was performed using two numerical models of a transmit RF high-pass birdcage body coil driven in quadrature mode and operating at 64 MHz and 128 MHz with a diameter/length of 750 mm/650 mm and 750 mm/350 mm respectively. The 64 MHz coil was the same as the one already described in section . Conversely, the 128 MHz coil was the model used in [244].

The calculation of the effective volume of the coil, for the RbSAR calculation, was done for six cylinders with two different diameters (60 mm and 660 mm) and three different homogeneous materials (ASTM: $\sigma = 0.47S/m$ and $\varepsilon = 80$ [110], fat: $\sigma = 0.07S/m$ and $\varepsilon = 13.6$, and Cerebrospinal Fluid (CSF): $\sigma = 2.06S/m$ and $\varepsilon = 97.3$).

²Part of this paragraph was presented at the BioEM 2016 conference in Ghent, Belgium [252]

6.2 Impact of the vague partial body SAR definition in the MRI safety standard IEC 60601-2-33 on actual patient exposure

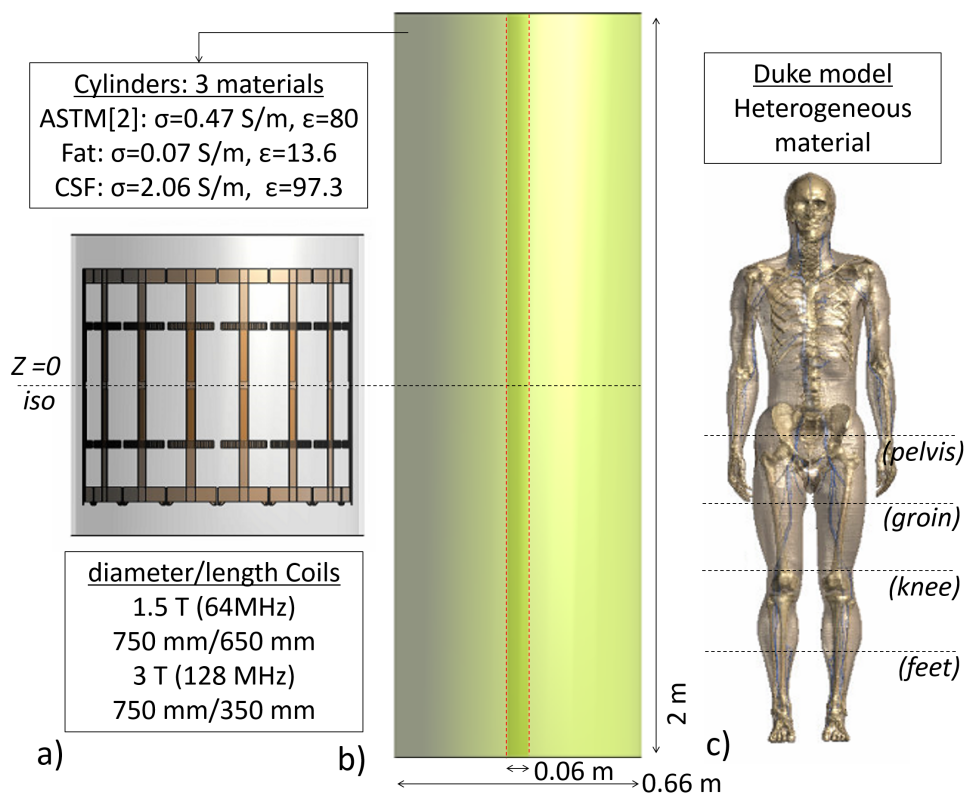


Figure 6.10: Numerical material used in the study: a) 64 and 128 MHz RF coil used (dimensions in the table); b) two cylinders used (materials in the table); c) "Duke" model with the four landmark position defined.

The simulation setup is summarized in Figure 6.10.

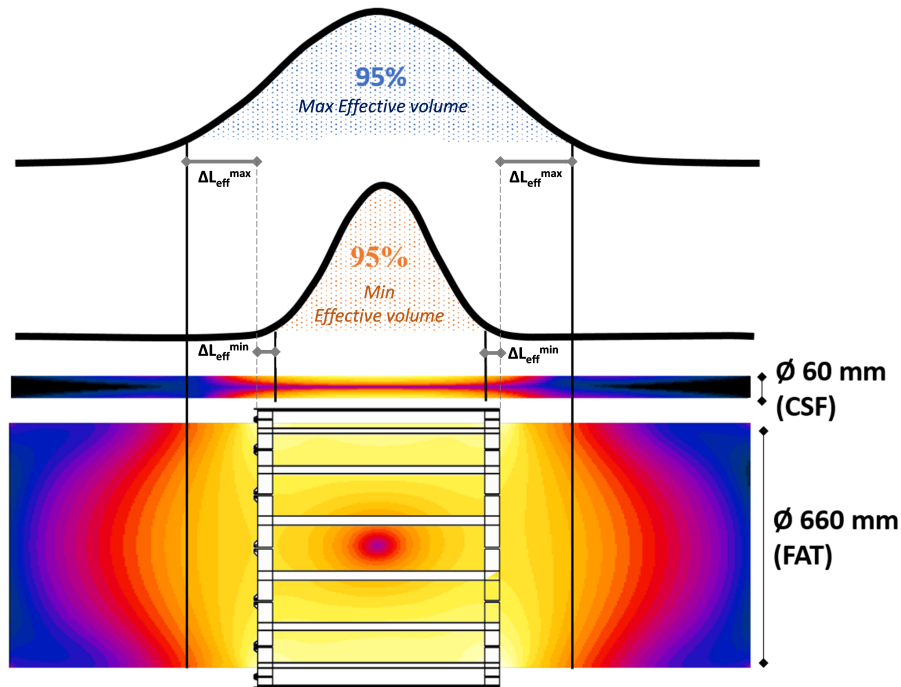


Figure 6.11: effective volume calculation for two different cylinders size and material. The "effective volume of the RF transmit coil" is defined as the volume of the coil in which no more than 95% of the total absorbed RF power is deposited. The effective volume is herein characterized using as parameter the ΔL_{eff} . For the 64 MHz coil the minimum effective volume was found for the 660mm cylinder made of FAT, while the maximum was found for the 60 mm cylinder made of CSF.

The effective volume calculation was based on the evaluation of the power absorbed by the model as already explained earlier in this chapter (figure 6.2). Herein the effective volume was characterized using as parameter the ΔL_{eff} , i.e., the distance between the edge of the effective volume and the end rings of the coil, as shown in figure 6.11.

Figure 6.12 shows that the ΔL_{eff} found for the six cylinders ranges from -0.02 m to 0.413 m considering both coils at 64 and 128 MHz. Despite what might be expected, the effective volume may be smaller than the volume physically occupied by the coil (i.e., $\Delta L_{eff} = -0.02m$).

The effective volume at both 64 and 128 MHz increases as the conductivity of the cylinder decreases, with the biggest volume found for the fat material and the smallest for the CSF.

6.2 Impact of the vague partial body SAR definition in the MRI safety standard IEC 60601-2-33 on actual patient exposure

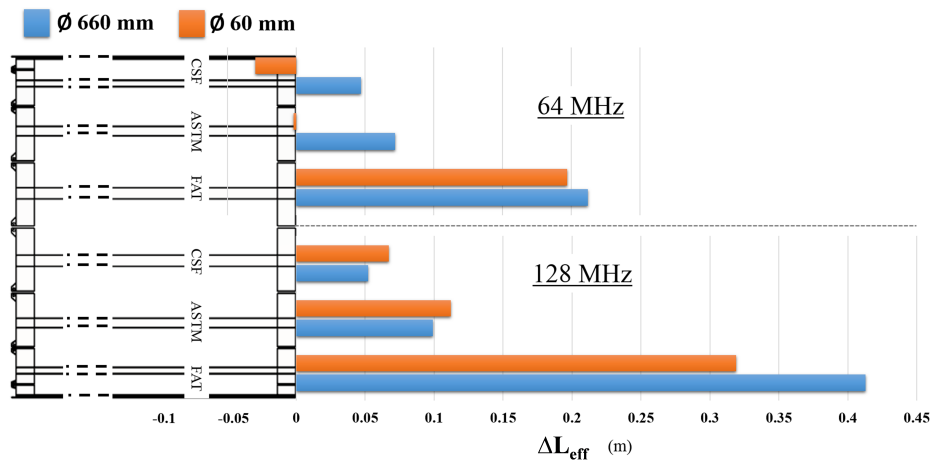


Figure 6.12: Results at 64 and 128 MHz of the ΔL_{eff} for the two cylinders used with different homogenous materials: CerebrospinalFluid (CSF): $\sigma = 2.06S/m$ and $\varepsilon = 97.3$, ASTM: $\sigma = 0.47S/m$ and $\varepsilon = 80$, and fat: $\sigma = 0.07S/m$ and $\varepsilon = 13.6$. The value 0 m denotes the end ring.

Contextualization of PbSAR limits for body exposure To contextualize the evaluation of the PbSAR in a model, the PbSAR limits for the human model "Duke" were computed for the range of exposed masses contained between ΔL_{eff}^{min} and ΔL_{eff}^{max} in 10 mm increments as in the equation 5.4. The analysis was performed at both 64 and 128 MHz with four imaging landmarks (coil centered at pelvis, groin, knees, and feet as shown in figure 6.10) where the PbSAR is expected to be the limiting factor.

The systematic analysis shows that different effective volumes result not only in different PbSAR safety limits but also indifferent effective exposure levels and WbSAR for the Duke model. Figure 6.13 shows an example of the calculated PbSAR limits and the resulting WbSAR at 128 MHz in knee landmark.

While the PbSAR limit decreases monotonically as the effective volume increases (see eq 5.4) – the WbSAR does not show a well-defined trend (Figure 6.13 a). Fluctuations of the WbSAR are caused by the inclusion – in the calculation of the average – of either hotspots or regions with lower SAR outside of the coil when considering longer effective volumes. Such behavior was observed for Duke, for example, when the coil was centered at the knees landmark and a hotspot was found on the groin outside of the coil (Figure 6.13 b). For this imaging landmark, the maximum fluctuation of WbSAR when considering different effective volumes was found to be 38% and 43%, at 64 and 128 MHz respectively, both in the first level controlled operating mode.

For this first analysis results showed that the definition of the effective volume leaves the PbSAR calculation open to different interpretations, generating inconsistent results, suggesting the need for a revision of the current definition in IEC 60601-2-33.

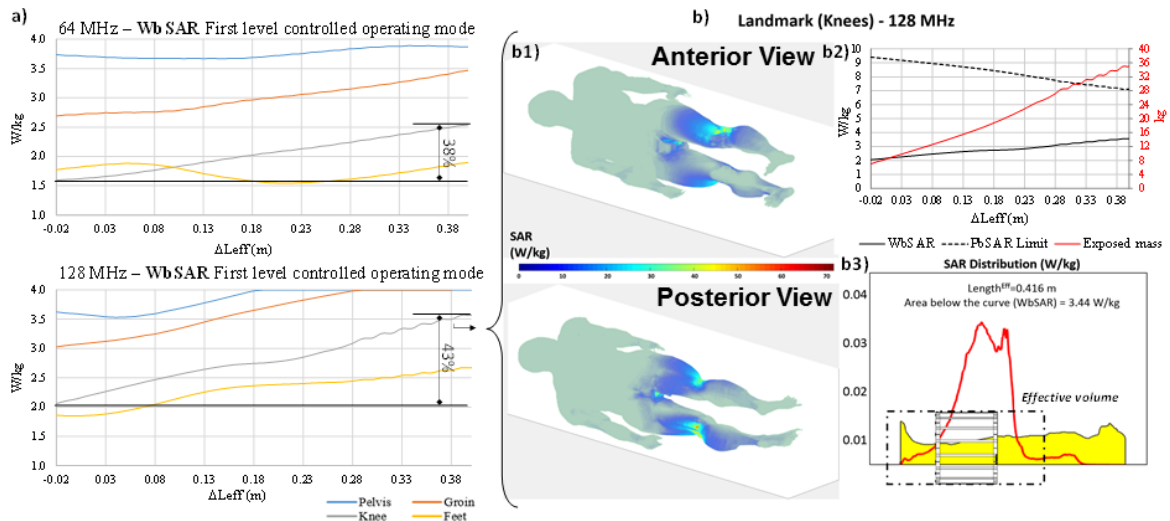


Figure 6.13: a) WbSAR distribution for Duke at the PbSAR limit for the first level controlled operating mode with respect to ΔL_{eff} at 64 and 128 MHz; b) Results for Duke in the landmark of the knees at 128 MHz. b1) 3D SAR distribution inside the model, hotspots are present in the model outside of the coil area (groin area); b2) profile of the WbSAR, PbSAR limit and the exposed mass with respect to ΔL_{eff} for the knee landmark at 128 MHz; b3) schematic of the calculated effective volume and SAR distribution inside the model.

6.2.2 Partial body SAR limits estimation through uniform human body models

The effective volume and the relative effective length ΔL_{eff} were also calculated loading the 64 MHz coil with three homogeneous models, based on Duke, Hugo, and Thelonious (as in section 6.1, see paragraph 1.4 for details about the human body models) filled with the three material used in the previous study (section 6.2). The three human body models were landmarked at the Pelvis. As a further step of comparison, simulations were also performed using other three cylinders each with length equal to the height of the each human body models, respectively, and with diameter equal to each of the three body models chest circumference (figure 6.14).

Results obtained with the new cylinders confirmed the overall message reported in the previous section, with the effective volume increasing with decreased conductivity of the cylinder material. Overall, the values of ΔL_{eff} found with the new cylinders were within the values obtained with the study in the previous section (figure 6.15). Hence, the strategy followed in the previous study correctly identified the entire variability range, with the smallest cylinder (i.e., 60 mm diameter) showing the shortest ΔL_{eff} , and the biggest cylinder (i.e., 660 mm diameter) showing the longest ΔL_{eff} .

However, including the new cylinders in between the sensitivity of the results with respect to the cylinder diameter was not straightforward. As shown by figure 6.15

6.2 Impact of the vague partial body SAR definition in the MRI safety standard IEC 60601-2-33 on actual patient exposure

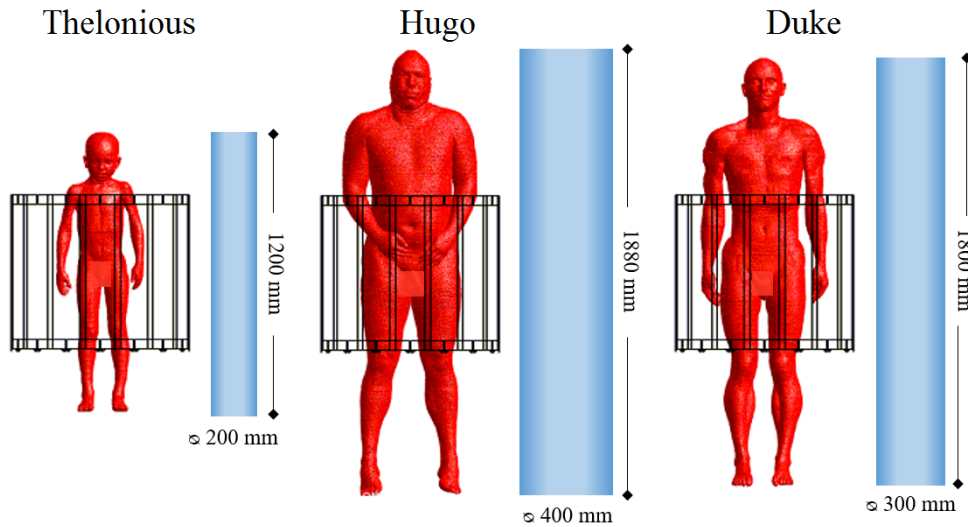


Figure 6.14: Uniform human body models Thelonious, Hugo and Duke loaded inside the coil model. Net to each model the relative cylinder used is also reported. Simulations were carried out for three materials: CerebrospinalFluid (CSF): $\sigma = 2.06$ S/m and $\varepsilon = 97.3$, ASTM: $\sigma = 0.47$ S/m and $\varepsilon = 80$, and fat: $\sigma = 0.07$ S/m and $\varepsilon = 13.6$.

the results of the ΔL_{eff} can not be directly related to the cylinder diameter. Values suggest that ΔL_{eff} increased with the decreasing of the diameter. This was against the assumption made with respect to the results based on 660 and 60 mm cylinders. However the new three cylinders differed not only in diameter, but also in the length. As reported in figure 6.14, the cylinder with the biggest diameter was also the longest one, and so on. Thus the different behavior of results with respect to the 660 and 60 mm cylinders (figure 6.15) is due to the different cylinders length. In particular results suggested that ΔL_{eff} was inversely proportional to the length of the cylinder studied.

When comparing ΔL_{eff} results of the cylinders with the one of the uniform human body, values were up to 95 % higher (i.e., Hugo - CSF). As reported in figure 6.16,

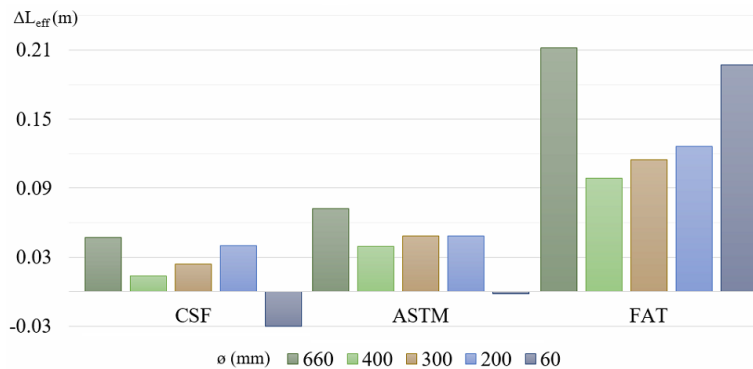


Figure 6.15: Summary of the ΔL_{eff} obtained with the two cylinders studied in the previous section (Φ : 660 mm, 60 mm) and the three used in this study (Φ : 400 mm, 300 mm, and 200 mm). Results are reported for the three tissue materials used.)

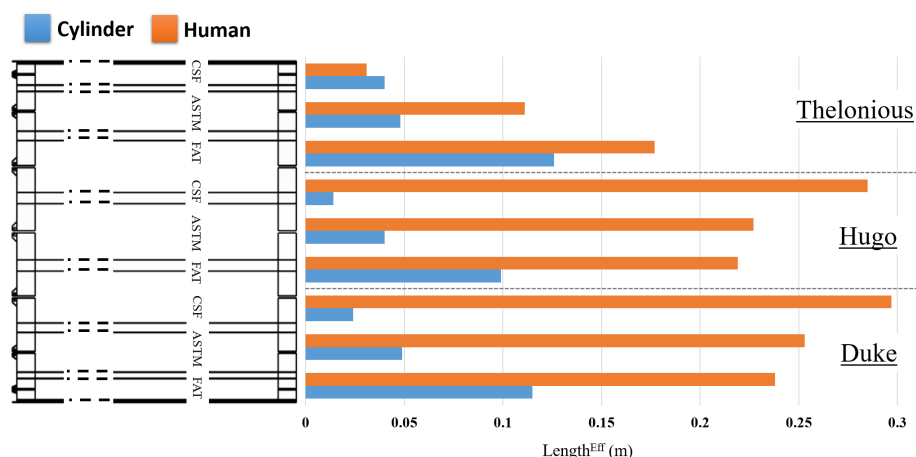


Figure 6.16: Results of the ΔL_{eff} for the cylinders (in blue) and uniform human body (in orange) with respect to the different homogenous materials: CerebrospinalFluid (CSF): $\sigma = 2.06S/m$ and $\varepsilon = 97.3$, ASTM: $\sigma = 0.47S/m$ and $\varepsilon = 80$, and fat: $\sigma = 0.07S/m$ and $\varepsilon = 13.6$. The value 0 m denotes the end ring.

cylinders and uniform human body models showed a different variability range with respect to the geometry size. The ΔL_{eff} found for the three cylinders was comparable, with the shortest for the cylinder of Hugo made of CSF (i.e., 0.0136 m) and the longest for the cylinder of Thelonious made of FAT (i.e., 0.126 m). Conversely, with the human models the results of the three models were not within the same range with the lowest values found in Thelonious between 0.031 m and 0.177 m, and the highest found in Duke between 0.238 m and 0.297 m.

Differences between cylinders and uniform human body models were mainly due to variability of power deposition between them as shown in figure 6.17. While the cylinders showed a smooth profile with a peak close to the center and a constant gradient, the profiles of the uniform human models were very jagged in line with the results obtained in the previous paragraph (6.1).

The profile of absorbed RF power with the FAT material showed a peak of absorption near the side of the cylinder, due to the specific interaction of the RF wavelength and the conductivity of the material. As known, the wavelength in a medium differs from the one in vacuum, and it is depended on the medium permittivity ε_r and permeability μ_r with the following equation:

$$\lambda = \frac{c_0}{\sqrt{\varepsilon_r \mu_r} \cdot f} \quad (6.1)$$

where f is the frequency of the RF field and c_0 is the speed of light in the vacuum. Additionally the difference in the material conductivity σ affect the resulting

6.2 Impact of the vague partial body SAR definition in the MRI safety standard IEC 60601-2-33 on actual patient exposure

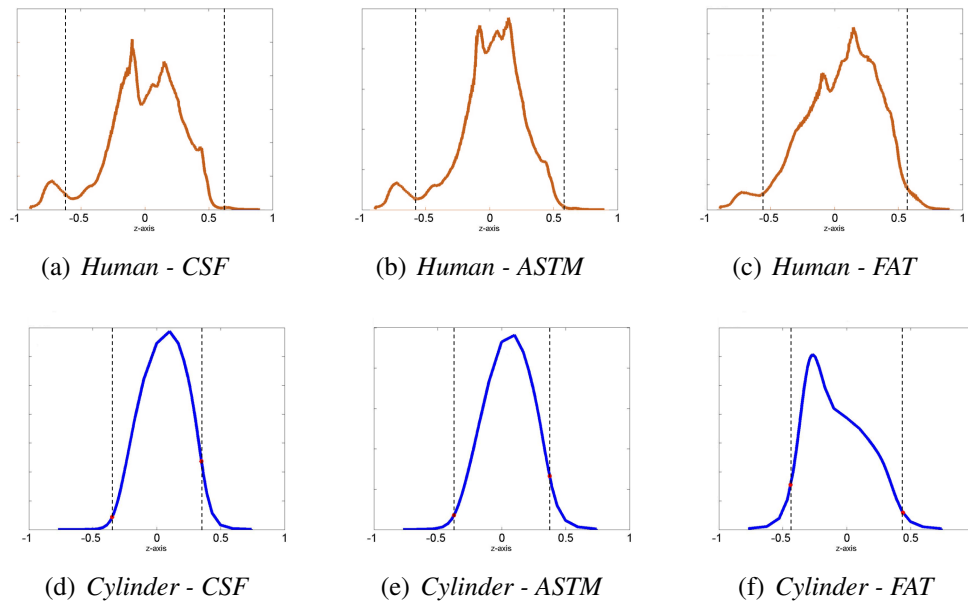


Figure 6.17: profiles of absorbed RF power for Duke (a-c) and the corresponding cylinder (d-e) for the three materials: CerebrospinalFluid (CSF): $\sigma = 2.06S/m$ and $\varepsilon = 97.3$, ASTM: $\sigma = 0.47S/m$ and $\varepsilon = 80$, and fat: $\sigma = 0.07S/m$ and $\varepsilon = 13.6$. The dotted lines indicate the length of the effective volume where 95% of the total absorbed RF power was deposited.

penetration depth (δ) in each cylinder, with the following equation:

$$\delta = \frac{1}{\sqrt{\pi f \sigma \mu}} \quad (6.2)$$

With respect to the three materials used in the study, the resulting wavelength inside the cylinder was 475 mm, 524 mm, and 1271 mm for the CSF, ASTM and FAT material respectively. Whereas the corresponding penetration depth was 44 mm, 92 mm, and 238 mm. Hence, both the wavelength and the penetration depth inside the FAT material was more than doubled with respect to the other two. The comparison of the values with respect to the cylinder size (i.e., 1800 mm long and 300 mm wide for Duke) suggests that possible standing waves occur as a result of constructive/destructive interference. In particular the FAT material differs from the other two, showing the longest wavelength and the highest penetration depth.

The effect of non uniformities of the field related to tissues properties was firstly observed by Glover et al. in 1985 [26] that studied the RF field nonuniformities in cylinder of different length and material. Glover and colleagues observed that nonuniformities patterns depended on the size of the object relative to the field wavelength, and that the dielectric standing wave effects, modified by eddy currents, can produce substantial RF field nonuniformities. They also observed that nonuniformities are most predominant at highest frequency and largest diameter. What was observed by Glover

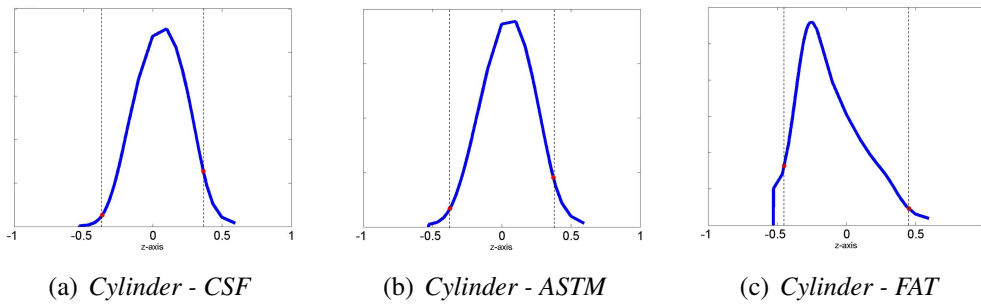


Figure 6.18: profiles of absorbed RF power for Thelonious corresponding cylinder (d-e) for the three materials: CerebrospinalFluid (CSF): $\sigma = 2.06S/mand\varepsilon = 97.3$, ASTM: $\sigma = 0.47S/mand\varepsilon = 80$, and fat: $\sigma = 0.07S/mand\varepsilon = 13.6$. The dotted lines indicate the length of the effective volume where 95% of the total absorbed RF power was deposited.

and colleagues is in line with the results on this study showing nonuniformities when comparing results with the FAT material in the three cylinder. While cylinders of Duke (figure 6.17) and Hugo showed higher nonuniformities, results with the cylinder of Thelonious showed a more homogeneous profile (figure 6.18). This showed the dependency profiles of absorbed RF with the cylinder size already reported by Glover et al. [26].

The results of this study can be contextualized with respect to the analysis of the different ΔL_{eff} for the evaluation of the PbSAR limits performed in the previous paragraph (section 6.2). What was herein found underlines that it is not possible to identify a specific length to define the worst case PbSAR. Thus the definition of the effective volume leaves the analysis open to different interpretations. The broad range of results may generate vague SAR limits, and differences with landmark positions, hence future work is needed to standardize the calculation of the PbSAR.

Chapter 7

A Numerical Investigation on effect of RF coil feed variability on global and local electromagnetic field exposure in human body models at 64 MHz

The text from paragraph 7.1 to paragraph 7.6 was submitted as it is to the journal Magnetic Resonance in Medicine [170]. It is currently under the second stage of revision. For this reason concepts and definitions maybe already previously discussed in this thesis. A first stage of this work was also presented as conference paper for the 2016 IEEE Engineering in Medicine and Biology Society [253]. The work was performed in collaboration with the DBP/CDRH/OSEL of the FDA (MD-USA) as part of Cooperative Research and Development Agreement with Imricor Medical Systems (MN-USA).

Paragraphs 7.7, 7.8, and 7.9 have been included in this thesis in addition to the original paper. The sections report additional results as supporting material to the original paper, and the extension of the analysis presented in the paper to the exposure of the superellipsoidal phantom.

7.1 Abstract

Purpose : This study aims to investigate how the positions of the feeding sources of the transmit RF coil, feed phase orientation with respect to the patient, and patient dimensions affect the global and local electromagnetic exposure in human body models.

Methods : Three excitation approaches of the RF coil were analyzed: S2, G32, and H16. 32 feeding conditions were studied for the S2, whereas two for the G32 and H16. The study was performed on five human body models. Additionally, a specific case

A Numerical Investigation on effect of RF coil feed variability on global and local electromagnetic field exposure in human body models at 64 MHz

study with a partially implanted lead was analyzed.

Results : The results showed an overall variation of the whole-body specific absorption rate of less than 20 %, but deviations up to 98% of the magnitude of the electric field tangential to a possible lead path. For the case study, a variation of local SAR at the tip of the lead of up to 60% was observed with respect to feed position and feed phase orientation.

Conclusion : The results of this study suggest that specific information about feed position and feed phase orientation need to be taken into account for an accurate evaluation of patient exposure.

7.2 Introduction

Magnetic resonance imaging (MRI) is a widely used diagnostic imaging technique which employs radio-frequency (RF) waves at Larmor frequencies to produce images. The exposure of the patient to the RF field during MRI is limited by specific guidelines [123]. In commercial MRI systems the exact conditions of the RF coil excitation (e.g., feed position, feed phase orientation) with respect to the patient are often unknown. It is expected that variation of RF coil excitation may result in variation of RF exposure in the body and the related possible RF-induced heating of tissue [254].

RF-induced heating may worsen in the presence of electrically conductive devices that are fully or partially implanted or in contact with the patient due to the “antenna effect” of the device [37, 111, 241, 255]. Computational modeling has been increasingly used to complement experimental results to evaluate RF energy absorption near electrically conductive devices. The Technical Specification (TS) ISO 10974 [111] describes a methodology to computationally assess the exposure of devices fully implanted in the body. In particular, the document states how the study of a system in the meters range (i.e., the RF coil) including an object in the μm range (i.e., implant lead) implies a high computational cost when using computational approaches based on finite-difference time domain (FDTD) method. An interesting solution included in the TS (i.e., “Tier 3 approach”) is the use of the so called “transfer function”, first proposed by Park et al [241]. This approach consists of decoupling the problem of the lead sensitivity (i.e., transfer function) with respect to the electric field incident to the lead from the effective exposure level. The power deposited in the tissue surrounding the lead tip can be computed by multiplying the transfer function of the specific lead with the incident electric field tangential to the lead. The Tier 3 approach has been used by several studies [37, 124, 256–258], all limited however to fully implanted devices.

7.3 Methods

Currently, there is no standardized methodology to assess RF exposure in patients with partially implanted devices during MRI. MRI systems have been used beyond diagnostics to guide or track devices for real-time interventional procedures (interventional MRI or iMRI) [165, 259, 260]. When used to monitor catheters insertion inside the patient, such as in cardiac ablation or diagnostic catheterization, iMRI requires the presence of partially implanted leads. Evaluation of RF exposure in patients with partially implanted leads is further complicated because a portion of the catheter is outside of the body, where the electric fields may be high in magnitude and strongly influenced by the coil design and coil excitation [129].

This study aims to assess how the numerical model complexity and coil excitation variability may affect patient exposure. Variability of global and local exposure was studied for five human body models landmarked at the heart inside the RF coil. Additionally, for two of the five models, a case study was performed evaluating the local exposure with a generic lead partially implanted inside the body. Numerical model complexity was performed by using three excitation approaches of the coil. The three RF coil models included a two-port feed (S2) and two multi-port feed configurations (G32 and H16). Coil excitation variability was studied by evaluating the feed phase orientation for all the three models and the feeding source position for the S2 model only.

7.3 Methods

7.3.1 Computational models of RF transmit coils

Electromagnetic (EM) field simulations were implemented using the commercially available FDTD software Sim4Life V2.2 (ZurichMedTech, Zurich, Switzerland). The numerical CAD model of a high-pass RF transmit body coil at 64 MHz was implemented based on the MITS1.5 system available at the FDA laboratories as previously described in Lucano et al. [129] and briefly recalled here. The coil is composed of 16 rectangular strips (rungs) connected at each end by two end-rings and shielded by a 16-sided regular polygonal enclosure Figure 7.1a. Both the coil and the shield were modeled as perfect electric conductors (PEC).

Simulations were implemented following three excitation approaches (Figure 7.1) able to generate an accurate EM field distribution within the phantom loading the coil [129]. In the first model (S2), the coil excitation represented a dual port quadrature driven coil with lossy components (i.e., a resistor and a capacitor in parallel, $C = 70\pi F$ and $R = 1k\Omega$) distributed in the coil end-rings. The second (G32) and third (H16) model, extensively used in literature, were simplified models with a multi-port feeding

A Numerical Investigation on effect of RF coil feed variability on global and local electromagnetic field exposure in human body models at 64 MHz

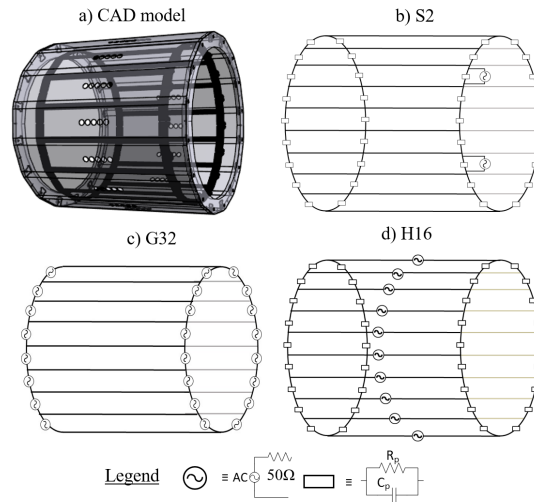


Figure 7.1: Electrical characterization of the RF coil models (a) 3-D view of the computational model. The computational RF body coil system was modeled to match the physical coil geometry. (b) specific two-source model (S2), (c) generic 32-source model (G32), (d) hybrid 16-source model (H16).

excitation. The G32 used 32 generic feeding sources distributed along the coil end-rings without any lossy components [261]. The H16 model was based on a “hybrid” approach using 16 feeding sources distributed within the middle of the rungs, and it included the same lossy components as the S2 model [78]. For all the models, the feeding sources were composed of an ideal voltage source with a resistor of 50Ω in series.

7.3.2 Models of the human body

Five anatomically precise human body models, all part of the virtual population ViP 3.0 [97, 100] were used to model a broad range of patient variability. The models included two females (i.e., “Ella” and “Billie”) and three males (i.e., “Glenn”, “Duke”, and “Fats”), age range from 11-year-old (i.e., “Billie”) to 84-year-old (i.e., “Glenn”) and body mass indexes (BMI) from 15.3 (“Billie”) to 36.1 kg/m^3 (“Fats”). The position of each human body model within the RF coil was landmarked at the heart (i.e., heart at the isocenter of the coil) in line with clinical scenario of heart imaging during iMRI (Figure 7.2a). The physical properties (i.e., electrical conductivity and permittivity, and mass density) of the anatomical structures of each model were based on existing literature for the specific frequency used (i.e., 64 MHz) [251].

7.3.3 Excitation variability

The human body exposure to the EM fields was studied with respect to coil excitation variability. With the G32 and H16 coil models, the field exposure variability was studied with respect to feed phase orientation:

$$\Delta\varphi = CW \wedge CCW \quad (7.1)$$

Specifically, the variability of $\Delta\varphi$ was imposed with respect to the patient by keeping the same current profile along the coil (i.e., same phase difference between the feeding sources) and loading the human body model either “head-first” for clockwise (CW) orientation or “feet-first” for counter-clockwise (CCW) orientation. In this way, the coil was proven to produce a B_1^+ field component always higher than the B_1^- by keeping the same coordinate system of the ideal static field (B_0). Conversely, if the $\Delta\varphi$ would have been obtained by switching the phase orientation of flowing currents inside the coil, the z-axis orientation of the coordinate system should have been reversed accordingly to ideal static field (B_0) to allow the prominence of B_1^+ over B_1^- .

With the S2 coil model, a total of 32 excitations were defined by varying feed phase orientation, as in [123], as well as feed position within the coil (i.e., 16 positions, 8 for each ring – see Figure 7.2b) as follows:

$$\Delta\pi = \begin{cases} \alpha \in 22.5^\circ : 45^\circ : 337.5^\circ \\ ring : Head \wedge Feet \end{cases} \quad (7.2)$$

Where α identifies the central angle for each pair and $\Delta\pi$ indicates position variability (Figure 7.2), implemented by rotating the 2-feed pair of 45° all around each of the two end-rings of the coil. EM field propagation for the G32 and H16 coil models was implemented by forcing the currents along the rings of the coil. This was done by exciting each feeding source with a sinusoidal signal at 64 MHz following a well-defined phase shift profile around the coil as reported in [129]. This procedure was the same both without and with the lead present.

Conversely, EM field propagation for the S2 coil model was numerically computed following two approaches for the simulations, namely without and with the lead. Without the lead each feeding source of the pair was excited by a broadband signal centered at 64 MHz with a frequency band of 150 MHz. For the purpose of field extraction, results were post-processed and combined imposing the same signal amplitude and a phase shift of 90° at the two feeds. This procedure allowed researchers to implement a patient exposures database where results could be post processed anytime imposing variable amplitude and a phase shift at the two sources. This process was performed using a feature embedded within the Sim4Life software. When the lead was included

A Numerical Investigation on effect of RF coil feed variability on global and local electromagnetic field exposure in human body models at 64 MHz

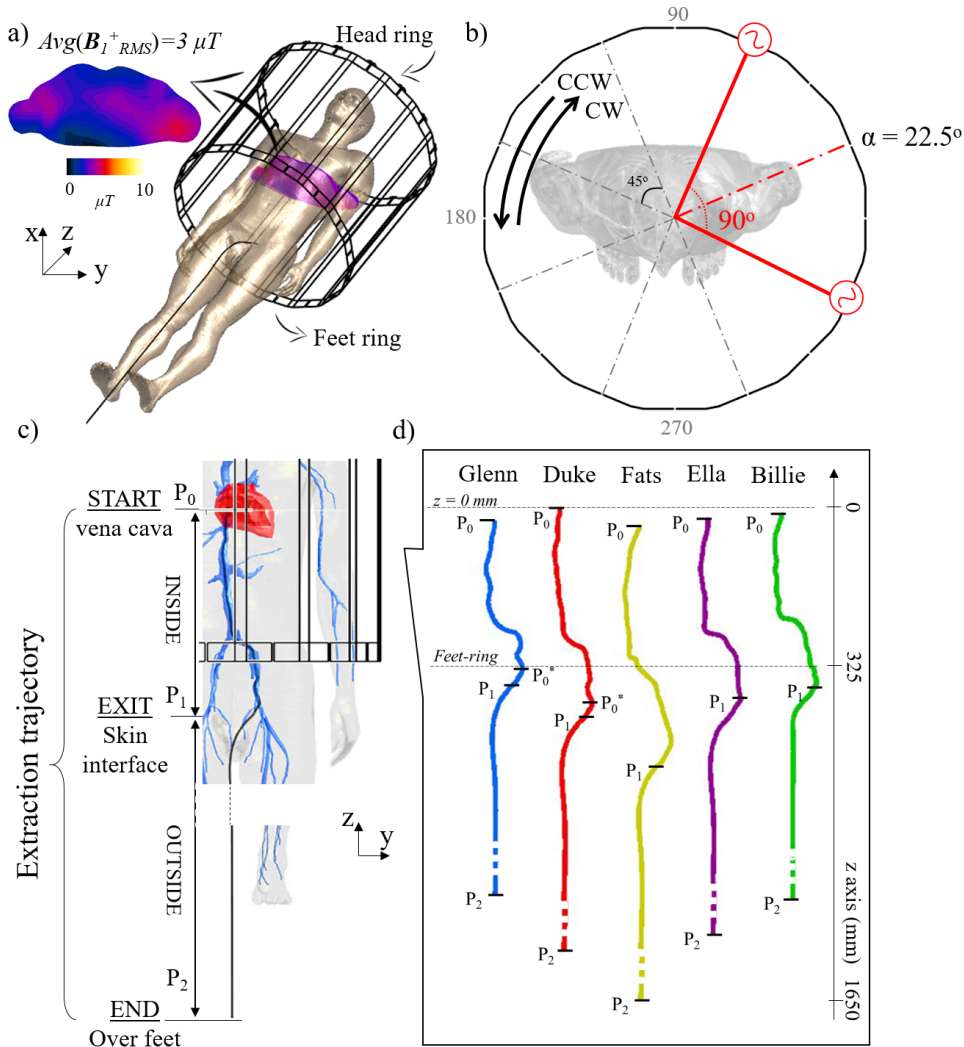


Figure 7.2: Numerical setup and data analysis definition. (a) Human body model Duke loaded in the RF coil landmarked at the heart with a generic catheter partially implanted at the groin. The B_1^+ RMS at the central axial slice for the area occupied by the body is shown. All the numerical results were normalized based on the B_1^+ RMS average equal to $3 \mu T$ in the selected area. Head and feet end-rings are defined. (b) S2 feed rotation within the coil end-ring where α defines the central angle of the two feeds at 90° used as exciting sources in the simulations. The feed phase orientation (CW and CCW) is also shown. A total of 32 feeding conditions were studied with the S2 coil model. (c) Extraction line trajectory shown both inside (P0-P1) and outside (P1-P2) the body for the Etan evaluation. (d) Extraction line trajectories for the five human body models used for the analysis. P0* indicates the point corresponding to the tip of the implant used in the case study.

7.3 Methods

in the model, the two feeds of each pair were simultaneously excited by a sinusoidal signal at 64 MHz with the two signals of the same amplitude but 90° out of phase.

All simulation results were normalized to an average $B_1^+ RMS$ field of $3\mu T$ within the human body model under test in the central axial slice (Figure 7.2b). This normalization was chosen according to the value suggested by the IEC [123].

7.3.4 Quantities of interest

The quantity of interest for evaluating global exposure of the human body model was the whole body average SAR (WbSAR). The WbSAR variability was analyzed with respect to $\Delta\pi$ (S2 only) and $\Delta\varphi$. The analysis was performed with the five human models under test (i.e., inter-subject) defining an inter-patient variability. This allowed researchers to characterize the level of exposure with respect to the human model when using a normalization based on the $B_1^+ RMS$.

The quantities of interest for evaluating local exposure were the local peak 10gSAR and the electric field tangential to a predefined trajectory (E_{tan}) [123]. The peak 10gSAR was evaluated for the five human body and the variability was analyzed with respect to $\Delta\pi$ (S2 only) and $\Delta\varphi$. Both magnitude and phase of the E_{tan} were extracted as the quantities affecting the induced currents along the lead [262]. For each model, the selected trajectory was both inside (P0 to P1) and outside the body (P1 to P2) (Figure 7.2c). The section inside the body was drawn along the vein path from the inferior vena cava down to the left femoral vein, and out from the vein at the groin. The section outside was drawn along the legs to mimic a possible catheter path which was the same for all models. Figure 7.2d reports the trajectories for the five human bodies used. Variations of extraction trajectory were due to differences in body morphologies, namely: i) length of the trajectory section inside the body; and consequently ii) P1 location, which was at different coordinates with respect to the coil. The extraction of E_{tan} magnitude ($\|E_{tan}\|$) and phase ($\angle E_{tan}$) was performed using the IMSAFE tool embedded inside the Sim4Life software. Finally to correlate the sensitivity of the E_{tan} to $\Delta\pi$ (S2 only) and $\Delta\varphi$ with power dissipation on a lead along the same path, an example including a theoretical simplified transfer function applied the E_{tan} data of the human body models was implemented.

A case study including the model of a partially implanted lead was performed with two of the human body models (i.e., Glenn and Duke). The local exposure was studied for the power absorbed in the tissue near the lead tip. Hence, the quantitative parameters were related to the local SAR identified by the SARtip as local unaveraged SAR (μSAR), 0.1g average SAR (0.1gSAR), 1g average SAR (1gSAR), and 10g average SAR (10gSAR). The computation of the averages SAR was performed using the inter-

A Numerical Investigation on effect of RF coil feed variability on global and local electromagnetic field exposure in human body models at 64 MHz

nal algorithm embedded in the Sim4Life software at the same location for all averages.

7.3.5 Computational model of partially implanted lead

The lead consisted of a 1.19 ± 0.01 m long partially insulated wire (i.e., 2 mm diameter with a 0.5 mm insulation) with a 7 mm bare tip (P0*-P2 in Figure 7.2d). The lead was inserted in the body at the groin region terminating in all models 40 mm inside the body by the left femoral vein. The position of the lead was in line with the initial stage of a catheterization. Within the numerical environment, the wire was modeled as a perfect electric conductor (PEC), and the insulator as teflon ($\sigma = 4.6e - 3S/m$, $\varepsilon = 2.08$).

7.4 Results

7.4.1 Global exposure

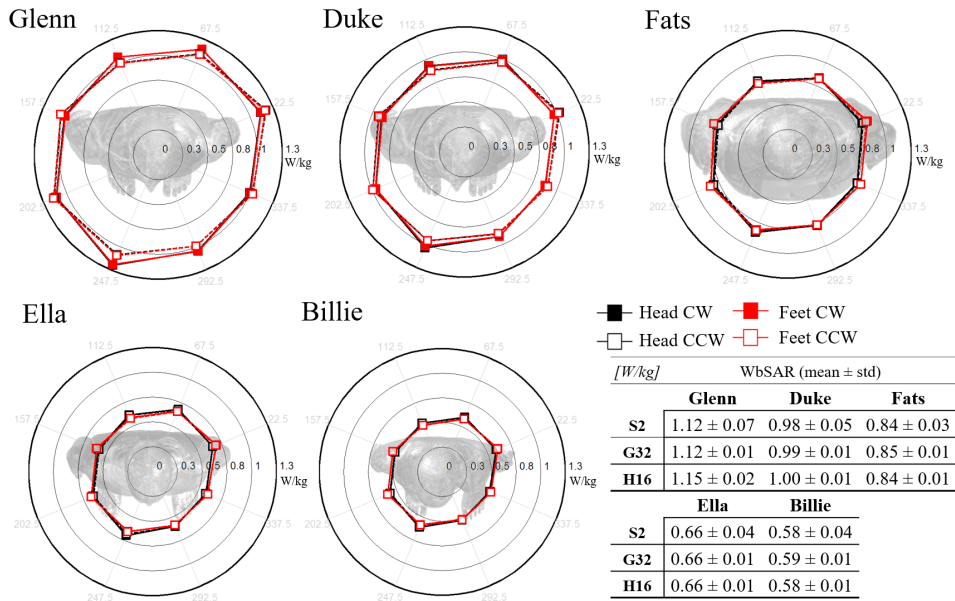


Figure 7.3: WbSAR results for the five human body models used for the analysis. The radar plots report the values with respect to $\Delta\pi$ and $\Delta\varphi$ for the S2 model. The bold external circle indicates the coil with each human body model inside plotted in scale. The table reports the WbSAR mean and standard deviations with respect to all the variables: $\Delta\pi$ and $\Delta\varphi$ for S2 and $\Delta\varphi$ for G32 and H16.

All the models showed WbSAR values lower than $2 W/kg$ with the selected normalization, the safety limit in the Normal Operating Mode with the selected normalization [123]. Additionally, results for the S2 showed less than 20% variability of

7.4 Results

		Glenn	Duke	Fats	Ella	Billie
WbSAR	$\Delta\pi$	18.7%	16.6%	12.7%	18.0%	17.5%
	$\Delta\varphi$	9.5%	7.3%	2%	1.4%	0.8%
$\ E_{tan}\ $	$\Delta\pi$	64%	92%	86%	93%	93%
$P_0 - P_2$	$\Delta\varphi$	93%	96%	93%	98%	98%
SAR_{tip}	$\Delta\pi$	49%	50%	-	-	-
	$\Delta\varphi$	51%	60%	-	-	-

Table 7.1: Global and local exposure percentage change with respect to $\Delta\pi$ and $\Delta\varphi$ (S2 model only). WbSAR and $\|E_{tan}\|$ along the entire trajectory (P0-P2) for the five human models studied. SAR_{tip} peak results are reported only for the two human body models selected for the case study

WbSAR with respect to either $\Delta\pi$ or $\Delta\varphi$. Figure 7.3 reports the WbSAR values observed for each human body under test with respect to: i) $\Delta\pi$ and $\Delta\varphi$, for the S2 coil (see radar plot), and ii) $\Delta\varphi$ for the G32 and H16 models (table). The radar plot reports the WbSAR relative to the specific feeding source pair identified by polar angle of the plot (i.e., internal angle α of the two feeds, Figure 7.1b). Inside each radar plot, the relative human model under test is reported in scale with the coil profile identified by the external bold circle in black. The radar plot representation of results allows for an immediate estimation of $\Delta\pi$ variability, as the closer the distribution to a circular shape, the less $\Delta\pi$ variability is present.

The intra-subject variability of WbSAR ranged between 12.7 % and 18.7 % with respect to $\Delta\pi$ and between 1% to 10% with respect to $\Delta\varphi$. Table 7.1 shows the maximum percentage WbSAR variability observed within each body model relating to $\Delta\pi$ and $\Delta\varphi$. The highest intra-subject variability was observed within Glenn both with respect to $\Delta\pi$ and $\Delta\varphi$. Additionally, the inter-subject variability was up to 57%, with maximum WbSAR obtained with Glenn and minimum WbSAR obtained with Billie.

With the G32 and the H16 models, WbSAR values were similar to the ones obtained with S2 model (Figure 7.3, table), but with a smaller standard deviation due to variability only related by design to $\Delta\varphi$. When comparing the results obtained with G32 vs. H16 there was less than 2% variability.

7.4.2 Local exposure

Results showed that the location of the 10gSAR peak varied for each body model (e.g., in the neck with Duke, lateral middle chest with Glenn). Moreover, the specific location of the peak 10gSAR for each model was independent with respect to $\Delta\varphi$, whereas with $\Delta\varphi$ it was specular with respect to the longitudinal axis of the body (z-axis). Peak 10gSAR values ranged from 6.6 W/kg in Billie to 15.4 W/kg in Glenn

A Numerical Investigation on effect of RF coil feed variability on global and local electromagnetic field exposure in human body models at 64 MHz

and Fats. The intra-subject variability ranged between 30.4 %– in Duke – and 47.1 %– in Ella –with respect to $\Delta\varphi$, and between 0.2 % – in Duke – to 39.6 % – in Glenn – with respect to $\Delta\varphi$. See the Supporting Materials (Sup. Fig. S1) for the full range of values.

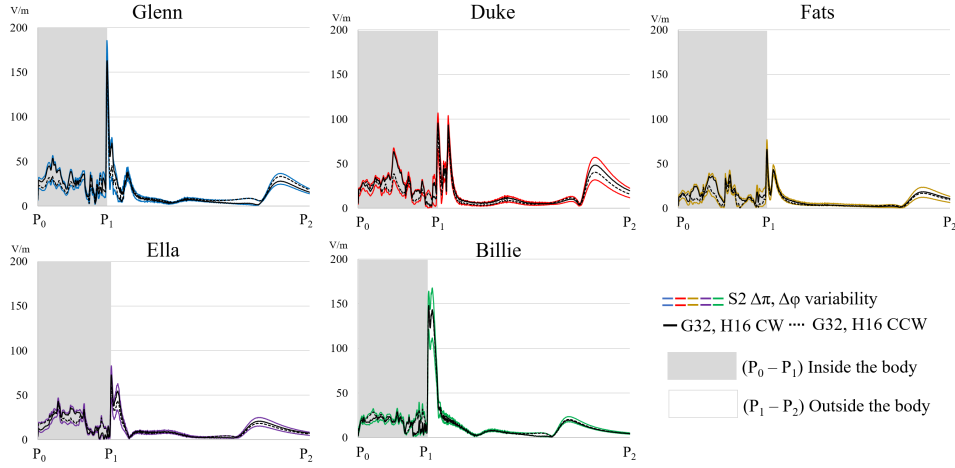


Figure 7.4: $\|E_{tan}\|$ profiles for each human body model studied along the extraction trajectory (Figure 7.2c and d). The grey area of each plots identify the extraction section inside the body. Results are shown as stripes (identified by two colored lines) including $\Delta\pi$ and $\Delta\varphi$ variability for the S2 model. Whereas profiles obtained with G32 and H16 are plotted as black lines with $\Delta\varphi$ variability reported by solid (CW) and dotted (CCW) line type. *N.B. An higher resolution representation of this figure is included in Appendix B.*

The variability of $\|E_{tan}\|$, as for WbSAR was evaluated with respect to coil excitation with the S2, G32 and H16 coil models (Figure 7.4) and the five body models. See the Supporting Material (Sup. Fig. S2) for the profiles of the $\angle E_{tan}$. As shown in Figure 7.4, results section by section for the S2 showed that:

- Inside the body (P0 to P1, grey area in Figure 7.4): the highest $\|E_{tan}\|$ dynamic range was observed in Duke with a peak of 67.7 V/m, and a nadir of 0.4 V/m. In Glenn, Duke, and Fats, the results in CW polarization showed higher $\|E_{tan}\|$ with respect to the CCW exposure for the majority of the trajectory. Conversely, the opposite was observed in Ella and Billie, indicating that neither of the two polarizations can be assumed as the worst case for $\|E_{tan}\|$ over the five human models considered.
- Interface groin/air: the highest $\|E_{tan}\|$ peaks were observed with Glenn and Billie, namely 183 V/m and 166 V/m, respectively. This is related to the specific location of the P1, close to the coil end-ring (i.e., $z = -325$ mm) (Figure 7.2d). Conversely, Fats showed the lowest peak of 77 V/m.
- Outside the body (P1 to P2): for the case defined in the study, the trajectory outside the body was always outside the coil. At the beginning of the trajectory,

7.4 Results

		Glenn				Duke			
		uSAR	0.1 g	1 g	10 g	uSAR	0.1 g	1 g	10 g
S2	Head CW	2354	285	81	12.4	2983	398	112	16.9
	Feet CW	2134	256	73	11.3	2557	345	97	14.6
	Head CCW	1914	213	62	9.7	2152	275	76	11.7
	Feet CCW	2028	221	65	10.2	2170	282	78	12.1
G32	CW	1700	205	58.2	9.0	2279	304	85.5	13.0
	CCW	1412	152	44.9	7.2	1543	196	54.2	8.4
H16	CW	1748	211	60.0	9.3	2271	302	84.9	12.9
	CCW	1351	146	43.0	6.9	1523	194	53.6	8.3

Table 7.2: Maximum SARTip for all the 32 feeding conditions ($\Delta\varphi$ and $\Delta\varphi$) defined in the S2 coil model and with respect to $\Delta\varphi$ for the G32 and H16 coil model.

Duke, Fats, and Ella showed well defined double peaks of electric field. This was related to the specific trajectory bending profile closed for the extraction. Along the trajectory, isolated peaks along the profile were related to the vicinity of the extraction trajectory to the body of the model. For each model, the highest peak was found at the end of the trajectory (P2), near the feet. This was due to the “antenna-effect” of the body itself, with induced currents along the body that generated a high peak of the Ez component in the proximity of the feet. Between models the highest peak at the feet was found for Glenn of up to 57 V/m. Even being up to 1.32 m away from the coil (i.e., in Fats), peaks values at the feet were of the same order of magnitude of the $\|E_{tan}\|$ inside the body.

Table 7.1 — $\|E_{tan}\|$ reports the maximum percentage of $\|E_{tan}\|$ variability observed within each body model relating to $\Delta\pi$ and $\Delta\varphi$. The results show a change of up to 93% with respect to $\Delta\pi$ and 98% with respect to $\Delta\varphi$.

Results obtained with the G32 and H16 coil models corresponded with the one obtained for S2 but averaged with respect to the $\Delta\pi$ variability for the specific feed phase orientation studied. Profiles are reported in Figure 7.4. As for the WbSAR, when comparing the results obtained with G32 vs. H16, there was less than 2% variability.

7.4.3 Case study: human body with partially implanted lead

For the case study considered, the variability of SARTip showed changes up to 51% with Glenn and up to 60% with Duke with respect to $\Delta\varphi$ (Table 7.1). Changes with respect to $\Delta\pi$ were up to 50% for both models. The results of the uSAR, 0.1gSAR, 1gSAR, and 10gSAR showed all the same variability with respect to $\Delta\pi$ and $\Delta\varphi$. This was expected as the local exposure is linearly proportional with respect to the specific mass used to average the quantity of interest. Hence the radar plots in Figure 7.5 report profiles valid for all four quantities but normalized to the maximum value of the

A Numerical Investigation on effect of RF coil feed variability on global and local electromagnetic field exposure in human body models at 64 MHz

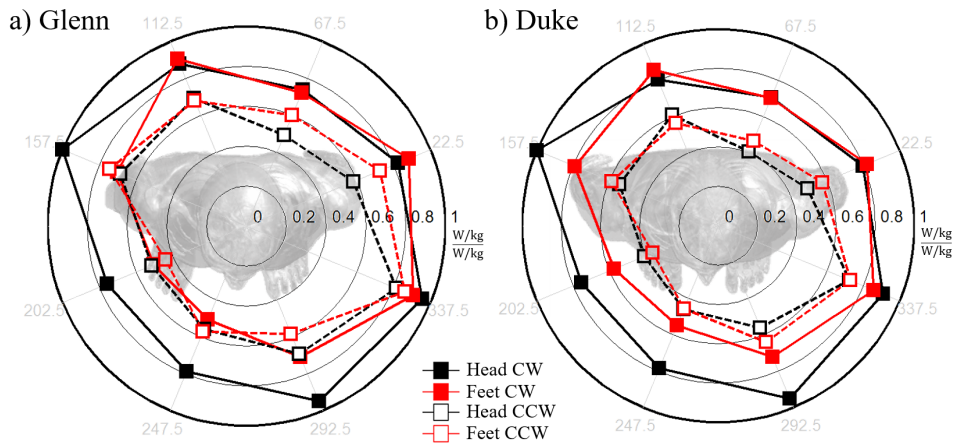


Figure 7.5: Values of SARtip obtained with each of the two body models selected for the analysis: Glenn (a) and Duke (b). As SARtip is only dependent by tip geometry, the profile with respect to $\Delta\pi$ and $\Delta\varphi$ applies to uSAR, 0.1gSAR, 1gSAR, and to 10gSAR. Each dataset was normalized to the maximum value of the quantity of interest (see table 7.2 – values in italic).

quantity of interest (italic values in 7.2). For each model, the dynamic range of results within the radar plot suggests the variability for different feed locations and feed phase orientation. Specifically, the dynamic range was 0.56 for Glenn and 0.64 for Duke; with a maximum value equal to 1 obtained with “Head-CW” excitation typology in 157.5° position in both models, whereas the minimum value equal to 0.44 and 0.36 for Glenn and Duke, respectively, obtained with the “Feet-CCW” excitation typology in 157.5° position.

The highest SARtip (7.2 - values in italic) with the S2 model was obtained with the “Head-CW” excitation. Results with the multi-port models (G32, H16) were lower than the maximum obtained with the S2 model (e.g., Glenn, uSAR S2/Head-CW vs G32/CW 28%), but they were within the $\Delta\pi$ variability range (e.g., Glenn, uSAR S2/CW from 1189 *W/kg* to 2354 *W/kg* vs G32/CW equal to 1700 *W/kg*). Higher values of SAR in the presence of the lead were observed in the tissue near the lead tip, at the interface between insulation and tip, and at the location where the lead exited the vein (Figure 7.6). Notably, while only one distribution relative to one coil excitation is shown, the same distributions – with different absolute values - were obtained when varying $\Delta\pi$ and $\Delta\varphi$.

7.5 Discussion

The main contribution of this study is to assess the effect of different excitation conditions of an MRI RF coil at 64 MHz on global and local exposure in human body

7.5 Discussion

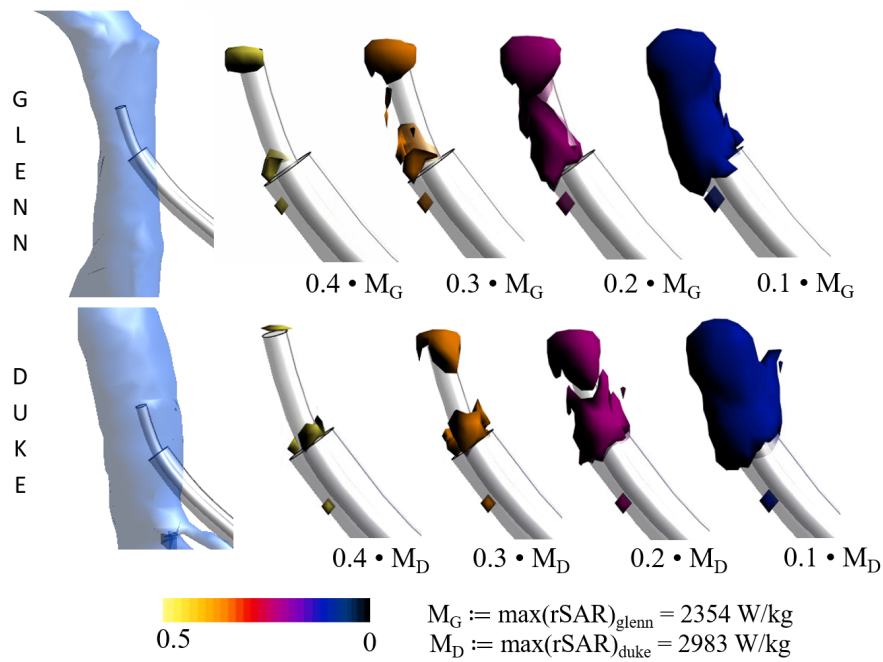


Figure 7.6: Map of uSAR around the tip of the partially implanted lead for one of the tested exposure conditions in Glenn and Duke. Values are reported as isosurfaces of SAR level with respect to the maximum value. The highest values were observed at the lead tip at the interface between bare tip and insulation and at the location where the lead exited the vein.

models. Five different human body models were considered in the analysis in order to take into account inter-subject variability [78]. For each human body model, variability with excitation conditions was achieved generating the EM field exposure of the human body with three numerical coil models previously proven to be accurate [129]. The selected quantities of interest were the variability of WbSAR, local 10gSAR, as well as E_{tan} along a predefined path, both inside and outside the body.

WbSAR results and inter-subject variability were in line with what was previously found in literature [78]. Such an inter-subject variability was mainly due to the applied normalization with B_1^+ RMS. In fact, the WbSAR is affected by factors such as body shape, muscle/fat ratio in the body, and total body mass. The B_1^+ homogeneity in a human body decreases getting closer to the coil rungs; thus larger sections of the body result in lower averages and higher normalization factors. The feed position did not affect the specific position of the peak 10gSAR value, but only its absolute value. Conversely, the position was affected by $\Delta\varphi$, due to the resulting opposite orientation of the induced currents within the body.

The $\|E_{tan}\|$ profiles along the selected trajectory were also affected by the specific body model, feed position and feed phase orientation. $\|E_{tan}\|$ results were characterized by peaks (inside the body, interface groin/air, feet) and nadirs. All five models

A Numerical Investigation on effect of RF coil feed variability on global and local electromagnetic field exposure in human body models at 64 MHz

showed a jagged $\|E_{tan}\|$ profile for the trajectory section inside the body, a high $\|E_{tan}\|$ peak at the interface groin/air, and a smoother profile for the trajectory section outside the body. Along the section inside the body (P0-P1), the E_{tan} was affected by all three field components (i.e., E_x , E_y and E_z) because the trajectory was not along a preferred axis. Conversely, along the section outside the body (P1-P2), the trajectory was user-defined along the z-axis with the exception of the first bended section (Figure 7.2c) and thus the E_{tan} profile was affected only by the E_z component. Peak values at the groin/air interface were affected by the specific location with respect to the coil rather than by the overall exposure. High values of $\|E_{tan}\|$ were observed with both Glenn and Billie (the point P1 was close to the coil ring in both models), even though the WbSAR with Glenn was twice as much as the WbSAR with Billie. Conversely, the $\|E_{tan}\|$ peak in Fats was 54 % lower with respect to Billie, even being the WbSAR 55% higher (i.e., Fats P1 location 240 mm further from the coil with respect to Billie).

Compared to the G32 and H16 coil models, the feeding position variability was the additional degree of freedom that allowed the S2 model to generate a broader range of exposure conditions. Consequently, for the case studied the G32 and H16 were able to generate results in line with the S2 model, but possible underestimations and defects with respect of the worst case exposure may need to be taken into account.

As shown in literature, multi-port models (G32, H16) do not take into account the coupling between the coil and the load [36]. Conversely, a specific model such as the S2 allows researchers to simulate this coupling and possible asymmetries in the exposure [36]. The asymmetric loading conditions, both along the coronal direction (z axis) and the axial direction (y axis), generated different coupling effects between the human body model and the S2 coil, thus generating different induced currents inside the body. For the S2 model, the combination of the asymmetric loading conditions and the $\Delta\pi$ affected the coupling. Similar coupling conditions were found for opposite feed locations (e.g., 22.5 ° and 202.5 °). Lower variability of WbSAR was observed for the Fats human model, because its mass almost filled the volume of the coil causing a lower difference of coil-model coupling with respect to $\Delta\pi$.

The coupling of conductive leads with the tangential component of the electric field is responsible for the induced heating at the tip of a lead. As suggested by the Tier3 approach of the TS [123], the transfer function method allows for a direct calculation of the power deposited at the tip of a defined lead, if E_{tan} and transfer function of the lead are known. When the transfer function of the lead is unknown, a possible approach is the use of a simplified transfer function to qualitatively determine a variability of power deposition with respect to different exposures. Mattei et al (10) have proposed the use of a unitary transfer function with a null phase. In this study, simplified transfer

7.5 Discussion

function with constant magnitude equal to 1, and three phase slopes (i.e., null, linear to -5 rad, and linear to -10 rad) were implemented as an example. The results showing variations of computed power deposition due to the E_{tan} results can be found in the Supporting Material (Sup. Fig. S3 for null phase, Sup. Fig. S4 for linear to -5 rad phase, and Sup. Fig. S5 for linear to -10 rad phase).

As a further step in the study, a case study with a lead partially implanted in a human body model was implemented as suggested by the Tier 4 of the TS [123]. One of the clinical hazards of partially implanted leads (e.g., catheters for cardiac ablation) in MRI is the possibility that these elongated conductive structures, coupling with the incident RF field, deposit energy in the patient body. Technical specifications for safety assessment of fully implanted medical devices in MRI have been presented [123] and studied in literature [37, 256, 263], whereas no standardized methodology exists for partially implanted devices. Simulations with the lead were implemented in two of the five human body models, as a trade-off between the need of evaluate inter-subject variability and computational cost of the simulations. The selection of the models was based on the high use in literature (i.e., Duke), and the interest to a model of an older patient (i.e., Glenn) as potentially the best patient candidate for an MRI interventional catheterization procedure. The quantity of interest of this case study was the local SAR at the tip of the lead.

As per antenna theory [241, 255, 264], given a specific lead geometry, the local SAR depends on the profile of E_{tan} profile which in turns depends on the trajectory of the lead with respect to the incident field. In this study, the trajectory inside the body was constrained by the morphology of the patient, following typical catheter-insertion procedures (i.e., through femoral vein). Conversely, the trajectory outside was chosen to follow a straight path as an example. It is expected that results would vary with variable trajectories outside the body, different body postures, or landmark positions. Additionally, as a verification of the computational framework, the results of SAR distribution near the tip were evaluated. As shown in Figure 7.6, the geometrical distribution of SAR around the electrically small tip of the lead – compared to the lead being an elongated structure - depended only on the tip shape, while the absolute value of peak SAR depends on the lead exposure, in line with previous literature [241, 255].

7.5.1 Limitations

More than one path for both the E_{tan} extraction and the lead should be studied. In fact, different E_{tan} extraction paths would results in different range of results variability with respect to $\Delta\pi$ and $\Delta\varphi$. Additionally different lead trajectory or penetration depth inside the body would create different coupling effects between the RF field and

A Numerical Investigation on effect of RF coil feed variability on global and local electromagnetic field exposure in human body models at 64 MHz

the lead. Hence diverse variability range with respect to $\Delta\pi$ and $\Delta\varphi$ will be observed. Different human body landmark as well as posture should be also. Finally, the applicability of the case study with the partially implanted lead would require the inclusion of thermal analysis and full uncertainty evaluation for assessment of safety in patients with respect to RF-induced thermal damage.

7.6 Conclusion

The results of this study indicate that the specific information about feed position and feed phase orientation with respect to the patient undergoing an MRI scan needs to be taken into account when evaluating local SAR in the presence of a conductive elongated structure within or in contact with the body of the patient. Results showed a variation of less than 20% for WbSAR, up to 47.1% for the local 10gSAR, and up to 98% of the incident electric field magnitude along a single trajectory. An additional case study with a partially implanted lead showed changes up to 60% of peak SAR at the lead tip with respect to feed phase orientation. Inter-subject analysis performed with five human body models showed of up to 58% variability in wbSAR. The results of this study are limited to the specific geometries evaluated and additional work is needed to include multiple lead paths and penetration depths, body postures, and landmark positions.

7.7 Supplementary material

Simulation setup, numerical environment details FDTD Courant-Friedrich-Levy stability was achieved by imposing a mesh grid resolution of $3\times 3\times 3\text{ mm}^3$ to the coil and human model, and a superimposed fine resolution to the electrical elements present within the coil (i.e., sources and lumped elements). This fine resolution was automatically generated by the software based on a heuristics algorithm. In addition for the simulations with the lead, a mesh grid of $0.8\times 0.8\times 0.8\text{ mm}^3$ with a geometrical resolution of 0.5 mm was imposed to the bended section of the lead (i.e., 150 mm from the insertion point), whereas a resolution of $0.8\times 0.8\times 3\text{ mm}^3$ was imposed to the remaining straight section of the lead. Free space padding was added at the boundaries to ensure free propagation of the field outside the coil volume without reflection. Additionally, seven absorbing layers were set as boundary conditions. Computing time was approximately one hour for each simulation without the lead, and approximately 8 hours with the lead present. Simulation run on a PC Intel(R) Core(TM) i7-4930K CPU @ 3.40GHz, with 64 GB of RAM and NVIDIA Tesla K40c graphic processing units.

7.7 Supplementary material

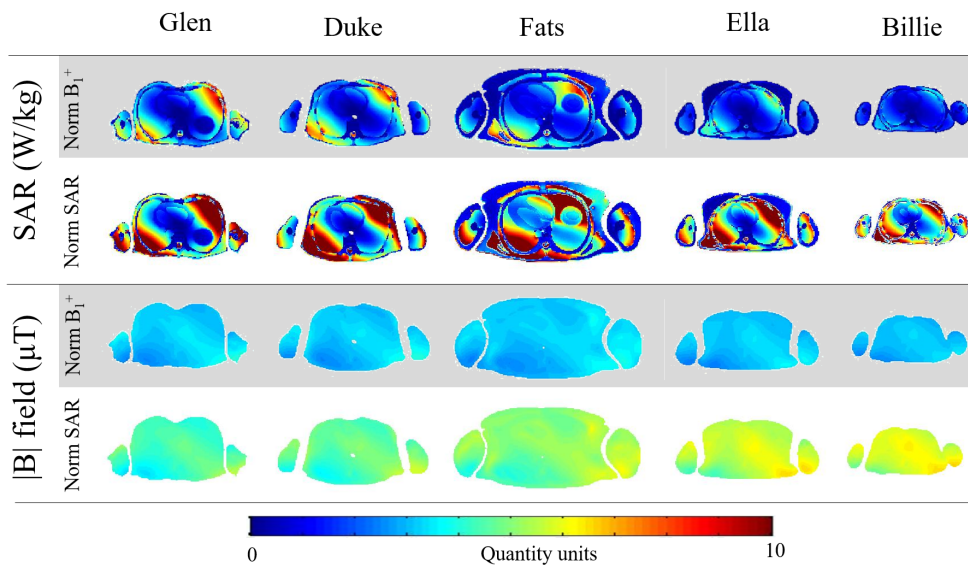


Figure 7.7: SAR and $\|B\|$ field maps for the central axial slice of the five human body models studied. Maps are reported for one of the 32 exposure conditions analyzed within the study. Results are reported imposing two normalization: the one used for the study ($B1+ = 3 \mu\text{T}$), and imposing a WbSAR equal to 2 W/kg.

$\|B\|$ and SAR maps In addition to the normalization based on the $B1+$, a second normalization based on WbSAR was also studied. The results obtained with the five models is herein reported. As an example the B field and SAR distributions normalized with respect to a WbSAR of 2 W/kg in all the five models are herein reported.

As shown by figure 7.7 the B field distribution shows a good homogeneity for the five human body models within the slice for both normalization factors. When normalizing the results with respect to the same $B1+$ the resulting WbSAR values were already reported in figure 7.3. In such case the highest WbSAR was found for Glenn (i.e., ~ 1.2 W/kg), whereas the lowest was found for Billie (i.e., ~ 0.58 W/kg). When comparing the radiated power with respect to the human mass, a direct relation with the WbSAR results was found. As an example the two human models Glenn and Duke required the same radiated power with respect to the defined normalization factor. However, because SAR is inversionally proportional to the mass, the WbSAR in Glenn was 1.14 times higher than in Duke (i.e., ~ 0.98 W/kg), having Duke a 1.14 times higher mass (i.e., Glenn 61 kg, Duke 70 kg).

The $\|\vec{B}\|$ distribution within the body slice (figure 7.7) increases when the SAR normalization factor was imposed due to the higher transmitted power. Results showed the highest values of $\|\vec{B}\|$ for Billie and the lowest for Glenn. This was in line with the results in figure 7.3 as higher transmit power has to be deliver to the coil when loaded with Billie to obtain the same WbSAR as in Glenn. Distribution of SAR in the section

A Numerical Investigation on effect of RF coil feed variability on global and local electromagnetic field exposure in human body models at 64 MHz

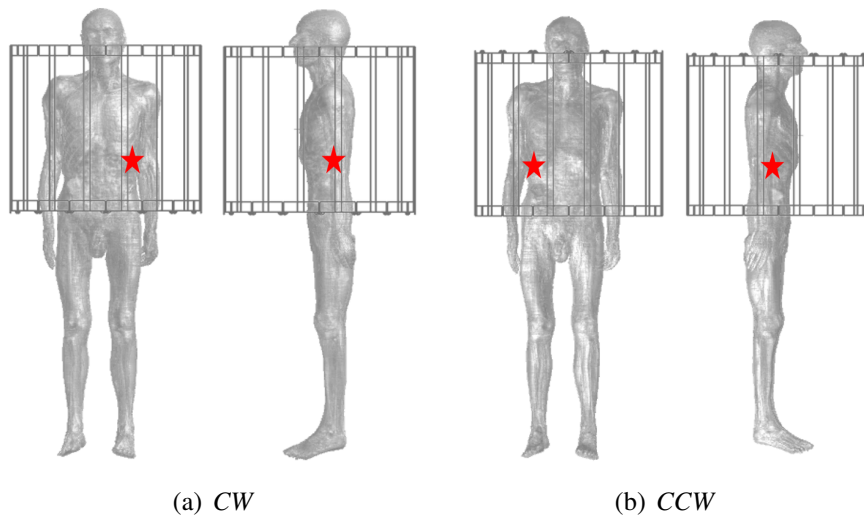


Figure 7.8: Location of the peak 10gSAR for the human body model Glenn, with respect to the CW and CCW feed orientation. The red star defines the peak 10gSAR location.

reported in figure 7.7 were in line with what already observed in section 6.1. Peaks were found in the lungs of all the models. Additionally comparison of results with respect to the two normalization factors was in line with the power absorption profile observed in the human body model Duke. Higher values of SAR were expected by results of power abortion already presented in figures 6.3 and 6.4.

10g local SAR and Head SAR As suggested by the the ICNIRP and IEC standards (section 5.1.1), the local SAR in each model was computed for the different exposures. The local SAR was computed within the Sim4Life software that bases the calculation using a cubic averaging algorithm according to the standard IEEE C95.3 [265]. The results showed peaks of local SAR always between neck and groin (figure 7.8 show location for Glenn), in line with what observed for Duke landmarked at the heart in section 6.1. Values observe for Glenn, Duke, Fats, Ella, and Billie were of (in W/kg) 15.4, 10.5, 15.4, 13.2, and 11.3, respectively (figure 7.9). The specific location of the peak 10gSAR for each model was independent with respect to $\Delta\varphi$, whereas with $\Delta\varphi$ it was specular with respect to the longitudinal axis of the body (z-axis).

Contrarily to the WbSAR, the results for the local SAR (fgiure 7.9) exceeded the limits for the normal operating mode (i.e., 10 W/kg, see table 5.1). However all the results were within the limits for the First Level Operating Mode with respect to the IEC standard, and within the experimental level operating mode for the ICNIRP standard.

7.7 Supplementary material

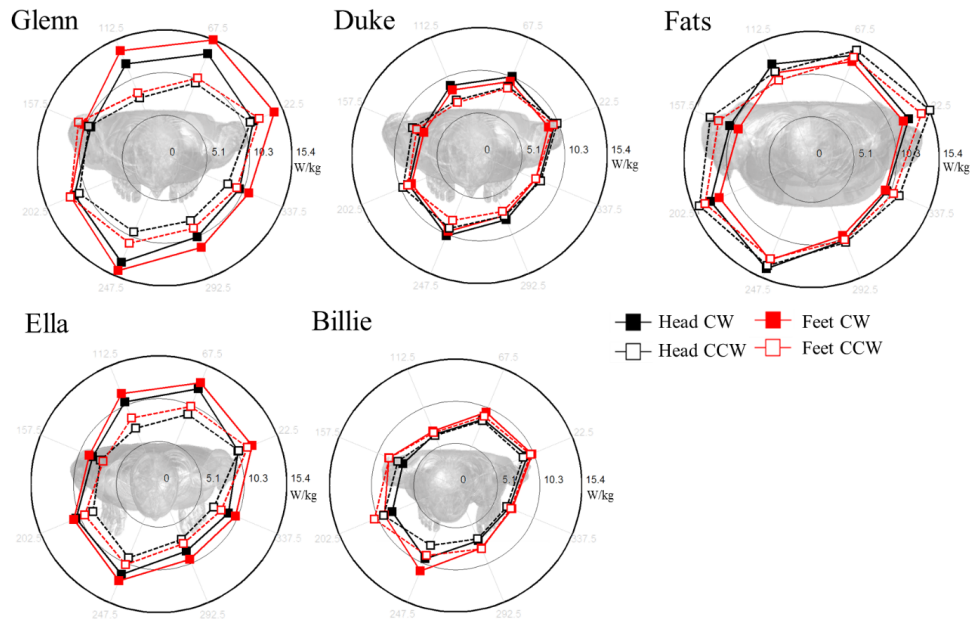


Figure 7.9: Maximum value of the local 10gSAR with respect to $\Delta\pi$ and $\Delta\varphi$ for the five human body models used for the study. Results are reported for the S2 coil model.

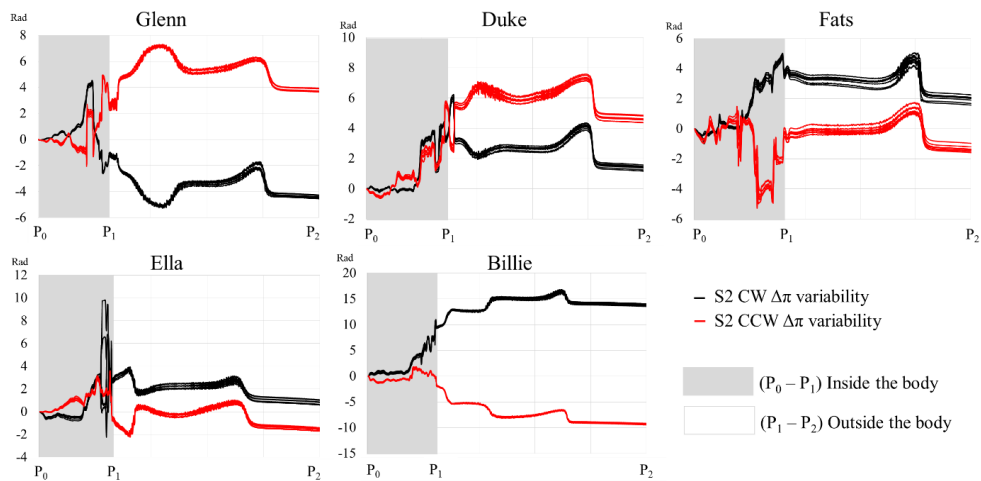


Figure 7.10: E_{tan} phase profiles for each human body model studied along the extraction trajectory (Figure 7.2c and d). The grey area of each plots identify the extraction section inside the body. Results are including $\Delta\varphi$ (CW in black, CCW in red) and $\Delta\pi$ variability for the S2 model.

7.7 Supplementary material

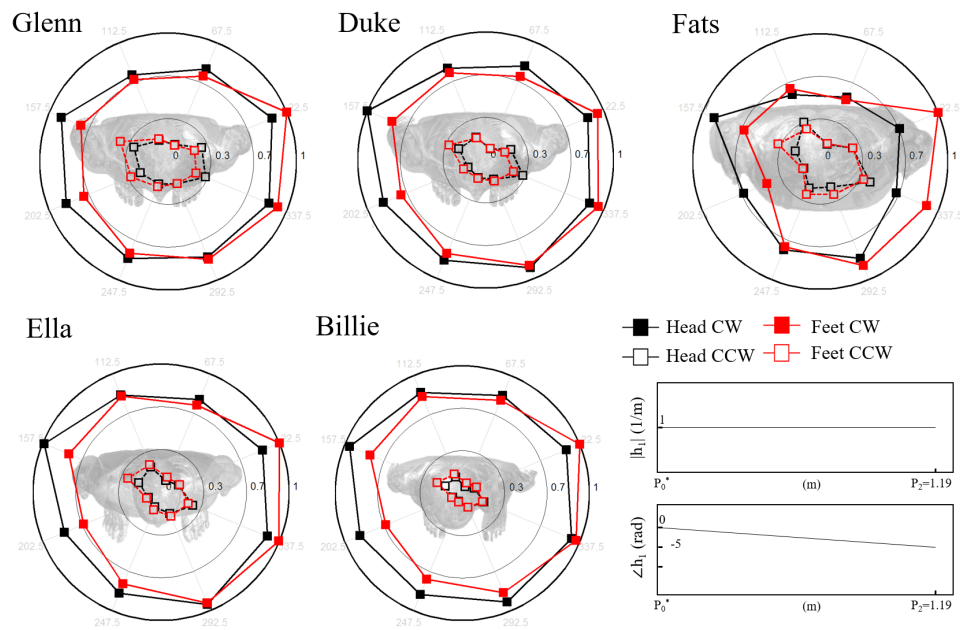


Figure 7.12: Results of the computed power deposition at the tip of the implant with a unitary transfer function (h_1) with a constant magnitude equal to 1 and linear to 5 rad phase slope (bottom right).

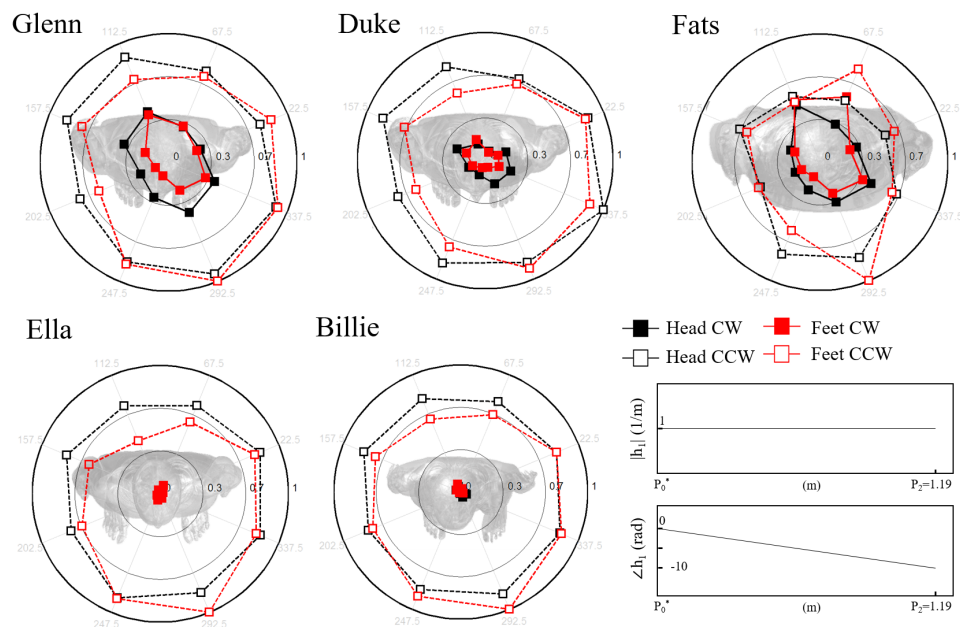


Figure 7.13: Results of the computed power deposition at the tip of the implant with a unitary transfer function (h_1) with a constant magnitude equal to 1 and linear to 10 rad phase slope (bottom right).

7.8 Effect of RF coil feed on current density and SAR

The variability of RF coil feed was herein evaluated with respect to current density $\|\vec{J}\|$ and SAR maps in Duke and Ella. The variation of feeding port position and feed phase orientation was the one defined by equations 7.2 and 7.1. As previously described in section 7.3 the simulations were all normalized based on the B_1^+ RMS average equal to $3 \mu\text{T}$ in the space occupied by the patient in the central axial plane. For the two quantities analyzed, additionally the maximum SMAPE was calculated based on equation 3.5. The maximum value was calculated with respect to $\Delta\pi$ and $\Delta\varphi$.

High values of SAR and $\|\vec{J}\|$ were predominant in the volume between the neck and the groin for both models. This was related to the specific landmark chosen for the models, and in line with what already presented about Duke in section 6.1. Overall higher values of both SAR and $\|\vec{J}\|$ were observed in Duke with respect to the one in Ella. In particular for the specific slice reported in figures 7.14, 7.15, 7.16, and 7.17 values in Duke showed up to 45 % higher local SAR and up to 26 % higher $\|\vec{J}\|$. This results were in line with both the WbSAR (figure 7.3) and the local 10gSAR (figure 7.8). With respect to the the current density the SAR was additionally affected by the density of the tissues (see eq 5.1). The results found were in line with what already shown in section 6.1. Higher values of SAR were found in the lungs where the tissue density is much lower than the one of the surrounding tissues.

With respect to results for the different feeding source settings, both the $\|\vec{J}\|$ (figure 7.14, and 7.16) and the SAR distribution (figure 7.15, and 7.17) were affected by $\Delta\pi$ and $\Delta\varphi$. In the two models the feeding position mainly affected the value of the strength of the quantity. This was particularly evident in Duke for the peak of SAR in the left lung. Conversely, the feeding phase orientation mainly affected the distribution of the values showing higher values on the left side of both models in CW and on the right side in CCW. For the opposite field orientation, on the two opposite sides the human body showed different current density distributions because of the heterogeneity of the human models. The curly electric field followed opposite flowing direction encountering different organs inside the body.

Specifically the dependency of the current density with $\Delta\pi$ and $\Delta\varphi$ was reported in Figure 7.18 for two points of interest. The two points were chosen in the models as areas of the body sensing one of the highest influence with feeding source settings (figure 7.19b). Additionally in the two models the points were chosen specular to prove the mirroring of the quantity with respect to $\Delta\varphi$ observed in figures 7.14, 7.15, 7.16, and 7.17. Current density values in the point selected in the brain of Duke and Ella models were affected respectively of up to 68 % and 78 % for $\Delta\varphi$, and up to 51 % and

7.8 Effect of RF coil feed on current density and SAR

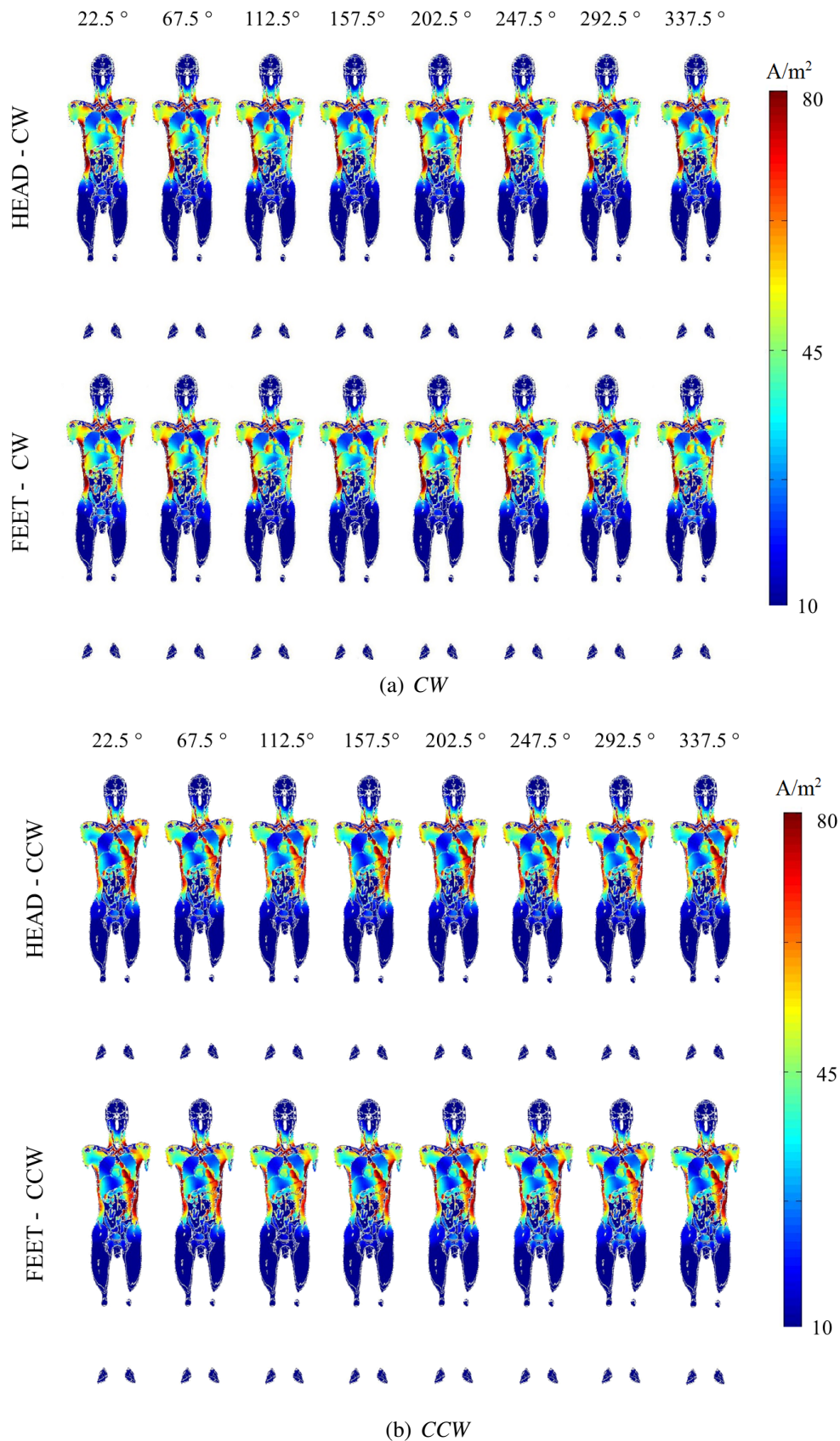
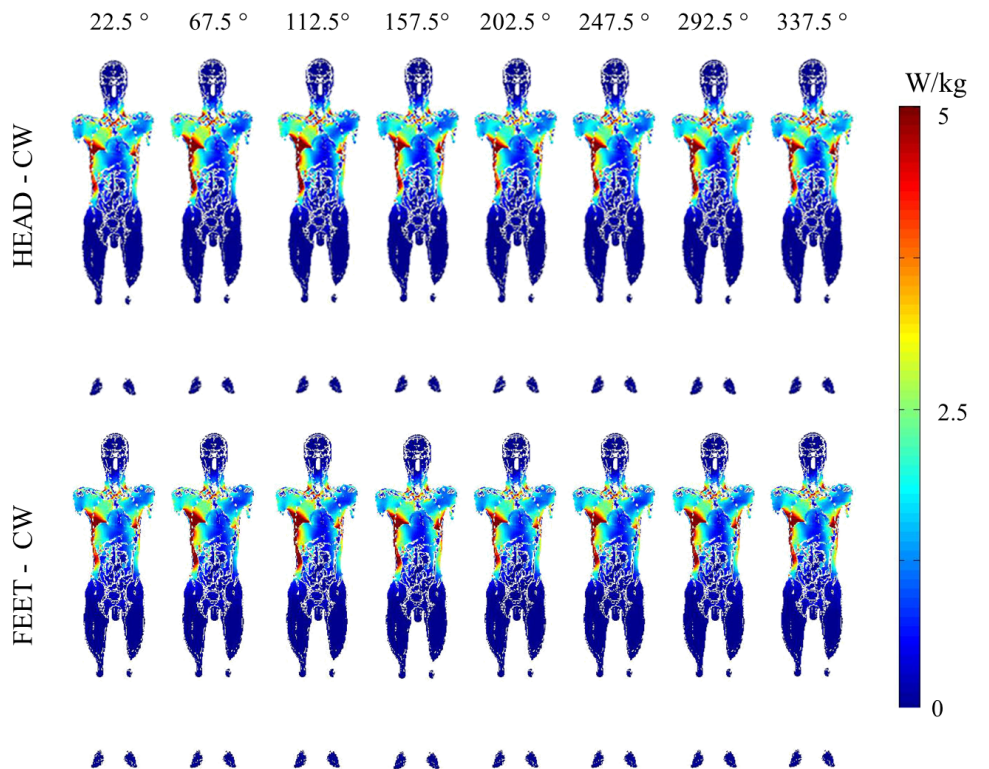
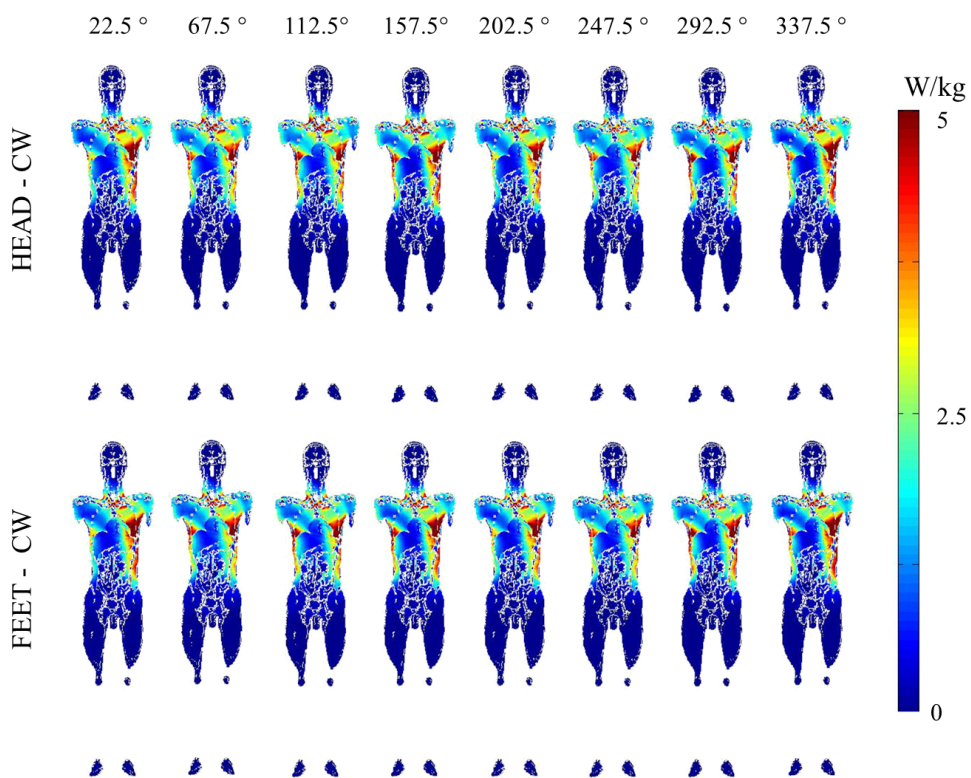


Figure 7.14: Current density maps in the central coronal slice of the Duke model with respect to $\Delta\pi$ and $\Delta\varphi$ (a) CW field orientation, and (b) CCW field orientation). The angle defines the location of the feeding sources (α in Figure 7.2b). *N.B. An higher resolution representation of this figure is included in Appendix B.*

A Numerical Investigation on effect of RF coil feed variability on global and local electromagnetic field exposure in human body models at 64 MHz



(a) CW



(b) CCW

Figure 7.15: SAR maps in the central coronal slice of the Duke model with respect to $\Delta\pi$ and $\Delta\varphi$ (a CW field orientation, and b) CCW field orientation). The angle defines the location of the feeding sources (α in Figure 7.2b). *N.B. An higher resolution representation of this figure is included in Appendix B.*

7.8 Effect of RF coil feed on current density and SAR

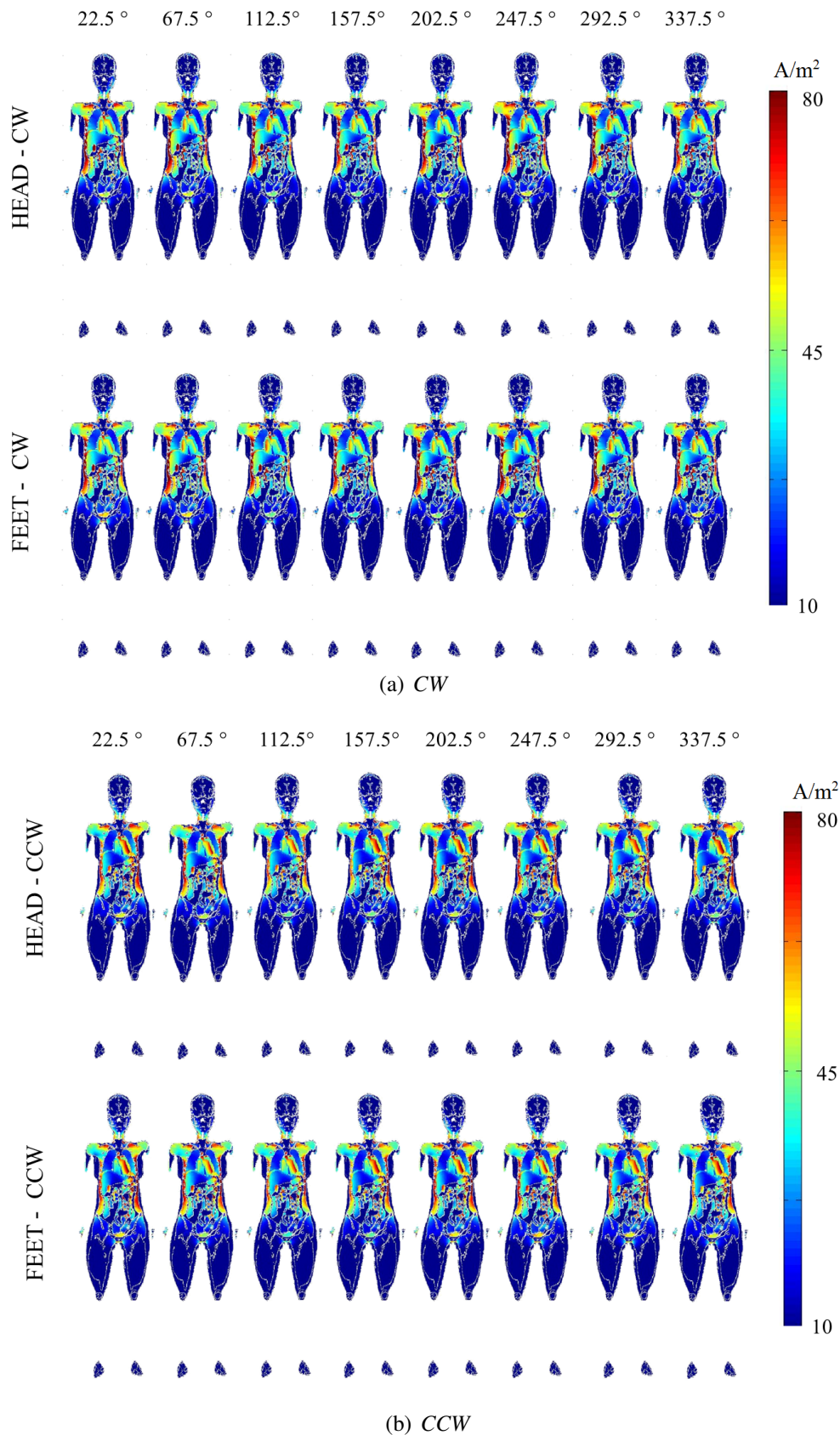
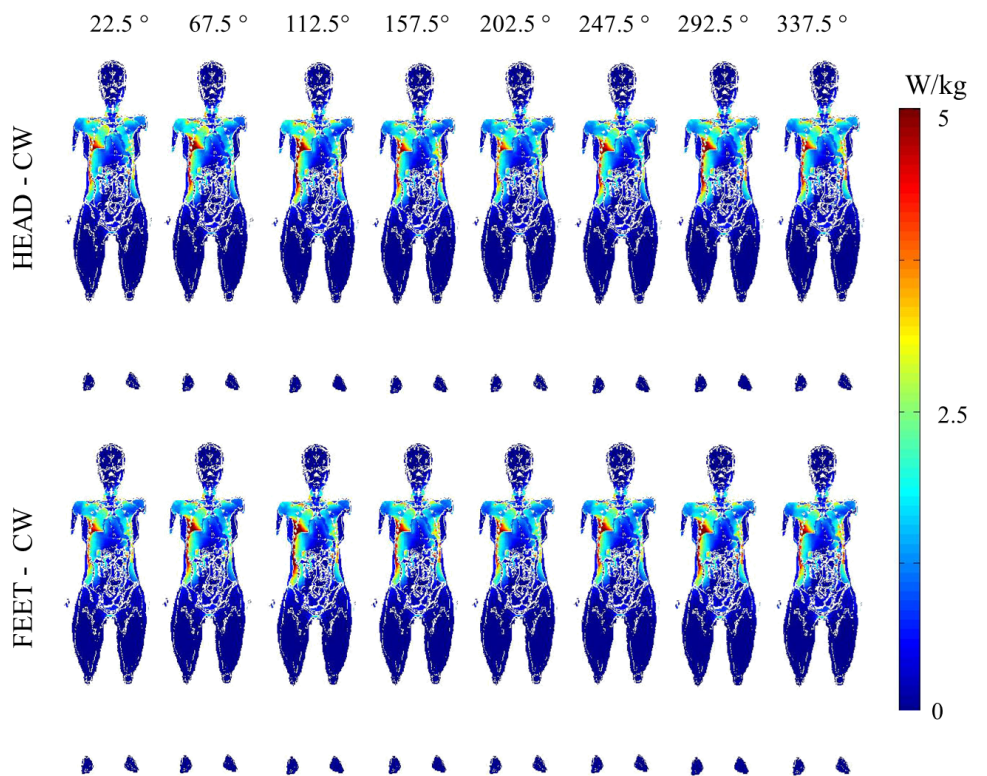
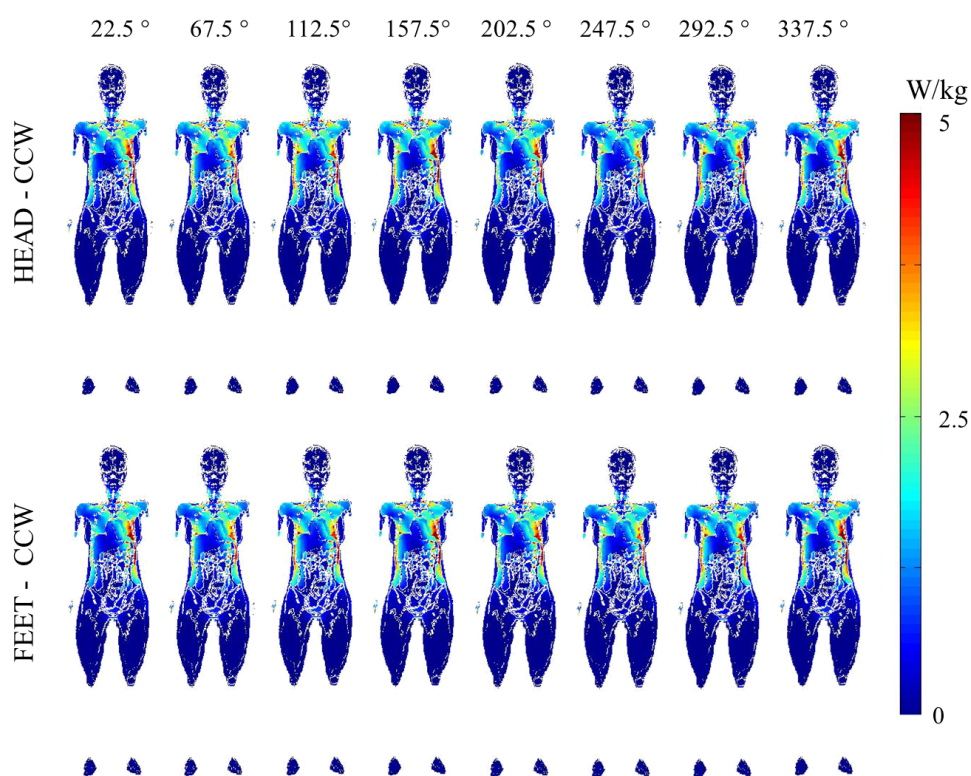


Figure 7.16: Current density maps in the central coronal slice of the Ella model with respect to $\Delta\pi$ and $\Delta\varphi$ (a CW field orientation, and b) CCW field orientation). The angle defines the location of the feeding sources (α in Figure 7.2b). *N.B. An higher resolution representation of this figure is included in Appendix B.*

A Numerical Investigation on effect of RF coil feed variability on global and local electromagnetic field exposure in human body models at 64 MHz



(a) CW



(b) CCW

Figure 7.17: SAR maps in the central coronal slice of the Ella model with respect to $\Delta\pi$ and $\Delta\varphi$ (a) CW field orientation, and (b) CCW field orientation). The angle defines the location of the feeding sources (α in Figure 7.2b). *N.B.* An higher resolution representation of this figure is included in Appendix B.

7.8 Effect of RF coil feed on current density and SAR

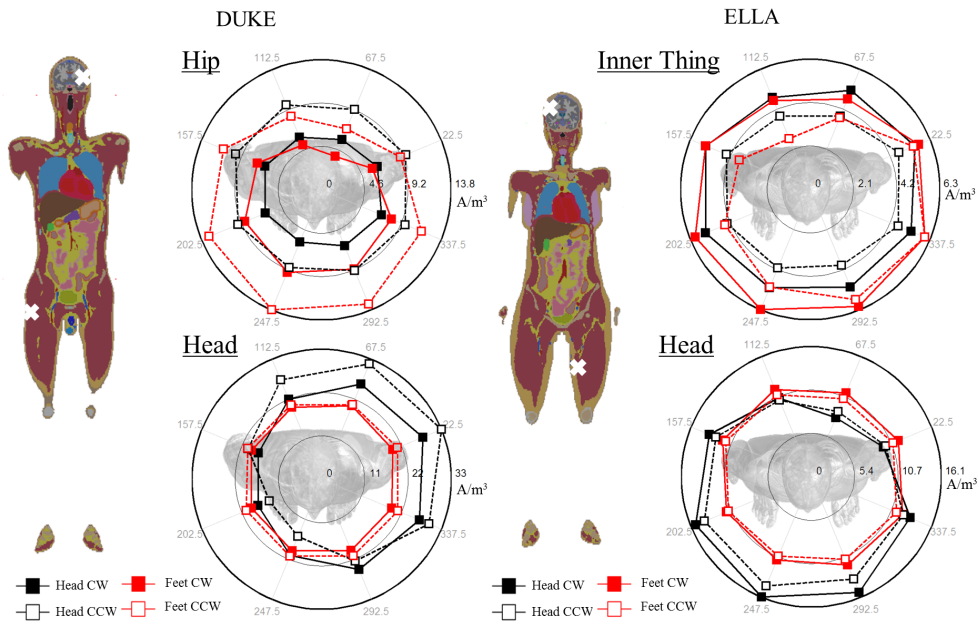
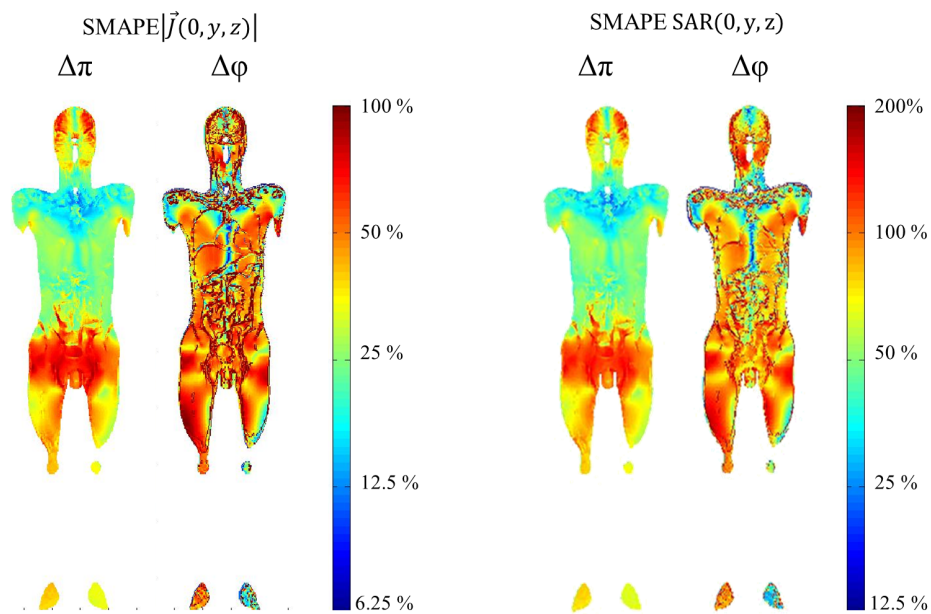


Figure 7.18: Radar plots define the specific local variation of current density $\Delta\pi$ and $\Delta\psi$ for one point in Duke and Ella. The location of the point is defined by the white cross.

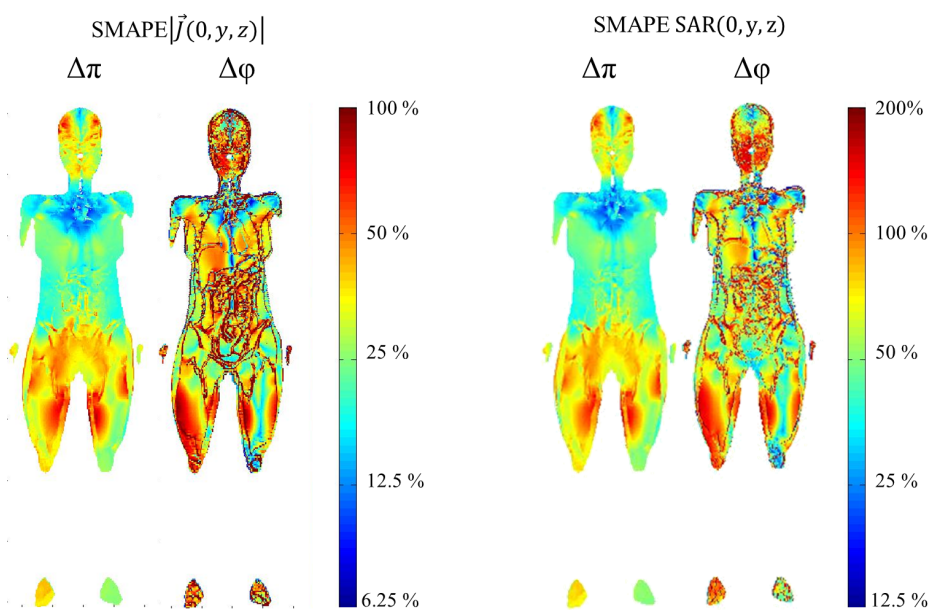
53 % for $\Delta\pi$. Whereas for the point in the hip for Duke and in the inner thing for Ella variations were up to 84 % and 77 % for $\Delta\psi$, and up to 82 % and 58 % for $\Delta\pi$. As expected, the points in the two models showed opposite dependency with the $\Delta\psi$. As an example the point in the brain for Duke in 247.5° showed the highest value for the Feet-CW configuration, whereas the point in the brain for Ella in 247.5° showed the highest value for the Feet-CCW configuration. The profiles of the results also suggest that it is not possible to fine a worst case exposure with respect to specific points within the body.

Variation of values is also shown by the SMAPE maps for the two models (figures 7.19a, and 7.19b). It is of interest to notice that the area with the highest SMAPE with respect to $\Delta\pi$ were the one with the lowest values of SAR and $\|\vec{J}\|$. This underlines the importance of numerically solve the entire body and do not limit the analysis to specific sections. As already discussed in section 5.1, this was already noticed for the evaluation of the SAR in the head with and without the inclusion of the shoulders [36, 103, 135, 147, 199]. With respect to the current density, with respect to $\Delta\pi$ up to 100 % SMAPE was found in the brain and in the hips for both models. Conversely, with respect to $\Delta\psi$ variation of field distribution was characterized by high values of SMAPE everywhere in the models and not in specific locations. Overall $\Delta\pi$ and $\Delta\psi$ affected the two models in the same way, but in Duke higher values were found for bigger volumes. For the SAR variability of results was as the one observed for $\|\vec{J}\|$, however values were almost doubled everywhere with SMAPE up to 200 %.

A Numerical Investigation on effect of RF coil feed variability on global and local electromagnetic field exposure in human body models at 64 MHz



(a) *Duke*



(b) *Ella*

Figure 7.19: map of maximum SMAPE found for the different feed positions ($\Delta\pi$) and feed phase orientation ($\Delta\phi$) in Duke and Ella for a) the current density and b) the SAR.

7.9 Evaluation of RF coil feed variability in the superellipsoidal phantom

Evaluation of results with respect to a phantom rather than the human body models, allows for the validation of the numerical data with measurements. Furthermore as already discussed a standardized methodology for testing partially implanted lead is not yet available. Thus, a study performed with a phantom lays the groundwork for the development of a systematic exposure procedure for RF heating evaluations of partially implanted leads.

The study of the exposure conditions with respect to port position and feed phase orientation was herein repeated loading the coil with a computation model of the Superellipsoidal phantom. Results of EM field distribution obtained with the same phantom were already previously described in sections 2.4, and 3.

The same numerical setup described in the previous study (7.3) was here in repeated. The S2, G32 and H16 coil models (Figure 7.1) were used for the study. For the two simplified models G32 and H16, results were analyzed with respect to both feed phase orientation. Whereas for the S2 model, 64 excitations were defined by varying both feed phase orientation, as well as feed position within the coil (i.e., 32 positions, 16 for each ring – see Figure 7.20c) as follows:

$$\Delta\pi = \begin{cases} \alpha \in 0^\circ : 22.5^\circ : 337.5^\circ \\ ring : Head \wedge Feet \end{cases} \quad (7.3)$$

where the head and feet labels for the end-rings were defined as for the case of the human body models. The feet-ring was on the side of the extraction path (figure 7.20b).

The \vec{E}_{tan} extraction path (black in Figure 7.20a) in the phantom was along a device mount track. The track was specially design for evaluation of a partially inserted catheter. As for the study with the human body models, the simulation results were normalized to an average $B_1^+ RMS$ field of $3\mu T$ in the central axial slice of the phantom (Figure 7.20a).

As for the study with the human body models, the WbSAR and the E_{tan} were evaluated for the different exposure conditions ($\Delta\varphi \Delta\pi$). Additionally, the E field distribution inside the phantom was also evaluated. For each exposure condition, the E field was extracted on the plane inside the phantom at the level of the catheter where also the E_{tan} extraction path lays.

Two case studies were simulated including in the phantom two partially implanted leads of different length (figure 7.21). The two leads were characterized by the same length on the part outside the phantom (i.e., equal to 430 mm), but the first lead length inside for 980 mm, whereas the second lead only for 670 mm. The two leads had the

A Numerical Investigation on effect of RF coil feed variability on global and local electromagnetic field exposure in human body models at 64 MHz

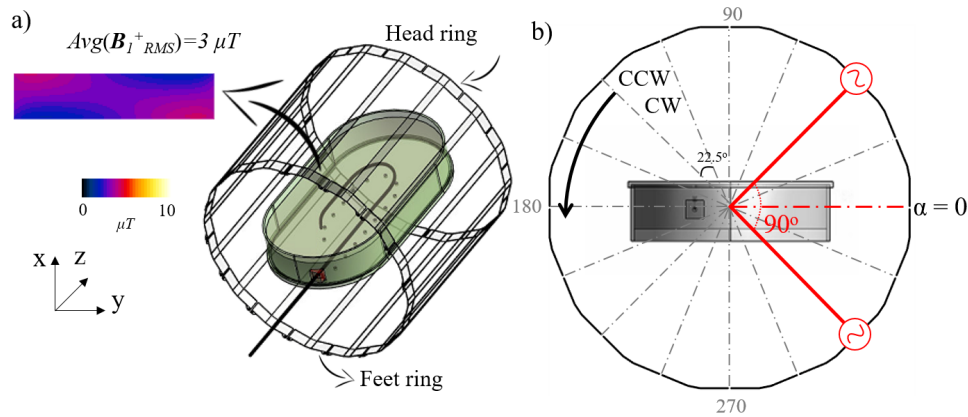


Figure 7.20: a) Coil loaded with the superellipoidal phantom. The black line identifies the extraction path for the \vec{E}_{tan} . The B_1^+ RMS at the central axial slice for the area occupied by the phantom is shown. All the numerical results were normalized based on the B_1^+ RMS average equal to $3 \mu T$ in the selected area. Head and feet end-rings are defined. (b) S2 feed rotation within the coil end-ring where α defines the central angle of the two feeds at 90° used as exciting sources in the simulations. The feed phase orientation (CW and CCW) is also shown. A total of 64 feeding conditions were studied with the S2 coil model.

same geometrical structure as the one used for the study with the human body models (i.e., 2 mm diameter insulated wire, with a 0.5 mm insulation). For the case study only the head-ring with a CW feeding phase orientation was chosen to assess $\Delta\pi$ variability within the same ring, because was the one showing the highest values of SAR tip in the study with the human body models.

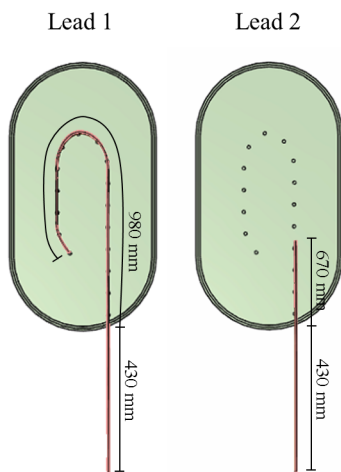


Figure 7.21: The two leads partially implanted in the superellipoidal phantom.

Figure 7.22 reports the WbSAR and average of the $\|E\|$ ($avg\|E\|$) values with respect to $\Delta\pi$. The maximum variation with feed position was of 1.6% for both the WbSAR and $avg\|E\|$, respectively. Whereas no differences were found with respect to $\Delta\varphi$.

The SMAPE map was calculated for the $\|E\|$ accordingly to eq. 3.5. High values of SMAPE up to 50 % were found at the center of the plane for both $\Delta\pi$ and $\Delta\varphi$. Overall SMAPE values of 10 % were found on the plane with respect to $\Delta\pi$. The SMAPE distribution with respect to $\Delta\varphi$ suggested a mirroring of the distribution with respect to the central line with SMAPE values of 7% on the sides of the phantom.

Dependency of the field with respect to $\Delta\pi$ and $\Delta\varphi$ can be more easily defined

7.9 Evaluation of RF coil feed variability in the superellipsoidal phantom

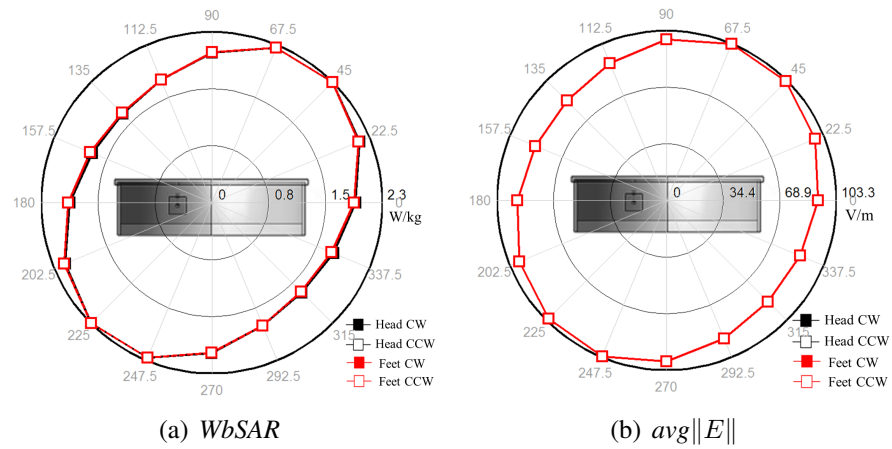


Figure 7.22: (a) $WbSAR$ and (b) $avg\|E\|$ results for the superellipsoidal phantom. The radar plots report the values with respect to $\Delta\pi$ for the S2 model. The bold external circle indicates the coil with the phantom inside plotted in scale.

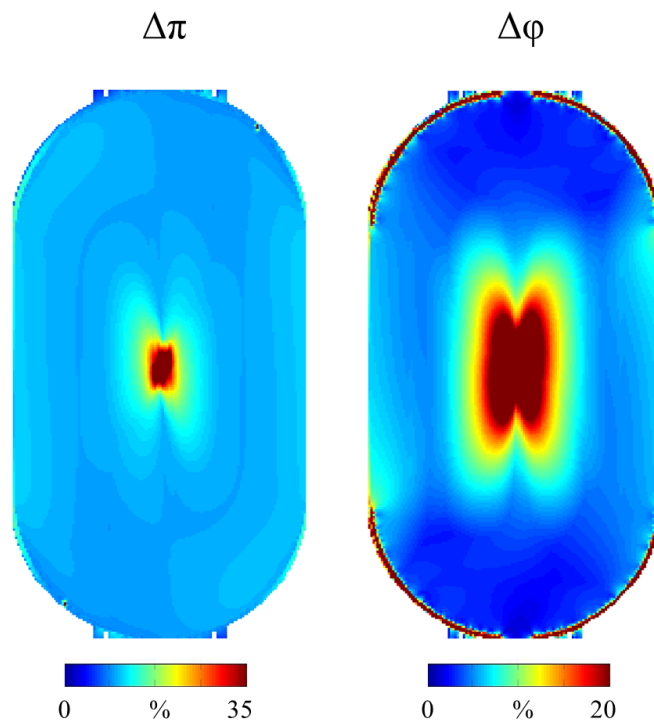


Figure 7.23: Map of SMAPE for the $\|E_{tan}\|$ on the plane of the lead. The SMAPE was calculated with respect to both $\Delta\pi$ and $\Delta\varphi$.

A Numerical Investigation on effect of RF coil feed variability on global and local electromagnetic field exposure in human body models at 64 MHz

looking at variation of the \vec{E}_z and \vec{E}_x components (Figure 7.24). The distribution of \vec{E}_z with respect to $\Delta\varphi$ shows the mirroring effect of both the magnitude and phase of the field component. Whereas the distribution of the \vec{E}_x was affected by the port position, in particular by the ring used as excitation (i.e., head or feet). Variation up to 87 % was found at the isocenter, and up to 3 % at the edges. This result it affected by the E field not being symmetrical with higher values of E field occurring on the opposite side of the excitation ring, as already reported in work described in section 3.

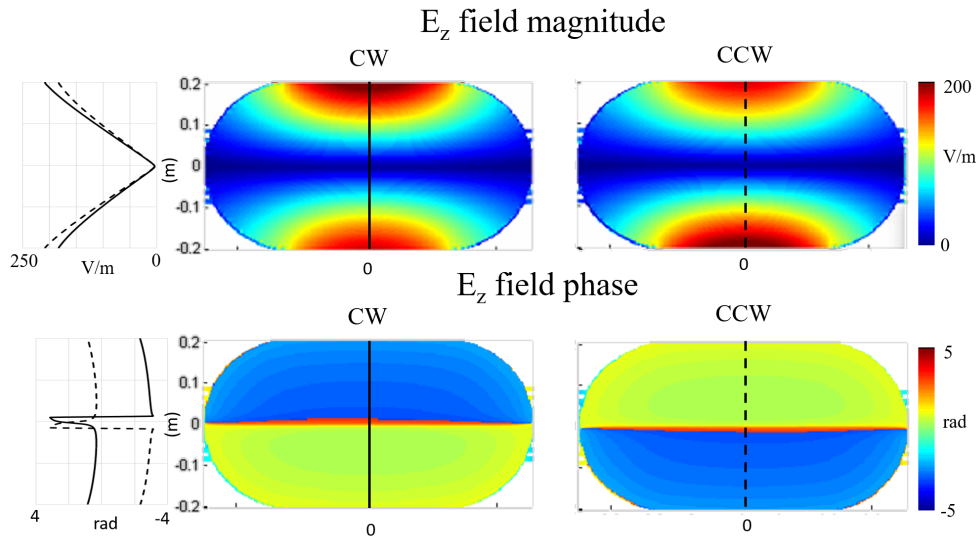
The variability of $\|E_{tan}\|$ and $\angle E_{tan}$, as for WbSAR and $\text{avg}\|E\|$ was evaluated with respect to coil excitation (Figure 7.25). As shown in Figure 7.4, results section by section for the S2 showed that:

- Inside the phantom (P0 to P1, grey area in Figure 7.25a): the overall variability of the $\|E_{tan}\|$ results was everywhere between 20 % and 30 %. As almost the entire path of the trajectory is aligned along the z axis, the highest peak of 90 V/m was observed around the the middle of the first part of the extraction trajectory and the bending level where the z component of the Electric field was proved to show high values of field (Figure 7.24a). Hence the second peak of 87 V/m was found at the same level but one the opposite side of the trajectory. A local minimum value was observed for all the extractions at the bending level of the trajectory. Here results showed the lowest percentage variability of 20 %. Neither of the two polarizations (i.e., CW and CCW) can be assumed as the worst case for $\|E_{tan}\|$ for the trajectory considered.
- Interface phantom/air: The highest $\|E_{tan}\|$ peak observed was of 82 V/m. The double peaks are due to the presence of the phantom "port" made of plexiglass. At the interphase a variability of up to 92 % was observed.
- Outside the body (P1 to P2): the trajectory outside the phantom was always outside the coil. Values of $\|E_{tan}\|$ were more halved with respect to the one inside the phantom, with the highest local peak of 25 V/m. Where the trajectory came out of the phantom "port" variability of 100 % was observed.

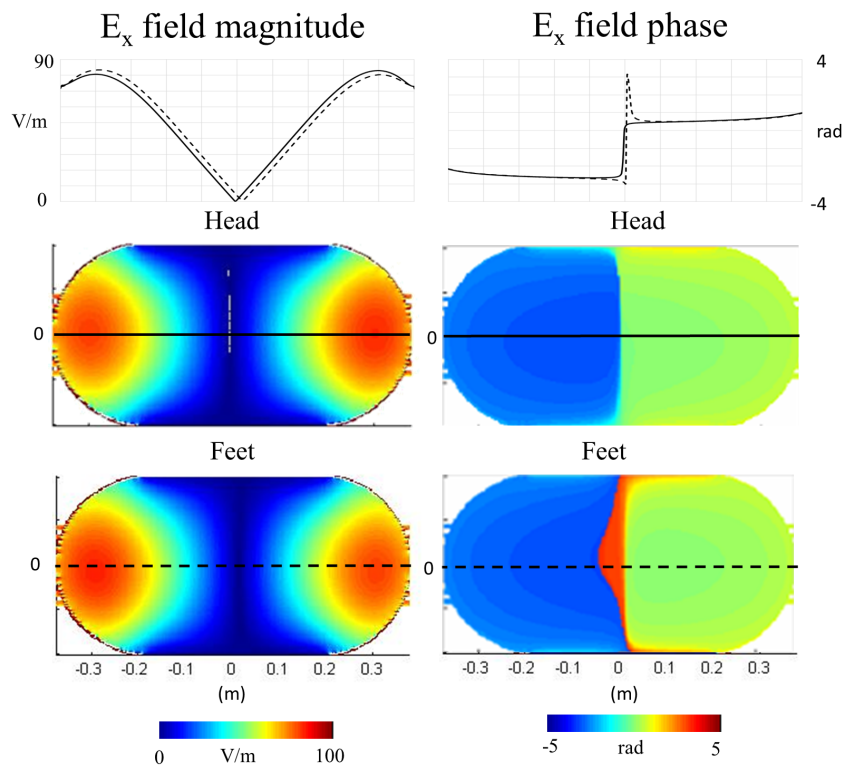
As expected by the phase results of the z component of the E field (figure 7.24), the phase profile was mostly affected by the $\Delta\varphi$, showing a mirroring of profile for the two opposite polarizations both inside and outside the phantom. In fact, as already shown by the phase map of figure 7.24, at the beginning of the extraction profile the CW polarization was characterized by a negative value of phase (i.e., -0.5 rad), whereas the CCW by a phase of the same quantity but with opposite sign.

As for the study with the human body models, both magnitude and phase results obtained with the G32 and H16 coil models corresponded with the one obtained for S2 but averaged with respect to the $\Delta\pi$ variability for the specific feed phase orientation

7.9 Evaluation of RF coil feed variability in the superellipsoidal phantom



(a) \vec{E}_z



(b) \vec{E}_x

Figure 7.24: Magnitude and phase distributions of the (a) \vec{E}_z and (b) \vec{E}_x components of the E field. The \vec{E}_z highlights the variation of the field with respect to $\Delta\varphi$, whereas \vec{E}_x with respect to $\Delta\pi$. Extraction of profiles inside the phantom plane was performed along the vertical line for the \vec{E}_z and along the longitudinal line for the \vec{E}_x .

A Numerical Investigation on effect of RF coil feed variability on global and local electromagnetic field exposure in human body models at 64 MHz

[W/kg]	Lead 1	Lead 2
uSAR	232.8	887.1
0.1gSAR	67.4	267.6
1gSAR	23.6	80.3
10gSAR	5.80	17.52

Table 7.3: Maximum SAR_{tip} for one of the two excitation rings in CW feed phase orientation ($\Delta\varphi$). Results are reported for the two case study simulated.

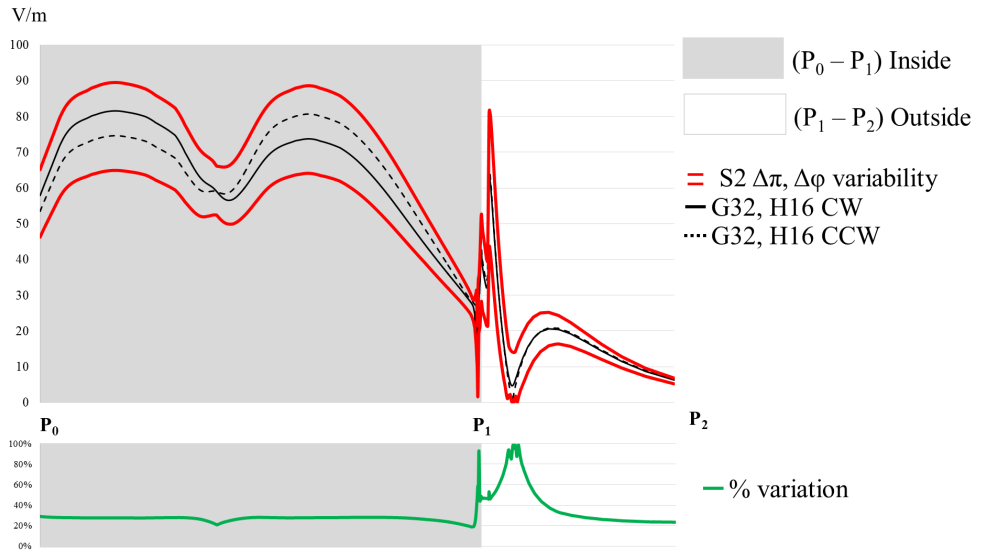
studied. Profiles are reported in Figure 7.25. As for the WbSAR, when comparing the results obtained with G32 vs. H16, there was less than 2% variability.

As in the study with the human body models, the results of the uSAR, 0.1gSAR, 1gSAR, and 10gSAR showed all the same variability with respect to $\Delta\pi$ and $\Delta\varphi$. Hence the radar plots in Figure 7.5 report profiles valid for all four quantities but normalized to the maximum value of the quantity of interest reported in table 7.3. Values found were more than doubled for Lead 2 with respect to Lead 1. In CW polarization, both lead showed a variability range with respect to $\Delta\pi$ equal to 0.28. However the Lead 1 had the maximum in 157.5° and the Lead 2 in 337.5° . In particular values with respect to $\Delta\pi$ showed the same profile for the two leads but turned 180° with respect to the corresponding feed phase couple used. This is due to the tip of the two leads being on the opposite side of the superellipsoidal phantom.

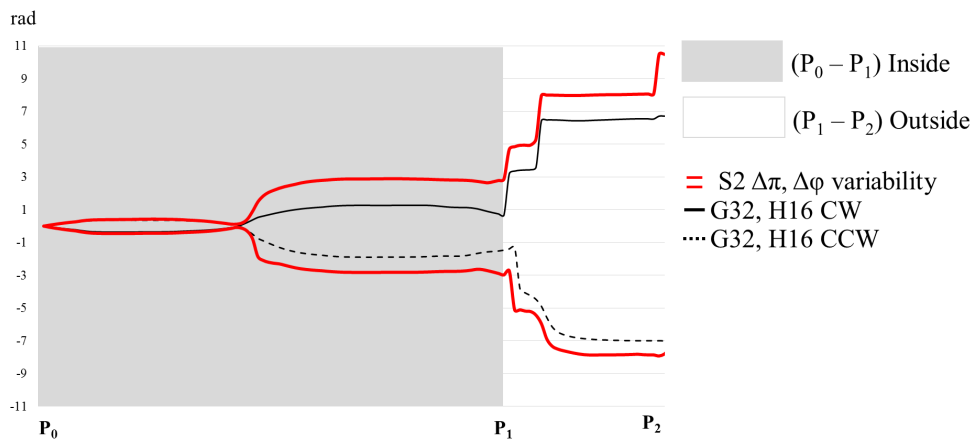
Using the same normalization procedure as with the human models, values of WbSAR up to 2.3 W/kg were observed. Thus, conversely with what observed with the human models, results were not in compliance with the limits defined by the standards in the first level of operation (table 5.1). The highest values of WbSAR caused a higher level of exposure with resulting higher $\|E_{tan}\|$ values inside and outside the phantom. Conversely, at the interface phantom/air $\|E_{tan}\|$ values were lower with respect to three of the five human models (i.e., Glenn, Duke and Billie). This is related to the specific location of the interface point with respect to the coil end-ring (i.e., $z = -325$ mm). For the phantom the extraction point was more similar to the one of Ella between the five human models.

Comparing the result with the leads with the case study in the two human models, Lead 1 showed values of SAR_{tip} out from the Head-CW variability of the human models. Conversely, SAR_{tip} obtained with Lead 2 showed values out from the Head-CW variability only for the uSAR and 0.1gSAR. 1g and 10gSAR obtained with Lead 2 were within the values found for the case study in both Glen and Duke. However both leads showed the variability range of 0.27 with respect to $\Delta\pi$ as the one found for the human models. Additionally, the profile of Lead 2 results resembled more the one obtained in the two human models Glen and Duke, even if Lead 1 showed the

7.9 Evaluation of RF coil feed variability in the superellipsoidal phantom



(a) $\|E_{tan}\|$



(b) phase E_{tan}

Figure 7.25: $\|E_{tan}\|$ and phase E_{tan} profiles for the superellipsoidal phantom along the extraction trajectory (Figure 7.20a). The grey area of each plots identifies the extraction section inside the phantom. Results are shown as stripes (identified by two red lines) including $\Delta\pi$ and $\Delta\varphi$ variability for the S2 model. Whereas profiles obtained with G32 and H16 are plotted as black lines with $\Delta\varphi$ variability reported by solid (CW) and dotted (CCW) line type.

A Numerical Investigation on effect of RF coil feed variability on global and local electromagnetic field exposure in human body models at 64 MHz

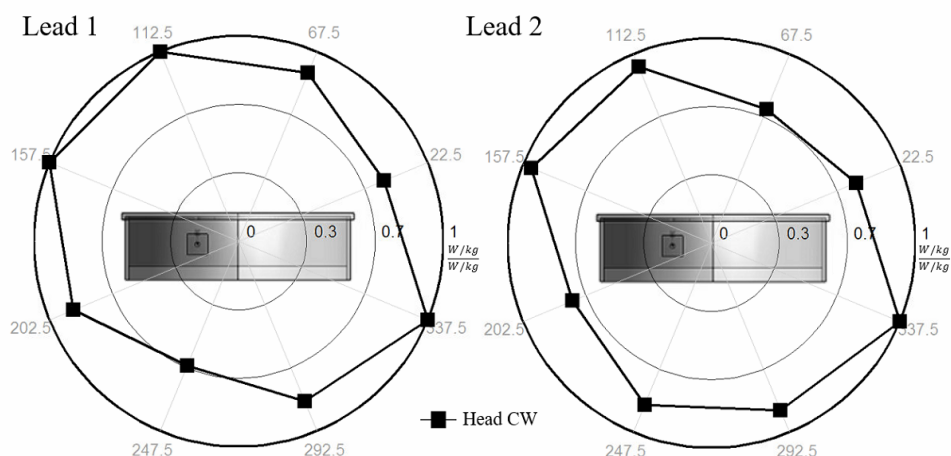


Figure 7.26: Values of SAR_{tip} obtained with each of the two leads (figure 7.21). As SAR_{tip} is only dependent by tip geometry, the profile with respect to $\Delta\pi$ and $\Delta\varphi$ applies to uSAR, 0.1gSAR, 1gSAR, and to 10gSAR. Each dataset was normalized to the maximum value of the quantity of interest.

maximum value of SAR_{tip} at the same feed pair (i.e., 157.5°).

All the results analyzed suggests some similarities between the superellipsoidal phantom and the human body models. However future work is needed to develop a systematic exposure procedure for RF heating evaluations of partially implanted leads in phantoms. These procedures must be able to mimic worst-case exposure in the patient.

Chapter 8

AIMD in MRI: evaluation of RF-coupling with leads

8.1 Physical phantom for testing of RF-induced heating in leads

8.1.1 Test field diversification method for the safety assessment of RF-induced heating of medical implants during MRI at 64 MHz

Experimental ¹ assessment of total dissipated lead tip power (TDLTP) is well defined by the standards presented in section 5.1.1. The total dissipated lead tip power (TDLTP) highly depends on the incident field characteristics (magnitude and phase of the \vec{E} , tangential to the conductive wire) [267]. However current experimental assessment suggested by the standards (section 5.1.1) typically only use a limited set of implant exposure conditions. While the amount of TDLTP is directly proportional to the incident field magnitude, diversity of the field polarization can also produce different phase distributions of the tangential E-field along the conductive lead. However, the dependency of the TDLTP on the phase of the tangential E-field is not trivial. In this section, a new experimental testing method which is able to diversify the RF-induced TDLTP of AIMDs. We evaluate the TDLTP for three generic implants for 1480 exposure conditions. An innovative cylindrical phantom was used as part of the testing procedure (Figure 8.1).

To determine the feasibility of the new diversification method over a wide range of lead lengths, three generic implants with 400 mm, 600 mm, and 800 mm insulated wires, similar to that in [241], were characterized with the piece-wise excitation method [268] at 64 MHz in homogeneous tissue-simulating medium ($\epsilon = 78$,

¹Part of this paragraph was presented at the BioEM 2016 conference in Ghent, Belgium. [266]

$\sigma = 0.47S/m$). The TDLTP was estimated for each exposure condition using the transfer function approach described in section 5.1.2 (eq. 5.9).

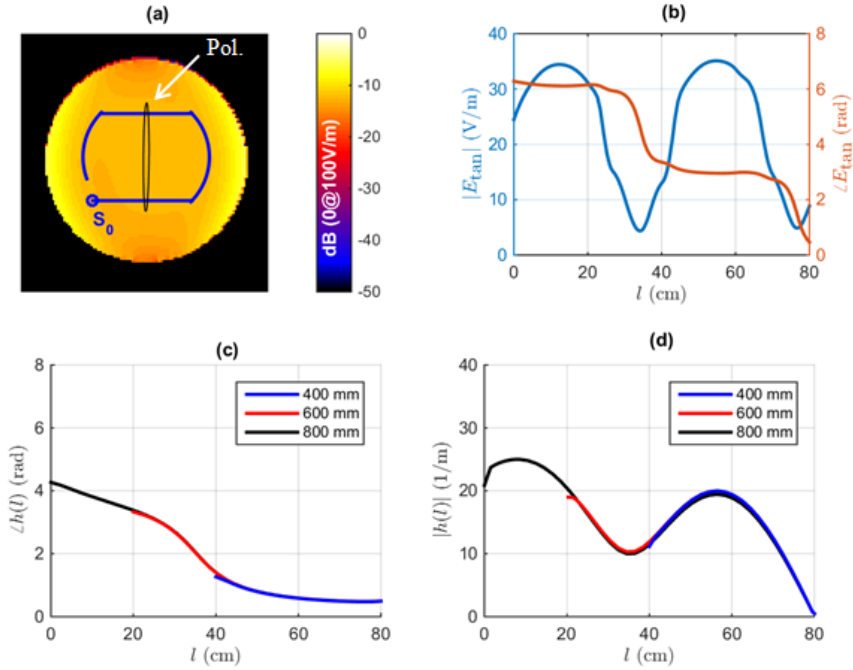


Figure 8.2: (a) Example incident B1 polarization (Pol. in black) and associated electric field distribution inside the cylindrical phantom through the implant plane; implant placement indicated in blue.(b) Amplitude and phase of \vec{E}_{tan} corresponding to (a). The transfer function of the three generic implants studied, phase (c) and amplitude (d).

Amplitude and phase of the E-field are defined along the length, L , of the lead with $L=0$ cm refers to S_0 indicated in Figure 8.2a). The implant is placed along a pathway that minimizes the coupling between different segments of the conductive wire with the phantom as illustrated in Figure 8.2a). The proposed test setup uses a cylindrical phantom landmarked at the isocenter of the MITS1.5 system.

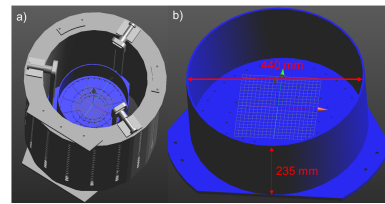


Figure 8.1: (a) Measurement setup: RF coil loaded with the Phase Phantom, (b) Phase phantom dimensions.

By adjusting the relative magnitude and phase between the two feeds of the coil, diverse exposure conditions can be achieved. The exposure condition was characterized with respect to the polarization of the B1-field at the center of the phantom. The spatial distributions of the total B1-field for 10 randomly chosen exposure conditions was validated against experimental results. The experimental evaluation was performed over a $260 \times 260 \text{ mm}^2$ area in the central axial plane of the cylindrical phantom. The

8.1 Physical phantom for testing of RF-induced heating in leads

experimental and numerical uncertainties are 0.8 and 0.5 dB, respectively. Thus the combined total uncertainty ($k=1$) is around 1.0 dB.

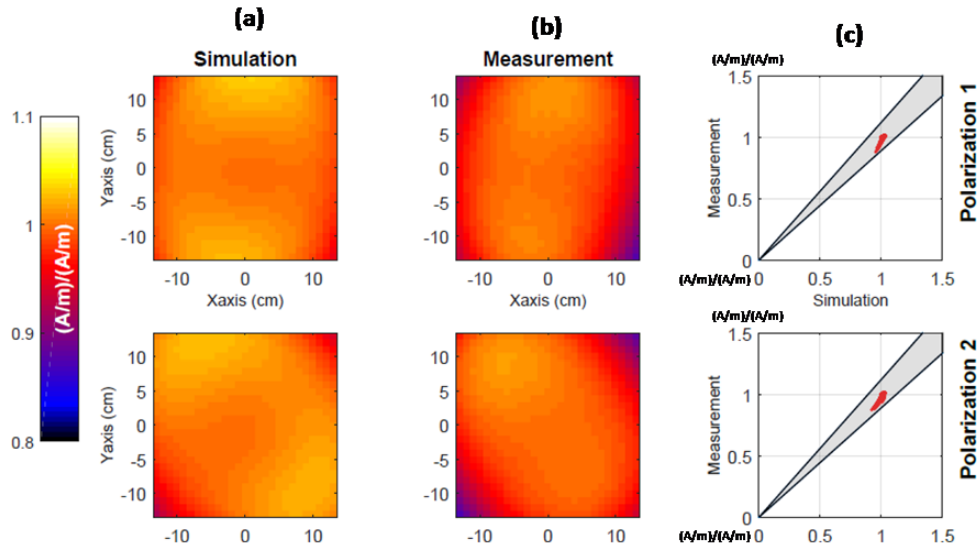


Figure 8.3: Examples of field diversification imposing two different polarizations of the \vec{B}_1 (i.e., polarizations 1 and 2). (a) Simulation of $\|\vec{H}\|$ at the central axial plane of Polarization 1 (TOP) and Polarization 2 (BOTTOM). (b) Corresponding measurement of (a). (c) One-by-one comparison between simulation and measurement, red points in the Figure are drawn with the coordinates based on the simulated value in the x-axis and the same measured value in the y-axis, the two black lines indicated variation of ± 1 dB between measure and simulation.

For each exposure condition, \vec{E}_{tan} was additionally extracted from simulations performed with the Sim4Life software (ZMT, Zurich Switzerland). Coil excitation was the same as the reference S2 coil model already presented in sections 2, and 3. Figure 8.2a shows the spatial distribution of the total $\|\vec{E}\|$ in the axial plane of the implant and the polarization of the incident \vec{B}_1 for a selected exposure condition; the corresponding \vec{E}_{tan} along the implant pathway shown in figure 8.2a is illustrated in figure 8.2b. The amplitude and phase of the transfer function for the three generic implants are illustrated in figure 8.2c and d.

Figure 8.3 shows two of ten simulated and measured spatial distributions of the total \vec{B}_1 . The deviation between experimental and numerical evaluation of the total \vec{B}_1 was found to be less than 1 dB, which was within the combined total uncertainty. Examples of computed percentage difference between the numerical and measured field is reported in figure 8.4. Percentage errors for the points and polarizations reported were within 0.4 % and 1.7 %.

Figure 8.5 shows the histogram of the predicted TDLTP for the generic implants inside the test phantom for all incident field conditions generated from 1480 B1 polarizations. Figure 8.5 also indicates the TDLTP, for the implant configuration shown in

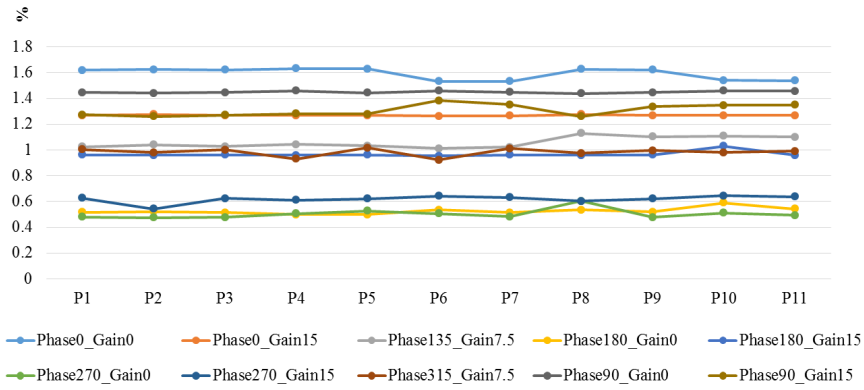


Figure 8.4: Percentage variation of the simulated magnetic field with respect to the measured one. Results are reported for 10 polarization setups for 11 points within the cylindrical phantom.

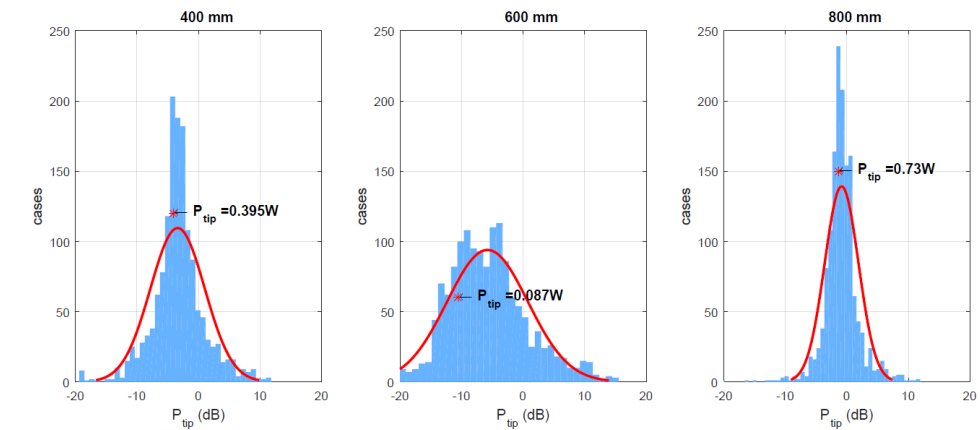


Figure 8.5: Histogram of deposited power (0 dB = 1 W), resulting from different incident B1 polarizations for the three generic implants studied.

8.1 Physical phantom for testing of RF-induced heating in leads

Figures 8.2a: 0.395 W, 0.087 W, and 0.730 W for the 400 mm, 600 mm, and 800 mm implant, respectively. The histogram was computed based on the distribution of deposited power with respect to the different phases and gain imposed to the two sources. Results in figure 8.6 show a resonance distribution of the power at the lead tip around the 180° with gain different from 0. The histogram relative to the same lead represents the enumeration of cases with respect to a defined computed power (e.g., 50 cases of polarization produced a 0 dB power at the tip).

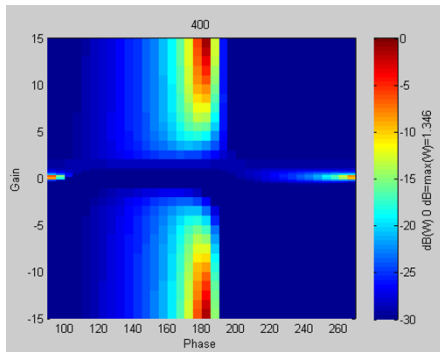


Figure 8.6: Deposited power for the 400 mm implant with respect to 180° variation in phase and 30 in the gain between the two sources of the coil.

For all implant lengths and all 1480 exposure conditions a dynamic range for the RF-induced TDLTP of over 30 dB was found. Thus the different exposure conditions may be sampled in practice to obtain an optimized set of diverse high-fidelity testing conditions for the assessment of implant safety due to RF-induced heating.

Once proven practical, the proposed method, which is in compliance with the radiated immunity tests required in ISO/TS 10974 [111], may improve the safety assessment of medical implants.

dB	Point1	Point2	Point3	Point4	Point5	Point6	Point7	Point8	Point9
Pol1	1.62	1.63	1.62	1.63	1.53	1.53	1.63	1.62	1.54
Pol2	1.03	1.04	1.03	1.04	1.03	1.01	1.02	1.13	1.10
Pol3	1.49	1.44	1.44	1.46	1.44	1.46	1.45	1.44	1.45
Pol4	1.27	1.26	1.27	1.28	1.28	1.36	1.35	1.26	1.337
Pol5	1.27	1.27	1.27	1.27	1.27	1.26	1.27	1.28	1.27
Pol6	1.00	0.98	1.00	0.93	1.02	0.92	1.01	0.98	1.00
Pol7	0.96	0.96	0.96	0.96	0.96	0.95	0.96	0.96	1.03
Pol8	0.63	0.54	0.62	0.61	0.62	0.64	0.63	0.60	0.62
Pol9	0.48	0.48	0.48	0.50	0.530	0.50	0.45	0.60	0.48
Pol10	0.52	0.52	0.51	0.50	0.54	0.51	0.53	0.52	0.59

Table 8.1: field percentage error of simulated dataset with respect to the measured plane for the selected 10 polarizations (in rows) imposing the measured polarization to the different 9 points (columns). For each polarization deviation within points was less than 4%

Polarization variance inside the cylindrical phantom Comparison of field polarization distribution inside the phantom showed that a small amount of field distortion can occur in different point of the phantom. This was due to interaction of the field

with the phantom and to physical limits of any exposure system. This is not to be considered a problem if similar distortion can easily be predicted by simulated data. The numerical dataset was indeed able to replicate the polarization distribution of the measurements with an overall error under 2 dB (as reported in table 8.1).

The location of the 9 measured points inside the phantom are reported in Figure 8.7. Hence it was verified that it is possible to measure only one point inside the phantom to properly account for the correct field polarization within the phantom in the numerical data. This result was considered important in the contest of safety assessment of an AIMD. Validation of numerical results is in fact fundamental allowing for trustable numerical evaluations of clinical scenarios that cannot be accounted for experimentally.

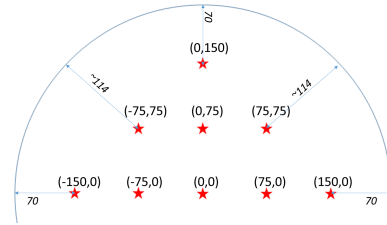


Figure 8.7: Measurement points selected inside the cylindrical phantom.

8.1.2 Applicability of the test field diversification method to AIMD

To assess the applicability of the described method for implant testing, the variability of power at the tip of a real implant was measured for different exposure.

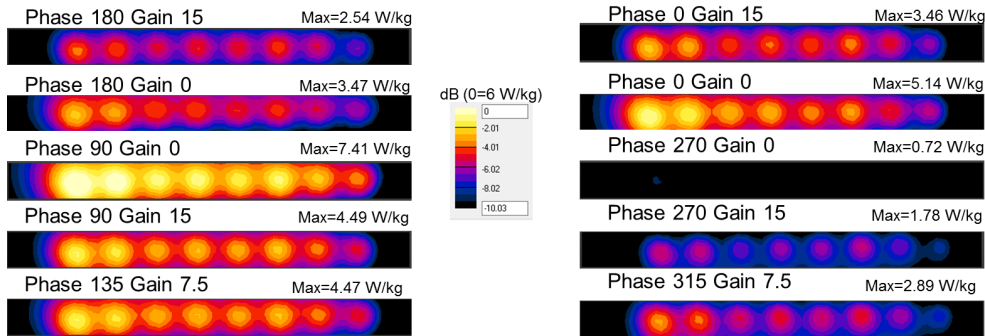


Figure 8.8: Measured SAR at the eight electrodes of a 700 mm lead for spinal cord stimulation. The SAR was measured for ten different exposure conditions.

The tested implant was a 700 mm lead for spinal cord stimulation. The lead was mounted inside the cylindrical phantom in accordance with the path defined in figure 8.2. A total of ten different sources settings were imposed to the physical coil, such that the implant was tested with respect to ten polarization. The lead was characterized by eight electrodes, and SAR mapping was measured for an area including all the electrodes of the lead.

As expected by the study performed with the transfer function, the power deposition at the tip of the implant was influenced by the variability of exposure. In particular

8.2 High dielectric material in MRI: numerical assessment of the reduction of the induced local power on implanted cardiac leads

differences up to 90 % were found for the two opposite settings characterized by the same gain but 180° phase difference (i.e., phase 90 - gain 0 vs. phase 270 - gain 0).

These results prove the feasibility of the proposed testing method.

8.2 High dielectric material in MRI: numerical assessment of the reduction of the induced local power on implanted cardiac leads

Section² 5.2 reported the context of the MR Conditional devices with respect to the exposure to RF field in MRI. However for patients with conventional implants there could be indications for MRI scans. In such situations with informed patient consent, the physician may decide to ignore the legal contraindications, weigh the risk factors, and perform off-label an MRI on an AIMD patient [269].

Pacemakers with MR Conditional labeling have been released into the EU market since 2008 [270] and into the US market since 2011 [271]. Additionally, the first MR Conditional ICD was approved for the EU market in 2011 [272] and for the US market in 2015 [273].

While the improved technologies have allowed such increase in access to MRI for patients with implanted PM/ICD, research is still ongoing to investigate additional solutions. Recently published papers have demonstrated that the appropriate placement of the high dielectric material (HDM) between human tissue and the RF coil is able to reduce the RF power level required for imaging while maintaining or even increasing B1 homogeneity [274], and thus increasing signal-to-noise (SNR) [275,276].

The coil model used for this study was the same as the reference S2 coil model already presented in sections 2, and 3. Conversely, the human body model used for this study was the Duke model from the Virtual Family V1.0 [100]. With respect to the one of the V3.0 (used in section 6.1) the model has only 70 anatomical structures with a spatial resolution of 1 mm.

Two MRI imaging positions were simulated, namely head and thorax (Figure 8.9). In the two cases, the position of the RF coil and the HDM pads was shifted to entirely cover the Region of Interest (RoI, figure 8.9).

The HDM was placed between the RF coil model and the body model, and was represented as two rectangular conformal pads with an average thickness of 20 mm, placed in contact with the anterior and posterior side of the body (Figure 8.10). Consistently with data reported in literature [274], a permittivity of 500 and an electrical

²Majour content of this paragraph was published as conference paper for the 2016 IEEE Engineering in Medicine and Biology Society [258]

conductivity of 0.35 S/m were assigned to the HDM.

The ideal deposited power at the end of the lead path was computed for the same value of $\|\vec{B}_1\|$ obtained in the RoI with and without the HDM pads. In particular, all simulations were normalized to obtain a $\|\vec{B}_1\|$ in the RoI corresponding to an average SAR of 2 W/kg without the HDM pads.

Table 8.2 summarizes the exposure conditions adopted in the simulations performed.

To predict the power induced by the MRI RF coil at the tip of an endocardial lead, the transfer function approach [241] was followed as suggested by the tier 3 approach of the technical specification ISO/TS 10974 [111]. The incident fields within the human

body model were obtained from the numerical analysis of the interactions between the RF birdcage coil the human body model. The E-fields induced in the body are responsible for the coupling mechanism produced in the implanted lead and, therefore, need to be studied at the location of the implant. For that purpose, a realistic clinical path of an endocardial lead implanted in the left pectoral region was implemented inside the human model as follows (Figure 8.10b): from the left subclavian vein through the left brachiocephalic vein, the superior cava, the right atrium, and down to the right ventricle, where the tip leaned against the heart wall.

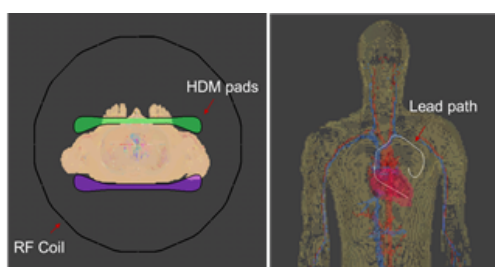


Figure 8.10: human body model inside the birdcage coil (a) Axial view; (b) Coronal view and lead path used for the study.

The distribution of local power deposition P at the lead tip was calculated from the E-field tangential to the lead path ($\|\vec{E}_{tan}\|$) determined as previously explained, according to the equation 5.9. The effect of the HDM was evaluated in terms of percentage

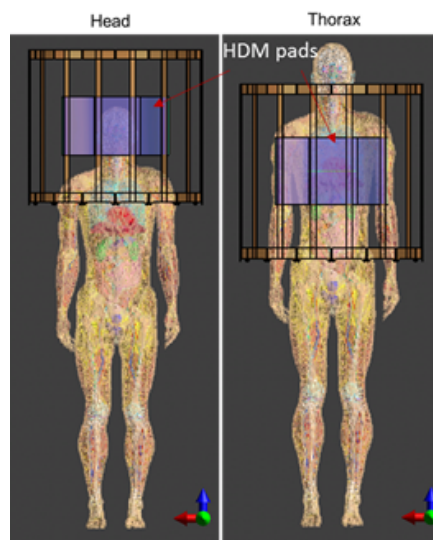


Figure 8.9: Human body model at head and thorax landmarks in the RF coil.

8.2 High dielectric material in MRI: numerical assessment of the reduction of the induced local power on implanted cardiac leads

	Without HDM Pads		With HDM Pads	
	Head	Thorax	Head	Thorax
$CoilInputPower(W)$	2260	865	1100	505
$Av.SAR_{RoI}(W/kg)^a$	2.00	2.00	0.86	0.64
$ B_1 (\mu T)^b$	6.3	3.6	6.3	3.6
$P(mW)$	673	1740	282	1578
$\%Av.SAR_{var}$	-	-	-57.0	-68.0
$\%P_{var}$	-	-	-58.0	-9.3

Table 8.2: My caption

variation of the estimated induced power:

$$\%P_{var} = \frac{P - P_{HDM}}{P} \cdot 100 \quad (8.1)$$

where PHDM and P are the induced power at the tip of the implant path with and without the HDM pads, respectively. Similarly, the variation in the average SAR induced in the ROI was estimated as:

$$\%Av.SAR_{var} = \frac{Av.SAR - Av.SAR_{HDM}}{Av.SAR} \cdot 100 \quad (8.2)$$

where $Av.SAR_{HDM}$ and $Av.SAR$ represent the average SAR induced in the ROI with and without the HDM pads, respectively.

Table 8.2 summarizes the results of the simulations performed. The HDM pads placed between the RF coil and the body allow achieving the same value of the magnitude of \vec{B}_1 at the isocenter, but significantly reducing the input power of the RF coil and, consequently, the SAR deposited in the patient. In particular, the average SAR measured in the RoI was reduced by 57% in the head and by 68% in the thorax. Such reduction in the average SAR corresponds to a similar significant reduction in the deposited power at the implanted path for the head, whereas a percentage variation of less than 10% is observed for the thorax.

Figure 8.11 reports the magnitude and phase of the \vec{E}_{tan} field computed along the lead path and used to estimate the induced power at the lead tip. The HDM pads do not affect the trend of the maxima and minima of the $\|\vec{E}_{tan}\|$: peaks and valleys are observed at the same points along the lead path, but the amplitude is decreased, in particular for the head landmark. The phase distribution does not substantially change with the presence of the HDM pads: as reported in Figure 8.11, the phase values do not change or are shifted by 2π all along the lead path.

Applicability of the method The use of HDM in magnetic resonance is a relatively recent but promising area of research. The fact that HDM are efficient magnetic field

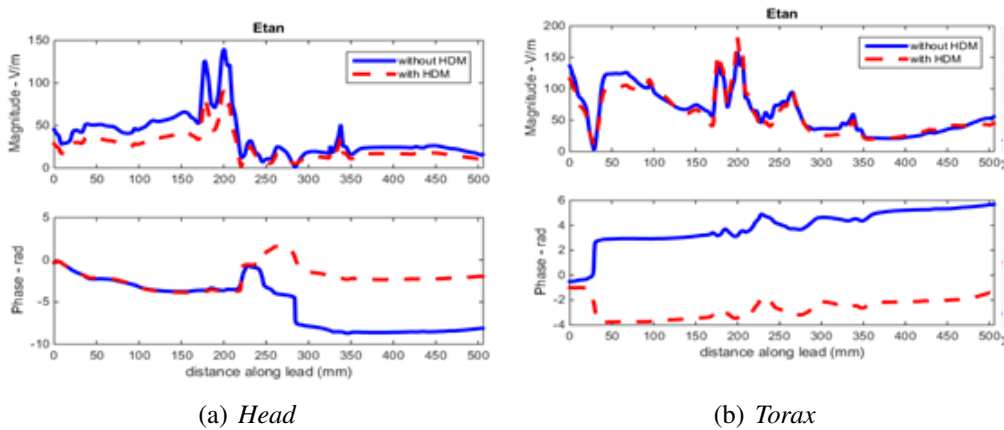


Figure 8.11: Magnitude and phase of the \vec{E}_{tan} field computed along the lead path for head (a) and thorax (b) landmarks.

storage devices [274] suggests that they could be incorporated into conventional RF coils (for example, either by providing a dielectric liner to the coil, or by filling the space between coil and shield), or could be placed as "pads" around the human body, to "tailor" the distribution and/or increase the homogeneity of the magnetic component of the RF field during MRI examinations.

It has been already demonstrated that HDM surrounding the head resulted in a reduction of required RF power by $\sim 50\%$ and an increase in image SNR by $\sim 27\%$ [275]. No local bias field induced by the dielectric pad in the entire cerebrum was observed in the images acquired and, on the contrary, the image uniformity within the cerebrum was shown to be somewhat improved.

In this study the effects of HDM on the induced heating at the tip of an endocardial lead was numerically assessed. In line to current literature, for all imaging landmark considered the HDM was able to significantly reduce the average SAR induced on the body, for a given magnitude of B1-field generated by the RF coil at the isocenter. Such SAR reduction corresponded to a marked decrease in the local-induced power at the tip of the implant path when the HDM pads do not cover the implant (head landmark), whereas only to a slight decrease when the implant is covered by the pads (thorax landmark).

The induced power along the implant depends on the Etan components of the E-field induced inside the human body, which is due to both the capacitive coupling with the coil and the inductive coupling with the time-varying B-field [277]. The HDM pads are able to reduce both the capacitive and the inductive coupling, only for the head landmark, whereas for the thorax only the capacitive coupling is reduced. Figure 8.12 show the effect of the HDM pads in the B1-field magnitude distribution. In addition, the results presented are valid of the specific lead path tested, and may vary for different

8.2 High dielectric material in MRI: numerical assessment of the reduction of the induced local power on implanted cardiac leads

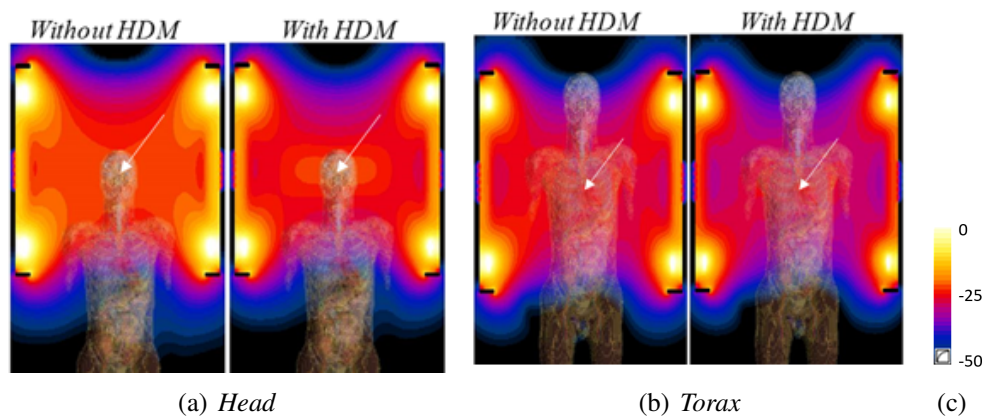


Figure 8.12: Comparison between the B₁-field distribution (magnitude RMS) on the implant coronal plane with and without the HDM pads: head (a) and thorax (b) landmarks. (c) Color maps are in log scale (0 dB=75 μT). $\|B_1\|$ RMS magnitude is the same at the isocenter (white arrows).

paths. Nevertheless, the study is to be intended as a proof of concept of the possible effect of HDM on local induced current in an endocardial lead. Future studies in this field could focus on the effects of different lead paths, different human models, or on the use of receive-only coils in combination with HDM.

Results suggest that HDM could be adopted in MRI scanning of patient with PM, ICD or, in general, with metal implants, to reduce the risk of unwanted overheating. In particular, when the implant was not included in the volume surrounded by the HDM, the pads placed between the RF coil and the patient allow obtaining the same magnitude of \vec{B}_1 with a lower input power of the RF coil, reducing significantly the local induced power around the implant. Conversely, if the implant is included in the volume surrounded by the HDM (i.e., thorax landmark), the use of HDM can still reduce the input power necessary to obtain the same magnitude of B₁, but the effect on the local induced power at the implant become less marked. In this case, optimization strategies to tailor the resulting magnetic field could be adopted to limit as much as possible the coupling with the implant: HDM could be used to maximize the B₁-field in the specific region that has to be imaged, and to limit it, where possible, along the lead path.

8.2.1 Evaluation of a third landmark position: Pelvis

As a proof of concepts of the results reported for the Head and and Torax landmark, herein the effect of the HDM pad was studied on a third landmark.

The third imaging position studied was the Pelvis. The human body model Duke was landmarked within the coil with the pelvis at the isocenter as reported in Fig-

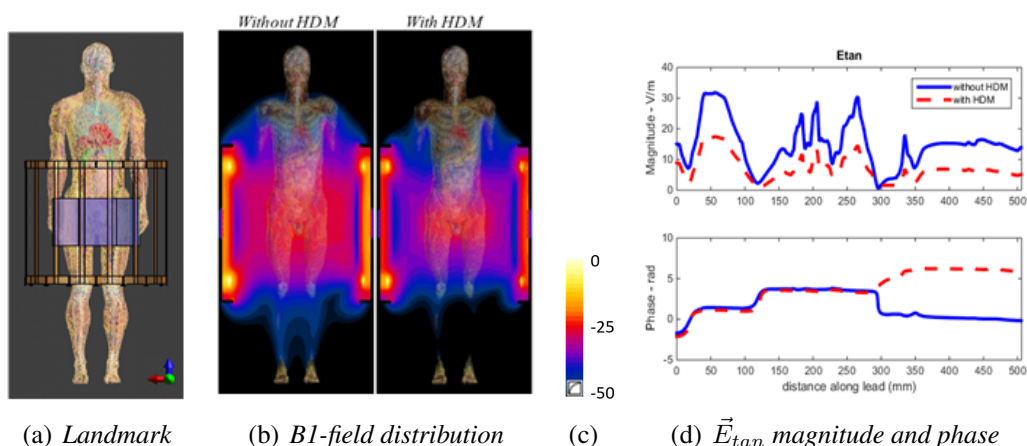


Figure 8.13: Magnitude and phase of the \vec{E}_{tan} field computed along the lead path for head (a) and thorax (b) landmarks.

Figure 8.13. Results in the pelvis landmark were within the same range of variability as the one of the head landmark. In particular, with the HDM pad present the average SAR measured in the RoI was reduced by 62.5%, and the computed deposited power at the implant tip was reduced by 75 %. Figure 8.13 reports the profile of the $\|\vec{E}_{tan}\|$ extracted along the lead path for the situation without and with the HDM pad present. Reduction of the $\|\vec{E}_{tan}\|$ is responsible for the 75 % reduction of the computed power at implant tip. As already reported in the paper, the reduction of SAR and tip power is related to the reduction of coil power when the HDM is present. Because of the lower radiated power, the magnetic field produced by the coil is everywhere lower except in the region under the HDM, as shown by Figure 8.13. Hence the lower magnetic field induces lower eddy currents inside the patient (section 5.1), with a resulting less power density. As a conclusion the results obtain with the additional landmark, confirm that HDM could be adopted in MRI scanning of patient with AIMD to reduce the risk of unwanted overheating.

Comprehensive Discussion Part II

In Part II the discussion of the RF MRI exposure was extended to the analysis of the interaction of the EM with phantoms of human body modeling a patient. With respect to the study of the modeling of human body, the second chapter of Part II carried out an analysis on the use of homogeneous and heterogeneous models. Interesting results of this study was the similarity between homogeneous and heterogeneous models with respect to the power absorption profile along the body of the model. The strength of this outcome can be found in the ability of homogeneous models to be used as simplified tools to determine a first step evaluation of the exposure within the body and to characterize which part of the body is subjected to an higher exposure. Conversely, results obtained with homogeneous models can be considered only qualitative and as supporting information to the one obtained with heterogeneous models. In fact homogeneous models were proved to underestimate the local hot spots of energy absorption due to the presence of the organs present in the heterogeneous ones. It is particularly important to evaluate this peaks of absorption for a complete estimation of the patient safety. Further investigations of this study should quantify the underestimation of the exposure for the homogeneous models in order to better identify when such models can be a useful simulating tool. An additional analysis should also investigate the thermal effects of such localized hot spots to contextualize the effect with respect to the tissue damage.

In chapter 6.2 homogeneous models were used to prove vague the definition of the PbSAR with respect to the effective length of the RF coil used. Results showed that an high variability of the exposure effective length depended on the model shape and material used. Outcomes of this study suggest that the actual definition of patient exposure provided by the standard IEC 60601-2-33 standard need to be revised. Further developments of the study should include additional testing variable that will allow to provide a derivation of an alternative definition of the PbSAR within the standard. Specific tests should be able to define the worst case effective length to be used by the user based on the geometrical characteristics of RF coil implemented. Such approach will allow for a generalization of the definition from the patient but with the specificity of the exposure system.

As already introduced in Part I for phantoms, Part II continues the analysis of the EM field distribution variability with respect to the coil model used. The first part of the study quantifies the sensitivity of the exposure with respect to the position of the feeding ports in the S2 coil model (for more details on the model see chapter 3) and compares it with the one produced by the G32 and H16 coil models. As in the case of the phantom, results proved that the G32 and H16 models were able to quantify the exposure but can not be used to drive any specific conclusion. In particular the G32 and H16 models were not able to reproduce the variability span imposed by the sensitivity of the S2 model with respect to the feeding conditions. This outcome is particularly important because until now the dependency of the exposure related to the feeding conditions was never explored. Further investigations of this study should expand the analysis to different landmarks of the human body model within the coil.

Part II also introduced the investigation of a compatibility study on the exposure of patient with partially or fully implanted medical devices. A first analysis was performed for a model of a partially implanted lead inserted at the groin of the human body model. The quantification of the exposure for such partially implanted lead was performed in the context of the analysis of the exposure variability with respect to the feeding coil conditions. This study can be considered particularly interesting because the question of partially implanted devices it is still considered unresolved by the scientific community. In fact currently no standardized procedure is available for testing the compatibility of partially implanted lead with MRI. Even if basic the results reported by the performed study showed that partially implanted lead are particularly affected by the exposure variability because part of the lead is outside the body where the fields are higher and more sensitive. Future investigation of this should include systematic simulations with the addition of thermal analysis.

A second interesting outcome of the results reported in chapter 7 is the powerful of the transfer function approach. This approach allows for an easy and versatile estimation of the power deposited at the tip of a lead. This estimation tool was also used to propose a new testing procedure and phantom for the evaluation of leads exposure (8.1), and to determine whether external materials with specific characteristics could be used to decrease the interaction between leads and the EM RF fields (8.2). Results proposed are both promising. The new testing procedure and phantom can be considered a valid improvement to the already standardized phantoms. In particular the procedure proposed does not require the lead to be moved during the testing, with a corresponding reduction of user's error. Additionally the geometry of the new phantom proposed allows for a highly controlled exposure during the test because the lead is placed along a path with constant field characteristics.

Part III

Computational modeling of human head models exposed to low frequency electromagnetic fields

Chapter 9

Background and State of the Art

EM fields have gained increasing importance in the field of healthcare. The major applications are based on direct interaction of the EM fields either to acquire diagnostic information, or to deliver energy for treatment. The figure [278] reports a synopsis of some application of the EM field in medicine.

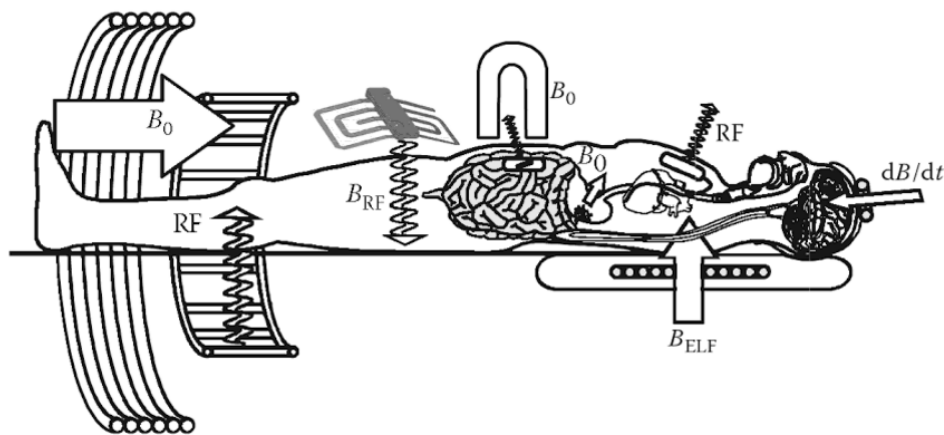


Figure 9.1: Figure riadapted from [278]. EM field application in medicine with static fields B_0 , extremely low-frequency (ELF) magnetic fields B_{ELF} , magnetic transients dB/dt , and RF EM fields for magnetic resonance imaging, diathermy, magnetic navigation and device tracking, capsular endoscope, magnetic therapy, transcranial magnetic stimulation, tracking nanoparticles, and remote transmission

The diagnostic application of the EM field trough MRI has been discussed in the first two parts of this thesis. Other examples of diagnostic applications of EM fields are: i) the Pulse Oximetry that makes use of the red and infrared light absorption characteristics of oxygenated and deoxygenated hemoglobin; or ii) the computed tomography (CT) that uses the X-ray to produce cross-sectional images of the body. This section of the thesis discusses the use of EM fields for treatment in healthcare.

9.1 Medical devices using EM fields for brain stimulation

Any instrument, apparatus, appliance, software, material and other device intended to be used for human medical purpose can be defined a medical device. The use of EM field for treatment and diagnostic includes a wide range of frequency of the fields used. Frequency range can go from the static and ELF to microwave radiation. For such broad range of frequencies, the physical nature of these fields as well as the mechanism behind the interactions and propagation within media changes. In medical therapy, electric, magnetic, and EM fields combined are applied to stimulate diverse type of tissues or cells (e.g., nerve and muscle), stimulate healing, or deliver heat for treatment or as a secondary effect such as for application in drug delivery. Among all the medical therapies that make use of EM field for treatment of diseases, the work performed within this thesis focused on the use of EM field for brain stimulation. Cerebral stimulation therapies involve activating or inhibiting areas of the brain directly with EM fields. The current can be directly be applied to the brain by means of electrodes implanted in the brain (i.e., invasive devices), or non invasively through the scalp (i.e., non invasive devices). The potential of the medical applications using electrical stimulation of the body has been recently evidenced by the coined term "electroceutical" by Famm et al. [279]. The term describes the all the multidisciplinary initiatives made to develop "medicines" that use electrical impulses to modulate the body's neural circuits (figure 9.2).



Figure 9.2: Electric and magnetic stimulation can affect and modify nervous system functioning, and this is an intriguing perspective in the field of biomedical applications (figure from Famm et al. [279]).

9.1 Medical devices using EM fields for brain stimulation

9.1.1 Invasive devices

Invasive brain stimulation is used to treat psychiatric and neurological disorders producing electrical impulses directly into specific area of the brain. The stimulus is given through electrodes implanted chronically into the brain. The stimuli, delivered through the electrodes, are generated by a neurostimulator named the Implanted Pulse Generator (IPG). As for the pacemakers introduced in section 8.2, the IPG of the neurostimulators is surgically implanted, typically under the clavicle near the collarbone [280]. The median battery life of the IPG is of 37.4 ± 17.3 months (range: 4–93 months) [281]. However the life of the battery is highly affected by the stimulus amplitude, pulse width, and stimulation settings used (e.g., bipolar, unipolar). Typical parameter settings of the neurostimulator range from 1–3.5 V, 60–210 μs , and from 30–185 Hz, for the voltage, pulse width, and frequency, respectively [282–286]. The most used neurostimulator are the Deep Brain Simulator (DBS) and the Vagus Nerve Stimulator (VNS).

DBS - Deep Brain Simulation (DBS) is an effective treatment of symptoms of several for several movement disorders, such as Parkinson's disease (PD), essential tremor (ET), and dystonia [287]. DBS is FDA and CE-approved for the treatment of these diseases in patients who no longer respond to pharmacological medication; it is an invasive stimulation technique, where a biphasic pulsed electric stimulus is delivered by implanted electrodes to the basal ganglia, the brain regions associated with the control of voluntary motor movements. The brain nuclei mostly chosen as stimulation targets are the subthalamic nucleus (STN) for the PD, and the globus pallidus (Gp) and ventral intermediate (VIM) nucleus for the ET [280, 288–291].

Despite the effectiveness of this treatment, currently there is no consensus on the mechanisms that explain the therapeutic effects of DBS; furthermore, there are some complications related to the DBS procedure (infections, strokes, intracerebral hemorrhages, seizures and even death). Hence its use is largely restricted to patients who have failed to respond to other therapies.

The aforementioned complications and the high cost of the surgical procedure, both in terms of costs and of human resources, are the main limitations of the DBS. Moreover, while some progress has been made in programming tools and current generators, there are limited capabilities in programming strategies.

VNS - As for the DBS, the Vagus Nerve Stimulation (VNS) is a procedure that involves electrodes implanted inside the body. The target of the VNS is to send electrical pulses through the left vagus nerve, that is one of the two nerves that run from the brain-

stem through the neck and down to each side of the chest and abdomen. The VNS has been originally used by physicians to treat epilepsy for patients that did not respond to anti-seizure drugs. Over the past years, VNS was also found to be beneficial for patients with depression. In fact, the use of the device affects areas of the brain that are involved in the mood regulation. The electric pulsed generated by the VNS alter the levels of neurotransmitters associated with mood, including serotonin, norepinephrine, GABA, and glutamate. Besides treatment of epilepsy, in 2005 the first VNS device was approved by the FDA as non first-line treatment for patient older than 18-year old with chronic, hard-to-treat depression.

9.1.2 Non invasive devices

In 1980 Merton and Morton [292] presented for the first time a technique to stimulate two areas of the human cortex without induce discomfort to the patient. Until that time, the stimulation of the brain was conducted only after the opening of the human skull by surgical procedure. Their success was related to the use of "brief but very high voltage shocks", that were previously used only for the stimulation of the human hand muscles. The voltage shocks used were up to 2000 V, and they were applied to the patient scalp through a couple of electrode. Following the work of Merton and Morton, over the years a large number of stimulators able to deliver brief but very high voltage shocks have been introduced in the market and in the clinical practice [293]. Examples of non-invasive stimulation of the brain are Transcranial Magnetic Stimulation (TMS), Pulsed Electromagnetic Fields (PEMFs), and transcranial Direct Current Stimulation (tDCS) [294].

TMS The TMS is a noninvasive and painless technique that delivers brain stimulations via externally applied magnetic fields generated by a coil positioned above the patient's scalp surface [295]. The coil, fed by a current pulse, generates a time varying magnetic field that penetrates into the head's tissues placed in the near field zone of the coil.

Over the past years, TMS has become an important tool for clinical applications, representing a promising alternative treatment for a broad range of neurological and psychiatric disorders including strokes, PD, tinnitus, epilepsy, and depression [296]. TMS has also been extensively used for diagnostic as a brain mapping tool. Stimulation of the motor cortex can evoke a jerk in muscles on the opposite side of the body, that can be measured with electrophysiological methods. One pulse directed to the back of the brain can generate a flash of light in the eyes.

A TMS device generates short ($\sim 100 \mu\text{s}$) but intense ($\sim 1 \text{ T}$) pulses of magnetic

9.1 Medical devices using EM fields for brain stimulation

field [297–299]. The magnetic field easily penetrates safely and painless the scalp and skull; the rapid changes of the stimulation signal (from zero to ~ 1 T, then back to zero again in hundreds of μs), induce electrical currents in the area of the brain beneath the coil whose amplitude is similar to the one produced by a conventional stimulator applied directly to the surface of the brain. The spatial resolution of TMS is highly dependent upon the shape of the stimulating coil, but can be on the order of a few millimeters with certain coil types (e.g., figure-eight coils with 45 mm circular diameter components).

Single pulse stimulation is characterized by a short response, while magnetic field pulses emitted in rhythmic succession, namely repetitive TMS, or rTMS, can have more prolonged and complex effects on the brain; some of these effects may relate to process of synaptic plasticity such long-term depression/potential [300]. Different or opposite effects can be obtained changing stimulation properties such as the number of pulses, the rate of application and the intensity of each stimulus.

rTMS has been under investigation for the treatment of depression, and recent reports indicate it to be at least as effective as other treatments. In theory, rTMS could be a useful therapy for any brain disorder involving dysfunctional behavior in a neural circuit [298]. However, little is known about the real functioning of rTMS at cellular level, thus hampering a conscious and focused development of biomedical applications. Moreover, because the strength of the magnetic field falls off rapidly with distance following the inverse-square law, a limitation of TMS is that only the outer cortex of the brain and the surface of cerebellum can be targeted; it is possible to reach sub-cortical regions using pulses with higher intensities, but also the outer regions would be affected [301]. For this reason, a new design for coils has been recently developed expanding the basic principles of TMS from the use of a single focal stimulation source to a summation of many elements (deep TMS [302]); in this way, it is possible to modulate cortical excitability up to a maximum depth of 6 cm. Because of these characteristics, this new technique is gaining the attention of the global medical community as a possible therapeutic tool in the treatment of numerous pathological conditions.

tDCS Compared to the TMS that uses pulses of magnetic field, the tDCS is a form of neurostimulation which uses constant, low current delivered to the brain via electrodes on the scalp. A constant, low intensity current is passed through two electrodes which modulates neuronal activity.

Two possible stimulations can be performed with the tDCS: anodal and cathodal stimulation. Anodal stimulation acts to excite neuronal activity while cathodal stimula-

tion inhibits or reduces neuronal activity. Although tDCS is still an experimental form of brain stimulation, it has several possible advantages over other brain stimulation techniques. Several studies suggest that tDCS may be a valuable tool for the treatment of neuropsychiatric conditions such as depression, anxiety, Parkinson's disease, and chronic pain [303–306]. Cognitive improvement in patients undergoing tDCS have been also reported [307–309]. Currently, tDCS is not an FDA-approved treatment.

PEMFs PEMFs are mostly used in orthopedic applications, because it has been demonstrated that a PEMF applied across a bone fracture can accelerate the healing process [310], this therapy has been approved by the FDA to stimulate bone growth.

However, a large number of recent studies (reviewed in [311]) have explored the effects of extremely low frequency (0-300 Hz) magnetic fields of few mT also for what concerns neurophysiological aspects, demonstrating that they can influence brain activity.

Studies on the central nervous system (CNS) revealed measurable changes in brain electrical activity and suggested modifications of several neuronal functions such as motor control, sensory perception, cognitive activities, sleep and mood [312–314]. Moreover, other studies showed PEMFs to influence biochemical reactions inside ischemic tissues inducing a protective effect against focal cerebral ischemia [315–317].

PEMFs are typically preferred to sinusoidal waveforms because the fast rate of change of magnetic field (order of T/s) is able to induce significant currents inside biological tissues, which, in turn, can trigger biological effects [311]. Waveforms and frequency content of PEMFs used in literature to expose CNS are various and flexible [318, 319], mostly chosen on empirical basis and without a solid rationale driven methodology [319]. They can be trains of monophasic, biphasic, quasi-rectangular, or quasi-triangular pulses, with repetition frequency on the order of tens of Hz [311, 318, 319]. A quite complex time pattern is exhibited by the complex neuroelectromagnetic pulse [318, 320–322], which has been shown to be effective in modulating neuronal activity by experimental [323–326] and modeling [327] studies.

Recently, other pulsed signals, similar to those adopted in the treatment of osteoarthritis [328, 329], e.g. the I-ONE (I-ONE; IGEA, Carpi, Italy), have been positively used [330–332] due to their proven effectiveness on other kinds of cells and tissues.

Despite such waveform variability, PEMFs signals have some common characteristics. Differently from TMS using quasi-monochromatic [333] signals, they may occupy a larger frequency band, from static up to some tens of kHz [334, 335], due to sharp rise and fall edges, although the pulse repetition frequency lies in the ELF range.

9.2 Numerical modeling of the quasistatic approximation

Moreover PEMFs are not so focalized as TMS, which act locally to affect a specific brain function; the neuronal targets regions of pulsed stimulation are not univocally defined, thus the adoption of exposure systems able to generate a homogeneous magnetic field in the whole brain volume becomes a need. A valid example is the Helmholtz coil arrangement used in many experimental studies [322, 336–340].

The increasing amount of available literature data confirm that PEMFs are widely used, nevertheless the experimental results on low-level PEMFs stimulation are often inconsistent and the action mechanisms on the brain are still poorly defined [311]. Possible causes of such conflicting results are the heterogeneity of the used exposure systems and the different characteristics of the stimulating PEMFs, such as frequency content, amplitude, duration, and waveform [311]. Therefore even considering the same signal amplitude, different PEMFs may interact differently with tissues and cells.

9.2 Numerical modeling of the quasistatic approximation

9.2.1 Theoretical background

While at RF the electric and magnetic field are always coupled, as described by Maxwell's equations, at the low frequency range a quasi-static approximation can be used. Such approximation consists on decoupling the E and H-field, because the dimensions of the exposed body are electrically small compared to the field wavelength. Specifically the approximations are strictly related to the dimensions of the exposed object with respect to the incident wave. In the static or quasi-static state ($\omega \rightarrow 0$), the E and H fields are completely decoupled, and therefore can be solved independently. For static field Maxwell's equation are heavily simplified into decoupled electrostatic and magnetostatic equations. Conversely, in quasi-static state only one of the two time derivative becomes important for the calculation depending on the relative importance of the two dynamic coupling terms. The Quasi-static approximation implies that the field at a given time are determined independently on what the sources of the field were at an earlier time [341, 342], because the process under consideration is much slower than the propagation time of an EM wave. Hence, quasistatics approximation assumes that the field strengths change so slowly in time (quasistatic) that the E and H fields induced by those changes (the contributions to E and H from the $\partial/\partial t$ terms in Maxwell's equations) are sufficiently small, and by consequence the induced fields ($\propto (\partial/\partial t)^2$) can be neglected (i.e., fields are decoupled); only the original and first-order induced fields are therefore of interest.

Three major quasistatic models can be considered: the electroquasistatic (EQS),

magnetoquasistatic (MQS), and Darwin models. Specifically the EQS model considers only the capacitive effects neglecting the temporal change of the magnetic flux (i.e., magnetic induction), the MQS model considers inductive effects neglecting the temporal change of the displacement currents, whereas the Darwin model includes both the capacitive and inductive effects.

Overall the quasi-static laws can be obtained from Maxwell's equations by neglecting some of the time dependent components. Specifically the quasi-static models act on the Faraday's and Ampere's law. The Faraday's law was already introduced in section 2.4 (eq. 1.12):

$$\nabla \times \vec{E} = -\frac{\partial \vec{B}}{\partial t} \quad (9.1)$$

Ampere's law is defined by:

$$\nabla \times \vec{B} = \mu_0 \left(\vec{J} + \varepsilon_0 \frac{\partial \vec{E}}{\partial t} \right) \quad (9.2)$$

The three quasistatic models, can be obtained as follow:

- **EQS:** the temporal change of the magnetic flux is neglected from the Faraday's law (1.12), that becomes: $\nabla \times \vec{E} = 0$.
- **MQS:** the temporal change of the displacement current is neglected from Ampere's law (9.2), that becomes: $\nabla \times \vec{B} = \mu_0 \vec{J}$
- **Darwin:** considers the magnetic flux defining the E field as a sum of a Faraday E field (\vec{E}_F), and a Coulumb E field (\vec{E}_C). Where the \vec{E}_F plays a role in the Faraday's law (1.12), that becomes: $\nabla \times \vec{E}_F = -\partial \vec{B} / \partial t$; and the \vec{E}_C plays a role in the Ampere's law (9.2), that becomes: $\nabla \times \vec{B} = \mu_0 \left(\vec{J} + \varepsilon_0 \partial \vec{E}_C / \partial t \right)$

where the \vec{E}_F is defined by the Biot-Savart integral:

$$\vec{E}_F(\vec{r}, t) = \frac{1}{4\pi} \iiint \frac{\partial \vec{B}(\vec{r}', t)}{\partial t} \times \frac{\hat{R}}{R^2} d\tau' \quad (9.3)$$

where r denotes the the position in the space τ of the point P , $\vec{R} = \vec{r} - \vec{r}'$, $R = |\vec{R}|$, and $\hat{R} = \vec{R}/R$ And \vec{E}_C is defined by Coulumb integral:

$$\vec{E}_C(\vec{r}, t) = \frac{1}{4\pi\varepsilon_0} \iiint \frac{\rho(\vec{r}', t) \hat{R}}{R^2} d\tau' \quad (9.4)$$

where $\rho(\vec{r}', t)$ is the charge density.

Scalar potentials - Numerical solutions of the quasistatic formulation are typically solved based on the potentials definition of the electric (V) an magnetic (A) fields.

9.2 Numerical modeling of the quasistatic approximation

Under the EQS approximation the \vec{E} can be considered irrotational (i.e., $\nabla \times \vec{E} = 0$), and the \vec{E} can be expressed as the gradient of the scalar electric potential V . Based on the gradient theorem, V can be expressed as the amount of work required to move a charge of $\vec{R} = \vec{r} - \vec{r}'$:

$$-\int_r^{r'} \vec{E} d\tau' = V(r) - V(r') \quad (9.5)$$

that follows

$$\vec{E} = -\vec{\nabla}V \quad (9.6)$$

thus from the first Gauss's law

$$\nabla \cdot \vec{E} = \rho/\varepsilon_0 \quad (9.7)$$

it is possible to define the equation of potential as:

$$\begin{aligned} \nabla \cdot (-\vec{\nabla}V) &= \frac{\rho}{\varepsilon_0} \\ \vec{\nabla}^2 V &= \frac{\rho}{\varepsilon_0} \end{aligned} \quad (9.8)$$

However if the time varying component of the magnetic field cannot be neglected, as for a MQS and Darwin model, it is not possible to describe the E field simply in terms of a scalar potential V , but also as a function of the magnetic potential \vec{A} . Form the second Gauss's law

$$\nabla \cdot \vec{B} = 0 \quad (9.9)$$

it is known that the total magnetic flux of a closed loop is zero, hence it is not possible to have magnetic monopoles. Additionally for any vector function \vec{F} it is true that $\nabla \cdot (\nabla \times \vec{F}) = 0$. Thus the second Gauss's law 9.9 can be rewritten as a function vector named the magnetic potential \vec{A} :

$$\begin{aligned} \nabla \cdot \vec{B} &= \nabla \cdot (\nabla \times \vec{A}) \\ \vec{B} &= \nabla \times \vec{A} \end{aligned} \quad (9.10)$$

Because now the E field cannot be considered irrotational anymore, the Faraday's law can be rewritten in function of A :

$$\nabla \times \vec{E} = -\frac{\partial(\nabla \times \vec{A})}{\partial t} \quad (9.11)$$

thus:

$$\nabla \times (\vec{E} + \frac{\partial \vec{A}}{\partial t}) = 0 \quad (9.12)$$

as the curl of the gradient of any twice-differentiable scalar field is always the zero vector, it is true that $\nabla \times (-\nabla V) = 0$. Hence, it is possible to write eq. 9.11 as follow:

$$\begin{aligned} \nabla \times (\vec{E} + \frac{\partial \vec{A}}{\partial t}) &= \nabla \times (-\nabla V) \\ \vec{E} + \frac{\partial \vec{A}}{\partial t} &= -\nabla V \\ \vec{E} &= -\frac{\partial \vec{A}}{\partial t} - \nabla V \end{aligned} \quad (9.13)$$

It can be concluded that the E filed in terms of gradients can be written as the sum of the Coulumb ($E_C = \nabla V$) and Faraday electric field ($E_F = -\partial \vec{A} / \partial t$). Then the magnetic vector potential \vec{A} at an arbitrary position r generated by a current stimulation flowing through a discretized coil (assuming a uniform current density over the coil cross section) is given by the following integral expression derived, for a filiform circuit, from the Poisson's equation:

$$\vec{A}(r) = \frac{\mu_0 I}{4\pi} \int_l \frac{dl}{R} \quad (9.14)$$

where I and dl are the intensity and direction of the current flowing through the coil, and $R = \|r - r'\|$ the distance from the observation point to the source point on the coil.

In particular from the definition of the models, in a EQS model only the Coulumb component of the E filed is considered. Conversely, for the MQS and Darwin solution both the Coulumb and Faraday has to be defined.

9.2.2 Numerical Methods and Numerical Software

Numerical software typically used for EQS and MQS problems solve the system in the frequency domain using the integral solutions of the quasistatic approximation of eq. 9.13. The ∇V can be expressed using the integral form defined by Coulumb integral (eq. 9.4), and \vec{A} by the Biot-Savart integral (eq. 9.3).

Impedance method — Quasi-static systems can be solved using the numerical methods introduced in the first part of this thesis, section 1.3. In addition to the methods previously described, the impedance method is a numerical method specifically meant for systems in the quasi-static approximation.

9.2 Numerical modeling of the quasistatic approximation

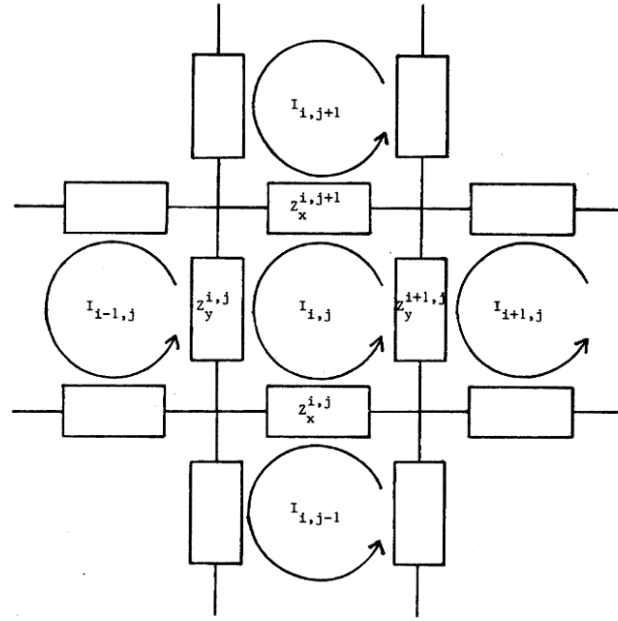


Figure 9.3: Impedance 2D network defined by Gandhi et al. in 1984 [343]. $I_{i,j}$ is the loop current corresponding to the i, j th cell; $Z_x^{i,j}$ and $Z_y^{i,j}$ are the impedances of the i, j th cell in the x and y directions, respectively.

The impedance method was firstly introduced by Gandhi et al. in 1984 [343], as a suitable computing method for solutions of quasistatic EM radiation problems. The method described by the authors was able to easily model anisotropic and inhomogeneous materials; thus it was particularly suitable for biomedical applications such as the study of radiation-induced currents in the heterogeneous human body. In this method, the region of interest is described by a 3D network of impedances.

Figure 9.3 shows the original sketch of the 2D network of the impedances described by Gandhi et al. [343]. Within the network, the impedances value can be obtained by the following expression:

$$Z_m^{i,j,k} = \frac{\delta_m}{\delta_n \delta_p (\sigma_m^{i,j,k} + j\omega \epsilon_m^{i,j,k})} \quad (9.15)$$

where i, j, k indicate the cell index; m is the direction in x, y or z , for which the impedance is calculated; σ_m and $j\omega \epsilon_m$ are the conductivities and the dielectric permittivities for the cell (i, j, k) ; δ_m is the thickness of the cell in the m^{th} direction, and δ_n and δ_p are the widths of the cell in directions at right angles to the m^{th} direction. So, the whole space is represented by a linear circuit and the circuit theory is applied to compute the currents in the impedances; this representation brings to a system of Kirchhoff's law equations, that can be solved using iterative process starting from an initial guess.

Admittance method — The admittance method is a finite difference approach to the solution of Maxwell’s equations. The method was firstly introduced by Armitage et al in 1983 [344] to study the SAR distribution within the human body resulting from the application of RF EM energy. Over the years the method has been reused, such as by D’Inzeo et al. in 1992 [345] to study the threshold for electric and magnetic nerve stimulation. The method is an alternative to the classical FEM numerical solution, however has the advantage of not requiring the meshing codes, needed in FEM software platforms. The admittance method is based on the solution of the quasi-static problem using both the vector potential, and the electric scalar potential. The method will be described in detail in the next section.

COMSOL multiphysics — COMSOL Multiphysics is a commercially available software that can be used to solve various physics and engineering applications. For the EQS and MQS solutions COMSOL uses the AC/DC Module. With the module it is possible to solve EMs field simulations for electrostatic, electric currents in conductive media, magnetostatics, and low-frequency EM solutions. Within this module it is possible to use for the models inhomogeneous and anisotropic materials, and complex-valued material properties.

If the simulation it is run at a known frequency, where both the and the magnetic fields are significant, or induced currents are present, the software solves the quasi-static regime computing a magnetic field at the interface based on eq. 9.13 in the frequency domain:

$$\nabla \times \mu^{-1}(\nabla \times \vec{A}) + (j\omega\sigma - \omega^2\varepsilon)\vec{A} = \vec{J}_s \quad (9.16)$$

where \vec{J}_s is the source current. The equation is solved for the magnetic fields, and the electric fields $\vec{E} = j\omega\vec{A}$.

The AC/DC module suggests to use a quasi-static regime if the length of the object is shorter than 1/100 of the wavelength. Additionally, the quasi-static approximation defined by the software implies that the electric charge density does not change with time, and consequently that the change of the displacement current can be neglected. COMSOL will be used in the following section of this thesis to verify the applicability of the admittance method to a EQS solution and to an anisotropic system.

9.3 Admittance method

As reported by Armitage et al. in 1983 [344], the Admittance method *can be regarded as essentially a near-field method which for human dimensions and dielectric*

9.3 Admittance method

properties is valid for frequencies at least up to 30 MHz. The method is in fact based on the solution of the quasi-static problem using both the vector potential, and the electric scalar potential (eq. 9.13). The magneto scalar potential A is defined a priori from eq. 9.14, and the electric scalar potential V is obtained through the method. The analysis domain is divided into N homogeneous cubic cells ($\Delta x \times \Delta y \times \Delta z$), corresponding to the cubical voxels of the volume studied (e.g., the anatomical brain model), centered at the point of coordinates (x, y, z) . The obtained Cartesian grid can be represented as a network of lumped electrical elements, including passive components (admittances) and current generators (see fig. 9.4 for a simplified 2D representation) [346, 347].

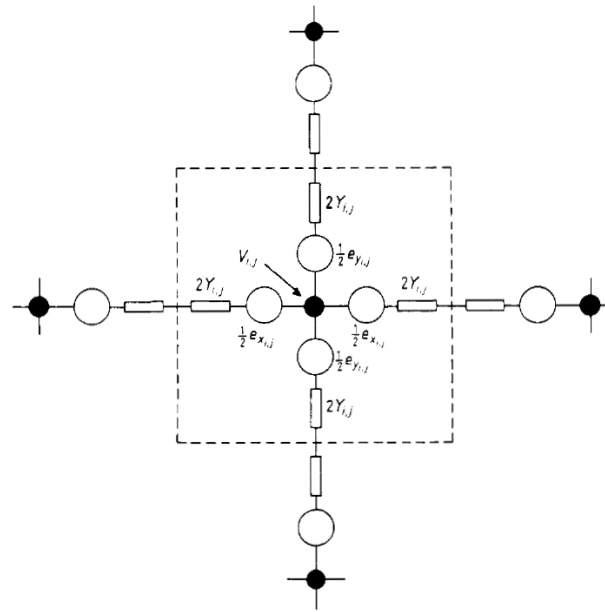


Figure 9.4: Two-dimensional representation of the basic cell used for the simulation by Armitage et al. in 1983 [344].

Kirchoff's law applied at each network node (x, y, z) leads to a linear system of the form:

$$V_{x,y,z} = \frac{1}{Y_{x^-} + Y_{x^+} + Y_{y^-} + Y_{y^+} + Y_{z^-} + Y_{z^+}} [Y_{x^+} V_{x+\Delta x,y,z} + Y_{x^-} V_{x-\Delta x,y,z} + Y_{y^+} V_{x,y+\Delta y,z} + Y_{y^-} V_{x,y-\Delta y,z} + Y_{z^+} V_{x,y,z+\Delta z} + Y_{z^-} V_{x,y,z-\Delta z} - Y_{x^-} \Delta x j \omega A_{x^-} + Y_{x^+} \Delta x j \omega A_{x^+} - Y_{y^-} \Delta y j \omega A_{y^-} + Y_{y^+} \Delta y j \omega A_{y^+} - Y_{z^-} \Delta z j \omega A_{z^-} + Y_{z^+} \Delta z j \omega A_{z^+}] \quad (9.17)$$

where $V_{x,y,z}$ is the unknown scalar electric potential at each network node, Y_i and A_i ($i = x^-, x^+, y^-, y^+, z^-, z^+$) are the admittance and the vector potential components at each surface of the discretizing cell and ω is the operating angular frequency.

The admittance values are calculated from the complex conductivity σ^* as:

$$Y_{x^+} = \frac{2\sigma_x^* \sigma_{x+\Delta x}^*}{\sigma_x^* + \sigma_{x+\Delta x}^*} \frac{\Delta y \Delta z}{\Delta x} \quad (9.18)$$

where, for a fixed frequency f , the complex conductivity can be expressed as:

$$\sigma^*(f) = \sigma_s + 2\pi f \epsilon_0 \epsilon''(f) + j2\pi f \epsilon_0 \epsilon'(f) = \sigma(f) + j2\pi f \epsilon_0 \epsilon'(f) \quad (9.19)$$

where ϵ_0 is the free space permittivity, f the operating frequency, $\epsilon'(f)$ is the real part of the relative permittivity, and $\sigma(f)$ the electric conductivity, including the loss term associated with the imaginary part of permittivity $\epsilon''(f)$ and the conductivity at $f = 0$, σ_s .

To solve the linear system of equations 9.17, it can be adopted the over relaxation iterative technique [346, 348, 349] since it represents the best compromise among easy implementation, computer memory occupation, and speed of convergence [350–352]. This technique calculates successive estimates of the potential from the one estimated at the previous step, to which is added a correction term in order to accelerate the convergence of the solution.

$$V^{n+1}(x, y, z) = V^n(x, y, z) + \alpha[V_{x,y,z} - V^n(x, y, z)] \quad (9.20)$$

α is a parameter which can take on values between 1 and 2; the higher α , the greater the speed of convergence, although for values too much close to 2, oscillation phenomena may occur. We chose for the convergence factor α a value equal to 1.8.

The iterative procedure ended when the error at the n^{th} step fell down below a tolerance level e , that we chose equal to 1×10^{-7} .

$$\frac{\sum_{i=1}^N |V_i^{n+1} - V_i^n|}{\sum_{i=1}^N |V_i^n|} < e \quad (9.21)$$

9.3.1 Applicability of the admittance method in time domain

Generally dosimetry for pulsed signals used in clinics is a static or a single frequency dosimetry, disregarding the actual signal frequency content. Hence the calculated E field is taken as the maximum value reached inside the tissue, without considering its time pattern [333]. In TMS applications, the stimulating signal is assimilated to a pure sinusoid having the same initial slope of the real monophasic or biphasic waveform and the tissues properties are taken at the frequency of the approximating sinusoid [333]. In DBS, a static solution can be adopted to calculate the maximum induced field [353]. Under the hypothesis that resistive behavior of tissues dominates the capacitive one in the spectral frequency band of the applied stimulation [354, 355], the stimulating waveform is preserved inside the brain. Tissues conductivities are set to the values assumed either at the pulse train repetition frequency (around 100 Hz) or at the maximum frequency of the signal band (around 2 kHz) [356]. Other authors

9.3 Admittance method

performed a time resolved dosimetry to calculate the influence of tissue features [357] on the DBS induced waveform and on the activating volume, but tissues dispersivity was not considered.

Recently, it has been shown [355, 356, 358] that tissues may filter the applied stimulatory fields or the endogenously generated fields altering the predicted stimulatory waveform size and shape. This may impact the expected neural response and electrochemical interactions taking place in the brain [359]. Therefore, the importance of a time resolved dosimetry, accounting for dispersive tissues behavior, becomes evident, even considering that the knowledge of the exact signal waveform is fundamental for studying neuronal responses using biophysical models.

The time-resolved dosimetry in commercially available softwares (e.g. COMSOL Multiphysics) is signal dependent. Thus to study a new dosimetry solution on the same system, for each input signal simulations need to be reperformed. This is also valid if a new discretization of the same original signal has to be studied. This entire process can be highly time consuming. Additionally for a time-resolved solution commercial software cannot take into account the dispersive quality of the tissues. In the next chapter (10) the time-resolved dosimetry was achieved by implementing a tool for the calculation of the E field based on an improved revision of the admittance method [346, 348, 349]. The calculation of $E_n(i, j, k)$ was performed for a set of n discrete frequencies, and then solution in time $E(t)$ was obtained in each voxel, $E_n(i, j, k)$ by means of its Inverse Discrete Fourier Transform. The frequency dependence of the dispersive electric properties of tissues was described by the complex conductivities $\sigma_n^*(i, j, k)$.

9.3.2 Applicability of the admittance method to an EQS problem

The admittance method described at the beginning of this section takes into account in its solution both the magnetic and electric potential (eq.9.17). Herein the applicability of the admittance method to EQS solutions was proven considering only the Coulomb component of the E field ($E_C = \nabla \vec{V}$) neglecting the temporal change of the magnetic flux. A solution based on the admittance method for EQS models can be useful for the analysis of medical devices stimulating through electrodes, such as BDS.

The solution was performed for a single frequency (i.e., $f = 0Hz$) for a sphere of 30.5 mm of radius made of gray matter tissue properties ($\sigma = 0.106S/m$ and $\varepsilon_r = 4.52e^7$), surrounded by CSF tissue properties ($\sigma = 2S/m$ and $\varepsilon_r = 109$). The solution was carried out including at the isocenter of the sphere a $3 \times 3 \times 3 \text{ mm}^3$ metallic electrode ($\sigma = 1e7S/m$ and $\varepsilon_r = 1$) assigned to a potential of 1 V. A ground plane was imposed to the bottom slice of the domain. The numerical solution of the admittance

method was verified solving the same system with the commercially available software COMSOL multiphysics.

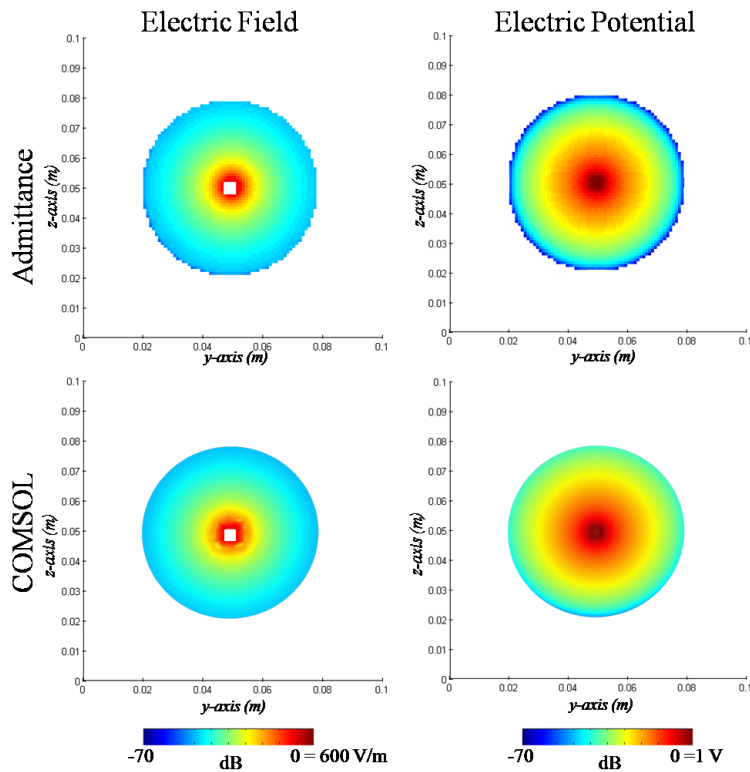


Figure 9.5: Results for the E field and potential within the phsere of 30.5 mm radius imposing a 1 V electrode at is isocenter. Results are reported for both the admittance method and COMSOL solution. The location of the electrode is evident where the E field is equal to zero,l and the E potential is equal to 1 V by definition. Distribution obtained by the two software was comparable.

The computation of results obtained with the admittance method was comparable with the one of COMSOL (figure 9.5). The highest discrepancy of 18 % observed for the E filed at the electrode interface, as additionally shown by the profile in figure 9.6). This was related to the discrepancies between the numerical mesh implementation of the two methods. COMSOL uses a tetrahedral mesh, thus the values reported on the plane showed in figure 9.5, and along the line in figure 9.6 are interpolated by the software to show a smooth profiles. Conversely, the mesh used by the admittance method is a voxel based mesh, that does not need to be interpolated over the specific plane. Effect of the mesh can be observed on the boundaries of the sphere where the admittance method was not able to correctly define the curved surface of the object. This discrepancy is particularly important in location of electric discontinuity, such as around the electrode, where the COMSOL mesh becomes finer by implementation. Everywhere else the difference between the two solution was less than 10%. With

9.3 Admittance method

respect to the E potential, the distributions were also comparable, but the admittance solution showed a lower potential at the boundaries of the sphere (figure 9.5). This can also be noticed for the profile along the z-axis, where the admittance method showed lower values of potential with an increasing difference between the two solution up to 20 % farther from the electrode.

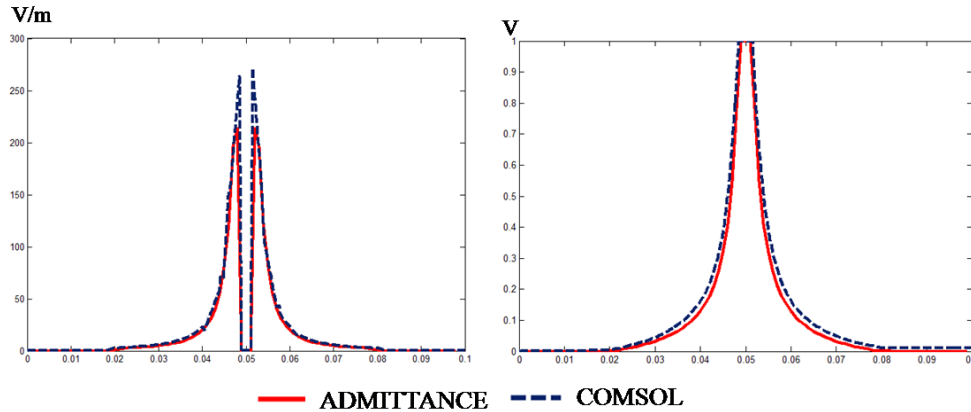


Figure 9.6: Profiles of the electric field and potential along the z-axis crossing the isocenter of the sphere. The location of the electrode is evident where the E field is equal to zero, and the E potential is equal to 1 V by definition. Distribution obtained by the two software was comparable.

9.3.3 Applicability of the admittance method for anisotropic tissues

As already described, the definition of the admittance method depends on the calculation of the field using a net of admittance calculated from the complex conductivity σ^* (eq. 9.18). The definition of the method leaves space to include within the solution the anisotropic properties of the tissues. Biological tissues can be anisotropic with respect to the direction of the field applied [360]. Herein a case study was performed to verify the applicability of the admittance method considering both isotropic and anisotropic characteristics of tissues.

The solution was performed for a single frequency (i.e., $f = 3000\text{Hz}$) for a sphere of 30.5 mm of radius made of gray matter tissue properties ($\varepsilon = 6.68e+4$), surrounded by CSF tissue properties ($\sigma = 2\text{S/m}$ and $\varepsilon = 109$). For the sphere the conductivity was considered anisotropic, with the one on the z direction 10-time higher than on the x and y direction ($\sigma_x = 0.106\text{S/m}$, $\sigma_y = 0.106\text{S/m}$, $\sigma_z = 1.06\text{S/m}$). As a comparison the same solution was repeated considering for the sphere an isotropic tissue ($\sigma = 0.106\text{S/m}$, and $\varepsilon = 6.68e+4$). The solution was carried for a bipolar stimulation type including at the isocenter of the sphere two $3 \times 3 \times 3\text{ mm}^3$ metallic electrodes ($\sigma =$

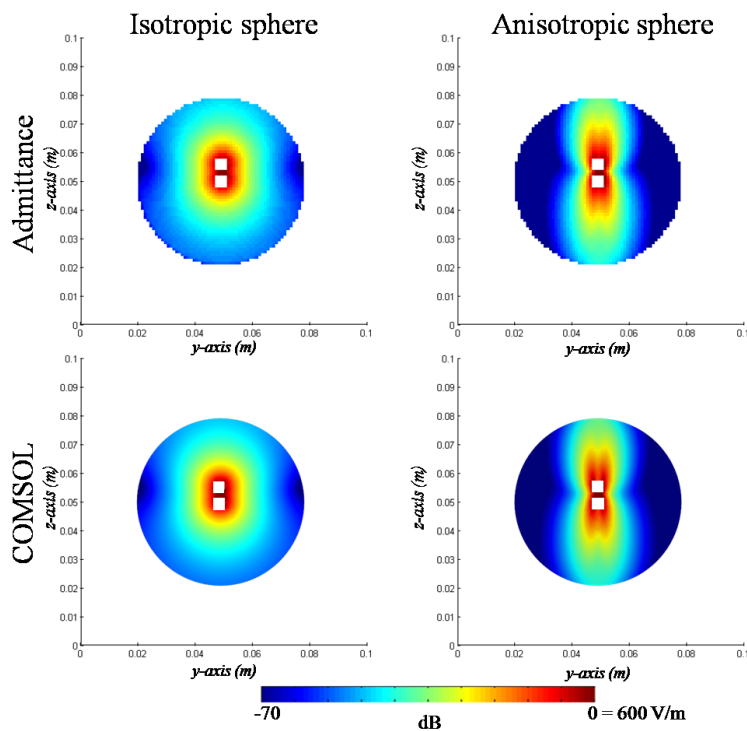


Figure 9.7: Results for the E field within the isotropic and anisotropic sphere of 30.5 mm radius imposing two electrodes at its isocenter with a 1 V and -1 V potential. Results are reported for both the admittance method and COMSOL solution. The location of the electrodes is evident where the E field is equal to zero. Distribution obtained by the two software was comparable.

9.3 Admittance method

$1e7S/m$ and $\varepsilon = 1$) spaced of 3 mm along the z-axis with an assigned potential of 1 V and -1 V. The numerical solution of the admittance method was verified solving the same system with the commercially available software COMSOL Mulyiphysics.

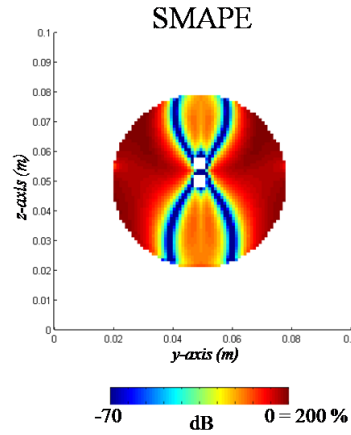


Figure 9.8: SMAPE distribution between the isotropic and anisotropic sphere for E field calculated with the admittance method for the distribution reported in figure 9.5

The computation of results obtained with the admittance method was comparable with the one of COMSOL (figure 9.7). The evaluation of the anisotropic tissue was evident on the field distribution that was deformed on the z direction with respect to the isotropic one. The anisotropic sphere also showed lower values of the $\|\vec{E}\|$ on the side of the electrodes along the y-direction (i.e., left and right sides in the figure 9.7).

The different behavior of the field between the isotropic and anisotropic sphere is particularly evident calculating the SMAPE of the plane accordingly to eq 3.5 (figure 9.8). High values of SMAPE up to 200 % were found on the electrodes sides in the y-direction. Whereas values of SMAPE up to 60 % were found along the z-axis. This proved the dependency of the E field distribution with the conductivity value of the material, and the applicability of the admittance method for anisotropic materials.

Chapter 10

Time resolved dosimetry of human brain exposed to low frequency pulsed magnetic fields

This chapter was published in *Physics in Medicine & Biology* [361]. Repetition of concepts and definitions already introduced in this thesis have to be excused. The work was performed in collaboration with the IGEA Clinical Biophysics company.

10.1 Abstract

An accurate dosimetry is a key issue to understanding brain stimulation and related interaction mechanisms with neuronal tissues at the basis of the increasing amount of literature revealing the effects on human brain induced by low-level, low frequency pulsed magnetic fields (PMFs).

Most literature on brain dosimetry estimates the maximum E field value reached inside the tissue without considering its time pattern or tissue dispersivity. Nevertheless a time-resolved dosimetry, accounting for dispersive tissues behavior, becomes necessary considering that the threshold for an effect onset may vary depending on the pulse waveform and that tissues may filter the applied stimulatory fields altering the predicted stimulatory waveform' s size and shape.

In this paper a time-resolved dosimetry has been applied on a realistic brain model exposed to the signal presented in Capone et al. [330], accounting for the broadband dispersivity of brain tissues up to several kHz, to accurately reconstruct electric field and current density waveforms inside different brain tissues.

The results obtained by exposing the Duke' s brain model to this PMF signal show that the E peak in the brain is considerably underestimated if a simple monochromatic dosimetry is carried out at the pulse repetition frequency of 75 Hz.

Keywords : dosimetry, pulsed magnetic fields, low frequency, brain stimulation

10.2 Introduction

During the last decades, there has been great development in brain stimulation techniques based on pulsed electric and magnetic fields on the human brain. The most popular ones are deep brain stimulation (DBS) and transcranial magnetic stimulation (TMS). DBS uses an electric rectangular pulse train to alleviate symptoms of motor disorders, e.g. Parkinson Disease [362]. TMS is a promising alternative treatment for a broad range of neurological and psychiatric disorders, based on brain stimulation via externally applied time varying magnetic fields [295]. The waveforms used in TMS are monophasic or biphasic pulses similar to damped sinusoids with an amplitude of about 2 T [363].

Recently, an increasing amount of literature data revealed intriguing effects on the human brain induced by low-level (three orders of magnitude less than in TMS) pulsed magnetic fields (PMFs), such as the complex neuroelectromagnetic pulse (CNP) [311, 318, 320, 321], or signals already adopted in the treatment of osteoarthritis [328, 329], e.g. the one developed by IGEA (Carpi, Italy), [330, 332, 364].

The observed effects consist of modifications to several neuronal functions, such as motor control, sensory perception, cognitive activities, sleep and mood [311, 312, 314, 365], and even a protective effect against focal cerebral ischemia [315–317].

All these PMFs signals consist of pulse trains, whose repetition frequency lies in the extremely low frequencies (ELF) range, and may occupy a large frequency band, from static up to some tens of kHz [334, 335], due to the sharp rise and fall edges.

Despite the increasing number of literature studies, the experimental results on low-level PMFs stimulation are often inconsistent and the action mechanisms are still poorly defined [311] mainly due to the heterogeneity of the stimulating PMFs, in terms of frequency content, pulse peak, duration, and waveform [311]. In fact, the threshold for an effect onset may vary depending on the pulse waveform, even considering the same rms value, analogously to what occurs in TMS applications [363].

An accurate dosimetry, i.e. the estimation of the electric field (E) and current density (J) distributions induced in the brain for each considered waveform, is a key issue to understanding brain magnetic stimulation and the related interaction mechanisms with biological tissues. In fact, dosimetric results, joined with biophysical models connecting the induced fields with the neuronal responses, may help to clarify the specific relationship between signal parameters and neuronal responses, and to identify stimulating thresholds, following a generally valid scheme of the multiscale/multiphysic

10.2 Introduction

approach [366,367].

Nevertheless, at present, very few papers deal with time resolved dosimetry for magnetic or electric brain stimulation.

Most literature on brain dosimetry pertains to DBS and TMS applications and estimates the maximum E field value reached inside the tissue without considering its time pattern [368, 369]. In TMS applications the stimulating signal is assimilated to a pure sinusoid having the same initial slope of the real monophasic or biphasic waveform and the tissues properties are taken at the frequency of the approximating sinusoid [333,370].

When considering the electric stimulus used in DBS, a static solution is adopted [353, 368, 369, 371] to calculate the maximum induced field. Under the hypothesis that resistive behavior of tissues dominates the capacitive one in the spectral frequency band of the applied stimulation [354, 355, 372] the stimulating waveform is preserved inside the brain. Tissues conductivities are set to the values assumed either at the pulse train repetition frequency (around 100 Hz) [368, 369, 373] or at the maximum frequency of the signal band (around 2 kHz) [169].

Other authors performed a time resolved dosimetry to calculate the influence of tissue features [357] on the DBS induced waveform and on the activating volume, but tissues dispersivity was not considered.

Recently, it has been shown [355, 358, 374] that tissues may filter the applied stimulatory fields or the endogenously generated fields altering the predicted stimulatory waveform's size and shape [359]. This may impact the expected neural response and electrochemical interactions taking place in the brain [359].

Therefore, the importance of a time resolved dosimetry, accounting for dispersive tissues behavior becomes evident, even considering that the knowledge of the exact signal waveform is fundamental for studying neuronal responses using biophysical models [327, 375–378].

Two different approaches can be followed to carry out a time resolved dosimetry: a straightforward solution in time domain or a weighted combination of frequency domain solutions following the harmonic decomposition of the stimulating signal. Methods based on the transient analysis in the time domain would not require any approximation of the stimulating waveform, but tissue dispersivity is rarely accounted for since it requires the transformation of the Cole– Cole dispersion relation into a time domain relation by a convolution integral [379].

Moreover, typical time-domain methods such as finite difference time domain (FDTD) cannot be adopted at low frequencies due to the prohibitively long computational time, so that Crozier and coworkers [348,380,381], evaluated the safety of patients and work-

Time resolved dosimetry of human brain exposed to low frequency pulsed magnetic fields

ers exposed to trapezoidal waveforms generated by MRI gradient coils, and developed a FDTD variant in the quasi-static approximation taking advantage of harmonic decomposition.

Even commercial codes based on FEM, such as Comsol (Comsol AB, Stockholm Sweden) and MagNet (Infolytica corporation, Montréal, Québec Canada), require the use of Fourier analysis to account for tissues dispersivity.

For this reason, only a few recent papers on DBS [358, 374] calculated the stimulating waveform in the brain accounting for tissues dispersivity. All of them used harmonic decomposition coupled with a FEM solver, which has the advantage of being adaptable to irregular objects, but usually requires a long computation time, especially when studying millimeter-resolution human models [348].

At present, similar studies on magnetic stimulation, particularly on PMF used in low-level brain exposure [311], cannot be found in literature, except for a numerical study [382] carried out inside well-plates exposed to the signal presented in Capone et al [330].

In this work, for the first time, a dosimetric study has been carried out on a realistic brain model exposed to this PMF signal, accounting for the broadband dispersivity of brain tissues up to several kHz [251].

To do that, an ad hoc procedure has been implemented based on the harmonic decomposition of the pulsed signal and the calculation of the induced E field in the frequency domain using the admittance method [346, 348, 349]. This method allows accounting for frequency dependence of both conductivity and permittivity of brain tissues in the signal frequency band and has been shown to be computationally efficient in a previous work by the authors [370] where real time calculations were needed. Moreover, with respect to a FEM solution, it directly imports a voxelated anatomical brain model coming from MRI, without the need to convert the medical image data into 3D models. This procedure allows the estimation of the real time-pattern of E and J induced in different points of the brain and to consider the specificity of the pulsed signal taking into account its whole information content.

Results on the peak of the E field time course have been compared to the amplitude of the induced E field calculated following a fast but simplified monochromatic analysis at the pulse repetition frequency that could furnish a rough estimate of the induced maximum E field. The method set-up for the time resolved dosimetry is described in section 2 ; section 3 reports on time courses of the fundamental dosimetric quantities E and J results in the different brain tissues due to exposure to a uniform magnetic field varying in time according to the signal of Capone et al. [330]. Discussion and conclusions are drawn in sections 4 and 5 , respectively.

10.3 Methods

10.3.1 Brain model

The human brain model is a $1 \times 1 \times 1mm^3$ resolution voxelized male model obtained from the Virtual Population member Duke (v.1.0, Zurich Med Tech AG, Zurich, Switzerland, [383]).

In this work, we considered the head section of the model contained in a box of $183 \times 219 \times 182mm^3$ including all 11 main brain structures: gray matter (GM), white matter (WM), cerebellum (CER), commissura anterior, commissura posterior, hippocampus (HIP), hypophysis, hypothalamus (HYP), midbrain (MID), thalamus (THA), and cerebrospinal fluid (CSF).

Each tissue was electromagnetically described by the free space magnetic permeability μ_0 and the complex conductivity:

$$\sigma^*(f) = \sigma + 2\pi f \varepsilon_0 \varepsilon''(f) + 2\pi f \varepsilon_0 \varepsilon'(f) \quad (10.1)$$

where ε_0 is the free space permittivity, f is the operating frequency, $\varepsilon'(f)$ and $\varepsilon''(f)$ are the real and imaginary parts of the relative permittivity, and σ is the ionic electric conductivity.

The frequency behaviors of $\varepsilon'(f)$ and $\varepsilon''(f)$ and the σ values were taken from the IT'IS Foundation database [384]. They are modeled using a four relaxations Cole–Cole expression as in [251].

10.3.2 Stimulation signal

In this work we considered the signal generated by the commercial pulse generator B-01 (IGEA, Carpi, Italy), as an example of PMF used to expose the human brain. Figure 10.1 (a) (Red line) shows the waveform of a single pulse. As reported in [315, 330, 385]), the signal is a monophasic, pulsed signal at $75 \pm 2Hz$ repetition frequency, with the 'active phase' of about 1.3 ms, defined as the duration of the rise edge, from 0 to the maximum value. The peak value of the magnetic field B has been estimated to be $1.8 \pm 0.2mT$ [330].

10.3.3 E field calculation

The E field calculation has been obtained, under the quasi-static approximation, solving the Poisson equation for the magnetic vector potential A and the Lorentz equation for the electric field: $E_n(f_n) = -j2\pi f_n A - \nabla V_n$, for each single frequency considered (f_n), as it will be better described in the following. The quasi-static ap-

Time resolved dosimetry of human brain exposed to low frequency pulsed magnetic fields

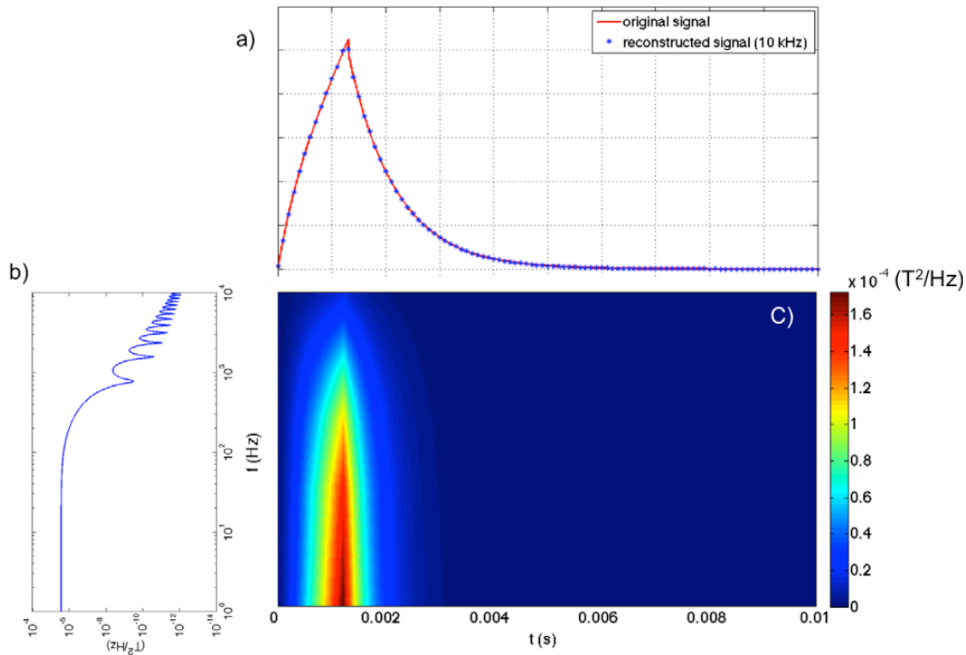


Figure 10.1: (a) Time course of the signal (red line) and reconstructed signal obtained using 10 000 (blue dotted line) frequency components of its spectrum, 1 Hz spaced; (b) SPD of the signal calculated using periodogram (c) spectrogram of the signal calculated using 0.16 ms Hanning windows, 50% overlapping.

proximation is valid due to the small dimensions of the human target with respect to the minimum signal wavelength [386].

In this study, the A field is chosen in order to have a uniform magnetic induction $\vec{B} = 2mT$ along the z direction in the whole stimulating box, mimicking an ideal situation of a magnetic field generated by a Helmholtz pair coil.

To compute the time dependent E field, an approach based on the signal spectral decomposition (figure 10.2) is considered [359,374]. First, the pulsed stimulating signal considered is converted in the frequency domain via DFT in the Matlab computing environment.

Second, the individual frequency component solution $E_n(f_n)$ is determined using the admittance method [346,348,349]. The electric scalar potential V_n induced inside the brain is calculated by solving a linear system representing currents balance at each node of the Cartesian cubic grid, according to the Kirchoff' s law [346,347,387]. It includes passive components (admittances) and current generators accounting for the applied A . The admittances at each face of the (i,j,k) cubic cell are calculated from the complex conductivity $\sigma_n^*(i, j, k)$ at each considered frequency. To solve the linear system we use the successive over the relaxation iterative technique (SOR) [346,348,349], with convergence factor α equal to 1.8, since it represents the best compromise for ease of implementation, computer memory occupation, and speed of convergence

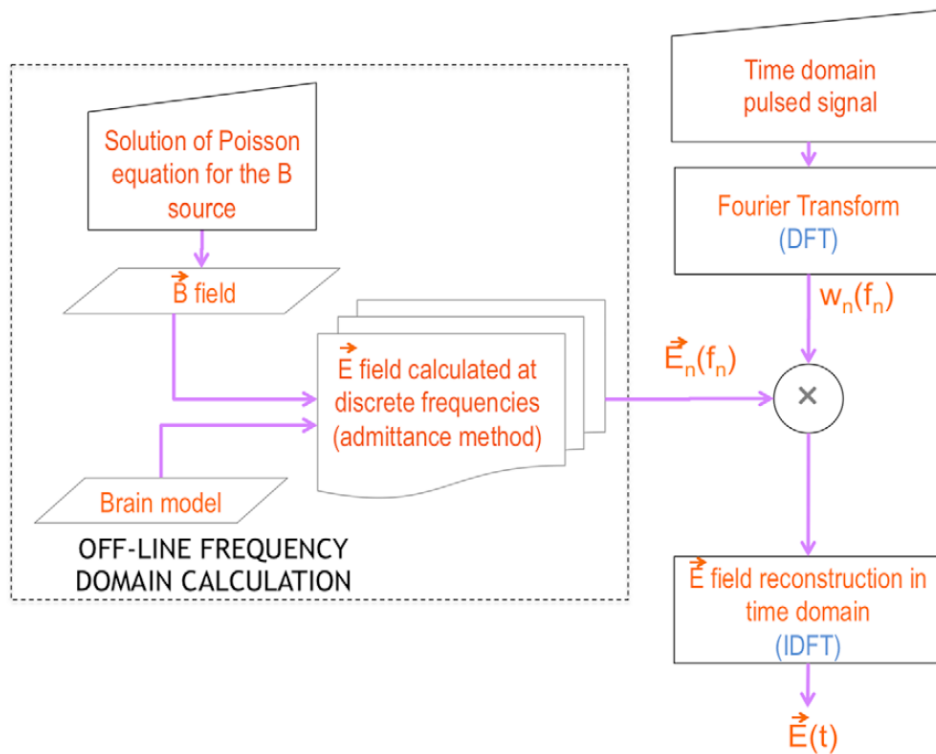


Figure 10.2: Flow-chart summarizing the strategy adopted to perform time resolved dosimetry of the pulsed signal.

[350, 351, 388]. The iterative procedure ended when the error at the i th step fell down below the tolerance level $e = 10^{-7}$. This termination criterion is within the range generally used in literature for these kind of applications ($10^{-9} - 10^{-5}$) [346, 389, 390] and guarantees accurate and fast E field calculations [370].

The E distribution in the brain is calculated by the superimposition of the primary $(-j2\pi f_n A)$ and the secondary ∇V_n fields [391]. The primary field is due to the Faraday's induction law and is generated by variations in time of the applied magnetic induction B. Conversely, the secondary field is due to the charge accumulation at the tissues interfaces with different complex conductivity under the action of the primary field [391]. The core of the E field calculation, i.e. the admittance method implementation, is developed in the C++ environment.

Finally, as in standard harmonic decomposition procedures [357, 359] the E field result at each frequency component is scaled and phase shifted according to the signal DFT weights $(w_n(f_n))$, and the time domain solution is rebuilt using the IDFT in the Matlab computing environment.

Similarly, the time course of the current density J induced in tissues is obtained using the IDFT on $J_n(f_n) = E_n(f_n) \times \Re(\sigma^*(f_n))$.

The main computational effort resides in the frequency domain E field calculation,

depending on the number of frequencies necessary to account for the pulsed signal spectrum and hence to reconstruct the time domain signal. Therefore, to speed up calculation, the brain transfer function, defined as the electric field $E(i, j, k, f_n)$ at the coordinates (i, j, k) and the frequency f_n , is calculated at 153 discrete frequencies not equally spaced between 1 Hz and 10 kHz and subsequently interpolated using piecewise cubic functions [374].

It is worth noting that, for a given brain model and a physical magnetic source, the transfer function $E(i, j, k, f_n)$ can be calculated off-line and stored in a database (see figure 2). This database can be used to obtain the time-domain response to every kind of applied PMFs. This approach allows a significant time saving, especially when different kinds of PMF have to be investigated, e.g. to check their clinical efficacy.

10.4 Results

10.4.1 Signal features

The waveform of a single pulse is reported in figure 10.1 (a), the red line. The signal spectral power density (SPD), estimated using the periodogram, exhibits a main half-lobe completely included within 1 kHz (figure 10.1 (b)). However, if one considers only the frequency samples from 1 Hz to 1 kHz, step 1 Hz, a coarse reconstruction and a peak underestimation of about 20% are obtained.

Therefore, in order to evaluate the frequency content in different time intervals of the signal, a time-frequency analysis has been carried out using the signal spectrogram [392]. It has been calculated on segments of 16 samples, 0.16 ms long, using the Hanning window and 50% overlapping.

Result of figure 10.1 (c) shows that corresponding to the signal peak, frequency components are present up to 10 kHz. Thus, to obtain the time domain solution, the signal spectrum has been considered up to 10 kHz. The reconstructed signal is reported in figure 10.1 (a) (blue dotted line), where it is possible to note how the peak shape is well represented.

10.4.2 E and J fields calculation

As described in section 2, the E field frequency response in the Duke's brain model was evaluated at discrete frequencies from 1 Hz to 10 kHz under the exposure to a uniform 2 mT B field distribution along the z axis. This exposure condition mimics those used in human studies with this signal.

As examples of the $|E_n|$ and $|J_n|$ distributions to be used in the reconstruction procedure, figure 10.3 shows three frequencies (75, 225, 1050 Hz) on the sagittal plane

10.4 Results

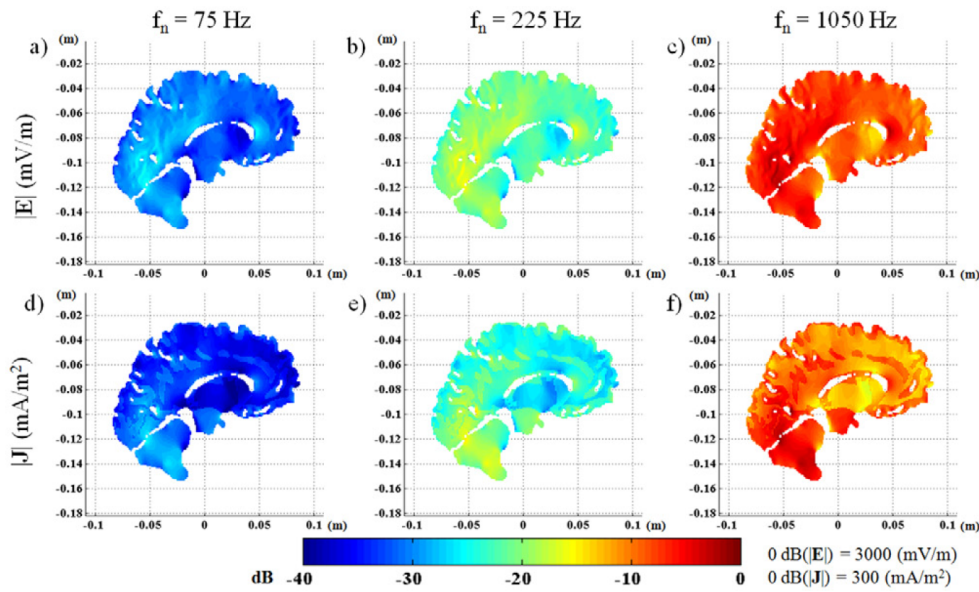


Figure 10.3: $|E|$ distributions on the sagittal plane $x = -1.1$ cm, through the left hemisphere, at 75 Hz (a), 225 Hz (b), and 1050 Hz (c); $|J|$ distributions on the sagittal plane $x = -1.1$ cm at 75 Hz (d), 225 Hz (e), and 1050 Hz (f). Fields are only saved inside the brain, and are normalized with respect to the maximum value found within the three frequencies.

passing through the left hemisphere, at 1.1 cm from the center of the brain. Results are normalized with respect to the rounded maximum value found within the three frequencies in the selected slice (3000 mV m^{-1} for E and 300 mA m^{-2} for J).

Looking at figure 10.3, it is evident that the induced E field increases as the frequency increases. This was an expected behavior since the primary E field is directly proportional to f . Even $|J|$ increases with frequency; moreover, its distribution is influenced by different conductivities of tissues and their dispersive behaviors.

Time courses of E and J, reconstructed as explained in section 2, are calculated corresponding to seven points of the brain placed inside seven different tissues. The points coordinates (in cm) are: $(-0.10; 3.60; -8.60)$ in GM, $(0.40; 2.80; -8.70)$ in WM, $(-0.50; 2.10; -8.50)$ in CER, $(-1.60; 2.50; -9.60)$ in HIP, $(-0.20; 8.20; -8.70)$ in HYP, $(-1.10; 4.50; -8.30)$ in MID, and $(-0.20; 6.00; -10.00)$ in THA.

Figure 10.4 shows time courses of the E and J components calculated on the point placed inside GM.

For both E and J, the time domain components present positive and negative peaks corresponding to the sharpest variations of the signal. One can see from figure 4 that, for this point, components x and z are in phase while y component has changed sign. Considering that the A components at this point are not negative, the primary field ($-\frac{dA}{dt}$) dominates the y component, while, in the other two the secondary field ($-\nabla V$) prevails.

Time resolved dosimetry of human brain exposed to low frequency pulsed magnetic fields

Tissue	Stimulating signal	Max (E_x)	Max (E_y)	Max (E_z)	Max (E)
GM	Monochromatic (75 Hz)	2.4	52.4	15.9	54.8
	PMF	5.5	142.3	44.0	149.0
WM	Monochromatic (75 Hz)	2.0	34.3	12.0	36.4
	PMF	5.1	93.4	23.2	95.1
CER	Monochromatic (75 Hz)	33.6	70.1	55.2	95.4
	PMF	75.7	175.0	55.2	95.4
HIPP	Monochromatic (75 Hz)	9.8	46.9	29.2	56.1
	PMF	21.9	121.3	75.4	144.4
HYP	Monochromatic (75 Hz)	3.6	48.2	4.5	48.6
	PMF	7.8	128.1	9.7	128.7
MID	Monochromatic (75 Hz)	25.5	93.8	42.4	106.0
	PMF	63.1	236.5	99.8	264.4
THA	Monochromatic (75 Hz)	24.2	72.8	38.9	86.0
	PMF	57.0	187.3	92.8	216.7

Table 10.1: Maximum values (mVm^{-1}) of E_x , E_y , E_z and E time courses in seven points inside different tissues, calculated using the pulsed signal (2 mT peak), compared to the amplitudes of the same magnitudes using a monochromatic stimulation at 75 Hz (2 mT amplitude).

The combination of the three E or J components gives the vector fields E and J that will lie in a specific direction and will change their verse with time, according to the biphasic time course of single components. From a biophysical point of view, the field direction with respect to the neuronal fibers orientation is of fundamental importance to predict neuron stimulation [363].

Figure 10.5 shows time courses of the E (panel (a)) and J (panel (b)) field strengths on all seven of the considered points.

From figure 10.5 one can see that for all points the time courses of the E and J field strength presents a positive peak, corresponding to the end of the ‘ active phase’ signal, which is always higher in magnitude than the negative one. While the maximum E strength lies in the Midbrain (light blue in figure 10.5 (a)), the current density reaches its maximum inside the Hypothalamus (magenta line in figure 10.2 (b)), due to its higher conductivity (almost one order of magnitude) with respect to other brain tissues [251].

Moving to a quantitative analysis, table 10.1 compares, in the seven points, the maximum strength of E_x , E_y , E_z and E calculated using the PMF signal, to the ones obtained by solving a monochromatic problem at the repetition frequency of 75 Hz (2 mT).

Table 10.1 shows that, for all considered points, monochromatic solution at 75 Hz underestimates, by about 60%, the maximum E field value induced in the brain. Thus if one considers a monochromatic signal at 75 Hz to approximate the exposure to the

10.5 Discussions

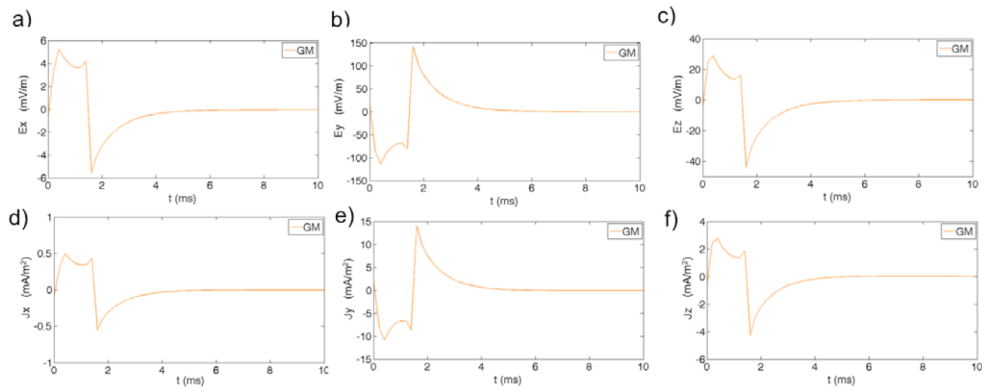


Figure 10.4: Time courses of E_x (a), E_y (b), E_z (c), J_x (d), J_y (e), J_z (f) calculated on the point of coordinates $(-0.10; 3.60; -8.60)$ placed in GM.

PMF signal, the maximum estimated E field is less than one half of the real maximum value. This confirms the importance of time domain dosimetry able to take into account the whole frequency content of the signal.

10.5 Discussions

In this work the time courses of E and J in seven different tissues of the brain exposed to the PMF signal are calculated.

The chosen approach is similar to that recently used by Schmidt et al. [374] in the context of electric brain stimulation and is based on the harmonic decomposition of the stimulating signal. With respect to a time domain solution, this allows one to account for, in a straightforward way, tissue dispersivity which cannot be neglected in a frequency range from 0 Hz up to tens of kHz [251].

Here, the adopted frequency domain solver is the admittance method since it is faster than other widespread used methods, such as FEM, even considering millimeter-resolution brain models, and directly imports voxelized models coming from MRI [370]. Results show that time courses of E and J strength, on points lying in seven different brain tissues, exhibit a biphasic behavior, with sharp positive and negative peaks. The maximum value corresponds to the end of the signal "active phase", when the signal time derivative is the maximum, and ranges from 95 to 265 mV m^{-1} , depending on the considered tissue. While the E strength is the maximum for the point lying in the mid-brain, the maximum J is obtained in the hypothalamus, due to its higher conductivity value.

The uncertainty budget of numerical assessment has been evaluated taking into account the uncertainty of 11% of the peak value of B [330], the variability of $\pm 20\%$ in conductivity and permittivity of each biological tissue [251], and the uncertainty

Time resolved dosimetry of human brain exposed to low frequency pulsed magnetic fields

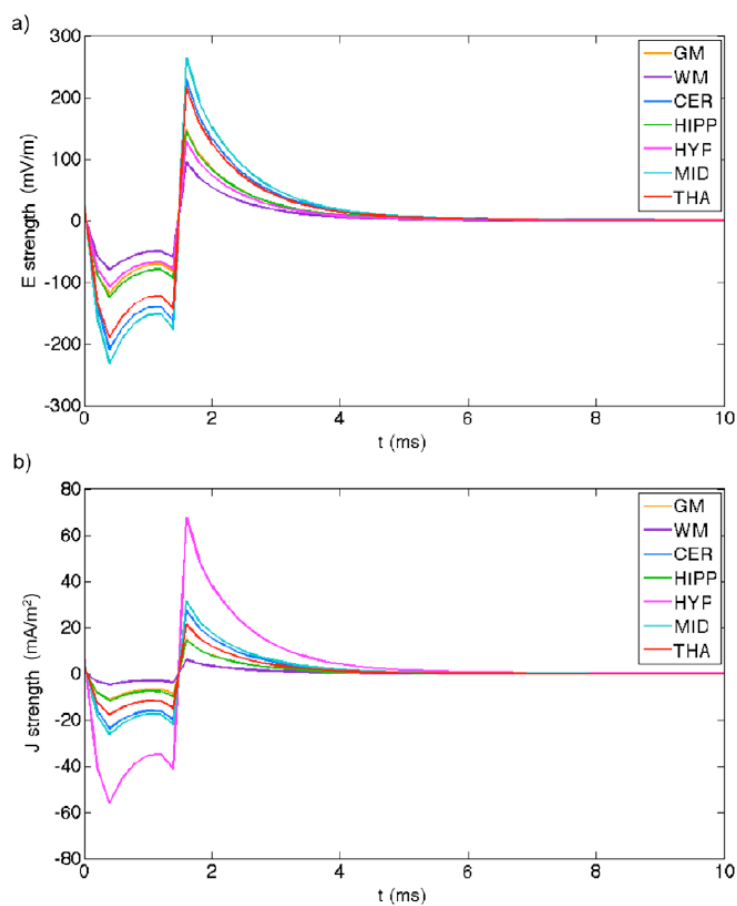


Figure 10.5: Time courses of E (panel (a)) and J (panel (b)) fields strengths on seven points lying in GM, WM, CER, HIPP, HYP, MID, and THA.

10.6 Conclusion

introduced by variations of $\pm 10\%$ in the maximum considered frequency. Due to the linear behavior, 11% of variations in B induce 11% of uncertainty in the estimated E peak. The uncertainty due to variability of tissues permittivity is much less (2%) than that due to variability of tissues conductivity (11%), showing that the induced E field is more sensitive to σ than to ε [389]. Finally, the uncertainty due the maximum considered frequency is around 2%. Pulling together all these contributions, the obtained total expanded uncertainty ($k = 2$) has been calculated to be around 32%, in line with dosimetric assessment used in the context of protection against electromagnetic fields [389].

Time resolved dosimetry assumes particular importance if one wants to identify a threshold for the onset of specific effects in the brain. Moreover, since observed experimental effects seem to be related to the specific waveform and frequency content [326, 378], the knowledge of E and J time courses in brain tissues is unavoidable to predict neuronal responses using biophysical models.

A possible limitation of the proposed approach relies on the simplified head anatomy, which does not account for the skull and scalp. However, the analysis in Golestanirad et al [387] showed that the inclusion of the skull would not affect the distribution of currents in the adjacent cortex of the brain.

Future works will account for a more realistic scenario in terms of the human head model and different typologies of field applicators in order to improve their stimulation efficacy.

10.6 Conclusion

In this work, a time resolved dosimetry, using the harmonic decomposition coupled with the admittance method, has been applied to a human brain model exposed to PMFs, specifically to the one presented by Capone et al. [330], a signal used in the osteoarthritis treatment [328, 329] but recently also applied to expose the central nervous system [330]. The high frequency content (up to tens of kHz) of such kinds of signals makes the use of a monochromatic dosimetry at the pulse repetition frequency inaccurate for the estimate of the maximum E and J fields induced in the brain. Moreover, a single frequency solution does not allow the reconstruction of the real waveforms induced in the brain tissue that interact with neuronal cells and networks. Results of time resolved dosimetry show that the PMF stimulation induces biphasic time courses of E and J in the brain. The E field peak values inside different brain tissue are considerably underestimated if a simplified monochromatic dosimetry is carried out at the pulse repetition frequency of 75 Hz. These results confirm the importance of a time

Time resolved dosimetry of human brain exposed to low frequency pulsed magnetic fields

resolved dosimetry for this kind of application, not only for calculating the real stimulation waveform but also for correct peak estimation. The more accurate dosimetry is, the more precise the interaction with neural tissues and the better the understanding of PMF applications. Future works will consider more realistic head models, including skull and scalp, and different kinds of magnetic field applicators.

Conclusions

CONCLUSIONS

The studies presented in this thesis evaluated computationally and experimentally the use of EM fields in the medical field for diagnostic and therapeutic applications. The evaluation of patient safety and effectiveness of the device is a fundamental step toward the use of EM fields in medical applications. Computational modeling is a powerful tool to quantitatively characterize the exposure of the human body in order to identify clinical outcomes, as it allows to study several variables affecting the EM field propagation with reduced costs and increased reproducibility compared to experimental measurements. Experimental validation of the numerical model remains a complementary and fundamental step to determine the degree to which a model is an accurate representation of the real world from the prospective of the intended uses of the model.

Among the medical applications, Magnetic Resonance Imaging is one of the most used diagnostic radiological imaging techniques in the clinical field, with over 33 million examinations a year in the US. The success of MRI is due to its clinical versatility, the use of non-ionizing radiation, and the high soft-tissue contrast. MRI is overall a safe technology, and its benefits need to be properly assessed against the possible risks to the patient, including heating of tissue induced by the RF field used to elicit the MRI signal. The evaluation of safety is additionally complicated for the increasing number of patients with implanted medical devices (e.g., pacemakers, deep brain stimulators, stents, orthopedic implants). One of the possible hazards posed to a patient with implanted devices during MRI is that elongated conductive structures may pick up RF-energy during the exposure, and locally deposit it in tissue near the implant electrodes. Traditionally, RF-induced heating has been evaluated by experimental methods, such as temperature measurements in gel-filled phantoms. EM absorption within phantoms can be controlled because of the geometrical simplicity. As for other EM field applications, computational modeling has been used increasingly to complement the experimental results to evaluate the RF-induced heating in patients without and with medical devices undergoing MRI. The computational cost of the simulations can be high because an object in the μm range (i.e. a lead) has to be evaluated inside one in the meters range (i.e. coil). This cost may be reduced by defeaturing the RF coil as well as decreasing the mesh resolution, but the accuracy of the simplified models needs to be verified. Results reported in the first part of this thesis showed that a correct numerical implementation is needed for accurate representation of the RF exposure. Results of the study showed that the specific numerical mesh used for the model affect the corresponding resonance frequency of the coil, with up to 3 % difference in coil resonance, and a related over 100 % of electric field magnitude difference within the coil. Additionally a proper selection of losses at the sources and within the

coil affects the coil performance both with respect to the radiated power and EM field distribution. As shown local differences in terms of electric and magnetic field magnitude can be observed for RF coil implemented through different software platforms, as well as with different losses.

The use of simplified models can be a powerful tool for the estimation of the RF exposure, although it may not allow for a proper estimation of the fields everywhere in the coil. Herein was shown that the use of models with diverse feeding conditions with respect to the physical coil may not allow an accurate modeling of the EM fields in air for the space between the phantom/human model and the coil. Defeatured coil models need to include properly selected lumped elements, in order to correctly estimate electric and magnetic field inside the phantom or human model. Additionally, when the numerical models are used to simulate local exposure, the model need to properly represent the feeding conditions of the real system (i.e., port position within the coil and feeding phase orientation); for human models with a partially implanted lead, different feeding position within the coil can lead to up to 50 % local SAR variability, whereas opposite feeding phase orientation up to 60%. Additionally it was shown that defeatured coil models can possibly underestimate the worst case exposure. Finally, the use of field diversification was proven as a useful tool for implant testing and numerical validation, by introducing a novel radiated testing method which utilizes the diversification of induced electric field inside the RF birdcage coil system through careful control and adjustment of the RF birdcage driving vector. The field diversity was produced imposing different polarizations into the RF coil system. The different exposure conditions may be sampled in practice to obtain an optimized set of diverse high-fidelity testing conditions for the assessment of implant safety due to RF-induced heating.

Evaluation of results with respect to a phantom rather than the human body models allows for the validation of the numerical data with measurements. Homogeneous models can help for preliminary evaluation of the average exposure with respect to the limits defined by the standard. In particular the standards categorize the limits with respect to three main body categories: the entire body, the partial body, and the head. The use of homogeneous models with respect to cylindrical phantoms was reported for the evaluation of the partial body SAR limit. Specifically the results showed that calculation open to different interpretations, suggesting the need for a revision of the current standard definition. Conversely, for the evaluation of local exposure in patients, it was also shown that the use of heterogeneous models can be fundamental for the assessment of regions with high level of absorption. The electrically heterogeneous anatomical structures generate field reflections and refractions at the tissue interfaces.

CONCLUSIONS

The RF inhomogeneities present within the heterogeneous model cannot be found in the homogeneous model. These field inhomogeneity create regions of high absorption inside the model that are up to 150% underestimated with homogeneous models. Additionally, a possible technique to reduce the power deposit at the tip of an implanted device was herein presented using high dielectric materials. The use of pads of such materials showed a possible reduction of SAR up to 57% in the head and by 68% in the thorax.

Finally, the powerful of the use of EM fields for therapy was presented. In medical therapy, electric, magnetic, and EM fields combined are applied to stimulate diverse type of tissues or cells (e.g., nerve and muscle), stimulate healing, or deliver heat for treatment or as a secondary effect such as for application in drug delivery. Among all the medical therapies that make use of EM field for treatment of diseases, the work performed within this thesis focused on the use of EM field for brain stimulation. Brain stimulation therapies involve activating or inhibiting areas of the brain directly with EM fields. The current can be directly be applied to the brain by means of electrodes implanted in the brain (i.e., invasive devices), or non-invasively through the scalp (i.e., non-invasive stimulation devices). The potential of the medical applications using electrical stimulation of the body has been recently evidenced by the coined term "electroceutical". The term describes the all the multidisciplinary initiatives made to develop "medicines" that use electrical impulses to modulate the body's neural circuits. The work performed in this thesis showed that accurate numerical models can be a support for the understanding of the mechanisms and biological interactions in an electroceutical perspective. The use of numerical methods was presented for the time domain calculation of the electric field within a model of the human brain. The numerical tool used to perform the low-frequency dosimetry was based on an improved revision of the admittance method. The time-domain dosimetry was implemented decomposing the signal in its harmonic components and then reconstructing it by means of its inverse Discrete Fourier Transform. Results confirmed the importance of a time resolved dosimetry for the evaluation of the tissue interaction with pulsed EM fields. The relevance of the time domain solution was shown not only for calculating the real stimulation waveform but also for correct peak estimation for the electric field and current density. The implemented method was also proved feasible to perform numerical evaluation of the electric scalar potential for unipolar and bipolar electrical stimulation (such as the one used by deep brain stimulators) within both isotropic and anisotropic materials. Further development of the methods should include neuronal tissue in the models.

Appendices

Appendix A

List of Acronyms

ASTM	American society for testing materials
BMI	Body Mass Index
BOMAB	Bottle Manikin Absorption
BREP	Boundary representation
CAD	Computer Aided Design
CCW	Counter-clockwise
CDRH	Center for Devices and Radiological Health
CNS	Central Nervous System
CSF	Cerebrospinal Fluid
CT	Computed Tomography
CW	Clockwise
DASY	Dosimetric assessment system
EEG	Electroencephalography
EM	Electromagnetic
EQS	electroquasistatic
FDA	Food and Drug Administration
FDTD	Finite-Difference Time-Domain
FEM	Finite Element Method
hSAR	head Specific Absorption Rate
ICNIRP	International Commission on Non-Ionising Radiation Protection
ICRP	International Commission on Radiological Protection
IEC	International Electrotechnical Commission
iMRI	interventional Magnetic Resonance Imaging
ISO	International Organization for Standardization
JWG	Joint Working Group

MIRD	Medical Internal Radiation Dose Committee
MITS	Medical Implant Test System
MoM	Method of Moments
MQS	magnetoquasistatic
MRI	Magnetic Resonance Imaging
NEMA	National Electrical Manufacturers Association
NMR	Nuclear Magnetic Resonance
NORMAN	NORmalized MAN
OECD	Organisation for Economic Co-operation and Development
PbSAR	Partial body Specific Absorption Rate
PEMFs	Pulsed Electromagnetic Fields
RF	Radio Frequency
RMS	Root Mean Square
rTMS	repetitive Transcranial Magnetic Stimulation
SAR	Specific Absorption Rate
SMAPE	Symmetric Mean Absolute Percentage Error
tDCS	transcranial Direct Current Stimulation
TEM	Transverse Electromagnetic
TMS	Transcranial Magnetic Stimulation
TS	Technical Specification
VHM	Visible Human Man
VHW	Visible Human Woman
VVUQ	Verification Validation and Uncertainty Quantification
WbSAR	Whole body Specific Absorption Rate

Appendix B

High resolution Figures

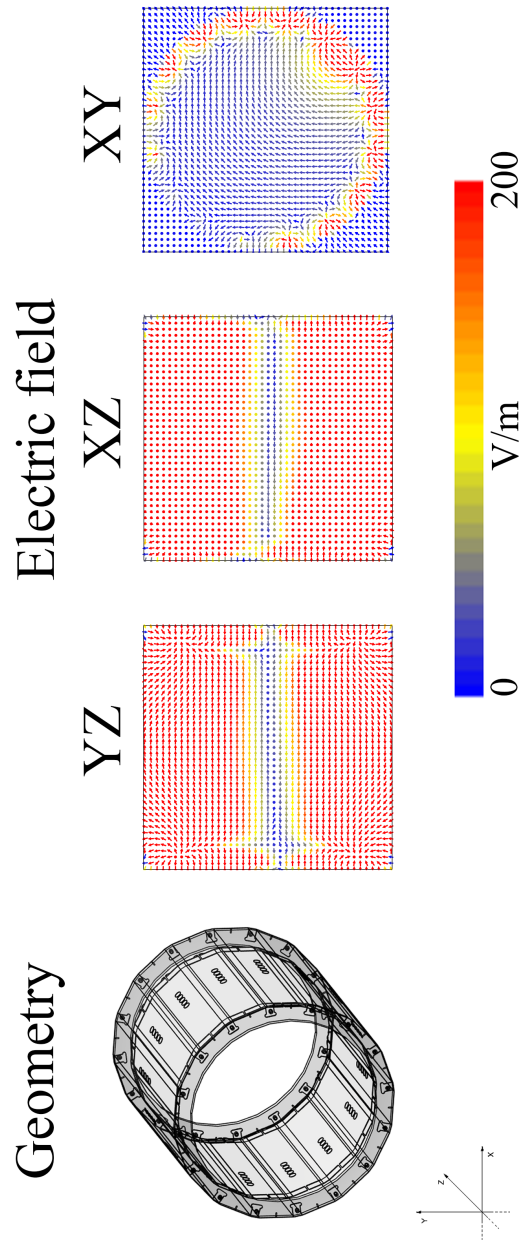


Figure B.1: Part I Figure 2.16

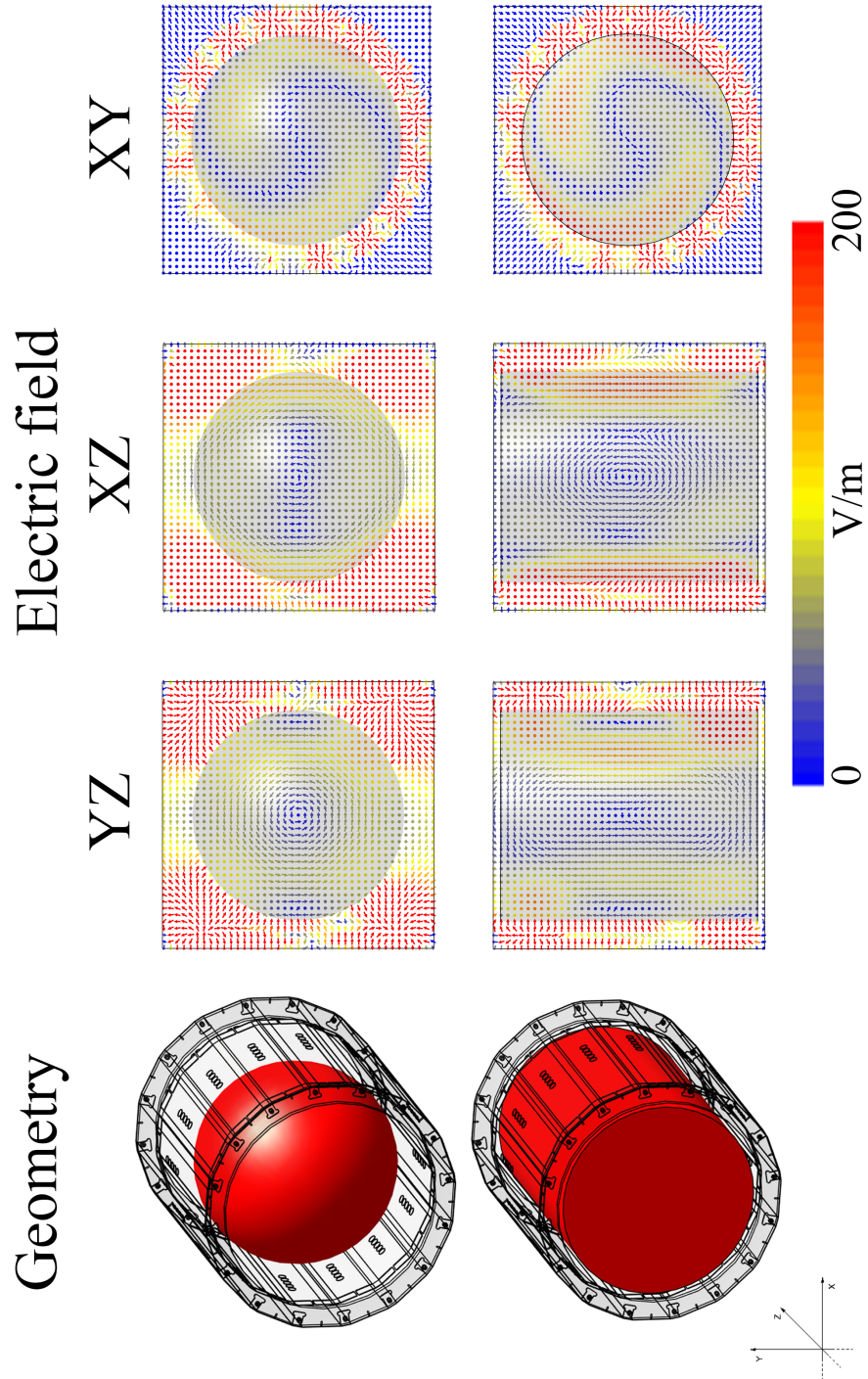


Figure B.2: Part II Figure 2.16

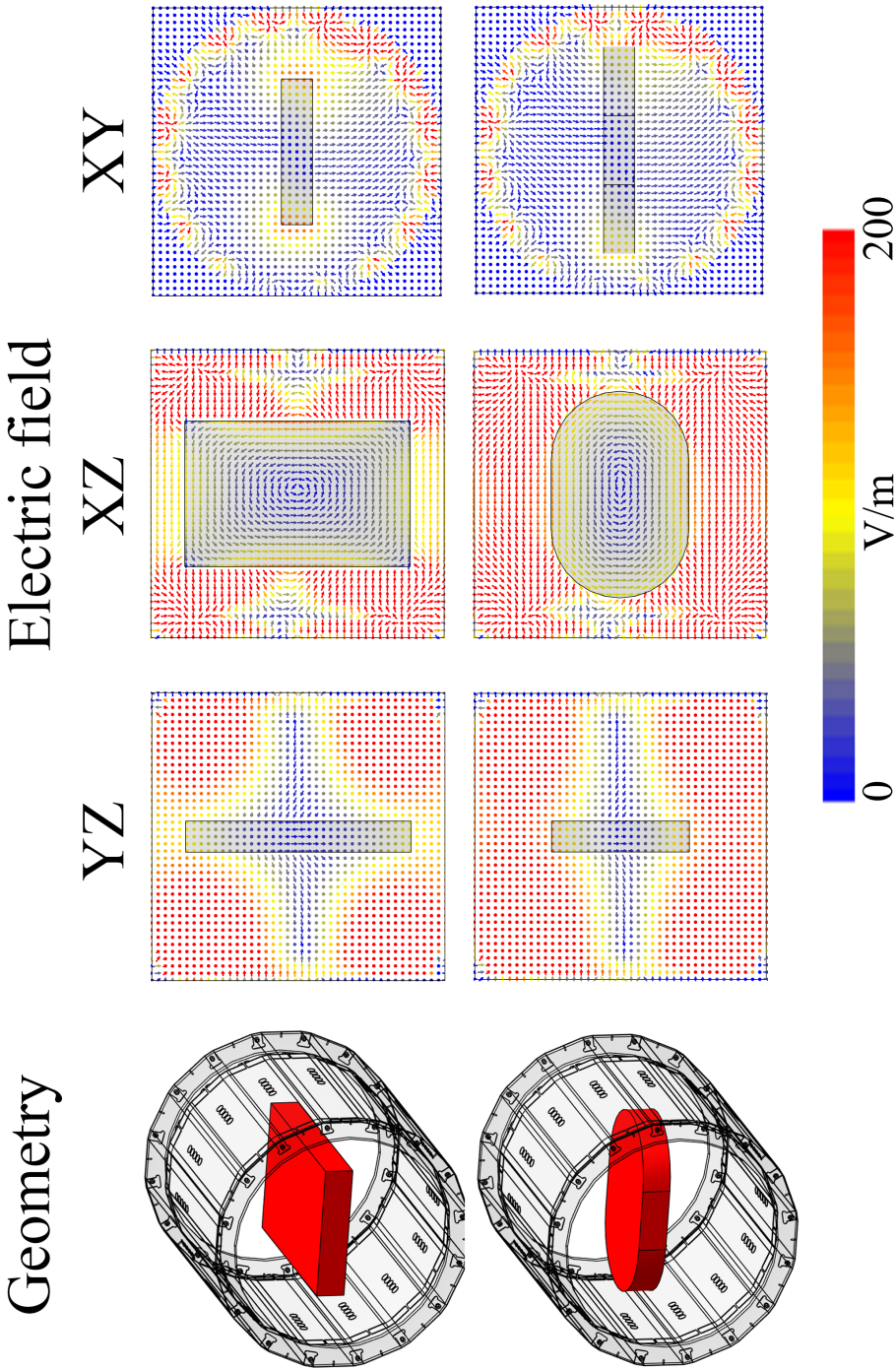


Figure B.3: Part I Figure 2.17

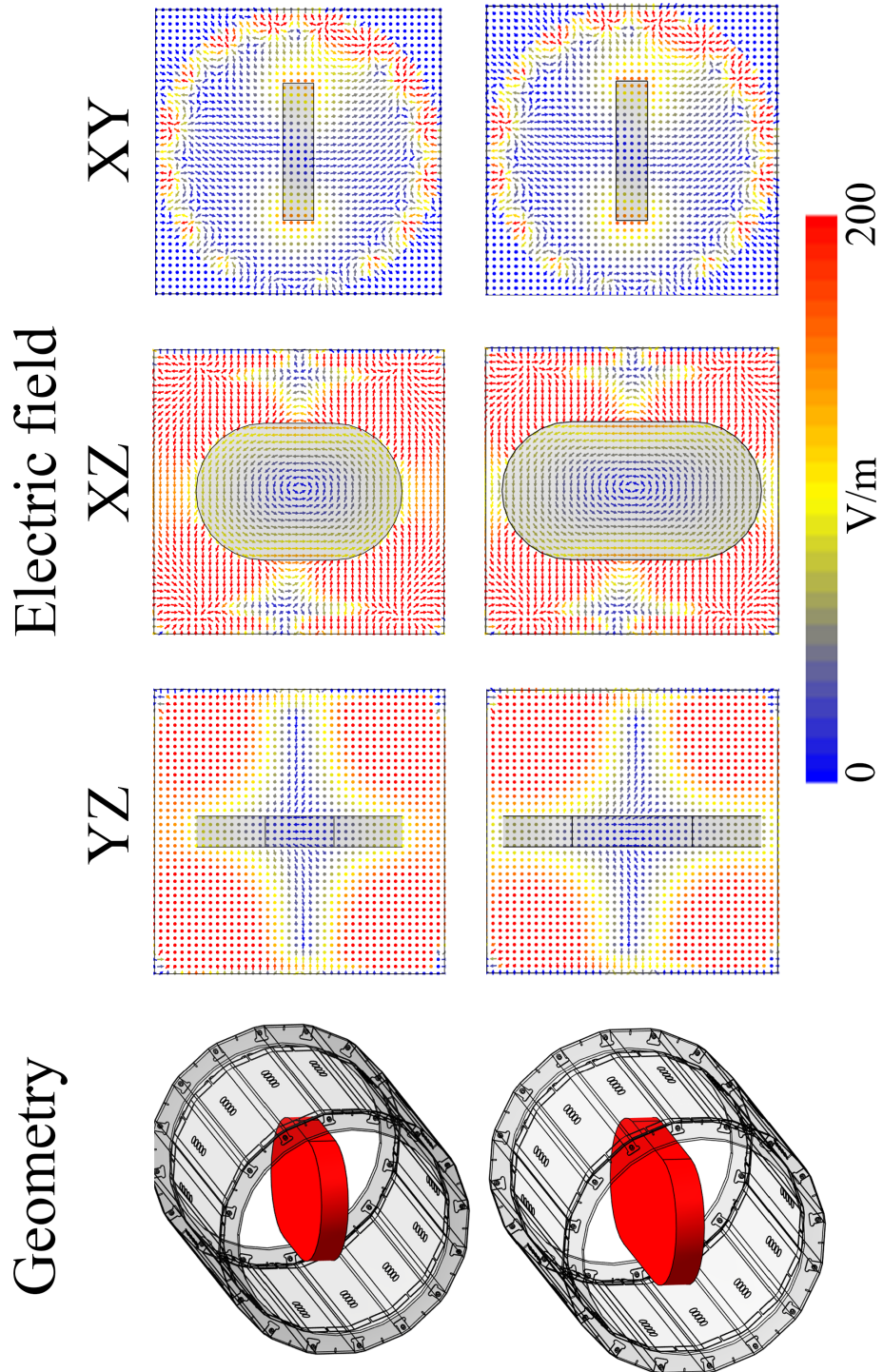


Figure B.4: Part II Figure 2.17

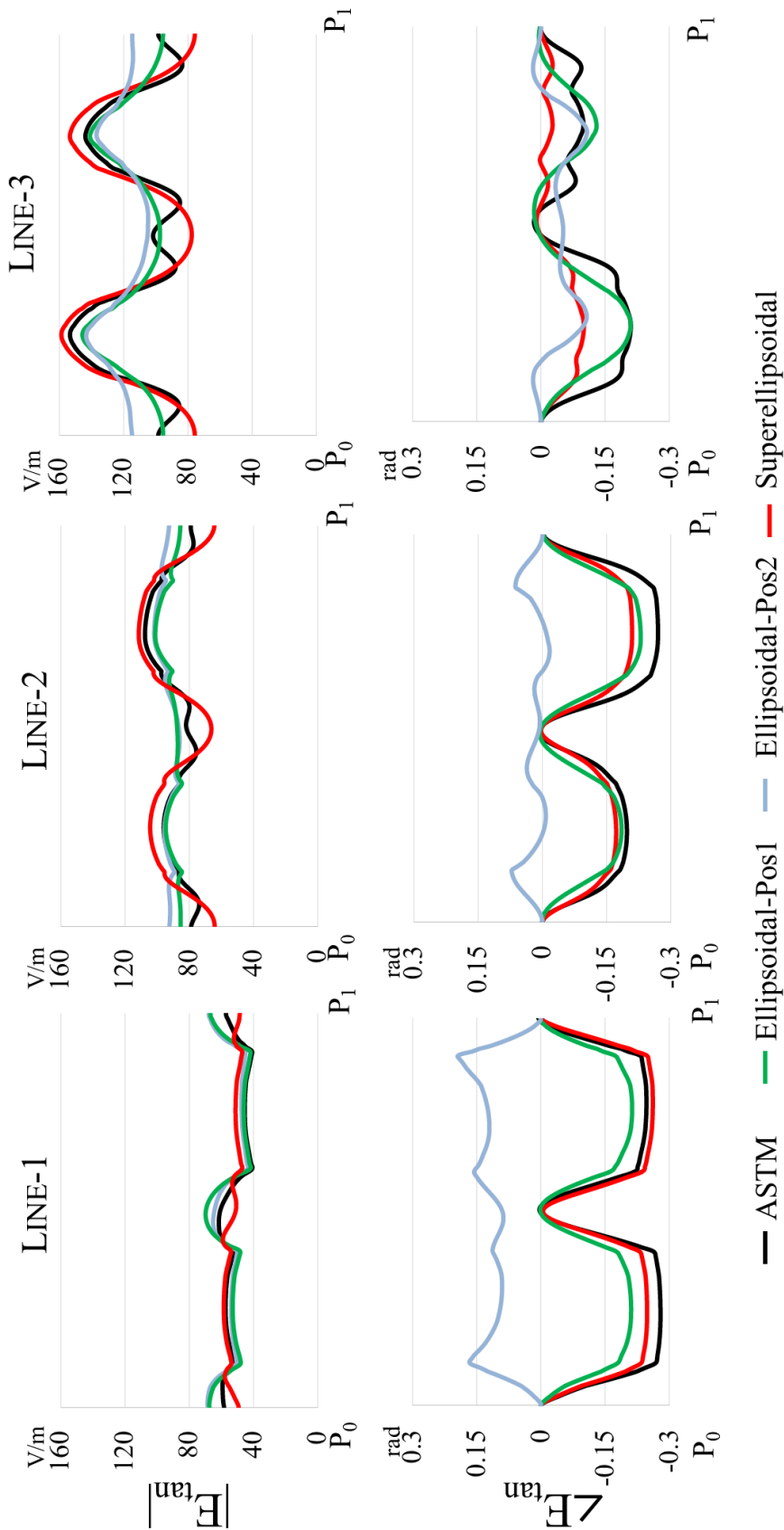


Figure B.5: Figure 2.17
234

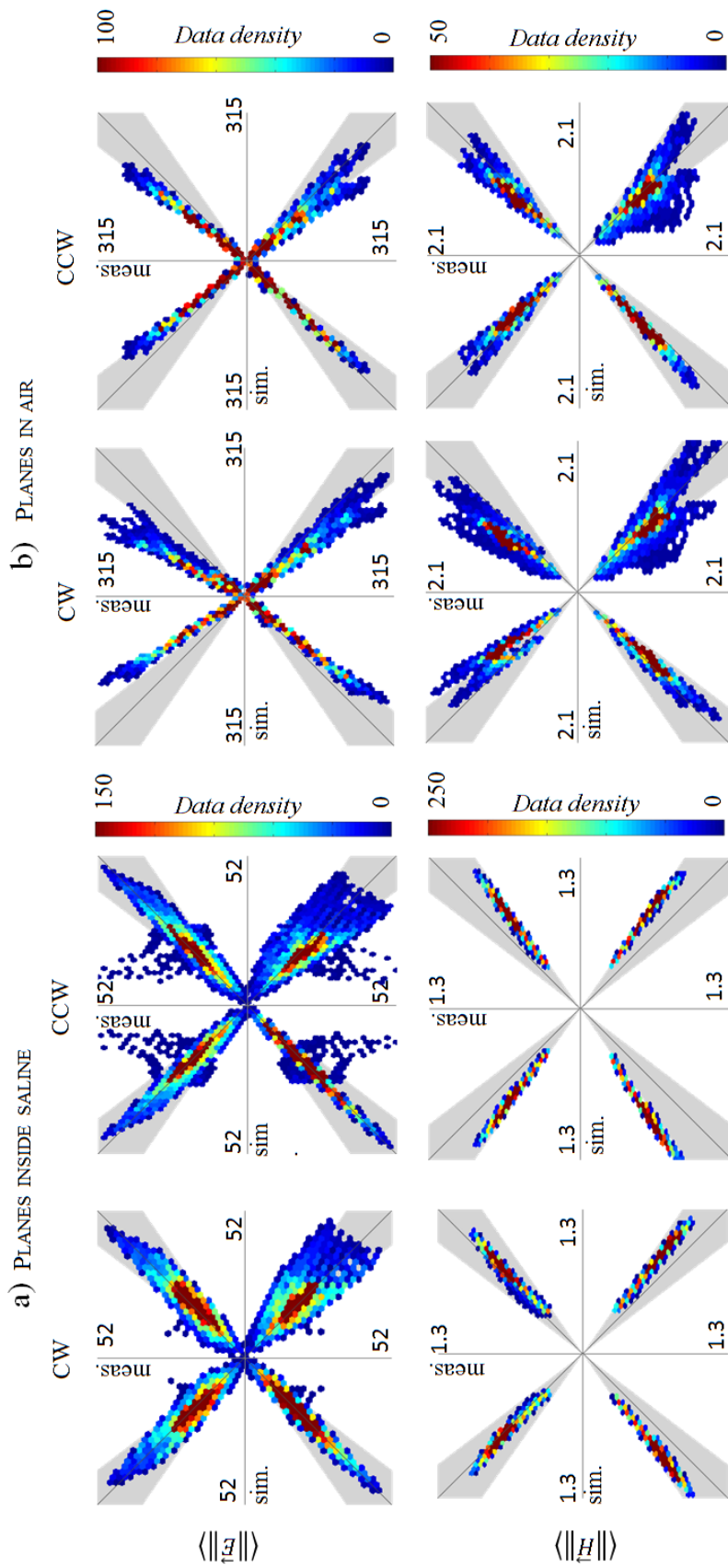


Figure B.7: Figure 4.9

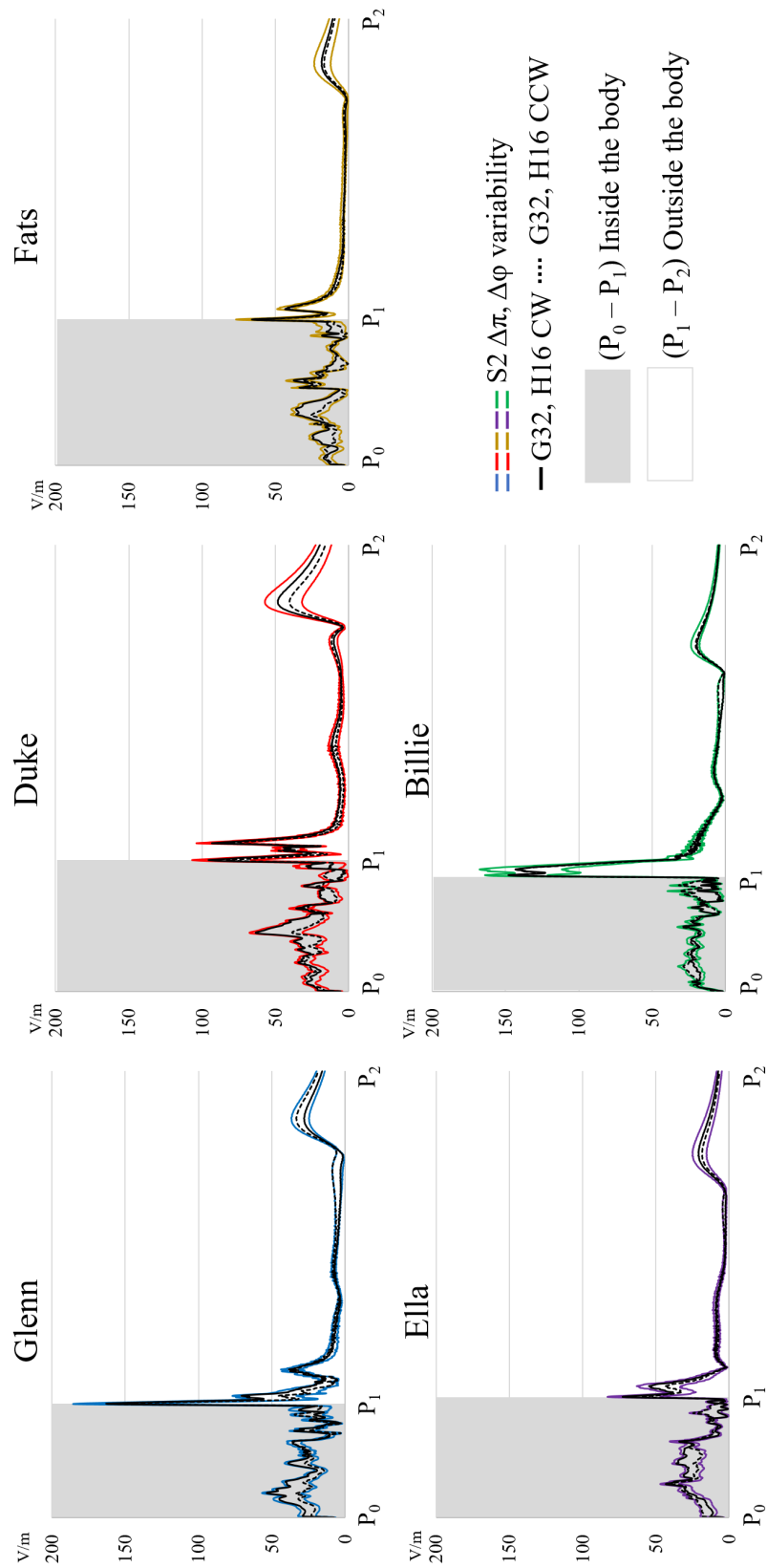


Figure B.8: Figure 7.4

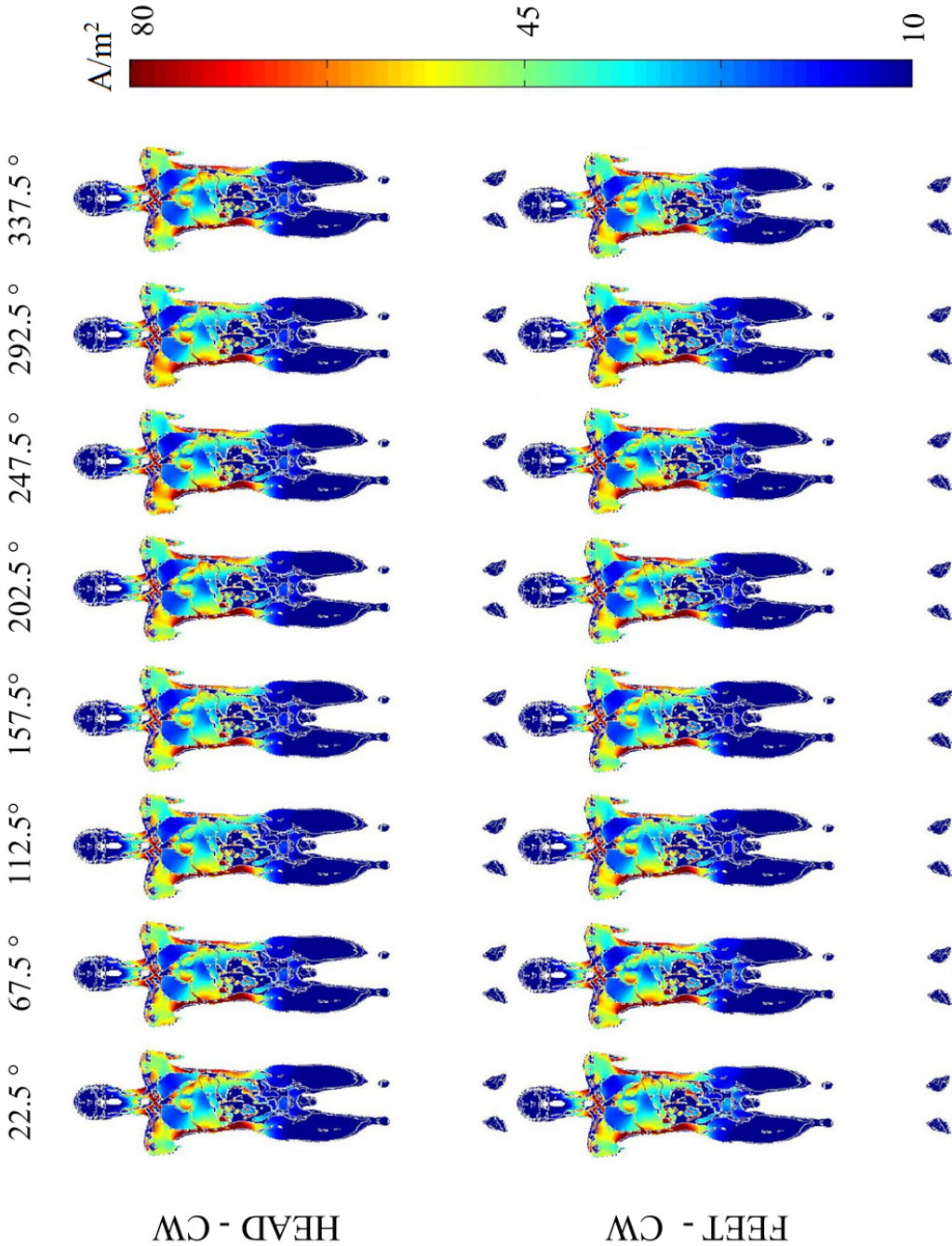


Figure B.9: Part I of Figure 7.14

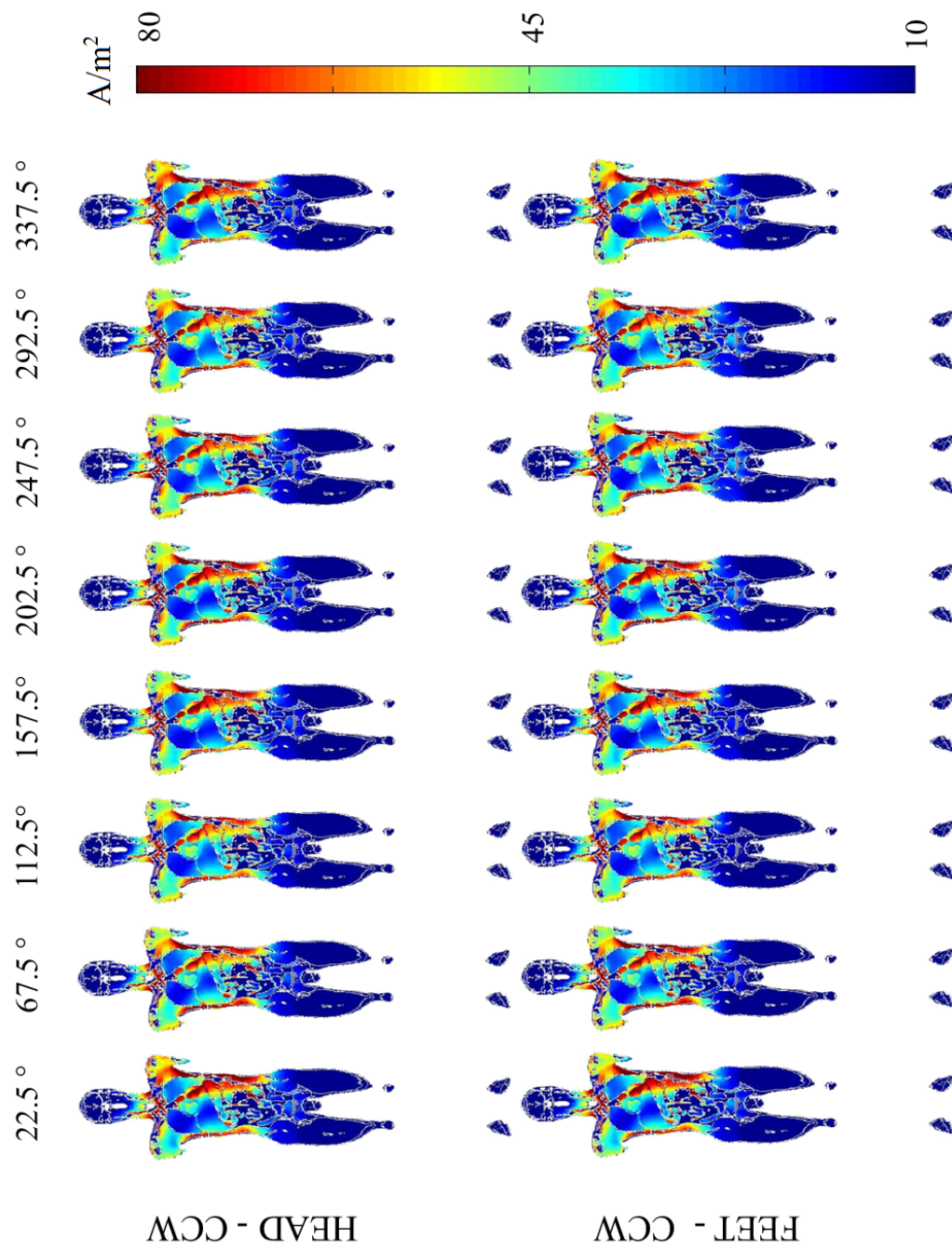


Figure B.10: Part II of Figure 7.14

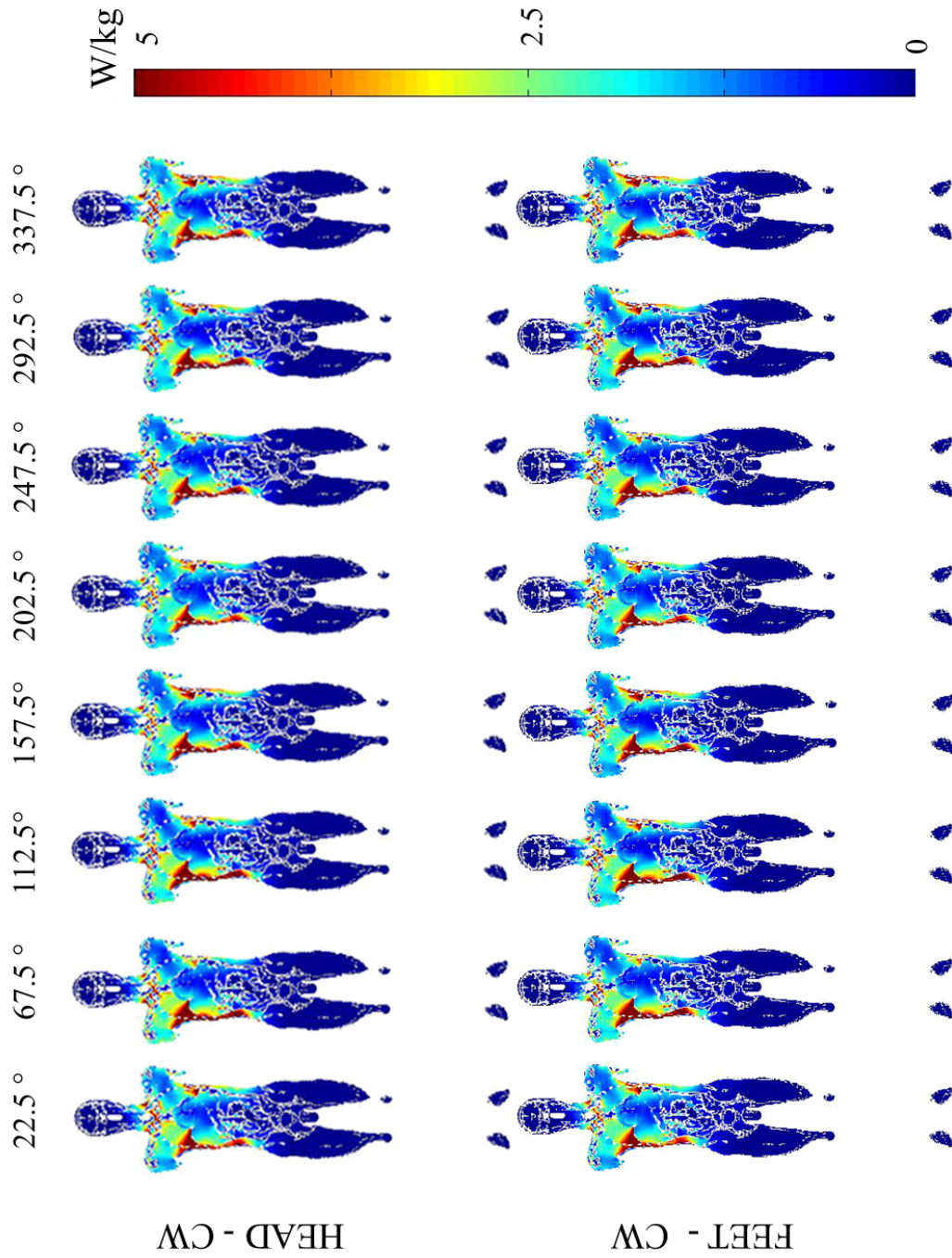


Figure B.11: Part I of Figure 7.15

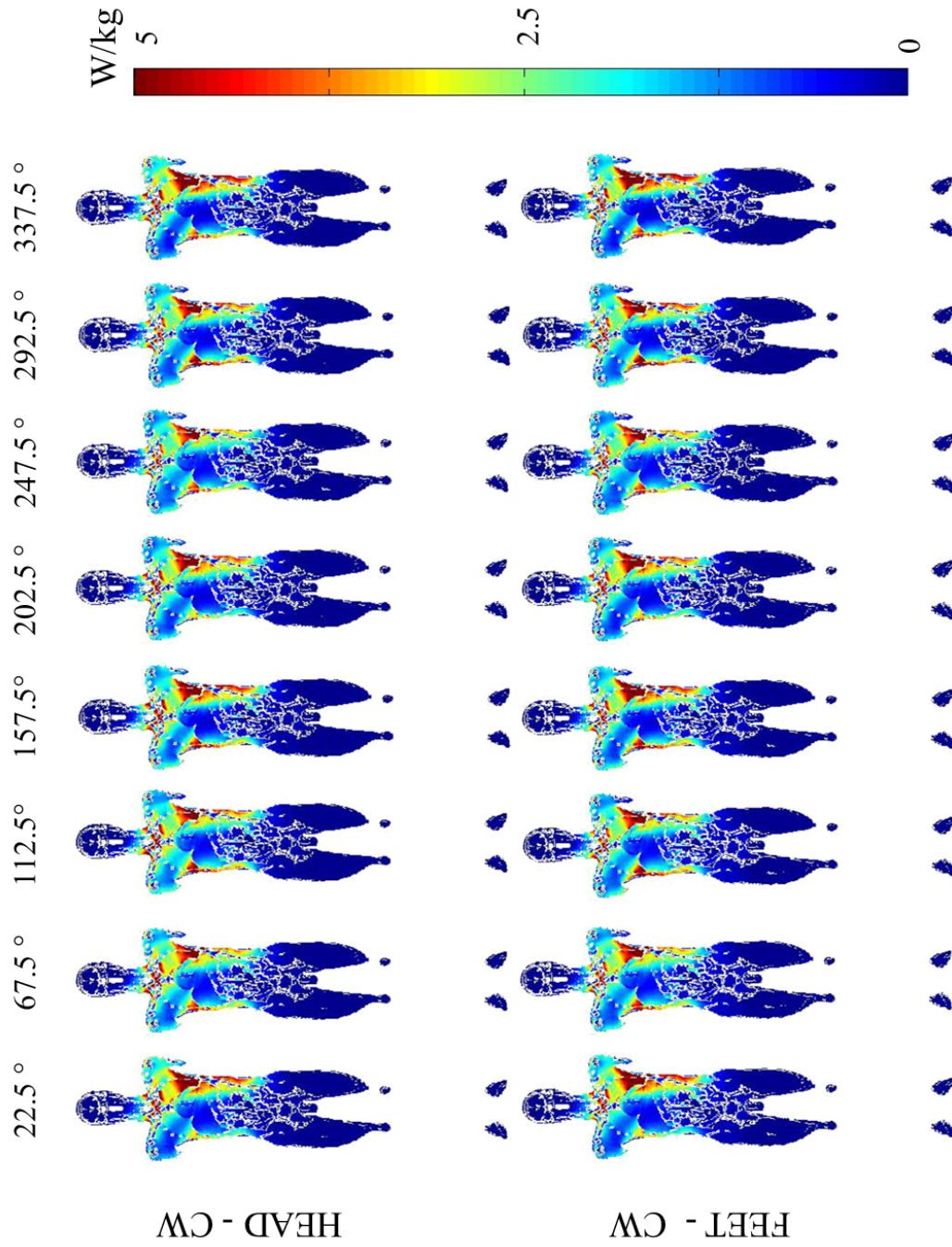


Figure B.12: Part II of Figure 7.15

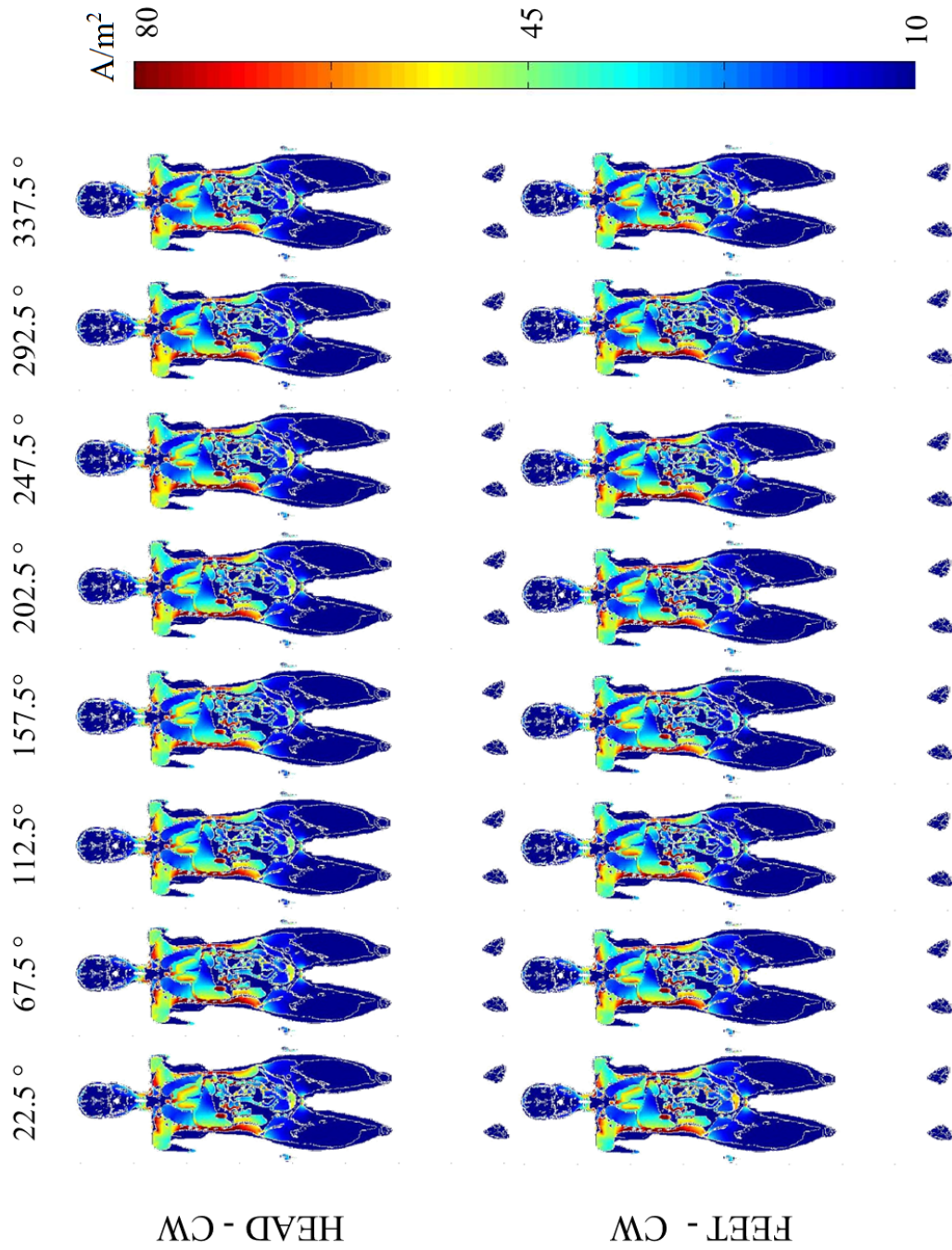


Figure B.13: Part I of Figure 7.16

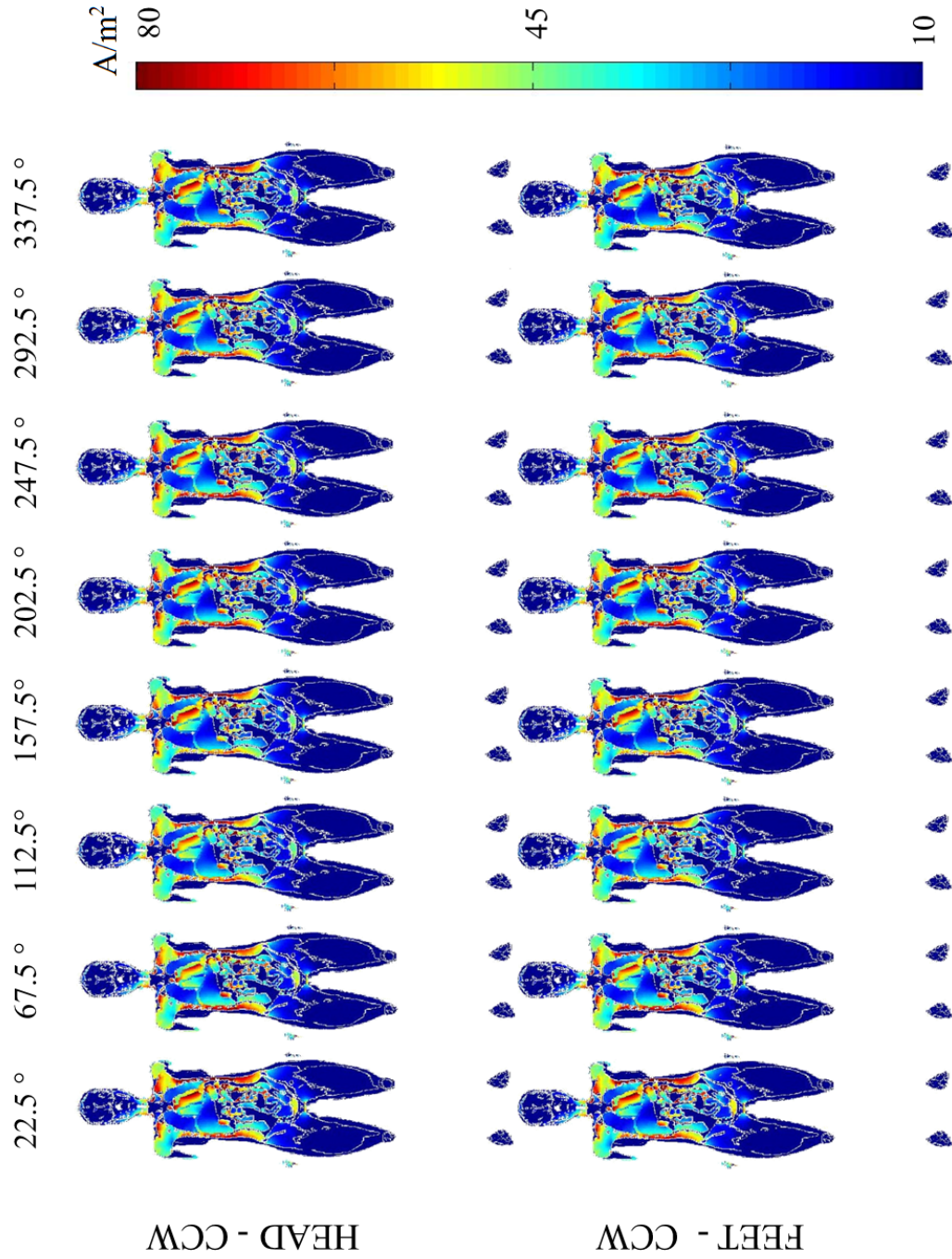


Figure B.14: Part II of Figure 7.16

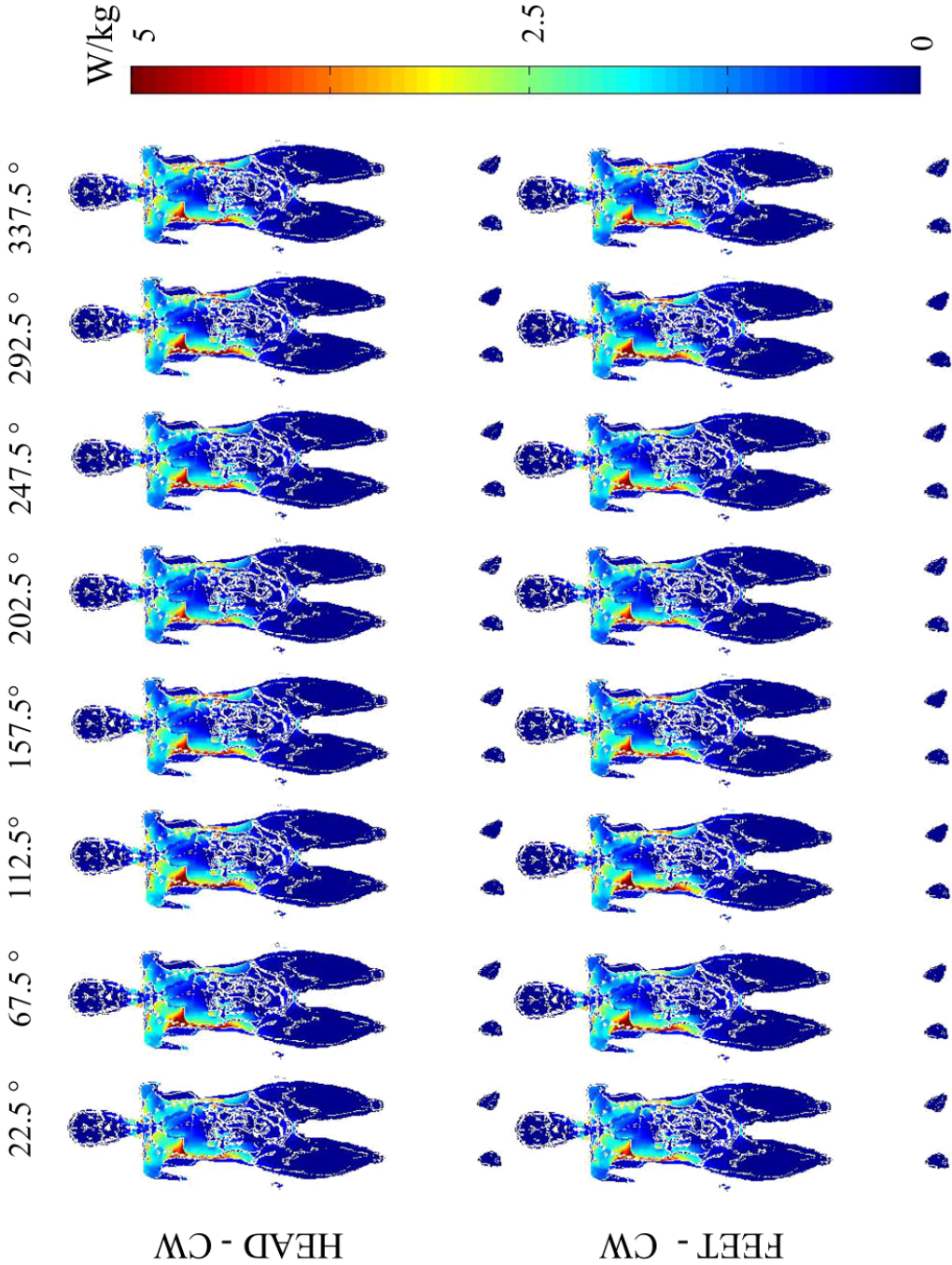


Figure B.15: Part I of Figure 7.17

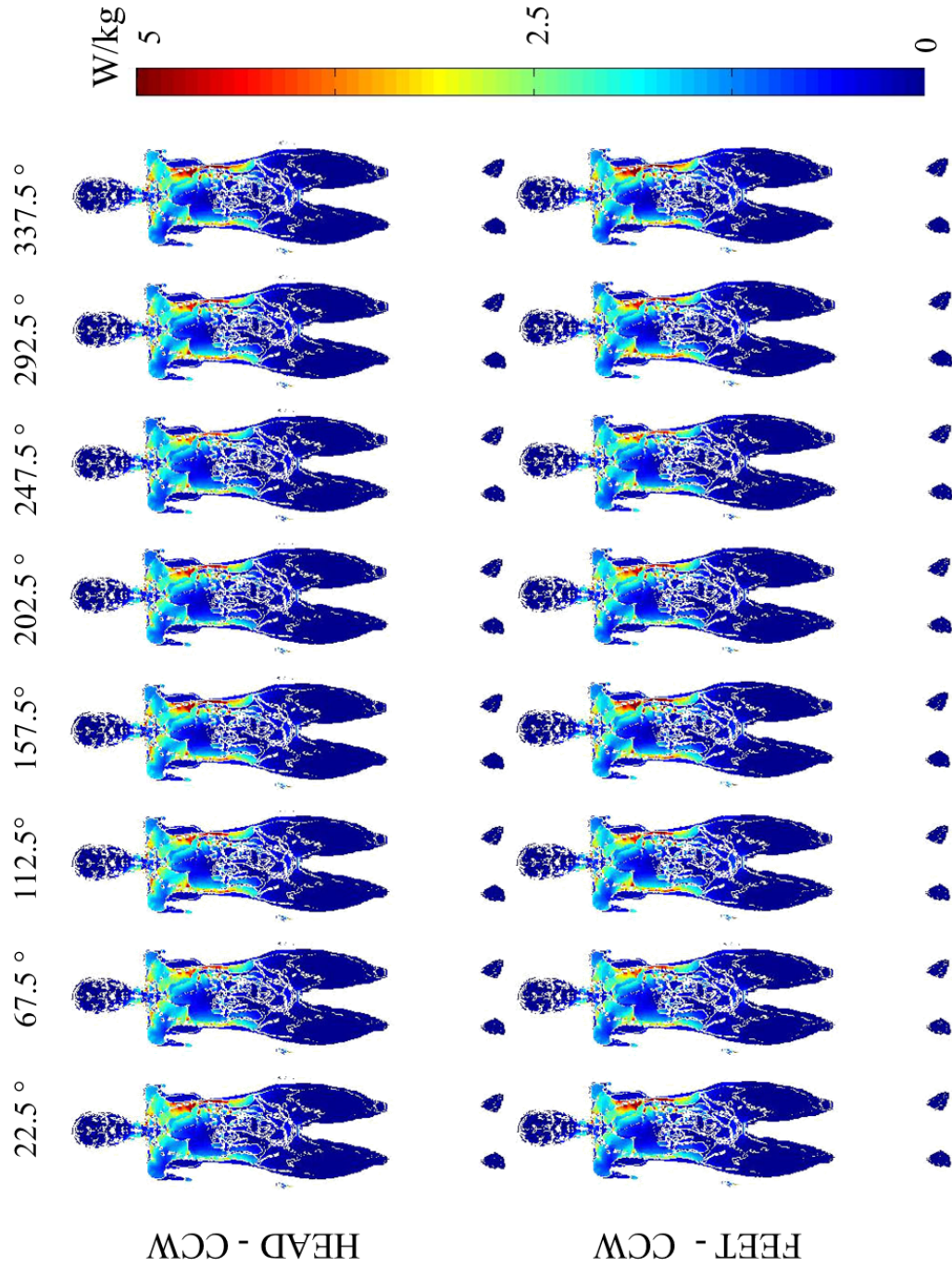


Figure B.16: Part II of Figure 7.17

Bibliography

Bibliography

- [1] R. Sutton, E. Kanal, B. L. Wilkoff, D. Bello, R. Luechinger, I. Jenniskens, M. Hull, and T. Sommer, "Safety of magnetic resonance imaging of patients with a new Medtronic EnRhythm MRI SureScan pacing system: clinical study design." *Trials*, vol. 9, p. 68, jan 2008. [Online]. Available: <http://www.pubmedcentral.nih.gov/articlerender.fcgi?artid=2629460&tool=pmcentrez&rendertype=abstract>
- [2] I. Rabi, "On the process of space quantization," *Physical Review*, vol. 49, no. 4, p. 324, 1936.
- [3] A. D. Elster. Questions and answers in mri. [Online]. Available: <http://mri-q.com/index.html>
- [4] E. M. Purcell, H. Torrey, and R. V. Pound, "Resonance absorption by nuclear magnetic moments in a solid," *Physical review*, vol. 69, no. 1-2, p. 37, 1946.
- [5] F. Bloch, "Nuclear induction," *Physical review*, vol. 70, no. 7-8, p. 460, 1946.
- [6] E. L. Hahn, "Spin echoes," *Physical review*, vol. 80, no. 4, p. 580, 1950.
- [7] H. Y. Carr and E. M. Purcell, "Effects of diffusion on free precession in nuclear magnetic resonance experiments," *Physical review*, vol. 94, no. 3, p. 630, 1954.
- [8] P. C. Lauterbur, *Image formation by induced local interactions: examples employing nuclear magnetic resonance*. University of Chicago Press, 2010, 1973.
- [9] ———, "Magnetic resonance zeugmatography," *Pure and Applied Chemistry*, vol. 40, no. 1-2, pp. 149–157, 1974.
- [10] D. G. Nishimura, *Principles of magnetic resonance imaging*. Stanford Univ., 2010.
- [11] T. Schild, G. Aubert, C. Berriaud, P. Bredy, F. Juster, C. Meuris, F. Nunio, L. Quettier, J. Rey, and P. Vadrine, "The iseult/inumac whole body 11.7 t mri magnet design," *IEEE Transactions on Applied Superconductivity*, vol. 18, no. 2, pp. 904–907, 2008.
- [12] V. H. Prevost, O. M. Girard, V. Callot, P. J. Cozzone, and G. Duhamel, "Fast imaging strategies for mouse kidney perfusion measurement with pseudocontinuous arterial spin labeling (pcasl) at ultra high magnetic field (11.75 tesla)," *Journal of Magnetic Resonance Imaging*, vol. 42, no. 4, pp. 999–1008, 2015.
- [13] H. Kanithi, D. Blasiak, J. Lajewski, C. Berriaud, P. Vadrine, and G. Gilgrass, "Production results of 11.75 tesla iseult/inumac mri conductor at luvata," *IEEE Transactions on Applied Superconductivity*, vol. 24, no. 3, pp. 1–4, 2014.
- [14] R. Ouwerkerk, "Sodium mri," *Magnetic Resonance Neuroimaging: Methods and Protocols*, pp. 175–201, 2011.

- [15] J. Wang, W. Mao, M. Qiu, M. B. Smith, and R. T. Constable, "Factors influencing flip angle mapping in mri: Rf pulse shape, slice-select gradients, off-resonance excitation, and b0 inhomogeneities," *Magnetic resonance in medicine*, vol. 56, no. 2, pp. 463–468, 2006.
- [16] C. E. Hayes, "The development of the birdcage resonator: A historical perspective," *NMR in Biomedicine*, vol. 22, no. June, pp. 908–918, 2009.
- [17] Hoult, "Radio frequency coil technology in nmr scanning," *Proceedings of an International Symposium on NMR Imaging*, pp. 33–39, 1981.
- [18] C. E. Hayes, W. a. Edelstein, J. F. Schenck, O. M. Mueller, and M. Eash, "An efficient, highly homogeneous radiofrequency coil for whole-body NMR imaging at 1.5 T," *Journal of Magnetic Resonance (1969)*, vol. 63, no. 3, pp. 622–628, 1985.
- [19] L. R. Frank, E. C. Wong, W.-M. Luh, J. M. Ahn, and D. Resnick, "Articular cartilage in the knee: mapping of the physiologic parameters at mr imaging with a local gradient coil—preliminary results," *Radiology*, vol. 210, no. 1, pp. 241–246, 1999.
- [20] B. A. Chronik, R. Venook, S. M. Conolly, and G. C. Scott, "Readout frequency requirements for dedicated prepolarized and hyperpolarized-gas mri systems," in *Proceedings of the 10th Annual Meeting of ISMRM, Honolulu, HI, USA, 2002*, p. 0058.
- [21] F. D. Doty, "Mri gradient coil optimization," *Spatially Resolved Magnetic Resonance: Methods, Materials, Medicine, Biology, Rheology, Geology, Ecology, Hardware*, pp. 647–674, 1999.
- [22] M. C. Leifer, "Resonant modes of the birdcage coil," *Journal of Magnetic Resonance*, vol. 124, no. 1, pp. 51–60, 1997.
- [23] J. T. Vaughn Jr, "Radio frequency volume coils for imaging and spectroscopy," Sep. 17 1996, uS Patent 5,557,247.
- [24] A. Sotgiu and J. S. Hyde, "High-order coils as transmitters for nmr imaging," *Magnetic resonance in medicine*, vol. 3, no. 1, pp. 55–62, 1986.
- [25] U. Katscher and P. Börnert, "Parallel rf transmission in mri," *NMR in Biomedicine*, vol. 19, no. 3, pp. 393–400, 2006.
- [26] G. Glover, C. E. Hayes, N. Pelc, W. Edelstein, O. Mueller, H. Hart, C. Hardy, M. O'Donnell, and W. Barber, "Comparison of linear and circular polarization for magnetic resonance imaging," *Journal of Magnetic Resonance (1969)*, vol. 64, no. 2, pp. 255–270, 1985.
- [27] L. A. Vainshtein, *Electromagnetic waves*. Moscow Izdatel Radio Sviaz, 1988.
- [28] C. M. Collins and Z. Wang, "Calculation of radiofrequency electromagnetic fields and their effects in MRI of human subjects." *Magnetic resonance in medicine : official journal of the Society of Magnetic Resonance in Medicine / Society of Magnetic Resonance in Medicine*, vol. 65, no. 5, pp. 1470–82, may 2011. [Online]. Available: <http://www.pubmedcentral.nih.gov/articlerender.fcgi?artid=3078983&tool=pmcentrez&rendertype=abstract>
- [29] R. Plonsey, "The nature of sources of bioelectric and biomagnetic fields." *Biophysical Journal*, vol. 39, no. 3, p. 309, 1982.

BIBLIOGRAPHY

- [30] B. J. Klauenberg and D. Miklavcic, *Radio frequency radiation dosimetry and its relationship to the biological effects of electromagnetic fields*. Springer Science & Business Media, 2012, vol. 82.
- [31] Food, D. Administration *et al.*, “Reporting of computational modeling studies in medical device submissions—draft guidance for industry and food and drug administration staff only,” *Food and Drug Administration, Rockville, MD*, 2014.
- [32] D. Simunic, P. Wach, W. Renhart, and R. Stollberger, “Spatial distribution of high-frequency electromagnetic energy in human head during mri: numerical results and measurements,” *IEEE transactions on biomedical engineering*, vol. 43, no. 1, p. 88, 1996.
- [33] F. G. Shellock, “Radiofrequency energy-induced heating during MR procedures: a review.” *Journal of magnetic resonance imaging : JMRI*, vol. 12, no. 1, pp. 30–6, jul 2000.
- [34] S. Oh, A. G. Webb, T. Neuberger, B. Park, and C. M. Collins, “Experimental and numerical assessment of MRI-induced temperature change and SAR distributions in phantoms and in vivo.” *Magnetic resonance in medicine : official journal of the Society of Magnetic Resonance in Medicine / Society of Magnetic Resonance in Medicine*, vol. 63, no. 1, pp. 218–23, jan 2010. [Online]. Available: <http://www.pubmedcentral.nih.gov/articlerender.fcgi?artid=2836721> {&}tool=pmcentrez {&}rendertype=abstract
- [35] W. Liu, C. Collins, and M. Smith, “Calculations of B1 distribution, specific energy absorption rate, and intrinsic signal-to-noise ratio for a body-size birdcage coil loaded with different human subjects at 64 and 128 mhz,” *Applied magnetic resonance*, vol. 29, no. 1, pp. 5–18, 2005.
- [36] T. S. Ibrahim, R. Lee, B. a. Baertlein, and P. M. Robitaille, “B1 field homogeneity and SAR calculations for the birdcage coil.” *Physics in medicine and biology*, vol. 46, no. 2, pp. 609–19, feb 2001. [Online]. Available: <http://www.ncbi.nlm.nih.gov/pubmed/11229737>
- [37] E. Cabot, T. Lloyd, A. Christ, W. Kainz, M. Douglas, G. Stenzel, S. Wedan, and N. Kuster, “Evaluation of the rf heating of a generic deep brain stimulator exposed in 1.5 t magnetic resonance scanners,” *Bioelectromagnetics*, vol. 34, no. 2, pp. 104–113, 2013.
- [38] L. M. Angelone, J. Ahveninen, J. W. Belliveau, and G. Bonmassar, “Analysis of the role of lead resistivity in specific absorption rate for deep brain stimulator leads at 3t mri,” *IEEE transactions on medical imaging*, vol. 29, no. 4, pp. 1029–1038, 2010.
- [39] S. Pisa, E. PiuZZi, and P. Bernardi, *Interaction between the RF Field of MRI Apparatus and Pacemakers*. INTECH Open Access Publisher, 2011.
- [40] E. Mattei, G. Calcagnini, F. Censi, M. Triventi, and P. Bartolini, “Numerical model for estimating rf-induced heating on a pacemaker implant during mri: experimental validation,” *IEEE transactions on biomedical engineering*, vol. 57, no. 8, pp. 2045–2052, 2010.
- [41] J. F. Thompson, Z. U. Warsi, and C. W. Mastin, *Numerical grid generation: foundations and applications*. North-holland Amsterdam, 1985, vol. 45.

- [42] K. S. Yee *et al.*, “Numerical solution of initial boundary value problems involving maxwell’s equations in isotropic media,” *IEEE Trans. Antennas Propag*, vol. 14, no. 3, pp. 302–307, 1966.
- [43] A. Taflove, A. Oskooi, and S. G. Johnson, *Advances in FDTD computational electrodynamics: photonics and nanotechnology*. Artech house, 2013.
- [44] C. Railton and J. Schneider, “An analytical and numerical analysis of several locally conformal FDTD schemes,” *IEEE Transactions on Microwave Theory and Techniques*, vol. 47, no. 1, pp. 56–66, 1999. [Online]. Available: <http://ieeexplore.ieee.org/lpdocs/epic03/wrapper.htm?arnumber=740077>
- [45] Q. Liu, “An fdtd algorithm with perfectly matched layers for conductive media,” *Microwave and Optical Technology Letters*, vol. 14, no. 2, pp. 134–137, 1997.
- [46] J.-P. Berenger, “A perfectly matched layer for the absorption of electromagnetic waves,” *Journal of computational physics*, vol. 114, no. 2, pp. 185–200, 1994.
- [47] A. C. Cangellaris and D. B. Wright, “Analysis of the numerical error caused by the stair-stepped approximation of a conducting boundary in fdtd simulations of electromagnetic phenomena,” *IEEE transactions on antennas and propagation*, vol. 39, no. 10, pp. 1518–1525, 1991.
- [48] R. Holland, “Pitfalls of staircase meshing,” *IEEE Transactions on Electromagnetic Compatibility*, vol. 35, no. 4, pp. 434–439, 1993.
- [49] H. Yang and C. Railton, “Efficient and accurate fdtd algorithm for the treatment of curved material boundaries,” *IEE Proceedings-Microwaves, Antennas and Propagation*, vol. 144, no. 5, pp. 382–388, 1997.
- [50] W. Yu, R. Mittra, D. Arakaki, and D. H. Werner, “A conformal finite difference time domain (cfdd) algorithm for modeling perfectly conducting objects,” 2000.
- [51] T. JURGENS, A. Taflove, K. Umashankar, and T. MOORE, “Finite-difference time-domain modeling of curved surfaces,” *IEEE Transactions on Antennas and Propagation*, vol. 40, no. 4, pp. 357–366, 1992.
- [52] T. G. Jurgens and A. Taflove, “Three-dimensional contour fdtd modeling of scattering from single and multiple bodies,” *IEEE Transactions on Antennas and Propagation*, vol. 41, no. 12, pp. 1703–1708, 1993.
- [53] C. Railton, I. Craddock, and J. Schneider, “Improved locally distorted cpfdtd algorithm with provable stability,” *Electronics Letters*, vol. 31, no. 18, pp. 1585–1586, 1995.
- [54] C. Railton and I. Craddock, “Stabilised cpfdtd algorithm for the analysis of arbitrary 3d pec structures,” *IEE Proceedings-Microwaves, Antennas and Propagation*, vol. 143, no. 5, pp. 367–372, 1996.
- [55] S. Dey and R. Mittra, “A locally conformal finite-difference time-domain (fdtd) algorithm for modeling three-dimensional perfectly conducting objects,” *IEEE Microwave and Guided Wave Letters*, vol. 7, no. 9, pp. 273–275, 1997.
- [56] S. Benkler, N. Chavannes, and N. Kuster, “Mastering conformal meshing for complex cad-based c-fdtd simulations,” *IEEE Antennas and Propagation Magazine*, vol. 50, no. 2, pp. 45–57, 2008.

BIBLIOGRAPHY

- [57] R. Holland, "Finite-difference solution of maxwell's equations in generalized nonorthogonal coordinates," *IEEE Transactions on Nuclear Science*, vol. 6, no. 30, pp. 4589–4591, 1983.
- [58] M. Fusio, "FDTD algorithm in curvilinear coordinate," *IEEE Trans Antennas Propagat*, vol. 38, no. 1, pp. 76–89, 1990.
- [59] R. Palandech, R. Mittra *et al.*, "Modeling three-dimensional discontinuities in waveguides using nonorthogonal fdtd algorithm," *IEEE Transactions on Microwave Theory and Techniques*, vol. 40, no. 2, pp. 346–352, 1992.
- [60] K. S. Yee and J. S. Chen, "The finite-difference time-domain (fdtd) and the finite-volume time-domain (fvtd) methods in solving maxwell's equations," *IEEE Transactions on Antennas and Propagation*, vol. 45, no. 3, pp. 354–363, 1997.
- [61] A. Monorchio, A. R. Bretones, R. Mittra, G. Manara, and R. G. Martín, "A hybrid time-domain technique that combines the finite element, finite difference and method of moment techniques to solve complex electromagnetic problems," *IEEE Transactions on Antennas and Propagation*, vol. 52, no. 10, pp. 2666–2674, 2004.
- [62] T. Rylander and A. Bondeson, "Stable fem-fdtd hybrid method for maxwell's equations," *Computer Physics Communications*, vol. 125, no. 1, pp. 75–82, 2000.
- [63] A. R. Bretones, R. Mittra, and R. G. Martín, "A hybrid technique combining the method of moments in the time domain and fdtd," *IEEE Microwave and Guided Wave Letters*, vol. 8, no. 8, pp. 281–283, 1998.
- [64] Z. Huang, K. R. Demarest, and R. G. Plumb, "An fdtd/mom hybrid technique for modeling complex antennas in the presence of heterogeneous grounds," *IEEE Transactions on Geoscience and Remote Sensing*, vol. 37, no. 6, pp. 2692–2698, 1999.
- [65] W. Xu, F. Liu, L. Xia, and S. Crozier, "Accurate Evaluation of RF Coil-tissue Interactions Using a Hybrid FDTD-MoM Method," *PIERS Online*, vol. 6, pp. 212–216, 2010.
- [66] V. Nefedov, *Subgridding in FDTD*. Eindhoven University of Technology, Department of Mathematics and Computing Science, 2002.
- [67] S. S. Zivanovic, K. S. Yee, and K. K. Mei, "A subgridding method for the time-domain finite-difference method to solve maxwell's equations," *IEEE Transactions on Microwave Theory and Techniques*, vol. 39, no. 3, pp. 471–479, 1991.
- [68] D. T. Prescott and N. Shuley, "A method for incorporating different sized cells into the finite-difference time-domain analysis technique," *IEEE Microwave and Guided Wave Letters*, vol. 2, no. 11, pp. 434–436, 1992.
- [69] K. S. Yee, J. S. Chen, and A. H. Chang, "Conformal finite-different time-domain (fdtd) with overlapping grids," *IEEE Transactions on Antennas and Propagation*, vol. 40, no. 9, pp. 1068–1075, 1992.
- [70] M. J. White, M. F. Iskander, and Z. Huang, "Development of a multigrid fdtd code for three-dimensional applications," *IEEE Transactions on Antennas and Propagation*, vol. 45, no. 10, pp. 1512–1517, 1997.

- [71] M. W. Steeds, S. L. Broschat, and J. B. Schneider, "A comparison of two conformal methods for fdtd modeling," *IEEE transactions on electromagnetic compatibility*, vol. 38, no. 2, pp. 181–187, 1996.
- [72] P. Leuchtman, C. Fumeaux, and D. Baumann, "Comparison of errors and stability in fdtd and fvtd," *Advances in Radio Science*, vol. 1, no. 5, pp. 87–92, 2003.
- [73] A. L. H. M. W. van Lier, D. O. Brunner, K. P. Pruessmann, D. W. J. Klomp, P. R. Luijten, J. J. W. Lagendijk, and C. a. T. van den Berg, "B1(+) phase mapping at 7 T and its application for in vivo electrical conductivity mapping." *Magnetic resonance in medicine : official journal of the Society of Magnetic Resonance in Medicine / Society of Magnetic Resonance in Medicine*, vol. 67, no. 2, pp. 552–61, feb 2012. [Online]. Available: <http://www.ncbi.nlm.nih.gov/pubmed/21710613>
- [74] M. Padiaditis, N. Leitgeb, and R. Cech, "RF-EMF exposure of fetus and mother during magnetic resonance imaging." *Physics in medicine and biology*, vol. 53, no. 24, pp. 7187–95, dec 2008. [Online]. Available: <http://www.ncbi.nlm.nih.gov/pubmed/19033645>
- [75] N. Krishnamurthy, T. Zhao, and T. S. Ibrahim, "Effects of receive-only inserts on specific absorption rate, B1 (+) field, and Tx coil performance." *Journal of magnetic resonance imaging : JMRI*, vol. 000, aug 2013. [Online]. Available: <http://www.ncbi.nlm.nih.gov/pubmed/23913474>
- [76] E. Mattei, G. Calcagnini, M. Triventi, F. Censi, and P. Bartolini, "Numerical fdtd models of electromagnetic field generated by the rf coil of an mri scanner: comparison among different solutions," in *Proceedings of the Sixth IASTED International Conference, Biomedical Engineering, Innsbruck, Austria, 2008*.
- [77] Y. Liu, J. Chen, F. G. Shellock, and W. Kainz, "Computational and experimental studies of an orthopedic implant: Mri-related heating at 1.5-t/64-mhz and 3-t/128-mhz," *Journal of Magnetic Resonance Imaging*, vol. 37, no. 2, pp. 491–497, 2013.
- [78] M. Murbach, E. Neufeld, W. Kainz, K. P. Pruessmann, and N. Kuster, "Whole-body and local RF absorption in human models as a function of anatomy and position within 1.5T MR body coil." *Magnetic resonance in medicine : official journal of the Society of Magnetic Resonance in Medicine / Society of Magnetic Resonance in Medicine*, vol. 000, pp. 1–7, feb 2013. [Online]. Available: <http://www.ncbi.nlm.nih.gov/pubmed/23440667>
- [79] D. B. Davidson, *Computational electromagnetics for RF and microwave engineering*. Cambridge University Press, 2005.
- [80] L. E. Schwer, "An overview of the ptc 60/v&v 10: guide for verification and validation in computational solid mechanics," *Engineering with Computers*, vol. 23, no. 4, pp. 245–252, 2007.
- [81] J. Chen, Z. Feng, and J. M. Jin, "Numerical simulation of SAR and Si-field inhomogeneity of shielded rf coils loaded with the human head," *IEEE Transactions on Biomedical Engineering*, vol. 45, no. 5, pp. 642–649, 1998.
- [82] R. Bowtell and R. Bowley, "Analytic calculations of the e-fields induced by time-varying magnetic fields generated by cylindrical gradient coils," *Magnetic resonance in medicine*, vol. 44, no. 5, pp. 782–790, 2000.

BIBLIOGRAPHY

- [83] C. M. Collins, W. Liu, J. Wang, R. Gruetter, J. T. Vaughan, K. Ugurbil, and M. B. Smith, "Temperature and sar calculations for a human head within volume and surface coils at 64 and 300 mhz," *Journal of Magnetic Resonance Imaging*, vol. 19, no. 5, pp. 650–656, 2004.
- [84] F. Seifert, G. Wübbeler, S. Junge, B. Ittermann, and H. Rinneberg, "Patient safety concept for multichannel transmit coils," *Journal of Magnetic Resonance Imaging*, vol. 26, no. 5, pp. 1315–1321, 2007.
- [85] H. Homann, P. Börnert, H. Eggers, K. Nehrke, O. Dössel, and I. Graesslin, "Toward individualized sar models and in vivo validation," *Magnetic resonance in medicine*, vol. 66, no. 6, pp. 1767–1776, 2011.
- [86] T. Voigt, H. Homann, U. Katscher, and O. Doessel, "Patient-individual local sar determination: In vivo measurements and numerical validation," *Magnetic resonance in medicine*, vol. 68, no. 4, pp. 1117–1126, 2012.
- [87] C. A. Van den Berg, L. W. Bartels, B. van den Bergen, H. Kroeze, A. A. de Leeuw, J. B. Van de Kamer, and J. J. Lagendijk, "The use of mr b+ 1 imaging for validation of fdtd electromagnetic simulations of human anatomies," *Physics in medicine and biology*, vol. 51, no. 19, p. 4735, 2006.
- [88] T. Ibrahim, A. Abduljalil, B. Baertlein, R. Lee, and P. Robitaille, "Analysis of b1 field profiles and sar values for multi-strut transverse electromagnetic rf coils in high field mri applications," *Physics in medicine and biology*, vol. 46, no. 10, p. 2545, 2001.
- [89] L. Wang and C. D. Sarris, "A multi-resolution fdtd method for uncertainty quantification in the time-domain modeling of microwave structures," in *2014 IEEE MTT-S International Microwave Symposium (IMS2014)*. IEEE, 2014, pp. 1–3.
- [90] W. L. Oberkamp, S. M. DeLand, B. M. Rutherford, K. V. Diegert, and K. F. Alvin, "Error and uncertainty in modeling and simulation," *Reliability Engineering & System Safety*, vol. 75, no. 3, pp. 333–357, 2002.
- [91] E. Neufeld, S. Kühn, G. Szekely, and N. Kuster, "Measurement, simulation and uncertainty assessment of implant heating during MRI." *Physics in medicine and biology*, vol. 54, no. 13, pp. 4151–69, jul 2009. [Online]. Available: <http://stacks.iop.org/0031-9155/54/i=13/a=012?key=crossref.97948664c3c029b01eaf9d79b5d392ffhttp://www.ncbi.nlm.nih.gov/pubmed/19521007>
- [92] M. Cristy and K. Eckerman, "Specific absorbed fractions of energy at various ages from internal photon sources. vi. newborn," *ORNL/TM-8381*, vol. 6, 1987.
- [93] X. G. Xu, "An exponential growth of computational phantom research in radiation protection, imaging, and radiotherapy: a review of the fifty-year history." *Physics in medicine and biology*, vol. 59, no. 18, pp. R233–R302, 2014. [Online]. Available: <http://www.ncbi.nlm.nih.gov/pubmed/25144730>
- [94] N. Petoussi-Hens, M. Zankl, U. Fill, and D. Regulla, "The gsf family of voxel phantoms," *Physics in medicine and biology*, vol. 47, no. 1, p. 89, 2001.
- [95] R. Kramer, J. Vieira, H. Khoury, F. Lima, and D. Fuelle, "All about max: a male adult voxel phantom for monte carlo calculations in radiation protection dosimetry," *Physics in medicine and biology*, vol. 48, no. 10, p. 1239, 2003.

- [96] M. Stabin, M. Tagesson, S. Thomas, M. Ljungberg, and S.-E. Strand, "Radiation dosimetry in nuclear medicine," *Applied Radiation and Isotopes*, vol. 50, no. 1, pp. 73–87, 1999.
- [97] M.-C. Gosselin, E. Neufeld, H. Moser, E. Huber, S. Farcito, L. Gerber, M. Jedensjö, I. Hilber, F. Di Gennaro, B. Lloyd *et al.*, "Development of a new generation of high-resolution anatomical models for medical device evaluation: the virtual population 3.0," *Physics in medicine and biology*, vol. 59, no. 18, p. 5287, 2014.
- [98] T. consortium of Computational Human Phantoms. Virtual human phantoms. [Online]. Available: <http://www.virtualphantoms.org/phantoms.htm>
- [99] P. Dimbylow, "FDTD calculations of the whole-body averaged SAR in an anatomically realistic voxel model of the human body from 1 MHz to 1 GHz," *Physics in medicine and biology*, vol. 42, no. 3, p. 479, 1997.
- [100] A. Christ, W. Kainz, E. G. Hahn, K. Honegger, M. Zefferer, E. Neufeld, W. Rascher, R. Janka, W. Bautz, J. Chen, B. Kiefer, P. Schmitt, H.-P. Hollenbach, J. Shen, M. Oberle, D. Szczerba, A. Kam, J. W. Guag, and N. Kuster, "The Virtual Family—development of surface-based anatomical models of two adults and two children for dosimetric simulations." *Physics in medicine and biology*, vol. 55, no. 2, pp. N23–38, Jan 2010. [Online]. Available: <http://www.ncbi.nlm.nih.gov/pubmed/20019402>
- [101] I. foundation. Virtual population overview. [Online]. Available: <https://www.itis.ethz.ch/virtual-population/virtual-population/overview/>
- [102] M. I. Iacono, E. Neufeld, E. Akinagbe, K. Bower, J. Wolf, I. Vogiatzis Oikonomidis, D. Sharma, B. Lloyd, B. J. Wilm, M. Wyss, K. P. Pruessmann, A. Jakab, N. Makris, E. D. Cohen, N. Kuster, W. Kainz, and L. M. Angelone, "MIDA: A Multimodal Imaging-Based Detailed Anatomical Model of the Human Head and Neck," *Plos One*, vol. 10, no. 4, p. e0124126, 2015. [Online]. Available: <http://dx.plos.org/10.1371/journal.pone.0124126>
- [103] N. Makris, L. Angelone, S. Tulloch, S. Sorg, J. Kaiser, D. Kennedy, and G. Bonmassar, "MRI-based anatomical model of the human head for specific absorption rate mapping," *Medical & biological engineering & computing*, vol. 46, no. 12, pp. 1239–1251, 2008.
- [104] M. K. Konings, L. W. Bartels, H. F. Smits, and C. J. Bakker, "Heating around intravascular guidewires by resonating RF waves." *Journal of magnetic resonance imaging : JMRI*, vol. 12, no. 1, pp. 79–85, Jul 2000. [Online]. Available: <http://www.ncbi.nlm.nih.gov/pubmed/10931567>
- [105] L. Alon, C. M. Deniz, R. Brown, D. K. Sodickson, and Y. Zhu, "Method for in situ characterization of radiofrequency heating in parallel transmit MRI." *Magnetic resonance in medicine : official journal of the Society of Magnetic Resonance in Medicine / Society of Magnetic Resonance in Medicine*, vol. 69, no. 5, pp. 1457–65, May 2013. [Online]. Available: <http://www.ncbi.nlm.nih.gov/pubmed/22714806>
- [106] C. J. Yeung, P. Karmarkar, and E. R. McVeigh, "Minimizing RF heating of conducting wires in MRI." *Magnetic resonance in medicine : official journal of the Society of Magnetic Resonance in Medicine / Society of Magnetic Resonance in Medicine*, vol. 58, no. 5, pp. 1028–34, Nov 2007. [Online]. Available: <http://www.ncbi.nlm.nih.gov/pubmed/17969097>

BIBLIOGRAPHY

- [107] T. S. Ibrahim, R. Lee, B. a. Baertlein, Y. Yu, and P.-M. L. M. Robitaille, "Computational analysis of the high pass birdcage resonator: finite difference time domain simulations for high-field MRI," *Magnetic Resonance Imaging*, vol. 18, no. 7, pp. 835–43, sep 2000. [Online]. Available: <http://linkinghub.elsevier.com/retrieve/pii/S0730725X00001612><http://www.ncbi.nlm.nih.gov/pubmed/11027877>
- [108] E. M. Shapiro, a. Borthakur, and R. Reddy, "MR imaging of RF heating using a paramagnetic doped agarose phantom." *Magma (New York, N.Y.)*, vol. 10, no. 2, pp. 114–21, jun 2000. [Online]. Available: <http://www.ncbi.nlm.nih.gov/pubmed/10873201>
- [109] U. Nöth, H. Laufs, R. Stoermer, and R. Deichmann, "Simultaneous electroencephalography-functional MRI at 3 T: an analysis of safety risks imposed by performing anatomical reference scans with the EEG equipment in place." *Journal of magnetic resonance imaging : JMRI*, vol. 35, no. 3, pp. 561–71, mar 2012. [Online]. Available: <http://www.ncbi.nlm.nih.gov/pubmed/22002900>
- [110] A. International, "Astm f2182 standard test method for measurement of measurement of radio frequency induced heating near passive implants during magnetic resonance imaging," 2008.
- [111] T. ISO, "10974: Assessment of the safety of magnetic resonance imaging for patients with an active implantable medical device," *Geneva, Switzerland: International Organization for Standardization*, 2012.
- [112] G. H. Kramer, L. Burns, and L. Noel, "The brmd bomab phantom family." *Health physics*, vol. 61, no. 6, pp. 895–902, 1991.
- [113] S. M. Boucousis, C. a. Beers, C. J. B. Cunningham, I. Gaxiola-Valdez, D. J. Pittman, B. G. Goodyear, and P. Federico, "Feasibility of an intracranial EEG-fMRI protocol at 3T: risk assessment and image quality." *NeuroImage*, vol. 63, no. 3, pp. 1237–48, nov 2012. [Online]. Available: <http://www.ncbi.nlm.nih.gov/pubmed/22902923>
- [114] C. K. Chou, J. a. McDougall, and K. W. Can, "Absence of radiofrequency heating from auditory implants during magnetic resonance imaging." *Bioelectromagnetics*, vol. 16, no. 5, pp. 307–16, jan 1995. [Online]. Available: <http://www.ncbi.nlm.nih.gov/pubmed/8554632>
- [115] A. Kangarlu, F. G. Shellock, and D. W. Chakeres, "8.0-tesla human mr system: Temperature changes associated with radiofrequency-induced heating of a head phantom," *Journal of Magnetic Resonance Imaging*, vol. 17, no. 2, pp. 220–226, 2003.
- [116] N. N. Graedel, J. R. Polimeni, B. Guerin, B. Gagoski, and L. L. Wald, "An anatomically realistic temperature phantom for radiofrequency heating measurements," *Magnetic Resonance in Medicine*, vol. 00, pp. 1–9, 2014.
- [117] G. Calcagnini, M. Triventi, F. Censi, E. Mattei, P. Bartolini, W. Kainz, and H. I. Bassen, "In vitro investigation of pacemaker lead heating induced by magnetic resonance imaging: role of implant geometry." *Journal of magnetic resonance imaging : JMRI*, vol. 28, no. 4, pp. 879–86, oct 2008. [Online]. Available: <http://www.ncbi.nlm.nih.gov/pubmed/18821629>
- [118] T. P. Laboratory. Rando® phantom. [Online]. Available: <http://www.imagingequipment.co.uk/product/1016-82/RANDO-phantoms>

- [119] T. S. Ibrahim, R. Lee, B. a. Baertlein, a. M. Abduljalil, H. Zhu, and P. M. Robitaille, "Effect of RF coil excitation on field inhomogeneity at ultra high fields: a field optimized TEM resonator." *Magnetic resonance imaging*, vol. 19, no. 10, pp. 1339–47, dec 2001. [Online]. Available: <http://www.ncbi.nlm.nih.gov/pubmed/11804762>
- [120] E. Mattei, M. Triventi, G. Calcagnini, F. Censi, and P. Bartolini, "Radiofrequency Dosimetry in Subjects Implanted with Metallic Structures Undergoing MRI: a Numerical Study," *American Journal of Biomedical Sciences*, vol. 1, no. 4, pp. 373–384, oct 2009. [Online]. Available: http://www.nwpii.com/ajbms/papers/AJBMS{}_2009{}_4{}_12.pdf
- [121] A. Kumar, W. a. Edelstein, and P. a. Bottomley, "Noise figure limits for circular loop MR coils." *Magnetic resonance in medicine : official journal of the Society of Magnetic Resonance in Medicine / Society of Magnetic Resonance in Medicine*, vol. 61, no. 5, pp. 1201–9, may 2009. [Online]. Available: <http://www.pubmedcentral.nih.gov/articlerender.fcgi?artid=2869245&tool=pmcentrez&rendertype=abstract>
- [122] C. Furse, D. A. Christensen, and C. H. Durney, *Basic introduction to bioelectromagnetics*. CRC press, 2009.
- [123] I. E. Commission *et al.*, "Iec 62570:2014 standard practice for marking medical devices and other items for safety in the magnetic resonance environment," 2014.
- [124] M. Kozlov, E. Lucano, and L. M. Angelone, "Effects of tuning conditions on near field of mri transmit birdcage coil at 64 mhz," in *Proceedings of 2016 38th Annual International Conference of the IEEE Engineering in Medicine and Biology Society*. IEEE, 2016.
- [125] M. Kozlov and R. Turner, "Effects of tuning condition, head size and position on the sar of a mri dual-row transmit array at 400 mhz," *Proceedings PIERS, Taipei*, pp. 422–426, 2013.
- [126] N. D. Zanche, *Birdcage Volume Coil Design*. Wiley Online Library, 2007.
- [127] M. Kozlov and R. Turner, "Engineering of 7t transmit multi-row arrays," in *2012 Annual International Conference of the IEEE Engineering in Medicine and Biology Society*. IEEE, 2012, pp. 1089–1092.
- [128] —, "Fast mri coil analysis based on 3-d electromagnetic and rf circuit co-simulation," *Journal of magnetic resonance*, vol. 200, no. 1, pp. 147–152, 2009.
- [129] E. Lucano, M. Liberti, G. Mendoza, T. Lloyd, M. I. Iacono, F. Apollonio, S. Wedan, W. Kainz, and L. Angelone, "Assessing the electromagnetic fields generated by a radiofrequency mri body coil at 64 mhz: defeating vs. accuracy," *IEEE Transactions on Biomedical Engineering*, 2015.
- [130] a. M. Blamire, "The technology of MRI—the next 10 years?" *The British journal of radiology*, vol. 81, no. 968, pp. 601–17, aug 2008. [Online]. Available: <http://www.ncbi.nlm.nih.gov/pubmed/18628329>
- [131] P. Boissoles and G. Caloz, "Magnetic field properties in a birdcage coil," *Archives-Ouvertes. fr*, 2006.
- [132] J. Tropp, "Image brightening in samples of high dielectric constant." *Journal of magnetic resonance (San Diego, Calif. : 1997)*, vol. 167, no. 1, pp. 12–24, mar 2004. [Online]. Available: <http://www.ncbi.nlm.nih.gov/pubmed/14987593>

BIBLIOGRAPHY

- [133] E. Atalar, "Radiofrequency safety for interventional MRI procedures." *Academic radiology*, vol. 12, no. 9, pp. 1149–57, sep 2005. [Online]. Available: <http://www.ncbi.nlm.nih.gov/pubmed/16112515>
- [134] H. Bassen, W. Kainz, G. Mendoza, and T. Kellom, "MRI-induced heating of selected thin wire metallic implants– laboratory and computational studies– findings and new questions raised." *Minimally invasive therapy & allied technologies : MITAT : official journal of the Society for Minimally Invasive Therapy*, vol. 15, no. 2, pp. 76–84, jan 2006. [Online]. Available: <http://www.ncbi.nlm.nih.gov/pubmed/16754190>
- [135] S. Wolf, D. Diehl, M. Gebhardt, J. Mallow, and O. Speck, "SAR simulations for high-field MRI: how much detail, effort, and accuracy is needed?" *Magnetic resonance in medicine : official journal of the Society of Magnetic Resonance in Medicine / Society of Magnetic Resonance in Medicine*, vol. 69, no. 4, pp. 1157–68, apr 2013. [Online]. Available: <http://www.ncbi.nlm.nih.gov/pubmed/22611018>
- [136] J. W. Hand, Y. Li, and J. V. Hajnal, "Numerical study of RF exposure and the resulting temperature rise in the foetus during a magnetic resonance procedure." *Physics in medicine and biology*, vol. 55, no. 4, pp. 913–30, feb 2010. [Online]. Available: <http://www.ncbi.nlm.nih.gov/pubmed/20090188>
- [137] A. Amjad, R. Kamondetdacha, A. Kildishev, S. Park, and J. Nyenhuis, "Power deposition inside a phantom for testing of mri heating," *IEEE transactions on magnetics*, vol. 41, no. 10, pp. 4185–4187, 2005.
- [138] M. Murbach, E. Cabot, E. Neufeld, M.-C. Gosselin, A. Christ, K. P. Pruessmann, and N. Kuster, "Local SAR enhancements in anatomically correct children and adult models as a function of position within 1.5 T MR body coil." *Progress in biophysics and molecular biology*, vol. 107, no. 3, pp. 428–33, dec 2011. [Online]. Available: <http://www.ncbi.nlm.nih.gov/pubmed/21964524>
- [139] W. Kainz, D. D. Chan, J. P. Casamento, and H. I. Bassen, "Calculation of induced current densities and specific absorption rates (SAR) for pregnant women exposed to hand-held metal detectors." *Physics in medicine and biology*, vol. 48, no. 15, pp. 2551–60, aug 2003. [Online]. Available: <http://www.ncbi.nlm.nih.gov/pubmed/12953914>
- [140] D. P. IL, "Imv medical information division," *Nuclear medicine Census Market summary report*, 2013.
- [141] S. Pisa, P. Bernardi, M. Cavagnaro, and E. Piuze, "Power absorption and temperature elevation produced by magnetic resonance apparatus in the thorax of patients with implanted pacemakers," *IEEE Transactions on Electromagnetic Compatibility*, vol. 52, no. 1, pp. 32–40, 2010.
- [142] D. W. Carmichael, J. S. Thornton, R. Rodionov, R. Thornton, A. W. McEvoy, R. J. Ordidge, P. J. Allen, and L. Lemieux, "Feasibility of simultaneous intracranial EEG-fMRI in humans: a safety study." *NeuroImage*, vol. 49, no. 1, pp. 379–90, jan 2010. [Online]. Available: <http://www.ncbi.nlm.nih.gov/pubmed/19651221>
- [143] S. a. Aussenhofer and A. G. Webb, "Design and evaluation of a detunable water-based quadrature HEM11 mode dielectric resonator as a new type of volume coil for high field MRI." *Magnetic resonance in medicine : official journal of the Society of Magnetic Resonance in Medicine / Society of Magnetic*

- Resonance in Medicine*, vol. 68, no. 4, pp. 1325–31, oct 2012. [Online]. Available: <http://www.ncbi.nlm.nih.gov/pubmed/22887743>
- [144] Y. Duan, T. S. Ibrahim, B. S. Peterson, F. Liu, and A. Kangarlu, “Assessment of a PML Boundary Condition for Simulating an MRI Radio Frequency Coil,” *International Journal of Antennas and Propagation*, vol. 2008, pp. 1–10, 2008.
- [145] M. Alecci, C. M. Collins, M. B. Smith, and P. Jezzard, “Radio frequency magnetic field mapping of a 3 Tesla birdcage coil: Experimental and theoretical dependence on sample properties,” *Magnetic Resonance in Medicine*, vol. 46, no. 2, pp. 379–385, aug 2001. [Online]. Available: <http://doi.wiley.com/10.1002/mrm.1201>
- [146] W. Liu, C. M. Collins, P. J. Delp, and M. B. Smith, “Effects of end-ring/shield configuration on homogeneity and signal-to-noise ratio in a birdcage-type coil loaded with a human head.” *Magnetic resonance in medicine : official journal of the Society of Magnetic Resonance in Medicine / Society of Magnetic Resonance in Medicine*, vol. 51, no. 1, pp. 217–21, jan 2004. [Online]. Available: <http://www.ncbi.nlm.nih.gov/pubmed/14705065>
- [147] J. M. Jin, J. Chen, W. C. Chew, H. Gan, R. L. Magin, and P. J. Dimbylow, “Computation of electromagnetic fields for high-frequency magnetic resonance imaging applications.” *Physics in medicine and biology*, vol. 41, no. 12, pp. 2719–38, dec 1996. [Online]. Available: <http://www.ncbi.nlm.nih.gov/pubmed/8971965>
- [148] L. M. Angelone, A. Potthast, F. Segonne, S. Iwaki, J. W. Belliveau, and G. Bonmassar, “Metallic electrodes and leads in simultaneous EEG-MRI: specific absorption rate (SAR) simulation studies.” *Bioelectromagnetics*, vol. 25, no. 4, pp. 285–95, may 2004. [Online]. Available: <http://www.ncbi.nlm.nih.gov/pubmed/15114638>
- [149] O. P. Gandhi and X. B. Chen, “Specific absorption rates and induced current densities for an anatomy-based model of the human for exposure to time-varying magnetic fields of MRI.” *Magnetic resonance in medicine : official journal of the Society of Magnetic Resonance in Medicine / Society of Magnetic Resonance in Medicine*, vol. 41, no. 4, pp. 816–23, apr 1999. [Online]. Available: <http://www.ncbi.nlm.nih.gov/pubmed/10332859>
- [150] J. Ruoff, C. Würslin, H. Graf, and F. Schick, “Resolution adapted finite element modeling of radio frequency interactions on conductive resonant structures in MRI.” *Magnetic resonance in medicine : official journal of the Society of Magnetic Resonance in Medicine / Society of Magnetic Resonance in Medicine*, vol. 67, no. 5, pp. 1444–52, may 2012. [Online]. Available: <http://www.ncbi.nlm.nih.gov/pubmed/22076824>
- [151] C. a. T. Van den Berg, L. W. Bartels, B. van den Bergen, H. Kroeze, A. a. C. de Leeuw, J. B. Van de Kamer, and J. J. W. Lagendijk, “The use of MR B+1 imaging for validation of FDTD electromagnetic simulations of human anatomies.” *Physics in medicine and biology*, vol. 51, no. 19, pp. 4735–46, oct 2006. [Online]. Available: <http://www.ncbi.nlm.nih.gov/pubmed/16985267>
- [152] H. I. Bassen and G. G. Mendoza, “In-vitro mapping of E-fields induced near pacemaker leads by simulated MR gradient fields.” *Biomedical engineering online*, vol. 8, p. 39, jan 2009. [Online]. Available: <http://www.pubmedcentral.nih.gov/articlerender.fcgi?artid=2801670&tool=pmcentrez&rendertype=abstract>

BIBLIOGRAPHY

- [153] W. Kainz, A. Christ, T. Kellom, S. Seidman, N. Nikoloski, B. Beard, and N. Kuster, "Dosimetric comparison of the specific anthropomorphic mannequin (SAM) to 14 anatomical head models using a novel definition for the mobile phone positioning." *Physics in medicine and biology*, vol. 50, no. 14, pp. 3423–45, jul 2005. [Online]. Available: <http://www.ncbi.nlm.nih.gov/pubmed/16177519>
- [154] C. L. Sammet, X. Yang, P. A. Wassenaar, E. C. Bourekas, B. A. Yuh, F. Shellock, S. Sammet, and M. V. Knopp, "Rf-related heating assessment of extracranial neurosurgical implants at 7t," *Magnetic resonance imaging*, vol. 31, no. 6, pp. 1029–1034, 2013.
- [155] C. M. Collins and M. B. Smith, "Signal-to-noise ratio and absorbed power as functions of main magnetic field strength, and definition of "90 degrees " RF pulse for the head in the birdcage coil." *Magnetic resonance in medicine : official journal of the Society of Magnetic Resonance in Medicine / Society of Magnetic Resonance in Medicine*, vol. 45, no. 4, pp. 684–91, apr 2001. [Online]. Available: <http://www.ncbi.nlm.nih.gov/pubmed/11283997>
- [156] G. Bit-Babik, a. W. Guy, C.-K. Chou, a. Faraone, M. Kanda, a. Gessner, J. Wang, and O. Fujiwara, "Simulation of exposure and SAR estimation for adult and child heads exposed to radiofrequency energy from portable communication devices." *Radiation research*, vol. 163, no. 5, pp. 580–90, may 2005. [Online]. Available: <http://www.ncbi.nlm.nih.gov/pubmed/15850420>
- [157] K. S. Kunz and R. J. Luebbers, *The finite difference time domain method for electromagnetics*. CRC press, 1993.
- [158] J. Armstrong, *Long-range Forecasting: From Crystal Ball to Computer*, ser. A Wiley interscience publication. John Wiley & Sons Canada, Limited, 1978.
- [159] C.-k. Chou and A. W. Guy, "Carbon-loaded Teflon electrodes for chronic EEG recordings in microwave research."
- [160] L. Lemieux, P. J. Allen, F. Franconi, M. R. Symms, and D. K. Fish, "Recording of eeg during fmri experiments: patient safety," *Magnetic Resonance in Medicine*, vol. 38, no. 6, pp. 943–952, 1997.
- [161] L. M. Angelone, C. E. Vasios, G. Wiggins, P. L. Purdon, and G. Bonmassar, "On the effect of resistive eeg electrodes and leads during 7 t mri: simulation and temperature measurement studies," *Magnetic resonance imaging*, vol. 24, no. 6, pp. 801–812, 2006.
- [162] H. Kugel, C. Bremer, M. Püschel, R. Fischbach, H. Lenzen, B. Tombach, H. Van Aken, and W. Heindel, "Hazardous situation in the MR bore: induction in ECG leads causes fire." *European radiology*, vol. 13, no. 4, pp. 690–4, apr 2003. [Online]. Available: <http://www.ncbi.nlm.nih.gov/pubmed/12664104>
- [163] S. Lange and Q. N. NGUYEN, "Cables and electrodes can burn patients during mri," *Nursing2016*, vol. 36, no. 11, p. 18, 2006.
- [164] T. Niendorf, L. Winter, and T. Frauenrath, "Electrocardiogram in an MRI environment: clinical needs, practical considerations, safety implications, technical solutions and future directions," ... *-methods and analysis*, ..., 2012. [Online]. Available: <http://cdn.intechweb.org/pdfs/27020.pdf>

- [165] W. R. Nitz, a. Oppelt, W. Renz, C. Manke, M. Lenhart, and J. Link, "On the heating of linear conductive structures as guide wires and catheters in interventional MRI." *Journal of magnetic resonance imaging : JMRI*, vol. 13, no. 1, pp. 105–14, jan 2001. [Online]. Available: <http://www.ncbi.nlm.nih.gov/pubmed/11169811>
- [166] R. Luechinger, P. Boesiger, and J. A. Disegi, "Safety evaluation of large external fixation clamps and frames in a magnetic resonance environment," *Journal of Biomedical Materials Research Part B: Applied Biomaterials*, vol. 82, no. 1, pp. 17–22, 2007.
- [167] F. D. Doty, G. Entzminger, C. D. Hauck, and J. P. Staab, "Practical aspects of birdcage coils." *Journal of magnetic resonance (San Diego, Calif. : 1997)*, vol. 138, no. 1, pp. 144–54, may 1999. [Online]. Available: <http://www.ncbi.nlm.nih.gov/pubmed/10329237>
- [168] X.-L. Chen, S. Benkler, N. Chavannes, V. De Santis, J. Bakker, G. van Rhoon, J. Mosig, and N. Kuster, "Analysis of human brain exposure to low-frequency magnetic fields: a numerical assessment of spatially averaged electric fields and exposure limits." *Bioelectromagnetics*, vol. 34, no. 5, pp. 375–84, jul 2013. [Online]. Available: <http://www.ncbi.nlm.nih.gov/pubmed/23404214>
- [169] C. Schmidt, P. Grant, M. Lowery, and U. van Rienen, "Influence of uncertainties in the material properties of brain tissue on the probabilistic volume of tissue activated." *IEEE transactions on bio-medical engineering*, vol. 60, no. 5, pp. 1378–87, may 2013. [Online]. Available: <http://www.ncbi.nlm.nih.gov/pubmed/23269746>
- [170] E. Lucano, M. Liberti, T. Lloyd, F. Apollonio, S. Wedan, W. Kainz, and L. M. Angelone, "A numerical investigation on the effect of rf coil feed variability on global and local electromagnetic field exposure in human body models at 64 mhz," *Under revision by Magnetic Resonance in Medicine*, 2016.
- [171] P. Serano, L. M. Angelone, H. Katnani, E. Eskandar, and G. Bonmassar, "A Novel Brain Stimulation Technology Provides Compatibility with MRI," *Scientific Reports*, vol. 5, p. 9805, 2015. [Online]. Available: <http://www.nature.com/doi/10.1038/srep09805>
- [172] M. Murbach, E. Neufeld, T. Samaras, J. Córcoles, F. J. Robb, W. Kainz, and N. Kuster, "Pregnant women models analyzed for rf exposure and temperature increase in 3t rf shimmed birdcages," *Magnetic resonance in medicine*, 2016.
- [173] O. Bottauscio, a. M. Cassarà, J. W. Hand, D. Giordano, L. Zilberti, M. Borsero, M. Chiampi, and G. Weidemann, "Assessment of computational tools for MRI RF dosimetry by comparison with measurements on a laboratory phantom," *Physics in Medicine and Biology*, vol. 60, no. 14, pp. 5655–5680, 2015. [Online]. Available: <http://stacks.iop.org/0031-9155/60/i=14/a=5655?key=crossref.bd134653a8bf162c56ea9111e2778a4c>
- [174] P. Nordbeck, F. Fidler, M. T. Friedrich, I. Weiss, M. Warmuth, D. Gensler, V. Herold, W. Geistert, P. M. Jakob, G. Ertl, O. Ritter, M. E. Ladd, W. R. Bauer, and H. H. Quick, "Reducing RF-related heating of cardiac pacemaker leads in MRI: implementation and experimental verification of practical design changes." *Magnetic resonance in medicine : official journal of the Society of Magnetic Resonance in Medicine / Society of Magnetic Resonance in Medicine*, vol. 68, no. 6, pp. 1963–72, dec 2012. [Online]. Available: <http://www.ncbi.nlm.nih.gov/pubmed/22383393>

BIBLIOGRAPHY

- [175] W. Liu, C.-p. Kao, C. M. Collins, M. B. Smith, and Q. X. Yang, "On consideration of radiated power in RF field simulations for MRI." *Magnetic resonance in medicine : official journal of the Society of Magnetic Resonance in Medicine / Society of Magnetic Resonance in Medicine*, vol. 69, no. 1, pp. 290–4, jan 2013. [Online]. Available: <http://www.ncbi.nlm.nih.gov/pubmed/22473620>
- [176] M. Carias and K. Hynynen, "The evaluation of steerable ultrasonic catheters for minimally invasive mri-guided cardiac ablation," *Magnetic resonance in medicine*, vol. 72, no. 2, pp. 591–598, 2014.
- [177] D. Li, J. Zheng, Y. Liu, C. Pan, W. Kainz, F. Yang, W. Wu, and J. Chen, "An efficient approach to estimate mri rf field induced in vivo heating for small medical implants," *IEEE Transactions on Electromagnetic Compatibility*, vol. 57, no. 4, pp. 643–650, 2015.
- [178] P. a. Bottomley, A. Kumar, W. a. Edelstein, J. M. Allen, and P. V. Karmarkar, "Designing passive MRI-safe implantable conducting leads with electrodes," *Medical Physics*, vol. 37, no. 7, p. 3828, 2010. [Online]. Available: <http://link.aip.org/link/MPHYA6/v37/i7/p3828/s1{&}Agg=doi>
- [179] A. Taflove and S. C. Hagness, *Computational electrodynamics*. Artech house, 2005.
- [180] M. Kozlov and R. Turner, "Fast MRI coil analysis based on 3-D electromagnetic and RF circuit co-simulation." *Journal of magnetic resonance (San Diego, Calif. : 1997)*, vol. 200, no. 1, pp. 147–52, sep 2009. [Online]. Available: <http://www.ncbi.nlm.nih.gov/pubmed/19570700>
- [181] T. Ai, J. N. Morelli, X. Hu, D. Hao, F. L. Goerner, B. Ager, and V. M. Runge, "A historical overview of magnetic resonance imaging, focusing on technological innovations," *Investigative radiology*, vol. 47, no. 12, pp. 725–741, 2012.
- [182] P. Mansfield and A. A. Maudsley, "Medical imaging by nmr," *The British journal of radiology*, vol. 50, no. 591, pp. 188–194, 1977.
- [183] R. Damadian, "Tumor detection by nuclear magnetic resonance," *Science*, 1971.
- [184] J. G. Delfino and T. O. Woods, "New developments in standards for mri safety testing of medical devices," *Current Radiology Reports*, vol. 4, no. 6, pp. 1–9, 2016.
- [185] b. p. f. b. l. OECD, *Health at a Glance 2015, OECD Indicators*, 2015.
- [186] P. A. Bottomley and E. R. Andrew, "Rf magnetic field penetration, phase shift and power dissipation in biological tissue: implications for nmr imaging," *Physics in Medicine and biology*, vol. 23, no. 4, p. 630, 1978.
- [187] M. Grandolfo and P. Vecchia, "Radiofrequency power deposition during magnetic resonance diagnostic examinations," in *Radiation protection practice*, 1988.
- [188] T. F. Budinger, "Thresholds for physiological effects due to rf and magnetic fields used in nmr imaging," *IEEE Transactions on Nuclear Science*, vol. 2, no. 26, pp. 2821–2825, 1979.
- [189] T. Budinger, "Potential medical effects and hazards of human nmr studies," *Nuclear magnetic resonance imaging in medicine*, pp. 207–231, 1981.

- [190] D. Schaefer, B. Barber, C. Gordon, J. Zielonka, and J. Hecker, "Thermal effects of magnetic resonance imaging," *Book of abstracts, Society for magnetic resonance in medicine Volume*, vol. 2, 1985.
- [191] E. R. Adair and L. G. Berglund, "On the thermoregulatory consequences of nmr imaging," *Magnetic resonance imaging*, vol. 4, no. 4, pp. 321–333, 1986.
- [192] D. Schaefer, F. Shellock, J. Crues, and C. Gordon, "Infrared thermographic studies of human surface temperature in magnetic resonance imaging," in *Proceedings of the Bioelectromagnetics Society, Eighth Annual Meeting*, 1986, p. 68.
- [193] C. J. Gordon, "Normalizing the thermal effects of radiofrequency radiation: body mass versus total body surface area," *Bioelectromagnetics*, vol. 8, no. 2, pp. 111–118, 1987.
- [194] W. P. Shuman, D. R. Haynor, A. Guy, G. Wesbey, D. Schaefer, and A. A. Moss, "Superficial-and deep-tissue temperature increases in anesthetized dogs during exposure to high specific absorption rates in a 1.5-t mr imager." *Radiology*, vol. 167, no. 2, pp. 551–554, 1988.
- [195] C. a. T. Van den Berg, B. van den Bergen, J. B. Van de Kamer, B. W. Raaymakers, H. Kroeze, L. W. Bartels, and J. J. W. Lagendijk, "Simultaneous B1 + homogenization and specific absorption rate hotspot suppression using a magnetic resonance phased array transmit coil." *Magnetic resonance in medicine : official journal of the Society of Magnetic Resonance in Medicine / Society of Magnetic Resonance in Medicine*, vol. 57, no. 3, pp. 577–86, mar 2007. [Online]. Available: <http://www.ncbi.nlm.nih.gov/pubmed/17326185>
- [196] C. Gabriel, S. Gabriel, and E. Corthout, "The dielectric properties of biological tissues: I. Literature survey." *Physics in medicine and biology*, vol. 41, no. 11, pp. 2231–49, nov 1996. [Online]. Available: <http://www.ncbi.nlm.nih.gov/pubmed/8938024>
- [197] B. J. Roth, "The electrical conductivity of tissues," pp. 10–1, 2000.
- [198] C. Gabriel, "Compilation of the dielectric properties of body tissues at rf and microwave frequencies." DTIC Document, Tech. Rep., 1996.
- [199] C. M. Collins, B. Yang, Q. X. Yang, and M. B. Smith, "Numerical calculations of the static magnetic field in three-dimensional multi-tissue models of the human head," *Magnetic resonance imaging*, vol. 20, no. 5, pp. 413–424, 2002.
- [200] P. J. Dimbylow, "FDTD calculations of the whole-body averaged SAR in an anatomically realistic voxel model of the human body from 1 MHz to 1 GHz." *Physics in Medicine and Biology*, vol. 42, no. 3, pp. 479–490, 1997. [Online]. Available: <http://www.ncbi.nlm.nih.gov/pubmed/9080530>
- [201] J. Massey, C. Geyik, N. Techachainiran, C. Hsu, R. Nguyen, T. Latson, M. Ball, E. Celik, and A. Yilmaz, "Austinman and austinwoman: High fidelity, reproducible, and open-source electromagnetic voxel models," in *The 34th Annual Meeting of the Bioelectromagnetics Society*, 2012.
- [202] L. M. Angelone, G. Bonmassar, A. A. Martinos, and B. Imaging, "Specific Absorption Rate Analysis of Heterogeneous Head Models with EEG Electrodes / Leads at 7T MRI," *Applied Biological Engineering - Principles and Practice*, 2012. [Online]. Available: <http://>

BIBLIOGRAPHY

- //www.intechopen.com/books/applied-biological-engineering-principles-and-practice/specific-absorption-rate-analysis-of-heterogeneous-head-models-with-eeg-and-7t-mri
- [203] D. T. Yeo, Z. Wang, W. Loew, M. W. Vogel, and I. Hancu, "Local specific absorption rate in high-pass birdcage and transverse electromagnetic body coils for multiple human body models in clinical landmark positions at 3t," *Journal of Magnetic Resonance Imaging*, vol. 33, no. 5, pp. 1209–1217, 2011.
- [204] R. Findlay and P. Dimbylow, "Effects of posture on fdtd calculations of specific absorption rate in a voxel model of the human body," *Physics in medicine and biology*, vol. 50, no. 16, p. 3825, 2005.
- [205] J. Nadobny, M. Szimtenings, D. Diehl, E. Stetter, G. Brinker, and P. Wust, "Evaluation of mr-induced hot spots for different temporal sar modes using a time-dependent finite difference method with explicit temperature gradient treatment," *IEEE Transactions on Biomedical Engineering*, vol. 54, no. 10, pp. 1837–1850, 2007.
- [206] G. C. van Rhoon, T. Samaras, P. S. Yarmolenko, M. W. Dewhurst, E. Neufeld, and N. Kuster, "Cem43 thermal dose thresholds: a potential guide for magnetic resonance radiofrequency exposure levels?" *European radiology*, vol. 23, no. 8, pp. 2215–2227, 2013.
- [207] Z. Wang, J. C. Lin, W. Mao, W. Liu, M. B. Smith, and C. M. Collins, "Sar and temperature: simulations and comparison to regulatory limits for mri," *Journal of Magnetic Resonance Imaging*, vol. 26, no. 2, pp. 437–441, 2007.
- [208] C. M. Collins, W. Liu, J. Wang, R. Gruetter, J. T. Vaughan, K. Ugurbil, and M. B. Smith, "Temperature and SAR calculations for a human head within volume and surface coils at 64 and 300 MHz." *Journal of magnetic resonance imaging : JMRI*, vol. 19, no. 5, pp. 650–6, may 2004. [Online]. Available: <http://www.ncbi.nlm.nih.gov/pubmed/15112317>
- [209] G. Carluccio, D. Erricolo, S. Oh, and C. M. Collins, "An approach to rapid calculation of temperature change in tissue using spatial filters to approximate effects of thermal conduction." *IEEE transactions on bio-medical engineering*, vol. 60, no. 6, pp. 1735–41, jun 2013. [Online]. Available: <http://www.ncbi.nlm.nih.gov/pubmed/23358947>
- [210] R. L. McIntosh, V. Anderson, and R. J. McKenzie, "A numerical evaluation of SAR distribution and temperature changes around a metallic plate in the head of a RF exposed worker," *Bioelectromagnetics*, vol. 26, no. 5, pp. 377–388, jul 2005. [Online]. Available: <http://doi.wiley.com/10.1002/bem.20112>
- [211] U. D. Nguyen, J. S. Brown, I. a. Chang, J. Krycia, and M. S. Mirotznik, "Numerical evaluation of heating of the human head due to magnetic resonance imaging." *IEEE transactions on bio-medical engineering*, vol. 51, no. 8, pp. 1301–9, aug 2004. [Online]. Available: <http://www.ncbi.nlm.nih.gov/pubmed/15311814>
- [212] S. A. Mohsin, N. M. Sheikh, and U. Saeed, "Mri Induced Heating of Deep Brain Stimulation Leads: Effect of the Air-Tissue Interface," *Progress In Electromagnetics Research*, vol. 83, pp. 81–91, 2008. [Online]. Available: <http://www.jpier.org/PIER/pier.php?paper=08040504>
- [213] C. A. V. D. Berg, J. B. V. D. Kamer, H. P. Kok, J. J. Lagendijk, and L. W. Bartels, "Multiport excitation at high field mri : Trade-off between b1 + homogeneity and rf heating," in

- Proceedings in 13th Intlational Society for Magnetic Resonance in Medicine*, vol. 18, no. 2, 2005, p. 2005.
- [214] D. Shrivastava, T. Hanson, J. Kulesa, J. Tian, G. Adriany, and J. T. Vaughan, "Radiofrequency heating in porcine models with a "large" 32 cm internal diameter, 7 T (296 MHz) head coil." *Magnetic resonance in medicine : official journal of the Society of Magnetic Resonance in Medicine / Society of Magnetic Resonance in Medicine*, vol. 66, no. 1, pp. 255–63, jul 2011. [Online]. Available: <http://www.pubmedcentral.nih.gov/articlerender.fcgi?artid=3339408&tool=pmcentrez&rendertype=abstract>
- [215] A. Massire, M. a. Cloos, M. Luong, A. Amadon, A. Vignaud, C. J. Wiggins, and N. Boulant, "Thermal simulations in the human head for high field MRI using parallel transmission." *Journal of magnetic resonance imaging : JMRI*, vol. 35, no. 6, pp. 1312–21, jul 2012. [Online]. Available: <http://www.ncbi.nlm.nih.gov/pubmed/22241685>
- [216] S. Oh, Y.-C. Ryu, G. Carluccio, C. T. Sica, and C. M. Collins, "Measurement of SAR-induced temperature increase in a phantom and in vivo with comparison to numerical simulation." *Magnetic resonance in medicine : official journal of the Society of Magnetic Resonance in Medicine / Society of Magnetic Resonance in Medicine*, vol. 00, pp. 1–9, jun 2013. [Online]. Available: <http://www.ncbi.nlm.nih.gov/pubmed/23804188>
- [217] S. Weinbaum and L. Jiji, "A new simplified bioheat equation for the effect of blood flow on local average tissue temperature," *Journal of biomechanical engineering*, vol. 107, no. 2, pp. 131–139, 1985.
- [218] V. M. M. Flyckt, B. W. Raaymakers, and J. J. W. Lagendijk, "Modelling the impact of blood flow on the temperature distribution in the human eye and the orbit: fixed heat transfer coefficients versus the Pennes bioheat model versus discrete blood vessels." *Physics in medicine and biology*, vol. 51, no. 19, pp. 5007–21, oct 2006. [Online]. Available: <http://www.ncbi.nlm.nih.gov/pubmed/16985284>
- [219] D. Shrivastava and J. T. Vaughan, "A generic bioheat transfer thermal model for a perfused tissue," *Journal of biomechanical engineering*, vol. 131, no. 7, p. 074506, 2009.
- [220] D. Yang, M. C. Converse, D. M. Mahvi, and J. G. Webster, "Expanding the bioheat equation to include tissue internal water evaporation during heating," *IEEE Transactions on Biomedical Engineering*, vol. 54, no. 8, pp. 1382–1388, 2007.
- [221] R. M. MHRA and M. Devices, "Safety Guidelines for Magnetic Resonance Imaging Equipment in Clinical Use," *Medicines and Healthcare Products Regulatory Agency*, no. March, 2015. [Online]. Available: https://www.gov.uk/government/uploads/system/uploads/attachment_data/file/476931/MRI_guidance_2015-4-02d1.pdf
- [222] J. W. Hand, Y. Li, E. L. Thomas, M. A. Rutherford, and J. V. Hajnal, "Prediction of specific absorption rate in mother and fetus associated with MRI examinations during pregnancy." *Magnetic resonance in medicine : official journal of the Society of Magnetic Resonance in Medicine / Society of Magnetic Resonance in Medicine*, vol. 55, no. 4, pp. 883–93, apr 2006. [Online]. Available: <http://www.ncbi.nlm.nih.gov/pubmed/16508913>
- [223] D. Levine, C. Zuo, C. B. Faro, and Q. Chen, "Potential heating effect in the gravid uterus during MR HASTE imaging." *Journal of magnetic resonance imaging : JMRI*, vol. 13, no. 6, pp. 856–61, jun 2001. [Online]. Available: <http://www.ncbi.nlm.nih.gov/pubmed/11382944>

BIBLIOGRAPHY

- [224] D. Wu, S. Shamsi, J. Chen, and W. Kainz, "Evaluations of specific absorption rate and temperature increase within pregnant female models in magnetic resonance imaging birdcage coils," *IEEE transactions on microwave theory and techniques*, vol. 54, no. 12, pp. 4472–4478, 2006.
- [225] S. Kikuchi, K. Saito, M. Takahashi, and K. Ito, "Temperature elevation in the fetus from electromagnetic exposure during magnetic resonance imaging." *Physics in medicine and biology*, vol. 55, no. 8, pp. 2411–26, apr 2010. [Online]. Available: <http://www.ncbi.nlm.nih.gov/pubmed/20360633>
- [226] S. A. Sapareto and W. C. Dewey, "Thermal dose determination in cancer therapy," *International Journal of Radiation Oncology* Biology* Physics*, vol. 10, no. 6, pp. 787–800, 1984.
- [227] V. Rieke and K. Butts Pauly, "Mr thermometry," *Journal of Magnetic Resonance Imaging*, vol. 27, no. 2, pp. 376–390, 2008.
- [228] W. Kainz, "Mr heating tests of mr critical implants," *Journal of Magnetic Resonance Imaging*, vol. 26, no. 3, pp. 450–451, 2007.
- [229] M. Murbach, E. Neufeld, M. Capstick, W. Kainz, D. O. Brunner, T. Samaras, K. P. Pruessmann, and N. Kuster, "Thermal Tissue Damage Model Analyzed for Different Whole-Body SAR and Scan Durations for Standard MR Body Coils." *Magnetic resonance in medicine : official journal of the Society of Magnetic Resonance in Medicine / Society of Magnetic Resonance in Medicine*, vol. 000, pp. 1–11, feb 2013. [Online]. Available: <http://www.ncbi.nlm.nih.gov/pubmed/23413107>
- [230] A. M. Ferreira, F. Costa, A. Tralhão, H. Marques, N. Cardim, and P. Adragão, "Mri-conditional pacemakers: current perspectives," *Medical devices (Auckland, NZ)*, vol. 7, p. 115, 2014.
- [231] P. Davis, L. Crooks, M. Arakawa, R. McRee, L. Kaufman, and A. Margulis, "Potential hazards in nmr imaging: heating effects of changing magnetic fields and rf fields on small metallic implants," *American Journal of Roentgenology*, vol. 137, no. 4, pp. 857–860, 1981.
- [232] S. Achenbach, W. Moshage, B. Diem, T. Bieberlea, V. Schibgilla, and K. Bachmann, "Effects of magnetic resonance imaging on cardiac pacemakers and electrodes," *American heart journal*, vol. 134, no. 3, pp. 467–473, 1997.
- [233] A. R. Rezai, D. Finelli, J. A. Nyenhuis, G. Hrdlicka, J. Tkach, A. Sharan, P. Rugieri, P. H. Stypulkowski, and F. G. Shellock, "Neurostimulation systems for deep brain stimulation: In vitro evaluation of magnetic resonance imaging–related heating at 1.5 tesla," *Journal of Magnetic Resonance Imaging*, vol. 15, no. 3, pp. 241–250, 2002.
- [234] C. Chou and A. Guy, "Carbon-loaded teflon electrodes for chronic eeg recordings in microwave research." *The Journal of microwave power*, vol. 14, no. 4, pp. 399–404, 1979.
- [235] J. Delfino, "U.s. federal safety standards, guidelines and regulations for mri systems: An overview," *Applied Radiology the Journal of practical medical imaging and management*, 2015.

- [236] I. C. on Non-Ionizing Radiation Protection *et al.*, “Medical magnetic resonance (mr) procedures: protection of patients,” *Health Physics*, vol. 87, no. 2, pp. 197–216, 2004.
- [237] I. E. Commission *et al.*, “International standard, medical equipment–iec 60601-2-33: particular requirements for the safety of magnetic resonance equipment,” 2010.
- [238] NEMA, “Standard ms 8-1993. characterization of the sar for mri system,” 2008.
- [239] T. O. Woods, “Standards for medical devices in MRI: present and future.” *Journal of magnetic resonance imaging : JMRI*, vol. 26, no. 5, pp. 1186–9, nov 2007. [Online]. Available: <http://www.ncbi.nlm.nih.gov/pubmed/17969160>
- [240] A. Standard, “Astm f2503–13. standard practice for marking medical devices and other items for safety in magnetic resonance environments. astm international, west conshohocken, pa. 2013. doi: 10.1520/f2503.”
- [241] S.-M. Park, R. Kamondetdacha, and J. a. Nyenhuis, “Calculation of MRI-induced heating of an implanted medical lead wire with an electric field transfer function.” *Journal of magnetic resonance imaging : JMRI*, vol. 26, no. 5, pp. 1278–85, nov 2007. [Online]. Available: <http://www.ncbi.nlm.nih.gov/pubmed/17969143>
- [242] P. Serano, L. M. Angelone, H. Katnani, E. Eskandar, and G. Bonmassar, “A novel brain stimulation technology provides compatibility with mri,” *Scientific reports*, vol. 5, 2015.
- [243] J. S. Shinbane, P. M. Colletti, and F. G. Shellock, “Magnetic resonance imaging in patients with cardiac pacemakers: era of" mr conditional" designs,” *Journal of Cardiovascular Magnetic Resonance*, vol. 13, no. 1, p. 1, 2011.
- [244] M. Murbach, E. Neufeld, E. Cabot, E. Zastrow, J. Córcoles, W. Kainz, and N. Kuster, “Virtual population-based assessment of the impact of 3 tesla radiofrequency shimming and thermoregulation on safety and b1+ uniformity,” *Magnetic Resonance in Medicine*, 2015.
- [245] E. Neufeld, M.-C. Gosselin, M. Murbach, A. Christ, E. Cabot, and N. Kuster, “Analysis of the local worst-case SAR exposure caused by an MRI multi-transmit body coil in anatomical models of the human body.” *Physics in medicine and biology*, vol. 56, no. 15, pp. 4649–59, aug 2011. [Online]. Available: <http://stacks.iop.org/0031-9155/56/i=15/a=002?key=crossref.1edac52c392123cedbcc6312bd96cb81http://www.ncbi.nlm.nih.gov/pubmed/21734334>
- [246] Y. Eryaman, B. Akin, and E. Atalar, “Reduction of implant RF heating through modification of transmit coil electric field.” *Magnetic resonance in medicine : official journal of the Society of Magnetic Resonance in Medicine / Society of Magnetic Resonance in Medicine*, vol. 65, no. 5, pp. 1305–13, may 2011. [Online]. Available: <http://www.ncbi.nlm.nih.gov/pubmed/21500259>
- [247] C. E. McElcheran, B. Yang, K. J. Anderson, L. Golenstani-Rad, and S. J. Graham, “Investigation of parallel radiofrequency transmission for the reduction of heating in long conductive leads in 3 tesla magnetic resonance imaging,” *PloS one*, vol. 10, no. 8, p. e0134379, 2015.
- [248] L. Golestanirad, B. Keil, L. M. Angelone, G. Bonmassar, A. Mareyam, and L. L. Wald, “Feasibility of using linearly polarized rotating birdcage transmitters and close-fitting receive arrays in mri to reduce sar in the vicinity of deep brain simulation implants,” *Magnetic resonance in medicine*, 2016.

BIBLIOGRAPHY

- [249] E. Lucano, L. M. Angelone, F. Apollonio, and M. Liberti, “Local and global electromagnetic absorption in homogeneous and heterogeneous human models exposed to 64 mhz mri rf field,” *Submitted to the Journal for Numerical Methods in Biomedical Engineering*, 2016.
- [250] C. A. Van den Berg, B. Van den Bergen, J. B. Van de Kamer, B. W. Raaymakers, H. Kroeze, L. W. Bartels, and J. J. Lagendijk, “Simultaneous b 1+ homogenization and specific absorption rate hotspot suppression using a magnetic resonance phased array transmit coil,” *Magnetic resonance in medicine*, vol. 57, no. 3, pp. 577–586, 2007.
- [251] S. Gabriel, R. W. Lau, and C. Gabriel, “The dielectric properties of biological tissues: II. Measurements in the frequency range 10 Hz to 20 GHz.” *Physics in medicine and biology*, vol. 41, no. 11, pp. 2251–69, nov 1996. [Online]. Available: <http://www.ncbi.nlm.nih.gov/pubmed/8938025>
- [252] E. Lucano, M. Murbach, W. Kainz, and M. I. Iacono, “Impact of the vague partial body sar definition in the mri safety standard iec 60601-2-33 on actual patient exposure,” *Book of abstracts, bioelectromagnetics (BioEM)*, 2016.
- [253] E. Lucano, M. Liberti, T. Lloyd, F. Apollonio, S. Wedan, W. Kainz, and L. M. Angelone, “Rf induced energy for partially implanted catheters: a computational study,” in *Proceedings of 2016 38th Annual International Conference of the IEEE Engineering in Medicine and Biology Society*. IEEE, 2016.
- [254] C. J. Yeung, R. C. Susil, and E. Atalar, “Rf heating due to conductive wires during mri depends on the phase distribution of the transmit field,” *Magnetic Resonance in Medicine*, vol. 48, no. 6, pp. 1096–1098, 2002.
- [255] D. a. Langman, I. B. Goldberg, J. P. Finn, and D. B. Ennis, “Pacemaker lead tip heating in abandoned and pacemaker-attached leads at 1.5 Tesla MRI.” *Journal of magnetic resonance imaging : JMRI*, vol. 33, no. 2, pp. 426–31, feb 2011. [Online]. Available: <http://www.ncbi.nlm.nih.gov/pubmed/21274985>
- [256] E. Zastrow, M. Capstick, E. Cabot, and N. Kuster, “Piece-wise excitation system for the characterization of local rf-induced heating of aimed during mr exposure,” in *Electromagnetic Compatibility, Tokyo (EMC’14/Tokyo), 2014 International Symposium on*. IEEE, 2014, pp. 241–244.
- [257] D. Li, J. Zheng, Y. Liu, J. Chen, C. Pan, and W. Kainz, “Using scaling approach to estimate mri rf field induced heating for small medical implant,” in *2014 IEEE International Symposium on Electromagnetic Compatibility (EMC)*. IEEE, 2014, pp. 109–112.
- [258] E. Mattei, E. Lucano, F. Censi, L. M. Angelone, and G. Calcagnini, “High dielectric material in mri: numerical assessment of the reduction of the induced local power on implanted cardiac leads,” in *Proceedings of 2016 38th Annual International Conference of the IEEE Engineering in Medicine and Biology Society*. IEEE, 2016.
- [259] F. A. Jolesz, “Invited. interventional and intraoperative mri: A general overview of the field,” *Journal of Magnetic Resonance Imaging*, vol. 8, no. 1, pp. 3–7, 1998.
- [260] C. J. Yeung, R. C. Susil, and E. Atalar, “Rf safety of wires in interventional mri: using a safety index,” *Magnetic resonance in medicine*, vol. 47, no. 1, pp. 187–193, 2002.

- [261] W. Liu, C. Collins, and M. B. Smith, "Calculations of B₁ Distribution, Specific Energy Absorption Rate, and Intrinsic Signal-to-Noise Ratio for a Body-Size Birdcage Coil Loaded with Different Human Subjects at 64 and 128 MHz," *Changes*, vol. 29, no. 6, pp. 997–1003, 2005.
- [262] C. A. Balanis, *Antenna theory: analysis and design*. John Wiley & Sons, 2016.
- [263] E. Mattei, M. Triventi, G. Calcagnini, F. Censi, W. Kainz, G. Mendoza, H. I. Bassen, and P. Bartolini, "Complexity of MRI induced heating on metallic leads: experimental measurements of 374 configurations." *Biomedical engineering online*, vol. 7, p. 11, jan 2008. [Online]. Available: <http://www.pubmedcentral.nih.gov/articlerender.fcgi?artid=2292730&tool=pmcentrez&rendertype=abstract>
- [264] A. W. Guy, "Biophysics- energy absorption and distribution," *1975. 14*, 1975.
- [265] I. C95.3, "Ieee recommended practice for measurements and computations of radio frequency electromagnetic fields with respect to human exposure to such fields, 100 khz–300 ghz," *New York: IEEE*, 2002.
- [266] E. Lucano, Y. Aiping, E. Zastrow, W. Kainz, M. Liberti, and N. Kuster, "Test field diversification method for the safety assessment of rf-induced heating of medical implants during mri at 64 mhz," *Book of abstracts, bioelectromagnetics (BioEM)*, 2016.
- [267] C. J. Yeung, R. C. Susil, and E. Atalar, "Rf safety of wires in interventional mri: using a safety index," *Magnetic resonance in medicine*, vol. 47, no. 1, pp. 187–193, 2002.
- [268] J. Córcoles, E. Zastrow, and N. Kuster, "Convex optimization of mri exposure for mitigation of rf-heating from active medical implants," *Physics in medicine and biology*, vol. 60, no. 18, p. 7293, 2015.
- [269] B. Stevenson, W. Dabney, and C. Frysz, "Issues and design solutions associated with performing mri scans on patients with active implantable medical devices," in *2007 29th Annual International Conference of the IEEE Engineering in Medicine and Biology Society*. IEEE, 2007, pp. 6166–6169.
- [270] Medtronic.com. (2008) Surescan® mri pacing systems. [Online]. Available: http://www.medtronic.com/mrisurescan-us/pdf/radiology_brochure.pdf
- [271] Fda.gov. (2009) Revo mri surescan pacing system. [Online]. Available: http://www.accessdata.fda.gov/cdrh_docs/pdf9/p090013a.pdf
- [272] Biotronik.com. (2011) Lumax 740 icd series. [Online]. Available: [http://www.biotronik.com/files/E4FCB9A04080338AC125795100519144/\\$FILE/BIOTRONIK_Lumax%20740%20Fact%20Sheet_EN.pdf](http://www.biotronik.com/files/E4FCB9A04080338AC125795100519144/$FILE/BIOTRONIK_Lumax%20740%20Fact%20Sheet_EN.pdf)
- [273] ——. (2015) Medtronic first to receive fda approval for mr-conditional implantable cardioverter defibrillator system. [Online]. Available: <http://newsroom.medtronic.com/phoenix.zhtml?c=251324&p=irol-newsArticle&ID=2087595>
- [274] A. Webb, "Dielectric materials in magnetic resonance," *Concepts in Magnetic Resonance Part A*, vol. 38, no. 4, pp. 148–184, 2011.
- [275] Q. X. Yang, J. Wang, J. Wang, C. M. Collins, C. Wang, and M. B. Smith, "Reducing sar and enhancing cerebral signal-to-noise ratio with high permittivity padding at 3 t," *Magnetic resonance in medicine*, vol. 65, no. 2, pp. 358–362, 2011.

BIBLIOGRAPHY

- [276] W. M. Brink and A. G. Webb, "High permittivity pads reduce specific absorption rate, improve b1 homogeneity, and increase contrast-to-noise ratio for functional cardiac mri at 3 t," *Magnetic resonance in medicine*, vol. 71, no. 4, pp. 1632–1640, 2014.
- [277] B. S. Park, S. S. Rajan, J. W. Guag, and L. M. Angelone, "A novel method to decrease electric field and sar using an external high dielectric sleeve at 3 t head mri: Numerical and experimental results," *IEEE Transactions on Biomedical Engineering*, vol. 62, no. 4, pp. 1063–1069, 2015.
- [278] J. C. Lin, *Electromagnetic fields in biological systems*. CRC press, 2011.
- [279] K. Famm, B. Litt, K. J. Tracey, E. S. Boyden, and M. Slaoui, "Drug discovery: a jumpstart for electroceuticals," *Nature*, vol. 496, no. 7444, pp. 159–161, 2013.
- [280] M. S. Okun and P. R. Zeilman, "Parkinson's Disease: Guide to Deep Brain Stimulation Therapy," in *National Parkinson Foundation, Second Edition*, 2014.
- [281] W. G. Ondo, C. Meilak, and K. D. Vuong, "Predictors of battery life for the activa@soletra 7426 neurostimulator," *Parkinsonism & related disorders*, vol. 13, no. 4, pp. 240–242, 2007.
- [282] E. Moro, R. J. A. Esselink, J. Xie, M. Hommel, A. L. Benabid, and P. Pollak, "The impact on Parkinson's disease of electrical parameter settings in STN stimulation," *Neurology*, vol. 59, no. 5, pp. 706–713, Sep. 2002.
- [283] P. E. O'Suilleabhain, W. Frawley, C. Giller, and R. B. Dewey, "Tremor response to polarity, voltage, pulsewidth and frequency of thalamic stimulation," *Neurology*, vol. 60, no. 5, pp. 786–790, Mar. 2003.
- [284] M. Rizzone, M. Lanotte, B. Bergamasco, A. Tavella, E. Torre, G. Faccani, A. Melcarne, and L. Lopiano, "Deep brain stimulation of the subthalamic nucleus in Parkinson's disease: effects of variation in stimulation parameters," *Journal of Neurology, Neurosurgery, and Psychiatry*, vol. 71, no. 2, pp. 215–219, Aug. 2001.
- [285] J. Volkmann, J. Herzog, F. Kopper, and G. Deuschl, "Introduction to the programming of deep brain stimulators," *Movement Disorders: Official Journal of the Movement Disorder Society*, vol. 17 Suppl 3, pp. S181–187, 2002.
- [286] R. O. Cersósimo, M. Bartuluchi, S. Fortini, A. Soraru, H. Pomata, and R. H. Caraballo, "Vagus nerve stimulation: effectiveness and tolerability in 64 paediatric patients with refractory epilepsies," *Epileptic Disorders*, vol. 13, no. 4, pp. 382–388, 2011.
- [287] M. S. Okun, B. V. Gallo, G. Mandybur, J. Jagid, K. D. Foote, F. J. Revilla, R. Alterman, J. Jankovic, R. Simpson, F. Junn, L. Verhagen, J. E. Arle, B. Ford, R. R. Goodman, R. M. Stewart, S. Horn, G. H. Baltuch, B. H. Kopell, F. Marshall, D. Peichel, R. Pahwa, K. E. Lyons, A. I. Tröster, J. L. Vitek, M. Tagliati, and SJM DBS Study Group, "Subthalamic deep brain stimulation with a constant-current device in Parkinson's disease: an open-label randomised controlled trial," *The Lancet. Neurology*, vol. 11, no. 2, pp. 140–149, Feb. 2012.
- [288] P. Limousin and I. Martinez-Torres, "Deep brain stimulation for Parkinson's disease," *Neurotherapeutics: The Journal of the American Society for Experimental NeuroTherapeutics*, vol. 5, no. 2, pp. 309–319, Apr. 2008.

- [289] A. L. Benabid, S. Chabardes, J. Mitrofanis, and P. Pollak, "Deep brain stimulation of the subthalamic nucleus for the treatment of Parkinson's disease," *The Lancet Neurology*, vol. 8, no. 1, pp. 67–81, 2009.
- [290] A. Chopra, B. T. Klassen, and M. Stead, "Current clinical application of deep-brain stimulation for essential tremor," *Neuropsychiatric Disease and Treatment*, vol. 9, pp. 1859–1865, 2013.
- [291] A. M. Lozano and M. Hallett, "Preface," in *Handbook of Clinical Neurology*, ser. Brain Stimulation, A. M. L. a. M. Hallett, Ed. Elsevier, 2013, vol. 116, pp. ix–x.
- [292] P. Merton and H. Morton, "Stimulation of the cerebral cortex in the intact human subject," *Nature*, vol. 285, no. 5762, pp. 227–227, 1980.
- [293] P. M. Rossini, A. Barker, A. Berardelli, M. Caramia, G. Caruso, R. Cracco, M. Dimitrijević, M. Hallett, Y. Katayama, C. Lücking *et al.*, "Non-invasive electrical and magnetic stimulation of the brain, spinal cord and roots: basic principles and procedures for routine clinical application. report of an ifcn committee," *Electroencephalography and clinical neurophysiology*, vol. 91, no. 2, pp. 79–92, 1994.
- [294] F. Camera, *Electrical and magnetic stimulation of the central nervous system: identification of action mechanisms and optimization of applications*. PhD thesis, 2016.
- [295] A. T. Barker, R. Jalinous, and I. L. Freeston, "Non-invasive magnetic stimulation of human motor cortex," *Lancet (London, England)*, vol. 1, no. 8437, pp. 1106–1107, May 1985.
- [296] R. J. Ilmoniemi, J. Ruohonen, and J. Karhu, "Transcranial magnetic stimulation—a new tool for functional imaging of the brain," *Critical Reviews in Biomedical Engineering*, vol. 27, no. 3-5, pp. 241–284, 1999.
- [297] D. M. McLoughlin, "Review: repetitive transcranial magnetic stimulation is of unknown effectiveness in people with depression," *Evidence-Based Mental Health*, vol. 6, no. 4, p. 118, Nov. 2003.
- [298] C. K. Loo and P. B. Mitchell, "A review of the efficacy of transcranial magnetic stimulation (TMS) treatment for depression, and current and future strategies to optimize efficacy," *Journal of Affective Disorders*, vol. 88, no. 3, pp. 255–267, Nov. 2005.
- [299] P. Anninos, A. Kotini, D. Tamiolakis, and N. Tsagas, "Transcranial magnetic stimulation. A case report and review of the literature," *Acta Neurologica Belgica*, vol. 106, no. 1, pp. 26–30, Mar. 2006.
- [300] M. C. Ridding and J. C. Rothwell, "Is there a future for therapeutic use of transcranial magnetic stimulation?" *Nature Reviews Neuroscience*, vol. 8, no. 7, pp. 559–567, 2007.
- [301] N. Bolognini and T. Ro, "Transcranial magnetic stimulation: disrupting neural activity to alter and assess brain function," *The Journal of Neuroscience*, vol. 30, no. 29, pp. 9647–9650, 2010.
- [302] F. S. Bersani, A. Minichino, P. Enticott, L. Mazarini, N. Khan, G. Antonacci, R. Raccah, M. Salviati, R. Delle Chiaie, G. Bersani *et al.*, "Deep transcranial magnetic stimulation as a treatment for psychiatric disorders: a comprehensive review," *European Psychiatry*, vol. 28, no. 1, pp. 30–39, 2013.

BIBLIOGRAPHY

- [303] A. R. Brunoni, M. A. Nitsche, N. Bolognini, M. Bikson, T. Wagner, L. Merabet, D. J. Edwards, A. Valero-Cabre, A. Rotenberg, A. Pascual-Leone *et al.*, “Clinical research with transcranial direct current stimulation (tdcs): challenges and future directions,” *Brain stimulation*, vol. 5, no. 3, pp. 175–195, 2012.
- [304] H. R. Siebner, N. Lang, V. Rizzo, M. A. Nitsche, W. Paulus, R. N. Lemon, and J. C. Rothwell, “Preconditioning of low-frequency repetitive transcranial magnetic stimulation with transcranial direct current stimulation: evidence for homeostatic plasticity in the human motor cortex,” *The Journal of neuroscience*, vol. 24, no. 13, pp. 3379–3385, 2004.
- [305] F. Fregni, P. Boggio, M. Nitsche, and A. Pascual-Leone, “Transcranial direct current stimulation,” *The British Journal of Psychiatry*, vol. 186, no. 5, pp. 446–447, 2005.
- [306] M. A. Nitsche, L. G. Cohen, E. M. Wassermann, A. Priori, N. Lang, A. Antal, W. Paulus, F. Hummel, P. S. Boggio, F. Fregni *et al.*, “Transcranial direct current stimulation: state of the art 2008,” *Brain stimulation*, vol. 1, no. 3, pp. 206–223, 2008.
- [307] M. A. Nitsche, A. Schauenburg, N. Lang, D. Liebetanz, C. Exner, W. Paulus, and F. Tergau, “Facilitation of implicit motor learning by weak transcranial direct current stimulation of the primary motor cortex in the human,” *Journal of cognitive neuroscience*, vol. 15, no. 4, pp. 619–626, 2003.
- [308] S. C. Andrews, K. E. Hoy, P. G. Enticott, Z. J. Daskalakis, and P. B. Fitzgerald, “Improving working memory: the effect of combining cognitive activity and anodal transcranial direct current stimulation to the left dorsolateral prefrontal cortex,” *Brain stimulation*, vol. 4, no. 2, pp. 84–89, 2011.
- [309] S. H. Ohn, C.-I. Park, W.-K. Yoo, M.-H. Ko, K. P. Choi, G.-M. Kim, Y. T. Lee, and Y.-H. Kim, “Time-dependent effect of transcranial direct current stimulation on the enhancement of working memory,” *Neuroreport*, vol. 19, no. 1, pp. 43–47, 2008.
- [310] C. A. Bassett, R. J. Pawluk, and A. A. Pilla, “Augmentation of bone repair by inductively coupled electromagnetic fields,” *Science (New York, N.Y.)*, vol. 184, no. 4136, pp. 575–577, May 1974.
- [311] V. Di Lazzaro, F. Capone, F. Apollonio, P. A. Borea, R. Cadossi, L. Fassina, C. Grassi, M. Liberti, A. Paffi, M. Parazzini, K. Varani, and P. Ravazzani, “A Consensus Panel Review of Central Nervous System Effects of the Exposure to Low-Intensity Extremely Low-Frequency Magnetic Fields,” *Brain Stimulation*, vol. 6, no. 4, pp. 469–476, Jul. 2013.
- [312] C. Cook, A. Thomas, and F. Prato, “Human electrophysiological and cognitive effects of exposure to ELF magnetic and ELF modulated RF and microwave fields: A review of recent studies,” *Bioelectromagnetics*, vol. 23, no. 2, pp. 144–157, Feb. 2002.
- [313] C. Cook, D. Saucier, A. Thomas, and F. Prato, “Exposure to ELF magnetic and ELF-modulated radiofrequency fields: The time course of physiological and cognitive effects observed in recent studies (2001–2005),” *Bioelectromagnetics*, vol. 27, no. 8, pp. 613–627, Dec. 2006.
- [314] V. Di Lazzaro and U. Ziemann, “The contribution of transcranial magnetic stimulation in the functional evaluation of microcircuits in human motor cortex,” *Frontiers in Neural Circuits*, vol. 7, p. 18, 2013.

- [315] G. Grant, R. Cadossi, and G. Steinberg, "Protection against focal cerebral ischemia following exposure to a pulsed electromagnetic field," *Bioelectromagnetics*, vol. 15, no. 3, pp. 205–216, 1994.
- [316] J. A. Robertson, A. W. Thomas, Y. Bureau, and F. S. Prato, "The influence of extremely low frequency magnetic fields on cytoprotection and repair," *Bioelectromagnetics*, vol. 28, no. 1, pp. 16–30, Jan. 2007.
- [317] J. C. Pena-Philippides, Y. Yang, O. Bragina, S. Hagberg, E. Nemoto, and T. Roitbak, "Effect of pulsed electromagnetic field (PEMF) on infarct size and inflammation after cerebral ischemia in mice," *Translational Stroke Research*, vol. 5, no. 4, pp. 491–500, Aug. 2014.
- [318] A. W. Thomas, M. Kavaliers, F. S. Prato, and K. P. Ossenkopp, "Antinociceptive effects of a pulsed magnetic field in the land snail, *Cepaea nemoralis*," *Neuroscience Letters*, vol. 222, no. 2, pp. 107–110, Jan. 1997.
- [319] J. Modolo, A. W. Thomas, R. Z. Stodilka, F. S. Prato, and A. Legros, "Modulation of neuronal activity with extremely low-frequency magnetic fields: Insights from biophysical modeling," *Proceedings 2010 IEEE 5th International Conference on Bio-Inspired Computing: Theories and Applications, BIC-TA 2010*, pp. 1356–1364, 2010.
- [320] B. E. McKay, M. A. Persinger, and S. A. Koren, "Exposure to a theta-burst patterned magnetic field impairs memory acquisition and consolidation for contextual but not discrete conditioned fear in rats," *Neuroscience Letters*, vol. 292, no. 2, pp. 99–102, Oct. 2000.
- [321] N. Lagace, L. S. St-Pierre, and M. Persinger, "Attenuation of epilepsy-induced brain damage in the temporal cortices of rats by exposure to LTP-patterned magnetic fields," *Neuroscience Letters*, vol. 450, no. 2, pp. 147–151, Jan. 2009.
- [322] A. Thomas, F. Prato, M. Kavaliers, and M. Persinger, "Electrotherapy device using low frequency magnetic pulses," May 22 2001, uS Patent 6,234,953. [Online]. Available: <http://www.google.com/patents/US6234953>
- [323] A. W. Thomas, K. Graham, F. S. Prato, J. McKay, P. M. Forster, D. E. Moulin, and S. Chari, "A randomized, double-blind, placebo-controlled clinical trial using a low-frequency magnetic field in the treatment of musculoskeletal chronic pain," *Pain Research & Management: The Journal of the Canadian Pain Society = Journal De La Société Canadienne Pour Le Traitement De La Douleur*, vol. 12, no. 4, pp. 249–258, 2007.
- [324] N. M. Shupak, F. S. Prato, and A. W. Thomas, "Human exposure to a specific pulsed magnetic field: effects on thermal sensory and pain thresholds," *Neuroscience Letters*, vol. 363, no. 2, pp. 157–162, Jun. 2004.
- [325] C. M. Cook, A. W. Thomas, and F. S. Prato, "Resting EEG is affected by exposure to a pulsed ELF magnetic field," *Bioelectromagnetics*, vol. 25, no. 3, pp. 196–203, Apr. 2004.
- [326] C. Cook, D. Saucier, A. Thomas, and F. Prato, "Changes in human EEG alpha activity following exposure to two different pulsed magnetic field sequences," *Bioelectromagnetics*, vol. 30, no. 1, pp. 9–20, Jan. 2009.

BIBLIOGRAPHY

- [327] R. Z. Stodilka, J. Modolo, F. S. Prato, J. A. Robertson, C. Cook, J. Patrick, A. Beuter, A. W. Thomas, and A. Legros, "Pulsed magnetic field exposure induces lasting changes in neural network dynamics," *Neurocomputing*, vol. 74, no. 12-13, pp. 2164–2175, Jun. 2011.
- [328] G. Thamsborg, A. Florescu, P. Oturai, E. Fallentin, K. Tritsarlis, and S. Dissing, "Treatment of knee osteoarthritis with pulsed electromagnetic fields: a randomized, double-blind, placebo-controlled study," *Osteoarthritis and Cartilage*, vol. 13, no. 7, pp. 575–581, Jul. 2005.
- [329] M. Fini, G. Giavaresi, P. Torricelli, F. Cavani, S. Setti, V. Canè, and R. Giardino, "Pulsed electromagnetic fields reduce knee osteoarthritic lesion progression in the aged Dunkin Hartley guinea pig," *Journal of Orthopaedic Research*, vol. 23, no. 4, pp. 899–908, Jul. 2005.
- [330] F. Capone, M. Dileone, P. Profice, F. Pilato, G. Musumeci, G. Minicuci, F. Ranieri, R. Cadossi, S. Setti, P. A. Tonali, and V. Di Lazzaro, "Does exposure to extremely low frequency magnetic fields produce functional changes in human brain?" *Journal of Neural Transmission*, vol. 116, no. 3, pp. 257–265, Mar. 2009.
- [331] P. Bech, M. Gefke, M. Lunde, L. Lauritzen, and K. Martiny, "The Pharmacopsychometric Triangle to Illustrate the Effectiveness of T-PEMF Concomitant with Antidepressants in Treatment Resistant Patients: A Double-Blind, Randomised, Sham-Controlled Trial Revisited with Focus on the Patient-Reported Outcomes," *Depression Research and Treatment*, vol. 2011, pp. 1–6, 2011.
- [332] K. Martiny, M. Lunde, and P. Bech, "Transcranial Low Voltage Pulsed Electromagnetic Fields in Patients with Treatment-Resistant Depression," *Biological Psychiatry*, vol. 68, no. 2, pp. 163–169, Jul. 2010.
- [333] N. De Geeter, G. Crevecoeur, L. Dupré, W. Van Hecke, and A. Leemans, "A DTI-based model for TMS using the independent impedance method with frequency-dependent tissue parameters," *Physics in Medicine and Biology*, vol. 57, no. 8, pp. 2169–2188, Apr. 2012.
- [334] C. Del Seppia, L. Mezzasalma, E. Choleris, P. Luschi, and S. Ghione, "Effects of magnetic field exposure on open field behaviour and nociceptive responses in mice," *Behavioural Brain Research*, vol. 144, no. 1-2, pp. 1–9, Sep. 2003.
- [335] C. Del Seppia, S. Ghione, P. Luschi, K.-P. Ossenkopp, E. Choleris, and M. Kavaliers, "Pain perception and electromagnetic fields," *Neuroscience & Biobehavioral Reviews*, vol. 31, no. 4, pp. 619–642, 2007.
- [336] J. A. Robertson, J. Theberge, J. Weller, D. J. Drost, F. S. Prato, and A. W. Thomas, "Low-frequency pulsed electromagnetic field exposure can alter neuroprocessing in humans," *Journal of The Royal Society Interface*, vol. 7, no. 44, pp. 467–473, Mar. 2010.
- [337] J. A. Robertson, N. Juen, J. Théberge, J. Weller, D. J. Drost, F. S. Prato, and A. W. Thomas, "Evidence for a dose-dependent effect of pulsed magnetic fields on pain processing," *Neuroscience Letters*, vol. 482, no. 2, pp. 160–162, Sep. 2010.
- [338] M. Fuller, J. Dobson, H. G. Wieser, and S. Moser, "On the sensitivity of the human brain to magnetic fields: evocation of epileptiform activity," *Brain Research Bulletin*, vol. 36, no. 2, pp. 155–159, 1995.

- [339] J. Dobson, T. St Pierre, H. G. Wieser, and M. Fuller, "Changes in paroxysmal brainwave patterns of epileptics by weak-field magnetic stimulation," *Bioelectromagnetics*, vol. 21, no. 2, pp. 94–99, Feb. 2000.
- [340] K. Heusser, D. Telschaft, and F. Thoss, "Influence of an alternating 3 Hz magnetic field with an induction of 0.1 millitesla on chosen parameters of the human occipital EEG," *Neuroscience Letters*, vol. 239, no. 2-3, pp. 57–60, Dec. 1997.
- [341] H. A. Haus and J. R. Melcher, *Electromagnetic fields and energy*. Prentice Hall, 1989.
- [342] J. Larsson, "Electromagnetics from a quasistatic perspective," *American Journal of Physics*, vol. 75, no. 3, pp. 230–239, 2007.
- [343] O. P. Gandhi, J. F. Deford, and H. Kanai, "Impedance method for calculation of power deposition patterns in magnetically induced hyperthermia," *IEEE Transactions on Biomedical Engineering*, no. 10, pp. 644–651, 1984.
- [344] D. W. Armitage, H. H. LeVeen, and R. Pethig, "Radiofrequency-induced hyperthermia: computer simulation of specific absorption rate distributions using realistic anatomical models," *Physics in Medicine and Biology*, vol. 28, no. 1, pp. 31–42, 1983.
- [345] G. d'Inzeo, C. Giacomozzi, and S. Pisa, "Analysis of the stimulation of a nerve fiber surrounded by an inhomogeneous, anisotropic, and dispersive tissue," *ACES J*, vol. 7, no. 2, pp. 179–190, 1992.
- [346] G. D'Inzeo, K. P. Esselle, S. Pisa, and M. A. Stuchly, "Comparison of homogeneous and heterogeneous tissue models for coil optimization in neural stimulation," *Radio Science*, vol. 30, no. 1, pp. 245–253, Jan. 1995.
- [347] S. Pisa, F. Apollonio, and G. d'Inzeo, "A Complete Model for the Evaluation of the Magnetic Stimulation of Peripheral Nerves," *The Open Biomedical Engineering Journal*, vol. 8, pp. 1–12, Jan. 2014.
- [348] F. Liu, H. Zhao, and S. Crozier, "On the induced electric field gradients in the human body for magnetic stimulation by gradient coils in MRI," *IEEE Transactions on Biomedical Engineering*, vol. 50, no. 7, pp. 804–815, Jul. 2003.
- [349] D. W. Armitage, H. H. LeVeen, and R. Pethig, "Radiofrequency-induced hyperthermia: computer simulation of specific absorption rate distributions using realistic anatomical models," *Physics in medicine and biology*, vol. 28, no. 1, p. 31, 1983.
- [350] Y. Saad and H. A. van der Vorst, "Iterative solution of linear systems in the 20th century," *Journal of Computational and Applied Mathematics*, vol. 123, no. 1–2, pp. 1–33, Nov. 2000.
- [351] H. A. van der Vorst, "Efficient and reliable iterative methods for linear systems," *Journal of Computational and Applied Mathematics*, vol. 149, no. 1, pp. 251–265, Dec. 2002.
- [352] A. Hirata, K. Yanase, I. Laakso, K. H. Chan, O. Fujiwara, T. Nagaoka, S. Watanabe, E. Conil, and J. Wiart, "Estimation of the whole-body averaged SAR of grounded human models for plane wave exposure at respective resonance frequencies," *Physics in Medicine and Biology*, vol. 57, no. 24, pp. 8427–8442, Dec. 2012.

BIBLIOGRAPHY

- [353] C. C. McIntyre, W. M. Grill, D. L. Sherman, and N. V. Thakor, "Cellular effects of deep brain stimulation: model-based analysis of activation and inhibition," *Journal of Neurophysiology*, vol. 91, no. 4, pp. 1457–1469, Apr. 2004.
- [354] L. Heller and D. B. van Hulsteyn, "Brain stimulation using electromagnetic sources: theoretical aspects." *Biophysical journal*, vol. 63, no. 1, p. 129, 1992.
- [355] T. A. Wagner, M. Zahn, A. J. Grodzinsky, and A. Pascual-Leone, "Three-dimensional head model simulation of transcranial magnetic stimulation," *IEEE transactions on bio-medical engineering*, vol. 51, no. 9, pp. 1586–1598, Sep. 2004.
- [356] C. Schmidt, P. Grant, M. Lowery, and U. van Rienen, "Influence of uncertainties in the material properties of brain tissue on the probabilistic volume of tissue activated," *Biomedical Engineering, IEEE Transactions on*, vol. 60, no. 5, pp. 1378–1387, 2013.
- [357] C. R. Butson and C. C. McIntyre, "Tissue and electrode capacitance reduce neural activation volumes during deep brain stimulation," *Clinical neurophysiology*, vol. 116, no. 10, pp. 2490–2500, 2005.
- [358] P. F. Grant and M. M. Lowery, "Effect of dispersive conductivity and permittivity in volume conductor models of deep brain stimulation," *IEEE transactions on bio-medical engineering*, vol. 57, no. 10, pp. 2386–2393, Oct. 2010.
- [359] T. Wagner, U. Eden, J. Rushmore, C. J. Russo, L. Dipietro, F. Fregni, S. Simon, S. Rotman, N. B. Pitskel, C. Ramos-Estebanez *et al.*, "Impact of brain tissue filtering on neurostimulation fields: a modeling study," *Neuroimage*, vol. 85, pp. 1048–1057, 2014.
- [360] D. Miklavčič, N. Pavšelj, and F. X. Hart, "Electric properties of tissues," *Wiley encyclopedia of biomedical engineering*, 2006.
- [361] A. Paffi, F. Camera, E. Lucano, F. Apollonio, and M. Liberti, "Time resolved dosimetry of human brain exposed to low frequency pulsed magnetic fields," *Physics in Medicine and Biology*, vol. 61, no. 12, p. 4452, 2016.
- [362] M. S. Okun, "Deep-brain stimulation for Parkinson's disease." *The New England journal of medicine*, vol. 367, no. 16, pp. 1529–38, oct 2012. [Online]. Available: <http://www.ncbi.nlm.nih.gov/pubmed/23075179>
- [363] R. Salvador, S. Silva, P. Basser, and P. Miranda, "Determining which mechanisms lead to activation in the motor cortex: a modeling study of transcranial magnetic stimulation using realistic stimulus waveforms and sulcal geometry," *Clinical neurophysiology*, vol. 122, no. 4, pp. 748–758, 2011.
- [364] P. Bech, M. Gefke, M. Lunde, L. Lauritzen, and K. Martiny, "The pharmacopsychometric triangle to illustrate the effectiveness of t-pemf concomitant with antidepressants in treatment resistant patients: a double-blind, randomised, sham-controlled trial revisited with focus on the patient-reported outcomes," *Depression research and treatment*, vol. 2011, 2011.
- [365] C. Cook, D. Saucier, A. Thomas, and F. Prato, "Exposure to elf magnetic and elf-modulated radiofrequency fields: the time course of physiological and cognitive effects observed in recent studies (2001–2005)," *Bioelectromagnetics*, vol. 27, no. 8, pp. 613–627, 2006.

- [366] F. Apollonio, M. Liberti, A. Paffi, C. Merla, P. Marracino, A. Denzi, C. Marino, and G. d’Inzeo, “Feasibility for microwaves energy to affect biological systems via nonthermal mechanisms: a systematic approach,” *IEEE Transactions on Microwave Theory and Techniques*, vol. 61, no. 5, pp. 2031–2045, 2013.
- [367] E. Neufeld, D. Szczerba, N. Chavannes, and N. Kuster, “A novel medical image data-based multi-physics simulation platform for computational life sciences,” *Interface Focus*, vol. 3, no. 2, p. 20120058, Apr. 2013.
- [368] A. Paffi, F. Apollonio, M. G. Puxeddu, M. Parazzini, G. d’Inzeo, P. Ravazzani, and M. Liberti, “A Numerical Study to Compare Stimulations by Intraoperative Microelectrodes and Chronic Macroelectrodes in the DBS Technique,” *BioMed Research International*, vol. 2013, p. e262739, Oct. 2013.
- [369] A. Paffi, F. Camera, F. Apollonio, G. d’Inzeo, and M. Liberti, “Numerical characterization of intraoperative and chronic electrodes in deep brain stimulation,” *Frontiers in Computational Neuroscience*, vol. 9, p. 2, 2015.
- [370] A. Paffi, F. Camera, F. Carducci, G. Rubino, P. Tampieri, M. Liberti, and F. Apollonio, “A computational model for real-time calculation of electric field due to transcranial magnetic stimulation in clinics,” *International Journal of Antennas and Propagation*, vol. 2015, 2015.
- [371] C. C. McIntyre, S. Mori, D. L. Sherman, N. V. Thakor, and J. L. Vitek, “Electric field and stimulating influence generated by deep brain stimulation of the subthalamic nucleus.” *Clinical neurophysiology : official journal of the International Federation of Clinical Neurophysiology*, vol. 115, no. 3, pp. 589–95, mar 2004. [Online]. Available: <http://www.ncbi.nlm.nih.gov/pubmed/15036055>
- [372] T. Wagner, A. Valero-Cabre, and A. Pascual-Leone, “Noninvasive human brain stimulation.” *Annual review of biomedical engineering*, vol. 9, pp. 527–65, jan 2007. [Online]. Available: <http://www.ncbi.nlm.nih.gov/pubmed/17444810>
- [373] M. Liberti, F. Apollonio, A. Paffi, M. Parazzini, F. Maggio, T. Novellino, P. Ravazzani, and G. D’Inzeo, “Fundamental electrical quantities in deep brain stimulation: influence of domain dimensions and boundary conditions,” *Conference proceedings: ... Annual International Conference of the IEEE Engineering in Medicine and Biology Society. IEEE Engineering in Medicine and Biology Society. Annual Conference*, vol. 2007, pp. 6669–6672, 2007.
- [374] C. Schmidt, T. Flisgen, and U. van Rienen, “Efficient computation of the neural activation during deep brain stimulation for dispersive electrical properties of brain tissue,” *IEEE Transactions on Magnetics*, vol. 52, no. 3, pp. 1–4, 2016.
- [375] A. Paffi, F. Camera, F. Apollonio, G. d’Inzeo, and M. Liberti, “Restoring the encoding properties of a stochastic neuron model by an exogenous noise,” *Frontiers in computational neuroscience*, vol. 9, 2015.
- [376] A. Paffi, F. Apollonio, G. d’Inzeo, and M. Liberti, “Stochastic resonance induced by exogenous noise in a model of a neuronal network,” *Network (Bristol, England)*, vol. 24, no. 3, pp. 99–113, 2013.

BIBLIOGRAPHY

- [377] M. Gianni, A. Paffi, M. Liberti, F. Apollonio, and G. D’Inzeo, “Channel noise may tune electromagnetic fields detectability in neurons: Stochastic resonance paradigm in a HH-like model,” *WSEAS Transactions on Communications*, vol. 4, no. 12, pp. 1406–1410, Dec. 2005.
- [378] F. Camera, A. Paffi, A. W. Thomas, F. Apollonio, G. D’Inzeo, F. S. Prato, and M. Liberti, “The CNP signal is able to silence a supra threshold neuronal model,” *Frontiers in Computational Neuroscience*, vol. 9, p. 44, 2015.
- [379] A. Canova, F. Freschi, L. Giaccone, and M. Repetto, “Exposure of working population to pulsed magnetic fields,” *IEEE Transactions on Magnetics*, vol. 46, no. 8, pp. 2819–2822, 2010.
- [380] F. Liu, S. Crozier, H. Zhao, and B. Lawrence, “Finite-difference time-domain-based studies of mri pulsed field gradient-induced eddy currents inside the human body,” *Concepts in Magnetic Resonance*, vol. 15, no. 1, pp. 26–36, 2002.
- [381] F. Liu and S. Crozier, “Electromagnetic fields inside a lossy, multilayered spherical head phantom excited by mri coils: models and methods,” *Physics in Medicine and Biology*, vol. 49, no. 10, p. 1835, 2004.
- [382] M. E. Mognaschi, P. Di Barba, G. Magenes, A. Lenzi, F. Naro, and L. Fassina, “Field models and numerical dosimetry inside an extremely-low-frequency electromagnetic bioreactor: the theoretical link between the electromagnetically induced mechanical forces and the biological mechanisms of the cell tensesgrity,” *SpringerPlus*, vol. 3, no. 1, p. 1, 2014.
- [383] A. Christ, W. Kainz, E. G. Hahn, K. Honegger, M. Zefferer, E. Neufeld, W. Rascher, R. Janka, W. Bautz, J. Chen *et al.*, “The virtual family—development of surface-based anatomical models of two adults and two children for dosimetric simulations,” *Physics in medicine and biology*, vol. 55, no. 2, p. N23, 2009.
- [384] P. A. Hasgall, E. Neufeld, M. C. Gosselin, A. Klingensböck, and N. Kuster, “ITIS Database for thermal and electromagnetic parameters of biological tissues, Version 2.2,” *ResearchGate*, Jan. 2011.
- [385] F. Benazzo, G. Zanon, L. Pederzini, F. Modonesi, C. Cardile, F. Falez, L. Ciolli, F. La Cava, S. Giannini, R. Buda *et al.*, “Effects of biophysical stimulation in patients undergoing arthroscopic reconstruction of anterior cruciate ligament: prospective, randomized and double blind study,” *Knee Surgery, Sports Traumatology, Arthroscopy*, vol. 16, no. 6, pp. 595–601, 2008.
- [386] D. Romano, S. Pisa, and E. PiuZZi, “Implementation of the newton-raphson and admittance methods for eit,” *International Journal of Bioelectromagnetism*, vol. 12, no. 1, pp. 12–20, 2010.
- [387] L. Golestanirad, M. Mattes, J. R. Mosig, and C. Pollo, “Effect of Model Accuracy on the Result of Computed Current Densities in the Simulation of Transcranial Magnetic Stimulation,” *IEEE Transactions on Magnetics*, vol. 46, no. 12, pp. 4046 – 4051, 2010.
- [388] A. Hirata, K. Yanase, I. Laakso, K. H. Chan, O. Fujiwara, T. Nagaoka, S. Watanabe, E. Conil, and J. Wiart, “Estimation of the whole-body averaged SAR of grounded human models for plane wave exposure at respective resonance frequencies.” *Physics*

in medicine and biology, vol. 57, no. 24, pp. 8427–42, dec 2012. [Online]. Available: <http://www.ncbi.nlm.nih.gov/pubmed/23202273>

- [389] V. De Santis, M. Douglas, J. Nadakuduti, S. Benkler, X. L. Chen, and N. Kuster, “Human exposure from pulsed magnetic field therapy mats: A numerical case study with three commercial products,” *Bioelectromagnetics*, vol. 36, no. 2, pp. 149–161, 2015. [Online]. Available: <http://doi.wiley.com/10.1002/bem.21894>
- [390] L. Liu, A. Trakic, H. Sanchez-Lopez, F. Liu, and S. Crozier, “An analysis of the gradient-induced electric fields and current densities in human models when situated in a hybrid mri-linac system,” *Physics in medicine and biology*, vol. 59, no. 1, p. 233, 2013.
- [391] B. J. Roth, J. M. Saypol, M. Hallett, and L. G. Cohen, “A theoretical calculation of the electric field induced in the cortex during magnetic stimulation,” *Electroencephalography and Clinical Neurophysiology*, vol. 81, no. 1, pp. 47–56, Feb. 1991.
- [392] A. Papoulis and S. U. Pillai, *Probability, random variables, and stochastic processes*. Tata McGraw-Hill Education, 2002.

Curriculum Vitae

Elena Lucano

PhD candidate in Electronic Engineering

+39 3889383656

✉ lucano@diet.uniroma1.it,
elena.lucano88@gmail.com

Personal Details

Name Elena Lucano
Date of Birth 19th October 1988
Birth Place Roma (RM), Italy
Place of Residence Via Collacchi 3,
02032 Fara in Sabina (RI), Italy
Citizenship Italian

Research Activity

Date (from-to) 1st November 2013 - 31st October 2016
Institute *Sapienza University of Rome*, DIET Department (Dipartimento di Ingegneria dell'Informazione, Elettronica e Telecomunicazioni); Rome, Italy.
Position PhD student
Research Activities **Development of computational models and measurements of RF body coils for MRI**, in collaboration with the U.S. Food and Drug Administration (Silver Spring, USA-MD).
Test field diversification method for the safety assessment of RF-induced heating of medical implants during MRI at 64 MHz, in collaboration with the IT'IS foundation (Zurich, Switzerland).
High dielectric material in MRI: numerical assessment of the reduction of the induced local power on implanted cardiac leads, in collaboration with National Institute of Health (Rome, Italy).

Date (from-to) 4th April 2013 - 29th February 2016
Institute *U.S. Food and Drug Administration*, Office of Science and Engineering Laboratories Center for Devices and Radiological Health, Division of Biomedical Physics; Silver Spring, USA-MD
Position ORISE Research Fellow
Research Activity **Development of computational models of a RF coil for MRI at 1.5 T, and compatibility studies of active implantable medical devices exposed to RF Electromagnetic fields of MRI systems**, in collaboration with Imricor Medical Systems (Burnsville, USA-MN).

Impact of the vague partial body SAR definition in the MRI safety standard IEC 60601-2-33 on actual patient exposure, in collaboration with the IT'IS foundation (Zurich, Switzerland).

Research Experience

- Date (from - to) 8th August 2016 - 8th September 2016
Host Institute Laboratories of the U.S. Food and Drug Administration, 10903 New Hampshire Avenue Silver Spring, MD 20993
Position ORISE Research Fellow
Supervisors Leonardo Maria Angelone
Research Activity Validation of numerical data with experimental measurements
- Date (from - to) 27th June 2016 - 6th July 2016
Host Institute Laboratories of the IT'IS foundation (Zurich, Switzerland), Zeughausstrasse 43 CH-8004 Zurich
Position Visiting scientist
Research Activity RF electric and magnetic field measurements in the MITS1.5 system using the dosimetric and near-field assessment system (DASY52) in different phantoms.
- Date (from - to) 19th October 2015 - 22nd January 2016
Host Institute Laboratories of the IT'IS foundation (Zurich, Switzerland), Zeughausstrasse 43 CH-8004 Zurich
Position Short Term Scientific Mission (STSM) in the framework of COST Action in the European network for innovative uses of EMFs in biomedical applications (COST BM 1309 Action EMF-MED).
Supervisors Earl Zastrow, Ph.D and Manuel Murbach, Ph.D.
Research Activity Participation to the development of a novel experimental testing method for safety assessment of implantable devices during MRI exposure. Measurements of exposure with MITS1.5 and the MITS3.0, and piX system (ZurichMedTech, Switzerland).
- Date (from - to) June 2012 - December 2012
Host Institute National Institute of Health(ISS), Viale Regina Elena, 299, 00161 Roma
Position Master's Degree Fellow
Supervisor Dr. Micaela Liberti
Co-Supervisor Dr. Eugenio Mattei
Research Activity Development of custom RFID antennas, and measurements of electromagnetic compatibility between RFID signals and pacemakers.
- Date (from - to) June 2010 - December 2010
Host Institute IRCCS Santa Lucia, laboratory of Neurophysiopathology; Via Ardeatina, 306/354, 00142 Roma

Position	Bachelor Degree Fellow
Supervisor	Dr. Serenella Salinari
Co-Supervisor	Dr. Fabio Aloise
Research Activity	Recording and processing of Electroencephalographic(EEG) signals in the context of the Brain Computer Interfaces (BCI).

Scholarship

19/10/2015 - 22/01/2016	Fellowship by the COST BM 1309 Action EMF-MED - European network for innovative uses of EMFs in biomedical applications for a Short Term Scientific Mission (STSM) at Laboratories of the IT'IS foundation, Zeughausstrasse 43 CH-8004 Zurich
----------------------------	---

Teaching Experience

Date (from - to)	November 2013 - October 2016
Institute	<i>Sapienza University of Rome</i> , DIET Department (Dipartimento di Ingegneria dell'Informazione, Elettronica e Telecomunicazioni), Italy.
Activity	Lecturer for the course of Electromagnetic Fields under the direction of Dr. Francesca Apollonio. Lecturer for the course of Electromagnetic Compatibility under the direction of Dr. Alessandra Paffi. Lab assistant for the course of Electromagnetic Fields and Nanosystems under the direction of Dr. Micaela Liberti. Lab assistant for the course of Electrical Measurements under the direction of Dr. Emanuele Piuze. Trainer, under the direction of Dr. Micaela Liberti, for four bachelor students for their intern period.

Educational Background

2013–2016	Research doctoral thesis in Electrical Engineering , <i>Sapienza University of Rome</i> , DIET Department (Dipartimento di Ingegneria dell'Informazione, Elettronica e Telecomunicazioni), Italy.
Thesis Title	<i>Computational modeling and measurements of electromagnetic fields for diagnostics and therapeutics.</i>
Supervisor	Dr. Micaela Liberti
Co-Supervisor	Dr. Emanuele Piuze
2009–2012	Master Degree in Biomedical Engineering , <i>Sapienza University of Rome</i> , Facoltà di Ingegneria, Italy.
Thesis Title	<i>Electromagnetic interference of RFI systems on pacemakers: measurements setup and experimental evaluations.</i>
Supervisor	Dr. Micaela Liberti

CURRICULUM VITAE

Co-Supervisor Dr. Eugenio Mattei
Grade 110/110 cum laude

2005–2008 **Bachelor Degree in Clinical Engineering**, *Sapienza University of Rome*, Facoltà di Ingegneria, Italy.

Thesis Title *Analysis of attentive state levels for the Brain Computer Interface context.*

Supervisor Dr. Serenella Salinari

Co-Supervisor Dr. Fabio Aloise

Grade 102/110

2000–2005 **High School Diploma for science**, "*Amedeo Avogadro*", Roma (RM), Italy.

Grade 95/100

Awards and Travel supports

ISMRRM 2016 *Summa Cum Laude*, award for the abstract: "Inter-laboratory study of a computational radiofrequency coil model at 64 MHz"

Magna Cum Laude, award for the abstract: "Incident electric field on implanted lead vs. source position and field polarization"

Travel supports *ISMRRM 2016 (Singapore)*, student travel award

BioEM 2015 (Asilomar – CA, US), student travel award

Certificates

English languages **Course of study in English as a Second Language**, International Center for Language Studies, Washington DC www.ICLS.com, February-April 2014

TOEFL ITP, 590/627, English Language Center (ELC), Boston (MA) www.elc.edu, July 2006

Languages

MOTHER TONGUE **Italian**

OTHER LANGUAGES **English**: fluent

Technical Skills and Competences

- Programming Languages: basis of C++ and Python
- Software Application: Matlab, Photoshop, basis of SPICE

- Numerical Simulation Programs: Sim4Life (ZurichMedTech, Switzerland), xFDTD (Remcom Inc., USA), CST (Computer Simulation Technology, USA).
- Devices for electrical measurements: Oscilloscope, Digital Multimeter, Network analyzer
- Lab instrumentation: use of the DASY52 and PiX system (ZurichMedTech, Switzerland), basic knowledge of circuits developments on stripboards

Activities

- **Student Member**, ISMRM, 2013 - 2016
- **Student Member**, EBEA and BEMS, 2014 -2016

Publications:

International Journal Papers

- 2016 Published, August 2016.
Title **Assessing the Electromagnetic Fields Generated By a Radiofrequency MRI Body Coil at 64 MHz: Defeating Versus Accuracy.**
Journal IEEE Transactions on Biomedical Engineering
Authors Lucano E., Liberti M., Mendoza G.G., Lloyd T., Iacono M.I., Wedan S., Kainz W., Angelone L.M.
- 2016 Published, June 2016.
Title **Time Resolved Dosimetry of Human Brain Exposed to Low Frequency Pulsed Magnetic Fields.**
Journal Physics in Medicine and Biology
Authors Paffi A., Camera F., Lucano E., Apollonio F., Liberti M.
- 2016 Published, February 2016.
Title **Provocative testing for the assessment of the electromagnetic interference of RFID and NFC readers on implantable pacemaker.**
Journal IEEE Transactions on Electromagnetic Compatibility
Authors Mattei E., Lucano E., Censi F., Triventi M., Calcagnini G.

In preparation / under review

- Title **An inter-laboratory computational and experimental study of a radiofrequency coil model at 64 MHz.**
- Journal Journal of Magnetic Resonance in Medicine (MRM)
- Authors Lucano E., Kozlov M., Zastrow E., Louise S., Liberti M., Cabot E., Kainz W., Horner M., Kuster N., Angelone L.M.
-
- Title **A numerical investigation on the effect of RF coil feed variability on global and local electromagnetic field exposure in human body models at 64 MHz.**
- Journal Journal of Magnetic Resonance in Medicine (MRM)
- Authors Lucano E., Liberti M., Lloyd T., Apollonio F., Wedan S., Kainz W., Angelone L.M.
-
- Title **Local and global electromagnetic absorption in homogeneous and heterogeneous human models exposed to 64 MHz MRI RF field.**
- Journal International Journal for Numerical Methods in Biomedical Engineering
- Authors Lucano E., Angelone L.M., Apollonio F., Liberti M.

Full length conference proceedings

- 2016 38th Annual International IEEE EMBS Conference, Orlando
- Title **High dielectric material in MRI: numerical assessment of the reduction of their-induced local power on implanted cardiac leads.**
- Authors Mattei E., Lucano E., Censi F., Angelone L.M., Calcagnini G.
-
- Title **Effects of Tuning Conditions on Near Field of MRI Transmit Birdcage Coil at 64 MHz.**
- Authors Kozlov M., Lucano E., Angelone L.M.
-
- Title **RF induced energy for partially implanted catheters: a computational study.**
- Authors Lucano E., Liberti M., Lloyd T., Apollonio F., Wedan S., Kainz W., and Angelone L.M.

International Scientific Conferences and Workshops

- 2016 Platform
- Title **Incident electric field on implanted lead vs. source position and field polarization**, *In: Abstract collection of BioEM 2016 Conference*, June 5-10, Ghent, Belgium.
- Authors Lucano E., Liberti M., Apollonio F., Mendoza G., Lloyd T., Wedan S., Kainz W., Angelone L.M.
-
- Title **Inter-laboratory study of a computational radiofrequency coil model at 64 MHz**, *In: International Society of Magnetic Resonance in Medicine (ISMRM) 24th Annual Meeting and Exhibition*, May 7-13, Singapore.
- Authors Lucano E., Kozlov M., Louie S., Zastrow E., Cabot E., Horner M., Mendoza G., Yao A., Kainz W., Kuster N., Angelone L.M.
-
- Title **Incident electric field on implanted lead vs. source position and field polarization**, *In: International Society of Magnetic Resonance in Medicine (ISMRM) 24th Annual Meeting and Exhibition*, May 7-13, Singapore.
- Authors Lucano E., Liberti M., Mendoza G.G., Lloyd T., Apollonio F., Wedan S., Kainz W., and Angelone L.M.
-
- 2016 Poster
- Title **Test field diversification method for the safety assessment of RF-induced heating of medical implants during MRI at 64 MHz**, *In: Abstract collection of BioEM 2016 Conference*, June 5-10 Ghent, Belgium.
- Authors Lucano E., Yao A., Zastrow E., Kainz W., Liberti M., and Kuster N.
-
- Title **Impact of the vague partial body SAR definition in the MRI safety standard IEC 60601-2-33 on actual patient exposure**, *In: Abstract collection of BioEM 2016 Conference*, June 5-10 Ghent, Belgium.
- Authors Lucano E., Murbach M., Kainz W., Iacono M.I.
-
- Title **Source position and field polarization effect on MR induced heating for partially implanted leads**, *In: Abstract collection of BMES 2016 Conference*, May 23-25, College Park, MD-USA.
- Authors Lucano E., Liberti M., Mendoza G.G., Lloyd T., Apollonio F., Wedan S., Kainz W., Angelone L.M.

CURRICULUM VITAE

- 2015 Poster
- Title **How does the accuracy of the RF body coil model affect the analysis of RF-induced electric field with partially implanted wires?**, *In: Abstract collection of BioEM 2015 Conference*, Jun 14-19, Asilomar, California USA.
- Authors Lucano E., Liberti M., Apollonio F., Mendoza G., Lloyd T., Wedan S., Kainz W., Angelone L.M.
- Title **How do spatial resolution and model features of a radiofrequency coil affect electromagnetic field?**, *In: Abstract collection of BMES 2015 Conference*, May 18-20, College Park, MD-USA.
- Authors Lucano E., Mendoza G., Apollonio F., Angelone L.M., Liberti M.
- Title **Computational and experimental field analysis in a phantom for controlled electromagnetic exposure.**, *In: Abstract collection of BMES 2015 Conference*, May 18-20, College Park, MD-USA.
- Authors Lucano E., Mendoza G., Lloyd T., Wedan S., Kainz W., Angelone L.M.
- 2014 Platform
- Title **Computational modeling of radiofrequency body coil at 64 MHz: a comparison across different software platforms and experimental measurements**, *In: Medical Device Innovation Consortium (MDIC)*, June 25, Silver Spring, MD-USA.
- Authors Lucano E., Mendoza G.G., Louie S., Lloyd T., Huang X., Chen J., Wedan S., Horner M., Kainz W., Angelone L.M.
- 2014 Poster
- Title **Numerical and Experimental Test Configuration for Evaluating MRI Induced RF Heating of Interventional Devices**, *In: 10th Interventional MRI Symposium*, Oct 10-11, Leipzig, Germany.
- Authors Lucano E., Mendoza G., Lloyd T., Iacono M.I., Wedan S., Kainz W., Angelone L.M.
- Title **Building a computational model of a transmit body coil at 1.5T: considerations on electromagnetic field for RF safety.**, *In: International Society of Magnetic Resonance in Medicine (ISMRM) 22th Annual Meeting and Exhibition*, May 10-16, Milan, Italy.
- Authors Lucano E., Mendoza G., Lloyd T., Wedan S., Kainz W., Angelone L.M.

February 10, 2017